NASA/TM–2014-218549

Experimental Aeroheating Study of Mid-L/D Entry Vehicle Geometries: NASA LaRC 20-Inch Mach 6 Air Tunnel Test 6966

Brian R. Hollis
Langley Research Center, Hampton, Virginia

Kevin E. Hollingsworth
Jacobs Technology Inc., Hampton, Virginia

November 2014

NASA STI Program . . . in Profile

Since its founding, NASA has been dedicated to the advancement of aeronautics and space science. The NASA scientific and technical information (STI) program plays a key part in helping NASA maintain this important role.

The NASA STI program operates under the auspices of the Agency Chief Information Officer. It collects, organizes, provides for archiving, and disseminates NASA's STI. The NASA STI program provides access to the NASA Aeronautics and Space Database and its public interface, the NASA Technical Report Server, thus providing one of the largest collections of aeronautical and space science STI in the world. Results are published in both non-NASA channels and by NASA in the NASA STI Report Series, which includes the following report types:

- TECHNICAL PUBLICATION. Reports of completed research or a major significant phase of research that present the results of NASA Programs and include extensive data or theoretical analysis. Includes compilations of significant scientific and technical data and information deemed to be of continuing reference value. NASA counterpart of peer-reviewed formal professional papers, but having less stringent limitations on manuscript length and extent of graphic presentations.

- TECHNICAL MEMORANDUM. Scientific and technical findings that are preliminary or of specialized interest, e.g., quick release reports, working papers, and bibliographies that contain minimal annotation. Does not contain extensive analysis.

- CONTRACTOR REPORT. Scientific and technical findings by NASA-sponsored contractors and grantees.

- CONFERENCE PUBLICATION. Collected papers from scientific and technical conferences, symposia, seminars, or other meetings sponsored or co-sponsored by NASA.

- SPECIAL PUBLICATION. Scientific, technical, or historical information from NASA programs, projects, and missions, often concerned with subjects having substantial public interest.

- TECHNICAL TRANSLATION. English-language translations of foreign scientific and technical material pertinent to NASA's mission.

Specialized services also include organizing and publishing research results, distributing specialized research announcements and feeds, providing information desk and personal search support, and enabling data exchange services.

For more information about the NASA STI program, see the following:

- Access the NASA STI program home page at *http://www.sti.nasa.gov*

- E-mail your question to help@sti.nasa.gov

- Fax your question to the NASA STI Information Desk at 443-757-5803

- Phone the NASA STI Information Desk at 443-757-5802

- Write to:
  STI Information Desk
  NASA Center for AeroSpace Information
  7115 Standard Drive
  Hanover, MD 21076-1320

NASA/TM–2014-218549

Experimental Aeroheating Study of Mid-L/D Entry Vehicle Geometries: NASA LaRC 20-Inch Mach 6 Air Tunnel Test 6966

Brian R. Hollis
Langley Research Center, Hampton, Virginia

Kevin E. Hollingsworth
Jacobs Technology Inc., Hampton, Virginia

National Aeronautics and
Space Administration

Langley Research Center
Hampton, Virginia 23681-2199

November 2014

Available from:

NASA Center for AeroSpace Information
7115 Standard Drive
Hanover, MD 21076-1320
443-757-5802

Table of Contents

List of Tables

List of Figures

THIS PAGE INTENTIONALLY LEFT BLANK

Abstract

Heat transfer and boundary-layer transition data on mid lift-to-drag ratio entry vehicle configurations has been obtained through hypersonic wind tunnel testing. The data obtained in this study are intended for use in mission design studies and for the development and validation of computational methods. Vehicles of this class have been proposed for high-mass Mars missions, such as sample return and crewed exploration, for which the conventional sphere-cone entry vehicle geometries of previous Mars missions provide insufficient aerodynamic performance. Three configuration families were investigated: elliptically-blunted cylinders with both circular and elliptical cross sections; biconic geometries based on launch vehicle dual-use shrouds; and parametrically-optimized analytic geometries. Testing was conducted at Mach 6 over a range of Reynolds numbers sufficient to generate laminar, transitional, and turbulent flow. Global aeroheating data were obtained using phosphor thermography and both stream-wise and cross-flow transition was observed on different configurations. Comparisons were made with laminar and turbulent computational predictions generated with an algebraic turbulence model. Predictions were generally in good agreement with the data in regions of either laminar or fully-turbulent flow. However, for transitional regions, the lack of a transition-onset prediction capability in the computational model resulted in less accurate comparisons.

Nomenclature

Symbols

a_{lower}	Ellipsled body cross-section major axis (in.)
a_{nose}	Ellipsled nose major axis (in.)
b_{lower}	Ellipsled body cross-section minor axis (in.)
b_{nose}	Ellipsled nose minor axis (in.)
C_D	drag coefficient
C_p	local surface pressure coefficient
$C_{p,max}$	maximum surface pressure coefficient
D	maximum diameter (in. or m)
h	heat-transfer film-coefficient (kg/m^2-s)
h_{FR}	heat-transfer film-coefficient based on Fay-Riddell theory (kg/m^2-s)
H_0	tunnel total enthalpy (J/kg)
H_{AW}	adiabatic wall surface enthalpy (J/kg)
H_w	surface enthalpy (J/kg)
H_{300K}	enthalpy at 300 K temperature (J/kg)
L	vehicle length (in. or m)
L_1	Hammerhead 1st cone segments length
L_2	Hammerhead 2nd cone segments length
L/D	lift-to-drag ratio
m	vehicle mass (kg)
M_∞	free stream Mach number
p_∞	free stream pressure (Pa)
q	heat-transfer rate (W/cm^2)
q_{FR}	heat-transfer rate based on Fay-Riddell theory (W/cm^2)
r_{nose}	Hammerhead nose radius (in.)
r_{upper}	Ellipsled upper body cross-section (in.)
Re_∞	free stream Reynolds number (1/m or 1/ft)
S	reference surface area for aerodynamics (m^2)
T_∞	free stream temperature (K)
U_∞	free stream velocity (m/s)
x, y, z	Cartesian coordinates (in. or m)
α	angle of attack (deg)
β	ballistic coefficient (kg/m^2)
γ	specific heat ratio
θ	angle between local surface normal and velocity vectors
θ_1	Hammerhead 1st cone segment included half-angle
θ_2	Hammerhead 2nd cone segment included half-angle
ρ_∞	free stream density (kg/m^3)
μ_∞	free stream viscosity (kg/m-s)

Subscripts

∞	free stream
0	total or stagnation
FR	Fay-Riddell

w	wall

Acronyms

CFD	Computational Fluid Dynamics
COBRA	Co-Optimization of Blunt-body Reentry Analysis
IHEAT	Imaging for Hypersonic Experimental Aerothermodynamic Testing
LaRC	Langley Research Center
LAURA	Langley Aerothermodynamic Upwind Relaxation Algorithm

Background

The long-term goals of NASA's Mars exploration program include both robotic sample return missions and long-duration crewed missions. Such missions will require safe and precise landing of much larger masses than any previous Mars missions (10 mt to 50 mt). Recent systems analysis studies for such future missions (Refs. 1 - 4) have demonstrated that the heritage, 70-deg sphere-cone entry vehicle architecture employed in every NASA landing on Mars from Viking to the Mars Science Laboratory (MSL) cannot provide sufficient aerodynamic performance to decelerate and precisely target a desired landing site. One of the architectures identified by these studies that would enable such missions is a Mid-L/D (L/D ~ 0.4 to 0.8) entry-vehicle geometry, as illustrated in Figure 1. Mid-L/D geometries also have been identified as candidates for outer planet missions (e.g. to Neptune) for which aerocapture could be employed (Ref. 5).

In order to ensure the success of a mission in which a Mid-L/D geometry would be employed, the aerodynamic and aerothermodynamic (both convective heating and shock-layer radiation) environments must be understood. Because Mid-L/D geometries do not have the test, evaluation, and flight heritage of sphere-cone geometry entry vehicles, the current study was conducted in order to obtain experimental information on the convective aeroheating environment. An engineering-level analysis was also conducted to provide aerodynamic performance comparisons between the geometries. Computational predictions were generated using both laminar and turbulent models for comparisons with the data.

Mid-L/D Geometries

Various geometries have been proposed to meet the Mid-L/D entry vehicle requirements depending on the mission in question. In the present study, three separate families of geometries identified as Ellipsled, COBRA Optimized, and Hammerhead-Biconic, were considered. Details of each family are provided below. The common factor for all geometries was the specification of a 30 m flight vehicle length with a length to maximum-diameter ratio of 3:1, which was the baseline defined in Ref. 1.

Ellipsled Geometries

"Ellipsled" geometries, which consist of an elliptically-blunted nose and a cylindrical aftbody, have been proposed for various exploration missions that require aerocapture (e.g. Refs. 5 - 6). Two sub-classes of ellipsleds were considered herein: axisymmetric and flattened. The axisymmetric ellipsled has a circular cross-section and the flattened ellipsled cross-section is split between a circular top-half and an elliptical bottom-half. Three axisymmetric and two flattened ellipsled geometries were defined. For the axisymmetric geometries, the ellipticity of the nose was varied in the longitudinal direction to create different nose bluntness factors. For the flattened ellipsleds, the cross-sectional ellipticity of the lower half of the geometry was varied to produce a flatter bottom. A parametric definition of the Ellipsled family is shown in Figure 2 and the geometric parameters are defined in Table 1. The naming convention employed is "Ellipsled-x.xx-y.yy", where "x.xx" represents the nose-axes ratio (a_{nose}/b_{nose}) and "y.yy" represents the cross-section axes ratio (a_{lower}/b_{lower}) of the lower body half. Multi-view renderings of the five geometries: Ellipsled-0.50-100, Ellipsled-1.00-1.00, Ellipsled-2.00-1.00, Ellipsled-2.00-0.50 and Ellipsled-2.00-0.25 are shown in Figure 3-Figure 7, respectively.

COBRA Optimized Geometries

The "COBRA" (Co-Optimization of Blunt-body Re-entry Analysis) geometries were taken from Ref. 7 in which an optimization algorithm was developed to meet certain mission performance criteria, e.g. landed mass, convective heating rate, and aerodynamic performance. Starting from a spherically-capped cylinder (equivalent to the Ellipsled-1.00-1.00 geometry), a family of optimized geometries were generated that met the specified criteria for a high-mass Mars entry mission. Three representative geometries, COBRA-8459B, COBRA-14297B and COBRA-14888B, were selected from this family for testing. Multi-view renderings of these geometries are shown in Figure 8-Figure 10. Additional information on these geometries is provided in Ref. 7.

Hammerhead-Biconic Dual Use Shroud Geometries

The "Hammerhead-Biconic" geometries are based on a dual-use shroud concept for NASA's proposed Ares V heavy-lifter (Refs. 8 - 9). Although the Ares V program was cancelled, the general concept is applicable to any launch vehicle shroud. The shroud would be used during both ascent from Earth and aerocapture/entry-descent-landing at the destination. Three parametric geometries were developed based on this Hammerhead-Biconic concept. Nose radius was the primary geometric variation, with the length of the first cone and angle of the second cone then being varied to fit the geometric constraints of a constant first-cone angle and constant second-cone length. The rationale for these constraints was to minimize changes to the internal volume of the vehicle, which is a function mainly of the geometry of the second cone and the cylindrical third section. A parametric representation of the Hammerhead-Biconic is shown in Figure 11 and the geometric parameters are listed in Table 2. Multi-view renderings of the Hammerhead-Sharp, Hammerhead-Nominal, and Hammerhead-Blunt are shown in Figure 12-Figure 14.

Comparison of Aerodynamic Performance

In order to obtain a first-order understanding of the aerodynamics of the various configurations, a Modified-Newtonian analysis was performed. According to Modified-Newtonian theory, the aerodynamics of a vehicle travelling at hypersonic speed can be approximated by integration of the pressure coefficient, C_p, over the surface of the vehicle, where C_p is defined as:

$$(1)\quad C_p = C_{p,\max}\left(\cos\theta\right)^2$$

The maximum pressure coefficient, $C_{p,max}$, is the value obtained for a given free stream Mach number and specific heat ratio using the perfect-gas, normal shock relations; for the current analyses, values of $M_\infty = 30$ and $\gamma = 1.25$ (to approximate hypersonic flight at Mars) were used. The parameter θ is defined as the angle between the local surface normal vector and the free stream velocity vector. For computations of force and moment coefficients from the C_p distributions, reference dimensions of $L = 30$ m and $S = 78.54$ m^2 (based on the area of a circular 10 m diam. base) were used for all geometries.

The figures-of-merit for the aerodynamic analysis were the lift-to-drag ratio (L/D) and the reduced (mass-less) ballistic coefficient, β/m, based on the ballistic coefficient definition:

$$\beta = \frac{m}{C_D S} \tag{2}$$

The optimum aerodynamic performance is obtained for the highest L/D (for maneuverability and precision landing) at the lowest β/m (for greatest vehicle payload). These figures-of-merit are plotted in terms of L/D vs. angle-of-attack and reduced ballistic coefficient in Figure 15-Figure 16 for the Ellipsled geometries, Figure 17-Figure 18 for the COBRA geometries, and Figure 19-Figure 20 for the Hammerhead-Biconic geometries. Additionally, the angle-of-attack and reduced ballistic coefficient are tabulated for all geometries in Table 3 at L/D values of 0.4 and 0.8, which bounds the range of performance requirements for future high-mass Mars missions.

The flattened Ellipsled-2.00-0.25 produces the best performance and the axisymmetric Ellipsled-0.50-1.00 produces the worst performance in terms of maximum L/D. All geometries meet the required L/D range at angles-of-attack between 30-deg to 70-deg except the Ellipsled-0.50-1.00, Ellipsled-1.00-1.00, and Hammerhead-Blunt. However, in a complete mission system analysis, other constraints also would be considered, e.g.: convective and shock-layer radiative heating; aerodynamic stability; internal payload layout and packaging; and vehicle structural strength and manufacturability.

Facility and Test Technique

Aeroheating testing of the Mid-L/D geometries was conducted in the NASA Langley Research Center (LaRC) 20-Inch Mach 6 Air Tunnel. Phosphor thermography was used to obtain global heating measurements at laminar, transition and turbulent conditions.

Description of NASA LaRC 20-Inch Mach 6 Air Tunnel

The NASA LaRC 20-Inch Mach 6 Air Tunnel (Figure 21-Figure 22) is a blow-down facility in which heated, dried, and filtered air is used as the test gas. A detailed description of this facility can be found in Ref. 10. The tunnel has a two-dimensional contoured nozzle that opens into a 20.5 in. × 20.0 in. (0.52 m × 0.508 m) test section. The tunnel is equipped with a bottom-mounted injection system that can transfer a model from a sheltered model box to the tunnel centerline in less than 0.5 sec. Run times of up to 15 minutes are possible in this facility, although for the current aeroheating study, run times of only a few seconds were required. The nominal reservoir conditions of this facility produce perfect-gas free stream flows with Mach numbers between 5.8 and 6.1 and unit Reynolds numbers of 0.5×10^6/ft to 8.3×10^6/ft (1.64×10^6/m to 27.2×10^6/m).

Test Conditions

Conditions for the current test series are listed in Table 4 and Table 5. Entries in Table 4 are sorted by model configuration and free stream Reynolds number, while entries in Table 5 are listed chronologically. The heat-transfer film coefficient (h_{FR}) values listed in these tables are based on Fay-

Riddell calculations for a reference 2.00-in. radius hemisphere (the same as the Ellipsled-1.00-1.00 nose radius) at cold-wall (300 K) conditions. The enthalpy difference (ΔH_{tot}) is based on the difference between the free stream total enthalpy and the wall enthalpy at 300K.

Six Reynolds number points with nominal values of 2.07×10^6/ft to 8.34×10^6/ft were employed to generate laminar, transitional, and turbulent data. The nominal values are listed in Table 6 and are based on the averaged values of all runs at each condition. As the run-to-run variations were very slight, all computations were performed using the nominal values. The majority of runs were performed with the models at a 40-deg angle-of-attack and a small number of runs were performed at a 30-deg angle-of-attack.

Wind Tunnel Model Design

Wind tunnel models for each of the Mid-L/D geometries were fabricated at 0.01016-scale, resulting in a length of 0.3048 m (12.0-in). The models were composed of cast ceramic and coated with thermographic phosphor with which global aeroheating measurements were made.

The cast ceramic models were fabricated as per the process discussed in Ref. 11. In this method, a rapid prototyping stereolithographic apparatus is first used to build a resin pattern of the geometry. Next, a wax mold of the resin pattern is made and then a fused silica ceramic investment slip-casting technique is used to make a thin ceramic shell model of the geometry. The model is backfilled with a hydraulically setting magnesia ceramic for strength and support into which a metallic sting is fixed. Finally, the model is coated with a mixture of phosphors that are suspended in a silica-based colloidal binder.

A primary model and one or more backup models were fabricated for each geometry in case of damage during handling and testing or problems with the coatings. Each model was given an alpha-numeric designation as per Table 4 and Table 5, e.g. "B-1" for the Ellipsled-1.00-1.00 primary model. Configurations with multiple model listings in the test matrices indicate that a backup model also was tested as a check on the primary model data. Multiple models were tested for each of the COBRA geometries and the Ellipsled-1.00-1.00 geometry owing to damage to the coatings and/or questionable data at some conditions (as detailed later).

A limited number of the configurations also were tested with boundary-layer trip arrays on the models in order to produce turbulence at well-defined locations. These arrays consisted of nine 0.05 × 0.05 in. square, 0.0035-in. height trips spaced span-wise across the model and oriented at a 45-deg rotation from the nose of the model (i.e. corner facing forward). Trips arrays were placed at x/L station of 0.10, 0.25, or 0.50.

Data Acquisition, Reduction and Uncertainty

Aeroheating data were obtained using the two-color, relative-intensity, global thermographic phosphor method (Ref. 12) and reduced using the IHEAT (Imaging for Hypersonic Experimental Aerothermodynamic Testing) code (Ref. 13). In this method, a model is illuminated by ultra-violet light sources that produce temperature-dependent fluorescence of the phosphor coating. Images of the model are taken in the tunnel before and during a run using a three-color, charge-coupled device camera. The IHEAT code uses calibrations to convert the intensity data from each image pixel to temperatures. Heat transfer film coefficients are then determined by assuming a step function in heat transfer beginning at injection of the model into the tunnel, which corresponds to a parabolic temperature-time history. Heat transfer data are reported in terms of ratio h/h_{FR}, where h/h_{FR} is the heat transfer coefficient resulting from a Fay-Riddell computation (Ref. 14) for a reference hemisphere (in this case of 2.00-in. radius, the same as the nose radius of the Ellipsled-1.00-1.00 geometry). The heat transfer coefficient is defined in terms of enthalpy as:

$$(3) \quad h = q/\Delta H_{tot} = q/\left(H_{AW} - H_{300K}\right) = q/\left(H_0 - H_{300K}\right)$$

In the calculation of the heat transfer coefficient it is assumed that the adiabatic wall enthalpy H_{AW} is equal to the free stream total enthalpy of the tunnel, H_0. This heat transfer coefficient definition provides a theoretically near-constant value over the course of a run since the decrease in time of the heat transfer rate in the numerator as the model surface becomes hotter is balanced by the decrease of the enthalpy-difference term in the denominator.

The two-dimensional (2-D) image data obtained from IHEAT are corrected for optical perspective effects and mapped to a three-dimensional (3-D) surface model for that geometry. To accomplish this mapping, perspective transformations are first performed on the 3-D surface model until its 2-D projection matches that of the 2-D image data. The image data are then assigned transformed (x, y, z) coordinates based on interpolation between the image and surface geometry, and then the transformation is inverted to obtain an orthographic 3-D heating distribution map. A sample 2-D image file from IHEAT, sample 3-D surface geometry, and the mapping of the image data onto the geometry are shown in Figure 23-Figure 25.

The experimental uncertainty of the measured heating levels is estimated as the root-mean-square summation of the component uncertainties due to: the data acquisition method (±10%); flow quality and test-condition repeatability (±5%); and the accuracy of the 3D mapping process (±10%), which results in an overall value of ±15%. Experience with this technique indicates that these values are usually conservative, however this estimate does not include multi-dimensional conduction effects such as experienced in regions of high surface curvature or imaging errors due to poor lighting or viewing angle. These effects are generally only significant at sharp nose-tips (as on the flattened ellipsleds) or corners (as on the Hammerhead-Biconic geometries at the junctions of the different segments) or on the sides of a model (which are almost parallel to the camera view plane).

Computational Method

Flow field predictions were performed using the LAURA (Langley Aerothermodynamic Upwind Relaxation Algorithm) code (Refs. 15, 16) to generate heating values for comparisons with the experimental data. LAURA is a three-dimensional, finite-volume solver that includes perfect-gas and non-equilibrium chemistry options, a variety of turbulence models, and ablation and radiative transport capabilities. In this study, the perfect-gas air model was used for the wind tunnel predictions. Both laminar and turbulent solutions were generated. For turbulent predictions, the Cebeci-Smith algebraic model (Ref. 17), which has been shown to provide good comparisons to perfect-gas, attached flow over blunt-body geometries (e.g. Ref. 18), was used.

Free stream conditions were set to the nominal conditions listed in Table 6 and the wall temperature was set to a constant 300 K. The use of a constant wall temperature is acceptable because the heat-transfer coefficient varies only very slightly over the range of wall temperatures produced in this facility.

Structured, half-body, multi-block computational grids were generated for each configuration with 96 body-normal cells, 128 circumferential cells, and 128 to 160 stream-wise cells (depending on configuration) with singularity-free nose blocks. For computational speed and simplicity, the aft cap and wake of the geometry was not modeled, thus the end of the geometry was treated as an extrapolation outflow boundary. Grid adaption to the solution features was performed to align the grid outer boundary with the shock and to cluster cells near the surface to produce wall cell Reynolds numbers on the order of 1 to 10. Since the intent of this study was to obtain experimental data, not to optimize computational methodology, grid resolution and topology refinement were not considered beyond the original grids.

Results and Analysis

Data Presentation

Aeroheating data for each geometry are presented in both qualitative form as global images and in quantitative form as line plots along centerline and off-centerline stations. Data are presented in Figure 26-Figure 76 for models without boundary-layer trips and in Figure 77-Figure 94 for models with boundary-layer trips. In the global image comparison figures (e.g. Figure 26), heating distributions are ordered from left-to-right, top-to-bottom in terms of increasing Reynolds numbers. In the line-cut plots (e.g. Figure 27-Figure 28), heating data at each Reynolds number are shown along with the geometry cross-section profile at that station. Additionally, higher resolution, full-page global images of the heating distributions are given in the Appendices for all runs.

For both sets of figures, all test Reynolds numbers are presented together to show the effects of transition and turbulence on heating. Since the ratio h/h_{FR} is nearly constant with Reynolds numbers for laminar flows, the onset of boundary-layer transition and progression to fully-turbulent flow can be seen as changes in the global heating images and in the plotted distributions at each station.

General Observations on Data Quality

For most test conditions, the expected invariance of h/h_{FR} with Reynolds numbers for laminar flow was observed. However, discrepancies were observed at the lowest test Reynolds number of 3.01×10^6/ft at α = 30-deg on the Ellipsled-0.50-1.00 (Figure 27-Figure 28) and the Ellipsled-1.00-1.00 (Figure 33-Figure 34) models and at α = 40-deg on the Ellipsled-2.00-1.00, COBRA-14297B (Model C-1), and Hammerhead-Nominal models (Figure 42-Figure 43, Figure 51-Figure 52, and Figure 71-Figure 72, respectively). Possible explanations for this behavior include: flow quality issues at lower Reynolds numbers; partial flow blockage due to the large model size and high angle of attack; and phosphor coating quality issues producing off-nominal response at the lower temperatures of this condition.

Additionally, on several of the geometries, streaks near the nose occurred at some Reynolds numbers. These streaks indicated transition due to slight imperfections in the original surface coating or cumulative damage to the coating over the test program, rather than natural "smooth surface" transition. In some cases, lightly wiping the model with a cloth between runs caused the streaks to vanish. For some geometries, these disturbances were quickly washed outboard and did not affect the centerline transition, while for others the disturbances did propagate downstream and influence boundary-layer transition. These streaks were noted on the Ellipsled-2.00-1.00 model at α = 30-deg and α = 40-deg (Figure 38 and Figure 41), COBRA-14297B (models C-1 and C-3) at α = 40-deg (Figure 50 and Figure 53), COBRA-14888B (model D-2) at α = 40-deg (Figure 56), and COBRA-8459B (models E-1 and E-2) at α = 40-deg (Figure 62 and Figure 66).

General observations on Boundary-Layer Transition and Tripping

Stream-wise boundary-layer transition was observed (at different *x*/*L* locations depending on Reynolds numbers) for all configurations except the Ellipsled-1.00-1.00 at α = 30-deg, and Ellipsled-2.00-1.00 at α = 30-deg and 40-deg. Stream-wise transition began on the centerline and propagated outboard to encompass some, or all, of the windward surface depending on configuration and Reynolds number. The stream-wise transition location progressed from the aft end of the configuration forward with increasing Reynolds number.

Cross-flow transition away from the centerline was noted on several configurations as evidenced by "feathered" heating streaks pointing outboard. This cross-flow transition was independent of stream-wise transition and in some cases produced localized transitional/turbulent heating levels higher than that due to stream-wise transition. Cross-flow transition appears to have occurred on several configurations (e.g. Ellipsled-0.50-1.00 at α = 40-deg, Figure 29) as will be noted later in the individual discussions of each configuration. The longitudinal (*x*/*L*) location of the cross-flow transition varied greatly from configuration to configuration.

For the runs with boundary-layer trips, transition to fully-turbulent flow was produced immediately downstream of the trips for all but one case (discussed later). This effect was by design and no attempt was made to vary trip heights to investigate roughness height effects on transition. The intent of these tripped runs was to generate data with fully-turbulent flow beginning at well defined locations in order to allow direct comparisons to turbulent computational predictions with fully-turbulent flow specified to begin at the trip location.

Ellipsled Heating Data

Ellipsled heating data are shown in Figure 26 through Figure 49. Stream-wise boundary-layer transition along the centerline was observed for all ellipsled configurations except the Ellipsled-1.00-1.00 at α = 30-deg, and Ellipsled-2.00-1.00 at α = 30-deg and 40-deg. The longest extent of fully-developed turbulent flow was produced on the axisymmetric Ellipsled-0.50-1.00 at α = 40-deg (Figure 29-Figure 31) and on the flattened Ellipsled-2.00-0.25 at α = 40-deg (Figure 47-Figure 49).

"Feathered" heating patterns that increased in magnitude with Reynolds number were observed outboard of the centerline on the Ellipsled-0.50-1.00 at α = 40-deg (Figure 29 and Figure 31), Ellipsled-1.00-1.00 at α = 40-deg (Figure 35 and Figure 37), Ellipsled-2.00-1.00 at α = 30-deg (Figure 38 and Figure 40) and at α = 40-deg (Figure 41 and Figure 43), and Ellipsled-2.00-0.50 at α = 40-deg (Figure 44 and Figure 46). These patterns were likely indicative of vortices from cross-flow transition. No such patterns were observed on other ellipsled configurations.

COBRA Heating Data

COBRA heating distributions are shown in Figure 50-Figure 67. Stream-wise transition and turbulent flow regions (of varying length) were observed for all configurations at the higher Reynolds numbers. However, with the exception of the highest Reynolds number COBRA-14297B case (Figure 50-Figure 55), the extent of transitional / turbulent flow regions was smaller and resulting turbulent heating levels were lower than observed on the Ellipsled configurations. The heating distribution for this single COBRA-14297B case likely was due to early transition produced by anomalous discrete roughness near the nose, as this transition onset pattern appears to be more wedge-like than planar. Also, faint outboard "feathering" patterns near the end of the COBRA-8459B geometry (Figure 62 and Figure 64 for model E-1 and Figure 65 and Figure 67 for model E-2) may indicate cross-flow transition.

Hammerhead-Biconic Heating Data

Hammerhead-Biconic geometry heating distributions are shown in Figure 68-Figure 76. The Hammerhead-Biconic configurations produced more complex heating distributions than the other configurations due to discontinuities in the geometric slopes between the different body segments and to the proximity of the stagnation point to the junction of the nose and first cone section. For the Hammerhead-Blunt (Figure 68-Figure 70) and Hammerhead-Sharp (Figure 74-Figure 76) configurations, boundary-layer transition occurred ahead of, or almost immediately downstream of, the junction of the first and second cone sections and rapidly evolved into fully-turbulent flow for all but the lowest two Reynolds numbers. In contrast, boundary-layer transition for the Hammerhead-Nominal geometry (Figure 71-Figure 73) did not occur until midway down the final cylindrical section. Additionally "feathering" patterns were observed toward the outboard of the second cone section on Hammerhead nominal configuration that indicated cross-flow transition.

Tripped Data

Global heating images and centerline plots of the heating data from the models with boundary-layer trips are presented in Figure 77-Figure 82 for Ellipsled-1.00-1.00, Figure 83-Figure 84 for Ellipsled-2.00-1.00, Figure 85-Figure 86 for Ellipsled-2.00-0.50, Figure 87-Figure 88 for Ellipsled-2.00-0.25, Figure 89-Figure 90 for COBRA-14297B, Figure 91 -Figure 92 for COBRA-14888B and Figure 93-Figure 94 for COBRA-8459B. Trips were placed at x/L = 0.10 for all models and runs were also performed with trips at x/L = 0.25 and 0.50 for the Ellipsled-1.00-1.00 model. In all cases, except for the Ellipsled-1.00-1.00 with trips at x/L=0.10 (Figure 77-Figure 78), a rapid increase in heating levels immediately behind the trips was observed that indicated fully-turbulent flow was produced. From the global images, it can be seen that this turbulent flow also spread outboard from the trip location.

Comparisons with Computational Predictions

Laminar Predictions

Centerline comparisons between measured and predicted laminar heating levels are presented in Figure 95-Figure 105. For conditions where the flow remained laminar (as determined by an approximate invariance of the heating levels with Reynolds numbers), the laminar predictions matched the data to within the estimated experimental uncertainty expect in a few small regions. At the geometric nose tip, or to its leeside (x/L < 0.1), larger differences were noted for most cases. These differences were attributed to the experimental data and were due to the difficulty in properly illuminating this region (because of optical access limitations) and the fact that the camera viewing plane was nearly parallel to this portion of the surface and thus subject to greater imaging errors. The other region where comparisons were less accurate was near the first-to-second cone junction on the Hammerhead-Biconic geometries, where predicted heating was much lower than measured heating (Figure 103-Figure 105). These differences were attributed mainly to computational error due to the lack of stream-wise grid clustering at this geometric slope discontinuity. It is also possible that the experimental data were biased slightly higher downstream of the junction due to multi-dimensional conduction effects (i.e. stream-wise in addition to in-depth) through this high temperature-gradient region. Despite these small discrepancies between predictions and data, the overall comparison provided confidence in the computational method for laminar conditions.

Turbulent Predictions

The prediction of transitional/turbulent flow is more challenging than that of laminar flow. For the current study, the greatest difficulty is that the Cebeci-Smith algebraic turbulence model, as currently implemented in LAURA, requires *a priori* specification of the transition onset location and transition zone length (as per the Dhawan-Narashima model of Ref. 19). In previous studies (e.g. Ref. 20), this limitation had little effect since data were obtained at conditions where the flow was fully-turbulent at, or close to, the stagnation point. At such conditions, specification of fully-turbulent flow over the entire geometry led to good comparisons with the data. However, in the current data set, there were few cases for which the flow reached fully-turbulent levels, and thus the transition onset location had a larger impact on the resulting heating.

For the geometries in which a significant length of fully-developed turbulent flow was generated, predictions were made assuming turbulent flow over the entire geometry. Comparisons for these cases are show for the Ellipsled-0.50-1.00 (Figure 106), Ellipsled-2.00-0.25 (Figure 107), Hammerhead-Sharp (Figure 108), and Hammerhead-Blunt (Figure 109) configurations. A clear trend toward closer agreement with stream-wise distance from the nose is evident in these comparisons. However, only for the Hammerhead geometries in which transition occurred close to the nose were the comparisons satisfactory. This trend both reinforces the conclusion of previous studies that algebraic turbulence models can produce reasonably good simulations of fully-turbulent flow and also highlights the need for a computational algorithm for transition prediction as opposed to explicit location specification by the user.

To provide additional confidence in the fundamental accuracy of the algebraic turbulence model (for fully-developed turbulent flow), comparisons were performed for the cases where transition was forced at specified locations by the use of boundary-layer trips. For these cases, relatively large trips (0.0035-in. height) were employed with the intent of producing instantaneous transition to fully-turbulent flow. In the computations, zero-length transition at the trip location was specified, thus providing a direct comparison between measurements and predictions. These comparisons are given in Figure 110-Figure 115. Overall, these comparisons were better than those for the natural-transition cases. Predictions and measurements agreed to within the estimated experimental uncertainty except for those cases where the trips did not produce instantaneous transition, e.g. the lowest tripped Reynolds number of 3.01×10^6/ft (for all geometries) and the Ellipsled-1.00-1.00 model with trips at x/L=0.10. For this somewhat anomalous Ellipsled-1.00-1.00 case, it is possible that the placement of the trips on the curved nose section where the boundary layer was relatively thin could have caused flow separation that disturbed the outer, inviscid flow structure. Much better comparisons were achieved on this geometry when the trips were located further downstream at x/L = 0.25 and 0.50 locations.

In general, these comparisons demonstrate the potential utility of simple algebraic turbulence models for simulation of Mid-L/D flow-fields. However, a transition algorithm would be required to produce accurate predictions at all conditions. While such algorithmic development is outside the scope of the present study, the data presented herein should be valuable for such work. Also note that these observations pertain only to the stream-wise transition along the centerline of the vehicle. No attempt was made to match the cross-flow transition patterns that were noted on several of the configurations, thus an algorithm for cross-flow transition prediction would also be required for more accurate predictions.

Heat-Transfer Global Image Data

Global heat-transfer distribution images are presented in the Appendices for each model. Ellipsled data are presented in Appendix A, Figure 116-Figure 158, COBRA data are presented in Appendix B, Figure 159-Figure 183 and Hammerhead data are presented in Appendix C, Figure 184-Figure 198. Tripped data are presented in Appendix D, Figure 199-Figure 229. These images are identical to those presented in the main text but are of higher resolution to better show the details of the heat-transfer distributions and boundary-layer transition patterns. Run conditions and model geometry information are also given for ease of reference.

Summary and Conclusions

Mid-L/D entry vehicle configurations have been proposed as an option to meet the aerodynamic performance requirements for high-mass missions to Mars and the outer planets. To provide data for mission concept development and system trade studies, the aerodynamic, convective heating, and boundary-layer transition characteristics of these configurations have been examined. Three families of Mid-L/D vehicles were considered: elliptically-blunted cylinders (Ellipsled family); parametrically-optimized geometries (COBRA family); and dual-use shroud (for both ascent and aerocapture) launch vehicles (Hammerhead-Biconic family).

Aerodynamic performance estimates were produced using modified Newtonian theory. Of the 11 geometries considered, only the Ellipsled-0.50-1.00, Ellipsled-1.00-1.00, and Hammerhead-Blunt did not meet the desired requirement of L/D between 0.4 to 0.8 within angles-of-attack of 30-deg to 70-deg.

Boundary-layer transition behavior was determined from the global aeroheating measurements. All geometries experienced centerline, stream-wise boundary-layer transition except the Ellipsled-1.00-1.00 (at α = 30-deg) and Ellipsled-2.00-1.00. Large regions of fully-developed turbulent flow were produced on the Ellipsled-0.50-1.00, Ellipsled-2.00-0.25, COBRA-14297B geometries, and the three Hammerhead geometries. In addition to stream-wise transition, "feathered" heating patterns indicative of cross-flow transition were noted on the Ellipsled-0.50-1.00, Ellipsled-1.00-1.00, Ellipsled-2.00-1.00, Ellipsled-2.00-0.50, COBRA-8459B, and Hammerhead-Nominal geometries.

Comparisons between predicted laminar heating levels and measured data along the centerline agreed to within the experimental uncertainty for all configurations with two exceptions: on the leeside of the nose (where camera view angle was non-optimal and the lighting was poor in the test); and on the Hammerhead-Biconic geometries at the junction of the first and second cones (where the grid resolution was likely insufficient). Comparisons between transitional/turbulent data and fully-turbulent predictions were less satisfactory. In regions of fully-developed turbulent flow, a trend toward better agreement with distance from the experimental transition location was noted, but good comparisons were produced only in limited regions. For the cases where trips were employed and produced near-instantaneous transition, predictions with zero-length transition at the trip location resulted in good comparisons expect for a single anomalous case (Ellipsled-1.00-1.00 with trips at x/L =0.10) where the trips may have produced separated flow.

These comparisons suggest that fully-turbulent predictions using an algebraic turbulence model can provide a reasonably good basis for preliminary mission design studies. However, to produce high-fidelity results for final mission design purposes, it is clear that both stream-wise and cross-flow transition algorithm development will be required. The experimental results from this study can provide the basis for such model development and also can provide a valuable database for mission design studies.

References

1. Dwyer-Cianciolo, A. M., Davis, J. L., Komar, D. R., et al, “Entry, Descent and Landing Systems Analysis Study: Phase 2 Report,” NASA TM-2010-216720, July, 2010.
2. Dwyer-Cianciolo, A. M., Davis, J. L., Engelund, W. C., et al, “Entry, Descent and Landing Systems Analysis Study: Phase 1 Report on Exploration Feed-Forward Systems,” NASA TM-2011-217055, February, 2010.
3. Cianciolo, A. D., Davis, J. L., Shidner, J. D., and Powell, R. W., “Entry, Descent and Landing Systems Analysis: Exploration Class Simulation Overview and Results,” AIAA Paper 2010-7970, AIAA/AAS Astrodynamics Specialists Conference, Toronto, Ontario Canada, August 2-5, 2010.
4. Zang, T. A., Dwyer-Cianciolo, A. M., Kinney, D. J., et al, “Overview of the NASA Entry, Descent and Landing Analysis Study,” AIAA Paper 2010-8649, AIAA SPACE 2010 Conference and Exhibit, Anaheim, CA, August 30 – September 2, 2010.
5. Lockwood, M. K., Edquist, K. T., Starr, B. R., Hollis, B. R., et al, “Aerocapture System Analysis for a Neptune Mission,” NASA TM-2006-214300, April 2006.
6. Drake, B. G., “Reference Mission Version 3.0 Addendum to the Human Exploration of Mars: The Reference Mission of the NASA Mars Exploration Study Team,” NASA SP-1998-6107/ADD, June 1998.
7. Garcia, J. A., Brown, J. L., Kinney, D. J., et al, “Co-Optimization of Mid Lift to Drag Vehicle Concepts for Mars Atmospheric Entry,” AIAA Paper 2010-5052, 10th AIAA/ASME Joint Thermophysics and Heat Transfer Conference, Chicago, IL, June 28 – July 1, 2010.
8. “Human Exploration of Mars Design Reference Architecture 5.0,” Drake, B. G., editor, NASA-SP-2009-566, July 2009.
9. Borowski, S. K., McCurdy, D. R., and Packard, T. W., “7-Launch NTR Space Transportation System for NASA’s Mars Design Reference Architecture (DRA) 5.0,” AIAA Paper 2009-5308, 45th AIAA/ASME/SAE/ASEE Joint Propulsion Conference and Exhibit, Denver, CO, August 2 – 5, 2009.
10. Hollis, B. R., Berger, K. T., Berry, S. A., Brauckmann, G. J., et al, “Entry, Descent, and Landing Aerothermodynamics: NASA Langley Experimental Capabilities and Contributions,” AIAA Paper 2014-1154, AIAA 52nd Aerospace Science Meeting, National Harbor, MD, January 13-17, 2014.
11. Buck, G. M., “Rapid Model Fabrication and Testing for Aerospace Vehicles,” AIAA Paper 2000-0826, 38th AIAA Aerospace Sciences Meeting and Exhibit, Reno, NV, January 10-13, 2000.
12. Buck, G. M., “Surface Temperature/Heat Transfer Measurement Using a Quantitative Phosphor Thermography System,” AIAA Paper 91-0064, 29th Aerospace Sciences Meeting, Reno, NV, January 7-10, 1991.
13. Merski, N. R., “Global Aeroheating Wind-Tunnel Measurements Using Improved Two-Color Phosphor Thermography Methods,” *Journal of Spacecraft and Rockets*, Vol. 36, No. 2, March-April 1999, pp. 160-170.
14. Fay, J. A., and Riddell, F. R., “Theory of Stagnation Point Heat Transfer in Dissociated Air,” *Journal of Aeronautical Sciences*, Vol. 25, No. 2., February 1958, pp. 73-85.
15. Gnoffo, P. A., “An Upwind-Biased, Point-Implicit Algorithm for Viscous, Compressible Perfect-Gas Flows,” NASA TP-2953, February 1990.
16. Mazaheri, A., Gnoffo, P. A., Johnston, C. O., and Kleb, B., “LAURA User’s Manual: 5.5-65135,” NASA TM-2013-217800, February 2011.

17. Cheatwood, F. M. and Thompson, R. A., “The Addition of Algebraic Turbulence Modeling to Program LAURA,” NASA TM-107758, April 1993.
18. Hollis, B. R., “Blunt-Body Entry Vehicle Aerothermodynamics: Transition and Turbulent Heating,” *Journal of Spacecraft and Rockets*, Vol. 49, No. 3, May-June 2012, pp. 435-449.
19. Dhawan. S., and Narashima, R., “Some Properties of Boundary Layer Flow from Laminar to Turbulent Motion,” *Journal of Fluid Mechanics*, Vol. 1, Part 4, Jan. 1958, pp. 418-436.
20. Hollis, B. R., and Collier, A. S., “Turbulent Aeroheating Testing of Mars Science Laboratory Entry Vehicle,” *Journal of Spacecraft and Rockets*, Vol. 45, No. 3, pp. 417-427, May-June 2008.

Table 1. Ellipsled Geometry Definition Parameters

Geometry	L (in.)	D (in.)	a_{nose} (in.)	b_{nose} (in.)	$a_{\text{nose}}/b_{\text{nose}}$	r_{upper} (in.)	a_{lower} (in.)	b_{lower} (in.)	$a_{\text{lower}}/b_{\text{lower}}$
Ellipsled-0.50-1.00	12.00	4.00	1.00	2.00	0.50	2.00	2.00	2.00	1.00
Ellipsled-1.00-1.00	12.00	4.00	2.00	2.00	1.00	2.00	2.00	2.00	1.00
Ellipsled-2.00-1.00	12.00	4.00	4.00	2.00	2.00	2.00	2.00	2.00	1.00
Ellipsled-2.00-0.25	12.00	4.00	4.00	2.00	2.00	2.00	0.50	2.00	0.25
Ellipsled-2.00-0.50	12.00	4.00	4.00	2.00	2.00	2.00	1.00	2.00	0.50

Table 2. Hammerhead Geometry Definition Parameters

Geometry	L (in.)	D (in.)	r_{nose} (in.)	θ_1 (deg)	L_1 (in.)	θ_2 (deg)	L_2 (in.)
Hammerhead-Sharp	12.000	4.000	0.8000	30.0000	1.7000	4.3333	4.2981
Hammerhead-Nominal	12.000	4.000	1.0000	30.0000	1.6000	2.8000	4.2981
Hammerhead-Blunt	12.000	4.000	1.2500	30.0000	1.4750	0.8781	4.2981

Table 3. Aerodynamic Performance Estimates

	$L/D = 0.4$		$L/D = 0.8$	
Geometry	α (deg)	β/m (1/m^2)	α (deg)	β/m (1/m^2)
Ellipsled-0.50-1.00	60.2	0.0038	N/A	N/A
Ellipsled-1.00-1.00	60.2	0.0037	N/A	N/A
Ellipsled-2.00-1.00	60.2	0.0038	34.8	0.0084
Ellipsled-2.00-0.50	64.8	0.0029	45.8	0.0052
Ellipsled-2.00-0.25	67.0	0.0026	49.0	0.0044
COBRA-8459B	62.1	0.0035	42.5	0.0064
COBRA-14297B	62.1	0.0031	43.9	0.0054
COBRA-14888B	62.1	0.0030	38.7	0.0063
Hammerhead-Blunt	60.0	0.0039	N/A	N/A
Hammerhead-Nominal	60.0	0.0038	35.3	0.0084
Hammerhead-Sharp	60.0	0.0037	38.2	0.0077

Table 4. Test 6966 Run Matrix (sorted)

Configuration	Model ID	Run	α (deg)	Re_∞ (1/ft)	M_∞	T_∞ (K)	ρ_∞ (kg/m^3)	U_∞ (m/s)	ΔH_{tot} (J/kg)	h_{FR} (kg/m^2-s)	Trips
Ellipsled-0.50-1.00	I-1	75	30	3.00E+06	5.97	54.9	4.37E-02	883.4	1.44E+05	2.34E-01	
Ellipsled-0.50-1.00	I-1	76	30	4.74E+06	5.99	56.3	6.97E-02	896.4	1.57E+05	3.01E-01	
Ellipsled-0.50-1.00	I-1	78	30	6.83E+06	6.01	57.5	1.02E-01	908.2	1.69E+05	3.69E-01	
Ellipsled-0.50-1.00	I-1	79	30	7.66E+06	6.02	57.9	1.14E-01	912.3	1.73E+05	3.93E-01	
Ellipsled-0.50-1.00	I-1	80	30	8.32E+06	6.03	58.5	1.25E-01	917.6	1.79E+05	4.14E-01	
Ellipsled-0.50-1.00	I-1	40	40	2.07E+06	5.96	62.0	3.21E-02	940.7	2.04E+05	2.16E-01	
Ellipsled-0.50-1.00	I-1	39	40	3.03E+06	5.97	54.9	4.42E-02	883.1	1.44E+05	2.35E-01	
Ellipsled-0.50-1.00	I-1	38	40	4.84E+06	5.99	55.9	7.11E-02	893.7	1.54E+05	3.02E-01	
Ellipsled-0.50-1.00	I-1	41	40	6.73E+06	6.01	57.8	1.00E-01	911.1	1.72E+05	3.68E-01	
Ellipsled-0.50-1.00	I-1	42	40	7.65E+06	6.02	58.0	1.14E-01	912.8	1.74E+05	3.93E-01	
Ellipsled-0.50-1.00	I-1	43	40	8.34E+06	6.03	58.5	1.25E-01	917.8	1.79E+05	4.14E-01	
Ellipsled-1.00-1.00	B-1	65	30	3.05E+06	5.97	54.5	4.43E-02	879.5	1.40E+05	2.34E-01	
Ellipsled-1.00-1.00	B-1	66	30	4.85E+06	5.99	55.9	7.12E-02	893.1	1.54E+05	3.02E-01	
Ellipsled-1.00-1.00	B-1	67	30	6.84E+06	6.01	57.5	1.02E-01	908.1	1.69E+05	3.69E-01	
Ellipsled-1.00-1.00	B-1	68	30	7.58E+06	6.01	58.1	1.13E-01	912.5	1.73E+05	3.92E-01	
Ellipsled-1.00-1.00	B-1	69	30	8.32E+06	6.03	58.6	1.25E-01	918.6	1.80E+05	4.14E-01	
Ellipsled-1.00-1.00	B-1	33	40	3.09E+06	5.99	62.1	4.78E-02	945.3	2.08E+05	2.66E-01	
Ellipsled-1.00-1.00	B-1	9	40	4.75E+06	5.99	56.1	6.98E-02	895.0	1.56E+05	3.00E-01	
Ellipsled-1.00-1.00	B-1	8	40	6.83E+06	6.01	57.4	1.02E-01	907.6	1.68E+05	3.68E-01	
Ellipsled-1.00-1.00	B-1	32	40	7.60E+06	6.02	58.0	1.13E-01	913.2	1.74E+05	3.92E-01	
Ellipsled-1.00-1.00	B-1	10	40	8.40E+06	6.02	58.4	1.26E-01	916.2	1.77E+05	4.15E-01	
Ellipsled-2.00-1.00	F-2	70	30	2.99E+06	5.97	55.1	4.37E-02	884.7	1.46E+05	2.34E-01	
Ellipsled-2.00-1.00	F-2	71	30	4.81E+06	5.99	56.1	7.06E-02	894.7	1.55E+05	3.02E-01	
Ellipsled-2.00-1.00	F-2	72	30	6.86E+06	6.01	57.6	1.02E-01	908.8	1.70E+05	3.70E-01	
Ellipsled-2.00-1.00	F-2	73	30	7.52E+06	6.02	58.2	1.12E-01	914.6	1.75E+05	3.91E-01	
Ellipsled-2.00-1.00	F-2	74	30	8.37E+06	6.03	58.5	1.25E-01	917.5	1.78E+05	4.15E-01	
Ellipsled-2.00-1.00	F-2	12	40	3.06E+06	5.97	54.3	4.44E-02	877.6	1.38E+05	2.34E-01	
Ellipsled-2.00-1.00	F-2	17	40	4.83E+06	6.00	55.8	7.07E-02	893.1	1.54E+05	3.01E-01	
Ellipsled-2.00-1.00	F-2	14	40	6.93E+06	6.01	57.1	1.03E-01	904.6	1.65E+05	3.69E-01	
Ellipsled-2.00-1.00	F-2	16	40	7.58E+06	6.02	58.1	1.13E-01	914.0	1.75E+05	3.92E-01	
Ellipsled-2.00-1.00	F-2	15	40	8.27E+06	6.03	58.7	1.24E-01	918.8	1.80E+05	4.13E-01	
Ellipsled-2.00-0.50	H-1	24	40	2.08E+06	5.96	62.0	3.22E-02	940.4	2.03E+05	2.17E-01	
Ellipsled-2.00-0.50	H-1	27	40	3.01E+06	5.97	54.8	4.39E-02	882.0	1.43E+05	2.34E-01	
Ellipsled-2.00-0.50	H-1	25	40	4.73E+06	5.99	56.5	6.97E-02	898.4	1.59E+05	3.01E-01	
Ellipsled-2.00-0.50	H-1	26	40	6.64E+06	6.13	55.3	9.50E-02	906.3	1.65E+05	3.56E-01	
Ellipsled-2.00-0.50	H-1	28	40	7.63E+06	6.02	58.0	1.14E-01	912.7	1.74E+05	3.93E-01	
Ellipsled-2.00-0.50	H-1	29	40	8.33E+06	6.03	58.7	1.25E-01	919.2	1.80E+05	4.15E-01	
Ellipsled-2.00-0.25	G-1	22	40	2.06E+06	5.96	61.9	3.20E-02	939.5	2.02E+05	2.16E-01	
Ellipsled-2.00-0.25	G-1	18	40	3.01E+06	5.97	54.7	4.37E-02	881.4	1.42E+05	2.33E-01	
Ellipsled-2.00-0.25	G-1	19	40	4.79E+06	6.00	55.9	7.02E-02	894.0	1.55E+05	3.00E-01	
Ellipsled-2.00-0.25	G-1	20	40	6.86E+06	6.01	57.3	1.02E-01	905.9	1.67E+05	3.68E-01	
Ellipsled-2.00-0.25	G-1	23	40	7.51E+06	6.02	58.6	1.12E-01	917.9	1.79E+05	3.93E-01	
Ellipsled-2.00-0.25	G-1	21	40	8.32E+06	6.03	58.5	1.25E-01	917.8	1.79E+05	4.14E-01	
Hammerhead-Blunt	L-1	100	40	2.97E+06	5.97	54.8	4.32E-02	882.6	1.43E+05	2.32E-01	
Hammerhead-Blunt	L-1	99	40	4.91E+06	5.99	55.4	7.18E-02	888.2	1.49E+05	3.02E-01	
Hammerhead-Blunt	L-1	101	40	6.88E+06	6.01	57.3	1.02E-01	905.8	1.67E+05	3.68E-01	
Hammerhead-Blunt	L-1	102	40	7.61E+06	6.02	57.9	1.13E-01	911.6	1.72E+05	3.91E-01	
Hammerhead-Blunt	L-1	103	40	8.34E+06	6.03	58.5	1.25E-01	917.8	1.79E+05	4.14E-01	
Hammerhead-Nominal	K-1	95	40	3.00E+06	5.97	54.9	4.37E-02	882.7	1.44E+05	2.34E-01	
Hammerhead-Nominal	K-1	93	40	4.80E+06	5.99	55.9	7.05E-02	893.1	1.54E+05	3.01E-01	
Hammerhead-Nominal	K-1	96	40	6.84E+06	6.01	57.6	1.02E-01	908.8	1.70E+05	3.69E-01	

Configuration	Model ID	Run	α (deg)	Re_∞ (1/ft)	M_∞	T_∞ (K)	ρ_∞ (kg/m^3)	U_∞ (m/s)	ΔH_{tot} (J/kg)	h_{FR} (kg/m^2-s)	Trips
Hammerhead-Nominal	K-1	97	40	7.55E+06	6.02	58.1	1.13E-01	913.9	1.75E+05	3.92E-01	
Hammerhead-Nominal	K-1	98	40	8.27E+06	6.03	58.8	1.24E-01	920.3	1.81E+05	4.14E-01	
Hammerhead-Sharp	J-1	87	40	2.98E+06	5.97	55.1	4.35E-02	884.6	1.45E+05	2.34E-01	
Hammerhead-Sharp	J-1	86	40	4.75E+06	5.99	56.5	7.00E-02	898.2	1.59E+05	3.02E-01	
Hammerhead-Sharp	J-1	88	40	6.88E+06	6.01	57.6	1.02E-01	909.0	1.70E+05	3.70E-01	
Hammerhead-Sharp	J-1	89	40	7.62E+06	6.03	57.9	1.14E-01	912.6	1.73E+05	3.92E-01	
Hammerhead-Sharp	J-1	90	40	8.33E+06	6.03	58.6	1.25E-01	918.6	1.80E+05	4.15E-01	
COBRA-14297B	C-1	45	40	3.03E+06	5.97	54.7	4.40E-02	881.2	1.42E+05	2.34E-01	
COBRA-14297B	C-1	44	40	4.80E+06	5.99	56.1	7.05E-02	895.2	1.56E+05	3.02E-01	
COBRA-14297B	C-1	48	40	6.84E+06	6.01	57.5	1.02E-01	908.5	1.69E+05	3.69E-01	
COBRA-14297B	C-1	49	40	7.60E+06	6.01	58.0	1.14E-01	912.0	1.73E+05	3.92E-01	
COBRA-14297B	C-1	50	40	8.35E+06	6.03	58.6	1.25E-01	918.0	1.79E+05	4.15E-01	
COBRA-14297B	C-3	110	40	6.81E+06	6.01	57.6	1.01E-01	909.2	1.70E+05	3.69E-01	
COBRA-14297B	C-3	111	40	7.59E+06	6.02	58.1	1.13E-01	913.9	1.75E+05	3.92E-01	
COBRA-14297B	C-3	113	40	8.27E+06	6.03	58.8	1.24E-01	920.1	1.81E+05	4.14E-01	
COBRA-14888B	D-2	63	40	4.80E+06	5.99	56.0	7.05E-02	893.9	1.55E+05	3.01E-01	
COBRA-14888B	D-2	36	40	6.84E+06	6.01	57.5	1.02E-01	908.5	1.69E+05	3.69E-01	
COBRA-14888B	D-2	37	40	7.66E+06	6.02	57.8	1.14E-01	910.8	1.72E+05	3.92E-01	
COBRA-14888B	D-2	61	40	8.28E+06	6.03	58.7	1.24E-01	919.0	1.80E+05	4.14E-01	
COBRA-14888B	D-3	105	40	2.95E+06	5.97	55.1	4.31E-02	884.9	1.46E+05	2.33E-01	
COBRA-14888B	D-3	104	40	4.72E+06	5.99	56.3	6.95E-02	897.1	1.58E+05	3.00E-01	
COBRA-14888B	D-3	107	40	6.91E+06	6.01	57.3	1.03E-01	906.0	1.67E+05	3.69E-01	
COBRA-14888B	D-3	108	40	7.59E+06	6.02	58.0	1.13E-01	912.6	1.73E+05	3.91E-01	
COBRA-14888B	D-3	109	40	8.28E+06	6.03	58.8	1.24E-01	919.6	1.81E+05	4.14E-01	
COBRA-8459B	E-1	54	40	3.03E+06	5.97	54.9	4.42E-02	883.0	1.44E+05	2.35E-01	
COBRA-8459B	E-1	52	40	4.74E+06	5.99	56.2	6.98E-02	896.3	1.57E+05	3.01E-01	
COBRA-8459B	E-1	56	40	6.93E+06	6.01	57.2	1.03E-01	905.2	1.66E+05	3.69E-01	
COBRA-8459B	E-1	55	40	7.55E+06	6.02	58.3	1.13E-01	915.1	1.76E+05	3.92E-01	
COBRA-8459B	E-2	81	40	4.80E+06	5.99	56.1	7.06E-02	895.2	1.56E+05	3.02E-01	
COBRA-8459B	E-2	82	40	6.87E+06	6.01	57.5	1.02E-01	908.1	1.69E+05	3.70E-01	
COBRA-8459B	E-2	83	40	7.60E+06	6.02	58.0	1.13E-01	912.9	1.74E+05	3.92E-01	
COBRA-8459B	E-2	85	40	8.31E+06	6.03	58.7	1.25E-01	918.8	1.80E+05	4.14E-01	
Ellipsled-1.00-1.00	B-1	120	40	4.76E+06	5.99	56.2	7.00E-02	896.3	1.57E+05	3.01E-01	x/L=0.10
Ellipsled-1.00-1.00	B-1	121	40	6.80E+06	6.01	57.7	1.01E-01	910.4	1.71E+05	3.69E-01	x/L=0.10
Ellipsled-1.00-1.00	B-1	122	40	7.57E+06	6.02	58.2	1.13E-01	914.9	1.76E+05	3.93E-01	x/L=0.10
Ellipsled-1.00-1.00	B-1	123	40	8.25E+06	6.03	58.9	1.24E-01	921.1	1.82E+05	4.14E-01	x/L=0.10
Ellipsled-1.00-1.00	B-2	153	40	6.78E+06	6.01	57.8	1.01E-01	910.5	1.71E+05	3.69E-01	x/L=0.25
Ellipsled-1.00-1.00	B-2	154	40	7.52E+06	6.02	58.3	1.13E-01	915.9	1.77E+05	3.92E-01	x/L=0.25
Ellipsled-1.00-1.00	B-2	155	40	8.40E+06	6.03	58.4	1.26E-01	916.4	1.77E+05	4.15E-01	x/L=0.25
Ellipsled-1.00-1.00	B-2	150	40	6.78E+06	6.01	57.8	1.01E-01	910.5	1.71E+05	3.69E-01	x/L=0.50
Ellipsled-1.00-1.00	B-2	151	40	7.52E+06	6.02	58.3	1.13E-01	915.9	1.77E+05	3.92E-01	x/L=0.50
Ellipsled-1.00-1.00	B-2	152	40	8.40E+06	6.03	58.4	1.26E-01	916.4	1.77E+05	4.15E-01	x/L=0.50
Ellipsled-2.00-1.00	F-2	124	40	4.77E+06	5.99	56.2	7.01E-02	896.0	1.57E+05	3.01E-01	x/L=0.10
Ellipsled-2.00-1.00	F-2	125	40	6.97E+06	6.01	57.1	1.03E-01	904.1	1.65E+05	3.70E-01	x/L=0.10
Ellipsled-2.00-1.00	F-2	126	40	7.59E+06	6.02	57.9	1.13E-01	912.2	1.73E+05	3.91E-01	x/L=0.10
Ellipsled-2.00-1.00	F-2	127	40	8.31E+06	6.03	58.6	1.24E-01	918.4	1.79E+05	4.14E-01	x/L=0.10
Ellipsled-2.00-0.50	H-1	128	40	4.79E+06	5.99	56.0	7.03E-02	894.0	1.55E+05	3.01E-01	x/L=0.10
Ellipsled-2.00-0.50	H-1	129	40	6.86E+06	6.01	57.5	1.02E-01	908.2	1.69E+05	3.69E-01	x/L=0.10
Ellipsled-2.00-0.50	H-1	130	40	7.48E+06	6.02	58.4	1.12E-01	916.1	1.77E+05	3.91E-01	x/L=0.10
Ellipsled-2.00-0.50	H-1	131	40	8.28E+06	6.03	58.8	1.24E-01	919.8	1.81E+05	4.14E-01	x/L=0.10

Configuration	Model ID	Run	α (deg)	Re_∞ (1/ft)	M_∞	T_∞ (K)	ρ_∞ (kg/m^3)	U_∞ (m/s)	ΔH_{tot} (J/kg)	h_{FR} (kg/m^2-s)	Trips
Ellipsled-2.00-0.25	G-1	132	40	4.77E+06	5.99	56.3	7.03E-02	896.4	1.57E+05	3.02E-01	x/L=0.10
Ellipsled-2.00-0.25	G-1	133	40	6.92E+06	6.01	57.3	1.03E-01	906.4	1.67E+05	3.70E-01	x/L=0.10
Ellipsled-2.00-0.25	G-1	134	40	7.57E+06	6.02	58.0	1.13E-01	912.8	1.74E+05	3.91E-01	x/L=0.10
Ellipsled-2.00-0.25	G-1	135	40	8.33E+06	6.03	58.6	1.25E-01	917.9	1.79E+05	4.14E-01	x/L=0.10
COBRA-14297B	C-3	141	40	6.85E+06	6.01	57.5	1.02E-01	908.2	1.69E+05	3.69E-01	x/L=0.10
COBRA-14297B	C-3	142	40	7.58E+06	6.02	58.1	1.13E-01	913.7	1.75E+05	3.92E-01	x/L=0.10
COBRA-14297B	C-3	143	40	8.36E+06	6.03	58.5	1.25E-01	917.5	1.78E+05	4.15E-01	x/L=0.10
COBRA-14888B	D-3	136	40	6.92E+06	6.01	57.3	1.03E-01	906.1	1.67E+05	3.70E-01	x/L=0.10
COBRA-14888B	D-3	137	40	7.57E+06	6.02	58.2	1.13E-01	914.8	1.76E+05	3.93E-01	x/L=0.10
COBRA-14888B	D-3	138	40	8.28E+06	6.03	58.8	1.24E-01	920.0	1.81E+05	4.14E-01	x/L=0.10
COBRA-8459B	E-2	145	40	6.78E+06	6.01	57.8	1.01E-01	910.5	1.71E+05	3.69E-01	x/L=0.10
COBRA-8459B	E-2	146	40	7.52E+06	6.02	58.3	1.13E-01	915.9	1.77E+05	3.92E-01	x/L=0.10
COBRA-8459B	E-2	147	40	8.40E+06	6.03	58.4	1.26E-01	916.4	1.77E+05	4.15E-01	x/L=0.10

Table 5. Test 6966 Run Matrix (chronological)

Configuration	Model ID	Run	α (deg)	Re_∞ (1/ft)	M_∞	T_∞ (K)	ρ_∞ (kg/m^3)	U_∞ (m/s)	ΔH_{tot} (J/kg)	h_{FR} (kg/m^2-s)	Trips
Ellipsled-1.00-1.00	B-1	8	40	6.83E+06	6.01	57.4	1.02E-01	907.6	1.68E+05	3.68E-01	
Ellipsled-1.00-1.00	B-1	9	40	4.75E+06	5.99	56.1	6.98E-02	895.0	1.56E+05	3.00E-01	
Ellipsled-1.00-1.00	B-1	10	40	8.40E+06	6.02	58.4	1.26E-01	916.2	1.77E+05	4.15E-01	
Ellipsled-2.00-1.00	F-2	12	40	3.06E+06	5.97	54.3	4.44E-02	877.6	1.38E+05	2.34E-01	
Ellipsled-2.00-1.00	F-2	14	40	6.93E+06	6.01	57.1	1.03E-01	904.6	1.65E+05	3.69E-01	
Ellipsled-2.00-1.00	F-2	15	40	8.27E+06	6.03	58.7	1.24E-01	918.8	1.80E+05	4.13E-01	
Ellipsled-2.00-1.00	F-2	16	40	7.58E+06	6.02	58.1	1.13E-01	914.0	1.75E+05	3.92E-01	
Ellipsled-2.00-1.00	F-2	17	40	4.83E+06	6.00	55.8	7.07E-02	893.1	1.54E+05	3.01E-01	
Ellipsled-2.00-0.25	G-1	18	40	3.01E+06	5.97	54.7	4.37E-02	881.4	1.42E+05	2.33E-01	
Ellipsled-2.00-0.25	G-1	19	40	4.79E+06	6.00	55.9	7.02E-02	894.0	1.55E+05	3.00E-01	
Ellipsled-2.00-0.25	G-1	20	40	6.86E+06	6.01	57.3	1.02E-01	905.9	1.67E+05	3.68E-01	
Ellipsled-2.00-0.25	G-1	21	40	8.32E+06	6.03	58.5	1.25E-01	917.8	1.79E+05	4.14E-01	
Ellipsled-2.00-0.25	G-1	22	40	2.06E+06	5.96	61.9	3.20E-02	939.5	2.02E+05	2.16E-01	
Ellipsled-2.00-0.25	G-1	23	40	7.51E+06	6.02	58.6	1.12E-01	917.9	1.79E+05	3.93E-01	
Ellipsled-2.00-0.50	H-1	24	40	2.08E+06	5.96	62.0	3.22E-02	940.4	2.03E+05	2.17E-01	
Ellipsled-2.00-0.50	H-1	25	40	4.73E+06	5.99	56.5	6.97E-02	898.4	1.59E+05	3.01E-01	
Ellipsled-2.00-0.50	H-1	26	40	6.64E+06	6.13	55.3	9.50E-02	906.3	1.65E+05	3.56E-01	
Ellipsled-2.00-0.50	H-1	27	40	3.01E+06	5.97	54.8	4.39E-02	882.0	1.43E+05	2.34E-01	
Ellipsled-2.00-0.50	H-1	28	40	7.63E+06	6.02	58.0	1.14E-01	912.7	1.74E+05	3.93E-01	
Ellipsled-2.00-0.50	H-1	29	40	8.33E+06	6.03	58.7	1.25E-01	919.2	1.80E+05	4.15E-01	
Ellipsled-1.00-1.00	B-1	32	40	7.60E+06	6.02	58.0	1.13E-01	913.2	1.74E+05	3.92E-01	
Ellipsled-1.00-1.00	B-1	33	40	3.09E+06	5.99	62.1	4.78E-02	945.3	2.08E+05	2.66E-01	
COBRA-14888B	D-2	36	40	6.84E+06	6.01	57.5	1.02E-01	908.5	1.69E+05	3.69E-01	
COBRA-14888B	D-2	37	40	7.66E+06	6.02	57.8	1.14E-01	910.8	1.72E+05	3.92E-01	
Ellipsled-0.50-1.00	I-1	38	40	4.84E+06	5.99	55.9	7.11E-02	893.7	1.54E+05	3.02E-01	
Ellipsled-0.50-1.00	I-1	39	40	3.03E+06	5.97	54.9	4.42E-02	883.1	1.44E+05	2.35E-01	
Ellipsled-0.50-1.00	I-1	40	40	2.07E+06	5.96	62.0	3.21E-02	940.7	2.04E+05	2.16E-01	
Ellipsled-0.50-1.00	I-1	41	40	6.73E+06	6.01	57.8	1.00E-01	911.1	1.72E+05	3.68E-01	
Ellipsled-0.50-1.00	I-1	42	40	7.65E+06	6.02	58.0	1.14E-01	912.8	1.74E+05	3.93E-01	
Ellipsled-0.50-1.00	I-1	43	40	8.34E+06	6.03	58.5	1.25E-01	917.8	1.79E+05	4.14E-01	
COBRA-14297B	C-1	44	40	4.80E+06	5.99	56.1	7.05E-02	895.2	1.56E+05	3.02E-01	
COBRA-14297B	C-1	45	40	3.03E+06	5.97	54.7	4.40E-02	881.2	1.42E+05	2.34E-01	
COBRA-14297B	C-1	48	40	6.84E+06	6.01	57.5	1.02E-01	908.5	1.69E+05	3.69E-01	
COBRA-14297B	C-1	49	40	7.60E+06	6.01	58.0	1.14E-01	912.0	1.73E+05	3.92E-01	
COBRA-14297B	C-1	50	40	8.35E+06	6.03	58.6	1.25E-01	918.0	1.79E+05	4.15E-01	
COBRA-8459B	E-1	52	40	4.74E+06	5.99	56.2	6.98E-02	896.3	1.57E+05	3.01E-01	
COBRA-8459B	E-1	54	40	3.03E+06	5.97	54.9	4.42E-02	883.0	1.44E+05	2.35E-01	
COBRA-8459B	E-1	55	40	7.55E+06	6.02	58.3	1.13E-01	915.1	1.76E+05	3.92E-01	
COBRA-8459B	E-1	56	40	6.93E+06	6.01	57.2	1.03E-01	905.2	1.66E+05	3.69E-01	
COBRA-14888B	D-2	61	40	8.28E+06	6.03	58.7	1.24E-01	919.0	1.80E+05	4.14E-01	
COBRA-14888B	D-2	63	40	4.80E+06	5.99	56.0	7.05E-02	893.9	1.55E+05	3.01E-01	
Ellipsled-1.00-1.00	B-1	65	30	3.05E+06	5.97	54.5	4.43E-02	879.5	1.40E+05	2.34E-01	
Ellipsled-1.00-1.00	B-1	66	30	4.85E+06	5.99	55.9	7.12E-02	893.1	1.54E+05	3.02E-01	
Ellipsled-1.00-1.00	B-1	67	30	6.84E+06	6.01	57.5	1.02E-01	908.1	1.69E+05	3.69E-01	
Ellipsled-1.00-1.00	B-1	68	30	7.58E+06	6.01	58.1	1.13E-01	912.5	1.73E+05	3.92E-01	
Ellipsled-1.00-1.00	B-1	69	30	8.32E+06	6.03	58.6	1.25E-01	918.6	1.80E+05	4.14E-01	
Ellipsled-2.00-1.00	F-2	70	30	2.99E+06	5.97	55.1	4.37E-02	884.7	1.46E+05	2.34E-01	
Ellipsled-2.00-1.00	F-2	71	30	4.81E+06	5.99	56.1	7.06E-02	894.7	1.55E+05	3.02E-01	
Ellipsled-2.00-1.00	F-2	72	30	6.86E+06	6.01	57.6	1.02E-01	908.8	1.70E+05	3.70E-01	
Ellipsled-2.00-1.00	F-2	73	30	7.52E+06	6.02	58.2	1.12E-01	914.6	1.75E+05	3.91E-01	
Ellipsled-2.00-1.00	F-2	74	30	8.37E+06	6.03	58.5	1.25E-01	917.5	1.78E+05	4.15E-01	
Ellipsled-0.50-1.00	I-1	75	30	3.00E+06	5.97	54.9	4.37E-02	883.4	1.44E+05	2.34E-01	
Ellipsled-0.50-1.00	I-1	76	30	4.74E+06	5.99	56.3	6.97E-02	896.4	1.57E+05	3.01E-01	
Ellipsled-0.50-1.00	I-1	78	30	6.83E+06	6.01	57.5	1.02E-01	908.2	1.69E+05	3.69E-01	
Ellipsled-0.50-1.00	I-1	79	30	7.66E+06	6.02	57.9	1.14E-01	912.3	1.73E+05	3.93E-01	
Ellipsled-0.50-1.00	I-1	80	30	8.32E+06	6.03	58.5	1.25E-01	917.6	1.79E+05	4.14E-01	
COBRA-8459B	E-2	81	40	4.80E+06	5.99	56.1	7.06E-02	895.2	1.56E+05	3.02E-01	

Configuration	Model ID	Run	α (deg)	Re_∞ (1/ft)	M_∞	T_∞ (K)	ρ_∞ (kg/m^3)	U_∞ (m/s)	ΔH_{tot} (J/kg)	h_{FR} (kg/m^2-s)	Trips
COBRA-8459B	E-2	82	40	6.87E+06	6.01	57.5	1.02E-01	908.1	1.69E+05	3.70E-01	
COBRA-8459B	E-2	83	40	7.60E+06	6.02	58.0	1.13E-01	912.9	1.74E+05	3.92E-01	
COBRA-8459B	E-2	85	40	8.31E+06	6.03	58.7	1.25E-01	918.8	1.80E+05	4.14E-01	
Hammerhead-Sharp	J-1	86	40	4.75E+06	5.99	56.5	7.00E-02	898.2	1.59E+05	3.02E-01	
Hammerhead-Sharp	J-1	87	40	2.98E+06	5.97	55.1	4.35E-02	884.6	1.45E+05	2.34E-01	
Hammerhead-Sharp	J-1	88	40	6.88E+06	6.01	57.6	1.02E-01	909.0	1.70E+05	3.70E-01	
Hammerhead-Sharp	J-1	89	40	7.62E+06	6.03	57.9	1.14E-01	912.6	1.73E+05	3.92E-01	
Hammerhead-Sharp	J-1	90	40	8.33E+06	6.03	58.6	1.25E-01	918.6	1.80E+05	4.15E-01	
Hammerhead-Nominal	K-1	93	40	4.80E+06	5.99	55.9	7.05E-02	893.1	1.54E+05	3.01E-01	
Hammerhead-Nominal	K-1	95	40	3.00E+06	5.97	54.9	4.37E-02	882.7	1.44E+05	2.34E-01	
Hammerhead-Nominal	K-1	96	40	6.84E+06	6.01	57.6	1.02E-01	908.8	1.70E+05	3.69E-01	
Hammerhead-Nominal	K-1	97	40	7.55E+06	6.02	58.1	1.13E-01	913.9	1.75E+05	3.92E-01	
Hammerhead-Nominal	K-1	98	40	8.27E+06	6.03	58.8	1.24E-01	920.3	1.81E+05	4.14E-01	
Hammerhead-Blunt	L-1	99	40	4.91E+06	5.99	55.4	7.18E-02	888.2	1.49E+05	3.02E-01	
Hammerhead-Blunt	L-1	100	40	2.97E+06	5.97	54.8	4.32E-02	882.6	1.43E+05	2.32E-01	
Hammerhead-Blunt	L-1	101	40	6.88E+06	6.01	57.3	1.02E-01	905.8	1.67E+05	3.68E-01	
Hammerhead-Blunt	L-1	102	40	7.61E+06	6.02	57.9	1.13E-01	911.6	1.72E+05	3.91E-01	
Hammerhead-Blunt	L-1	103	40	8.34E+06	6.03	58.5	1.25E-01	917.8	1.79E+05	4.14E-01	
COBRA-14888B	D-3	104	40	4.72E+06	5.99	56.3	6.95E-02	897.1	1.58E+05	3.00E-01	
COBRA-14888B	D-3	105	40	2.95E+06	5.97	55.1	4.31E-02	884.9	1.46E+05	2.33E-01	
COBRA-14888B	D-3	107	40	6.91E+06	6.01	57.3	1.03E-01	906.0	1.67E+05	3.69E-01	
COBRA-14888B	D-3	108	40	7.59E+06	6.02	58.0	1.13E-01	912.6	1.73E+05	3.91E-01	
COBRA-14888B	D-3	109	40	8.28E+06	6.03	58.8	1.24E-01	919.6	1.81E+05	4.14E-01	
COBRA-14297B	C-3	110	40	6.81E+06	6.01	57.6	1.01E-01	909.2	1.70E+05	3.69E-01	
COBRA-14297B	C-3	111	40	7.59E+06	6.02	58.1	1.13E-01	913.9	1.75E+05	3.92E-01	
COBRA-14297B	C-3	113	40	8.27E+06	6.03	58.8	1.24E-01	920.1	1.81E+05	4.14E-01	
Ellipsled-1.00-1.00	B-1	120	40	4.76E+06	5.99	56.2	7.00E-02	896.3	1.57E+05	3.01E-01	x/L=0.10
Ellipsled-1.00-1.00	B-1	121	40	6.80E+06	6.01	57.7	1.01E-01	910.4	1.71E+05	3.69E-01	x/L=0.10
Ellipsled-1.00-1.00	B-1	122	40	7.57E+06	6.02	58.2	1.13E-01	914.9	1.76E+05	3.93E-01	x/L=0.10
Ellipsled-1.00-1.00	B-1	123	40	8.25E+06	6.03	58.9	1.24E-01	921.1	1.82E+05	4.14E-01	x/L=0.10
Ellipsled-2.00-1.00	F-2	124	40	4.77E+06	5.99	56.2	7.01E-02	896.0	1.57E+05	3.01E-01	x/L=0.10
Ellipsled-2.00-1.00	F-2	125	40	6.97E+06	6.01	57.1	1.03E-01	904.1	1.65E+05	3.70E-01	x/L=0.10
Ellipsled-2.00-1.00	F-2	126	40	7.59E+06	6.02	57.9	1.13E-01	912.2	1.73E+05	3.91E-01	x/L=0.10
Ellipsled-2.00-1.00	F-2	127	40	8.31E+06	6.03	58.6	1.24E-01	918.4	1.79E+05	4.14E-01	x/L=0.10
Ellipsled-2.00-0.50	H-1	128	40	4.79E+06	5.99	56.0	7.03E-02	894.0	1.55E+05	3.01E-01	x/L=0.10
Ellipsled-2.00-0.50	H-1	129	40	6.86E+06	6.01	57.5	1.02E-01	908.2	1.69E+05	3.69E-01	x/L=0.10
Ellipsled-2.00-0.50	H-1	130	40	7.48E+06	6.02	58.4	1.12E-01	916.1	1.77E+05	3.91E-01	x/L=0.10
Ellipsled-2.00-0.50	H-1	131	40	8.28E+06	6.03	58.8	1.24E-01	919.8	1.81E+05	4.14E-01	x/L=0.10
Ellipsled-2.00-0.25	G-1	132	40	4.77E+06	5.99	56.3	7.03E-02	896.4	1.57E+05	3.02E-01	x/L=0.10
Ellipsled-2.00-0.25	G-1	133	40	6.92E+06	6.01	57.3	1.03E-01	906.4	1.67E+05	3.70E-01	x/L=0.10
Ellipsled-2.00-0.25	G-1	134	40	7.57E+06	6.02	58.0	1.13E-01	912.8	1.74E+05	3.91E-01	x/L=0.10
Ellipsled-2.00-0.25	G-1	135	40	8.33E+06	6.03	58.6	1.25E-01	917.9	1.79E+05	4.14E-01	x/L=0.10
COBRA-14888B	D-3	136	40	6.92E+06	6.01	57.3	1.03E-01	906.1	1.67E+05	3.70E-01	x/L=0.10
COBRA-14888B	D-3	137	40	7.57E+06	6.02	58.2	1.13E-01	914.8	1.76E+05	3.93E-01	x/L=0.10
COBRA-14888B	D-3	138	40	8.28E+06	6.03	58.8	1.24E-01	920.0	1.81E+05	4.14E-01	x/L=0.10
COBRA-14297B	C-3	141	40	6.85E+06	6.01	57.5	1.02E-01	908.2	1.69E+05	3.69E-01	x/L=0.10
COBRA-14297B	C-3	142	40	7.58E+06	6.02	58.1	1.13E-01	913.7	1.75E+05	3.92E-01	x/L=0.10
COBRA-14297B	C-3	143	40	8.36E+06	6.03	58.5	1.25E-01	917.5	1.78E+05	4.15E-01	x/L=0.10
COBRA-8459B	E-2	145	40	6.78E+06	6.01	57.8	1.01E-01	910.5	1.71E+05	3.69E-01	x/L=0.10
COBRA-8459B	E-2	146	40	7.52E+06	6.02	58.3	1.13E-01	915.9	1.77E+05	3.92E-01	x/L=0.10
COBRA-8459B	E-2	147	40	8.40E+06	6.03	58.4	1.26E-01	916.4	1.77E+05	4.15E-01	x/L=0.10
Ellipsled-1.00-1.00	B-2	150	40	6.78E+06	6.01	57.8	1.01E-01	910.5	1.71E+05	3.69E-01	x/L=0.50
Ellipsled-1.00-1.00	B-2	151	40	7.52E+06	6.02	58.3	1.13E-01	915.9	1.77E+05	3.92E-01	x/L=0.50
Ellipsled-1.00-1.00	B-2	152	40	8.40E+06	6.03	58.4	1.26E-01	916.4	1.77E+05	4.15E-01	x/L=0.50
Ellipsled-1.00-1.00	B-2	153	40	6.78E+06	6.01	57.8	1.01E-01	910.5	1.71E+05	3.69E-01	x/L=0.25
Ellipsled-1.00-1.00	B-2	154	40	7.52E+06	6.02	58.3	1.13E-01	915.9	1.77E+05	3.92E-01	x/L=0.25
Ellipsled-1.00-1.00	B-2	155	40	8.40E+06	6.03	58.4	1.26E-01	916.4	1.77E+05	4.15E-01	x/L=0.25

Table 6. Test 6966 Run-Averaged Conditions

Re_∞ (1/ft)	M_∞	T_∞ (K)	ρ_∞ (kg/m^3)	U_∞ (m/s)	ΔH_{tot} (J/kg)	h_{FR} (kg/m^2-s)
2.07E+06	5.96	61.9	3.201E-02	940.0	2.031E+05	2.163E-01
3.01E+06	5.97	54.8	4.380E-02	882.2	1.431E+05	2.336E-01
4.79E+06	5.99	56.1	7.034E-02	895.0	1.556E+05	3.013E-01
6.84E+06	6.02	57.4	1.016E-01	908.0	1.686E+05	3.685E-01
7.58E+06	6.02	58.1	1.132E-01	913.8	1.746E+05	3.921E-01
8.33E+06	6.03	58.6	1.249E-01	918.2	1.792E+05	4.172E-01

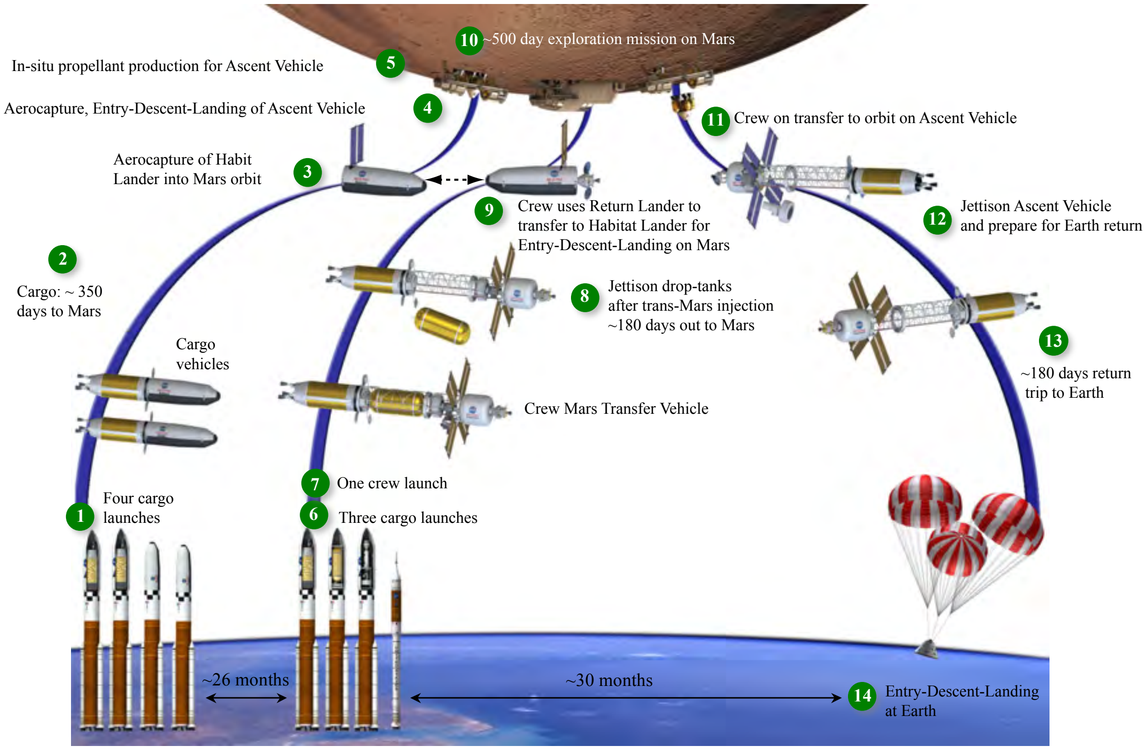

Figure 1. Mars Design Reference Mission

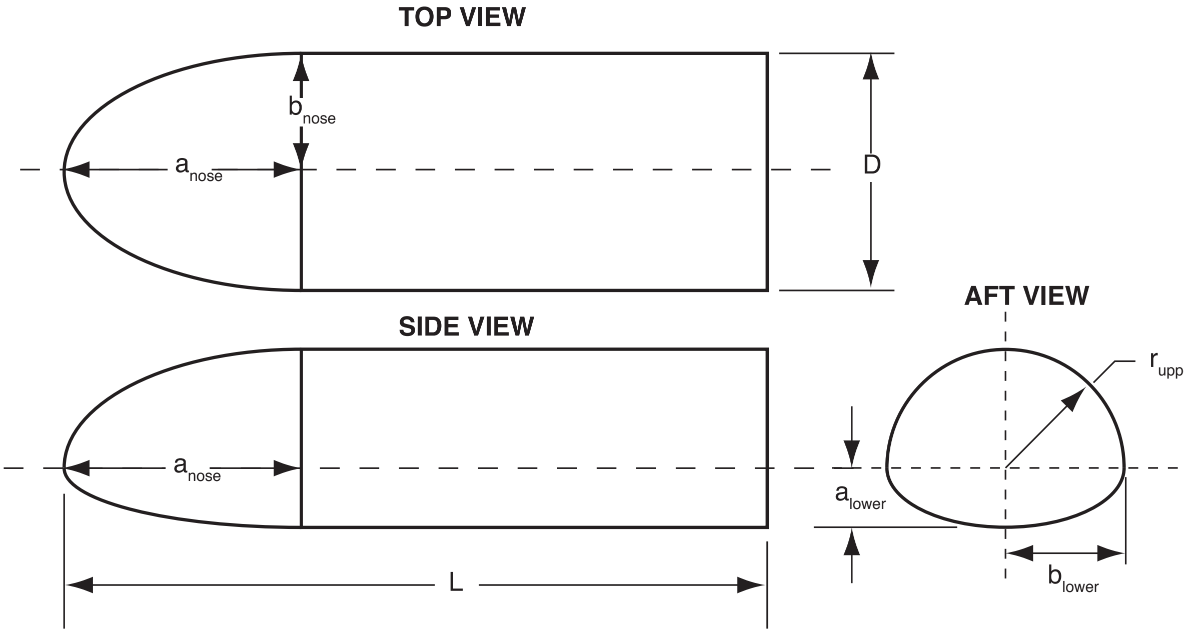

Figure 2. Ellipsled Geometry Definition

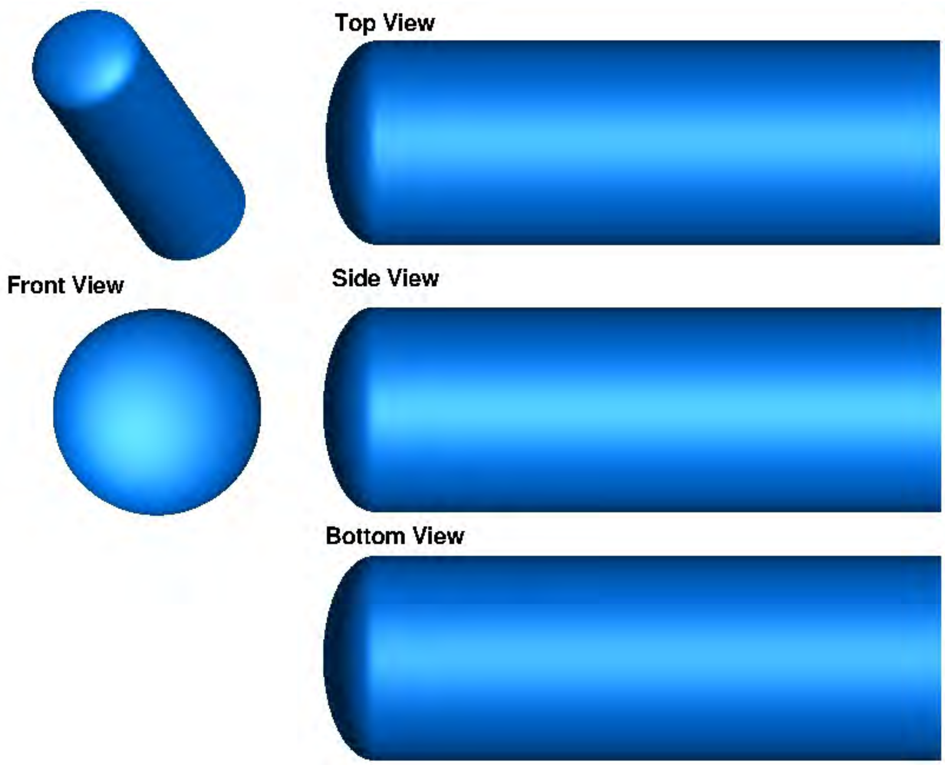

Figure 3. Schematic of Ellipsled-0.50-1.00 Configuration

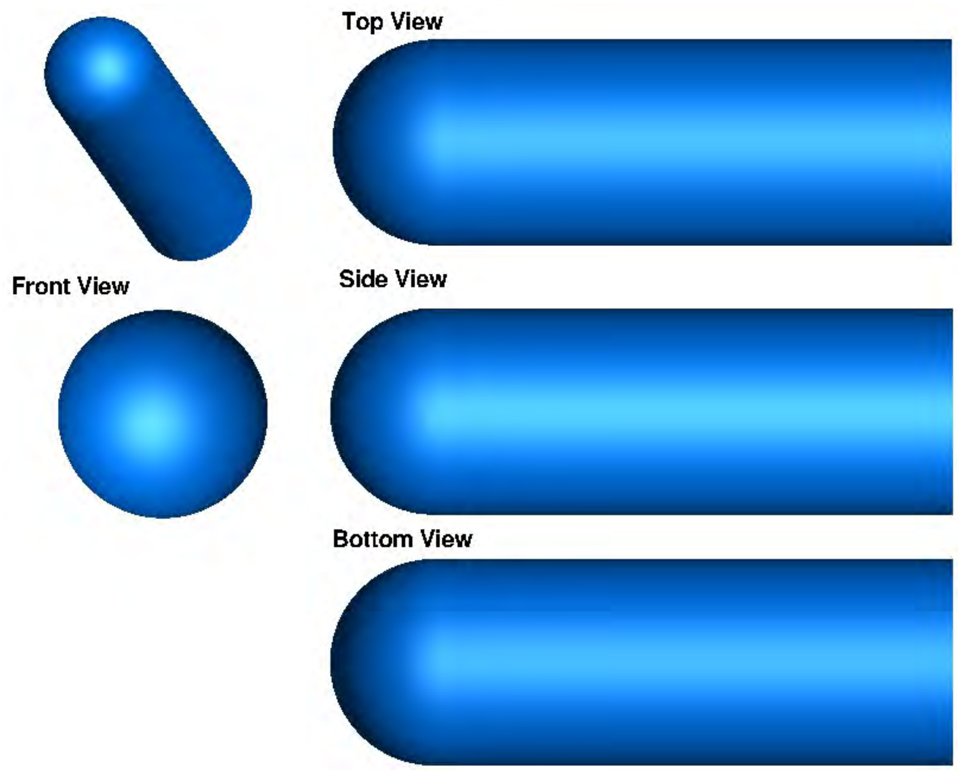

Figure 4. Schematic of Ellipsled-1.00-1.00 Configuration

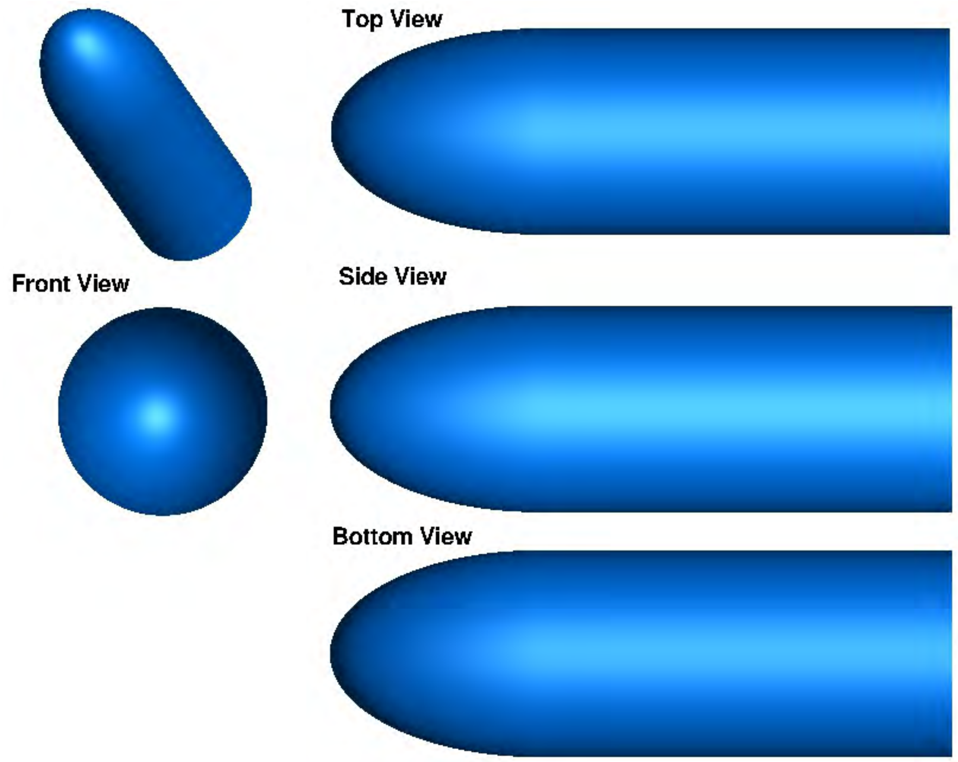

Figure 5. Schematic of Ellipsled-2.00-1.00 Configuration

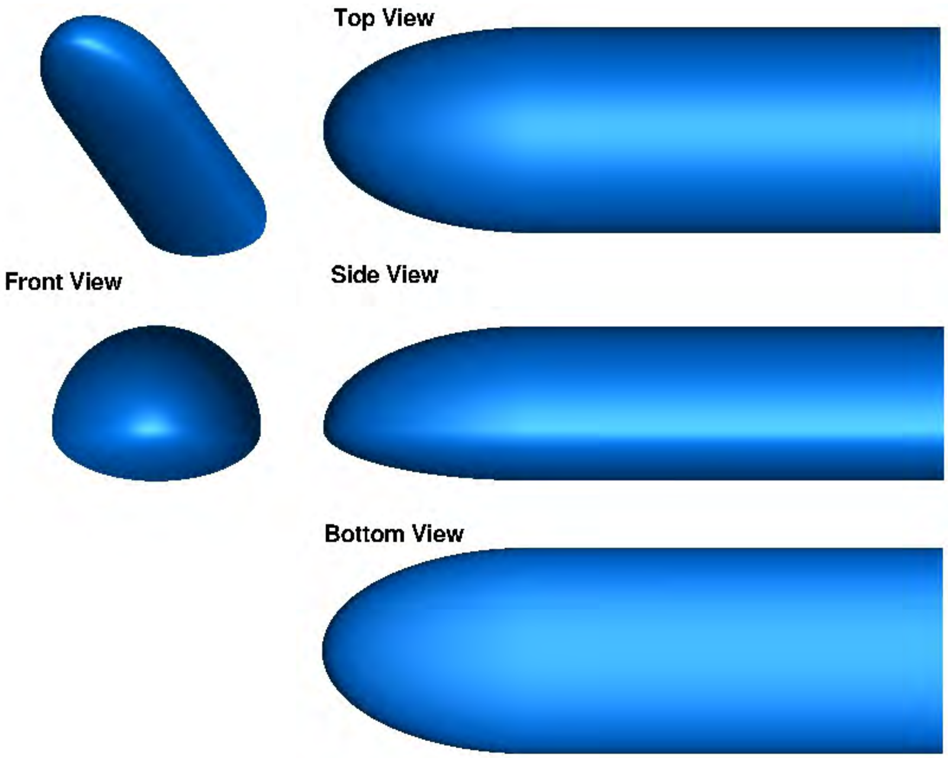

Figure 6. Schematic of Ellipsled-2.00-0.50 Configuration

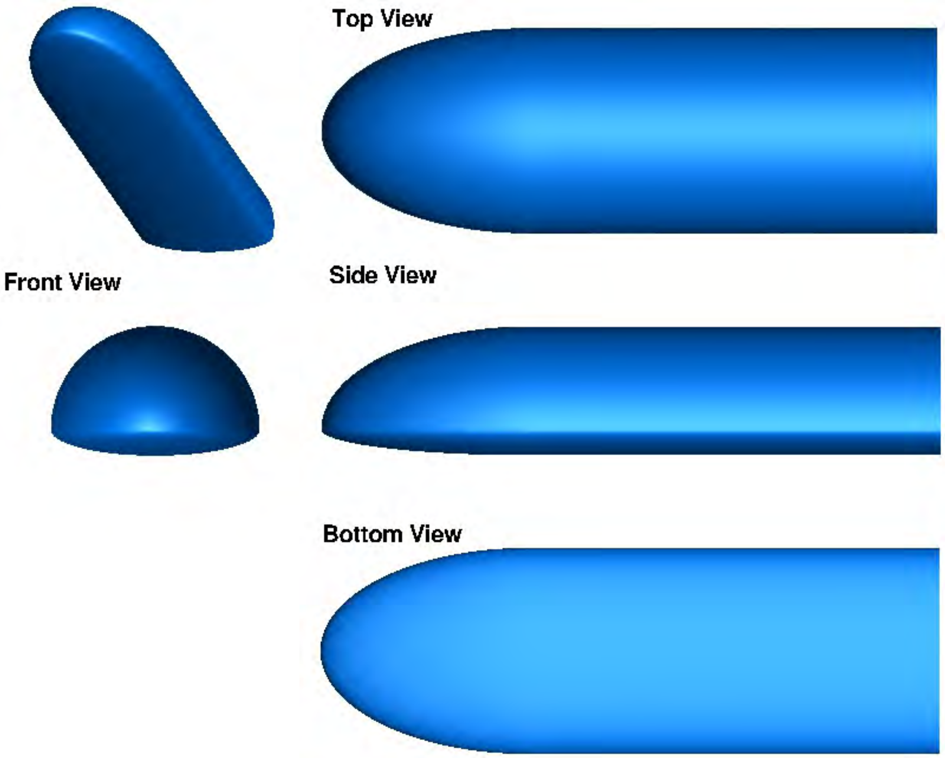

Figure 7. Schematic of Ellipsled-2.00-0.25 Configuration

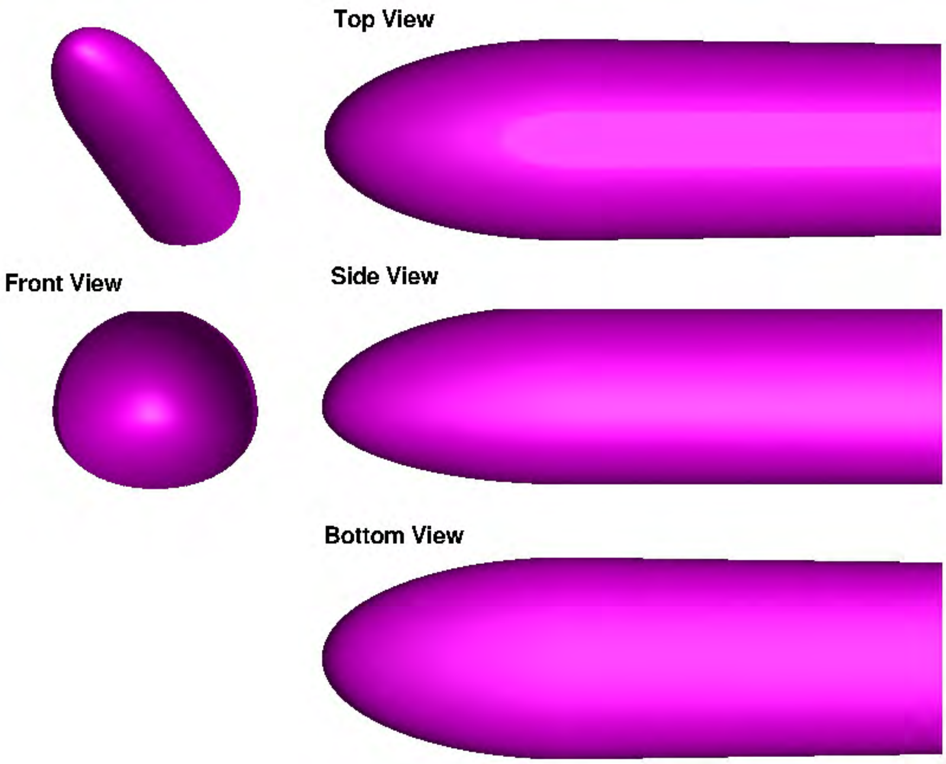

Figure 8. Schematic of COBRA-8459B Configuration

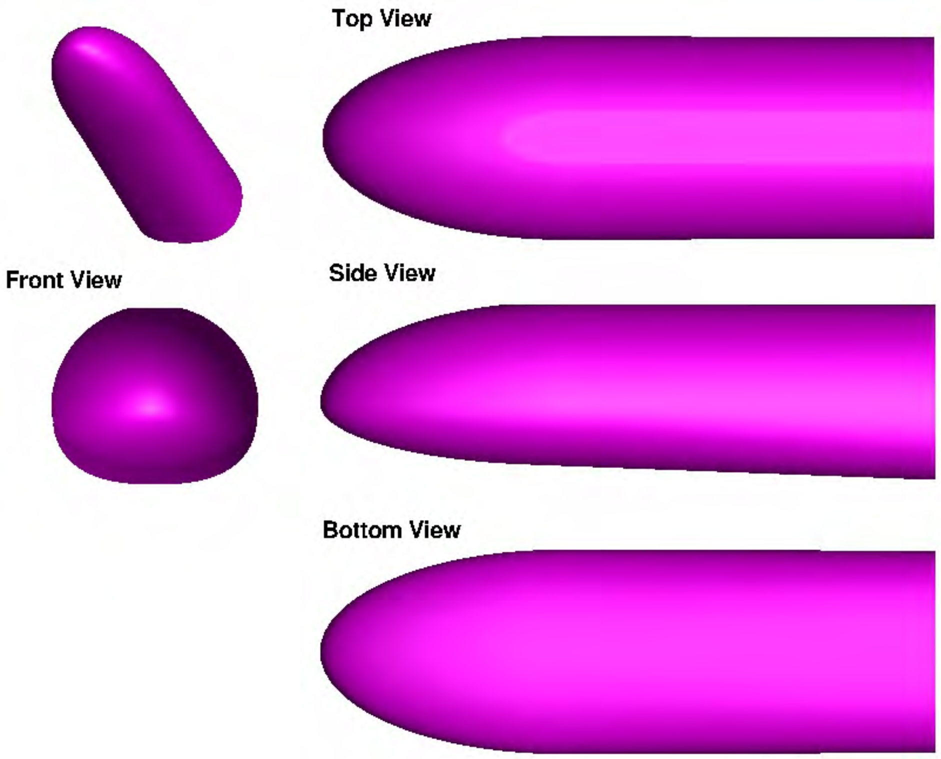

Figure 9. Schematic of COBRA-14297 Configuration

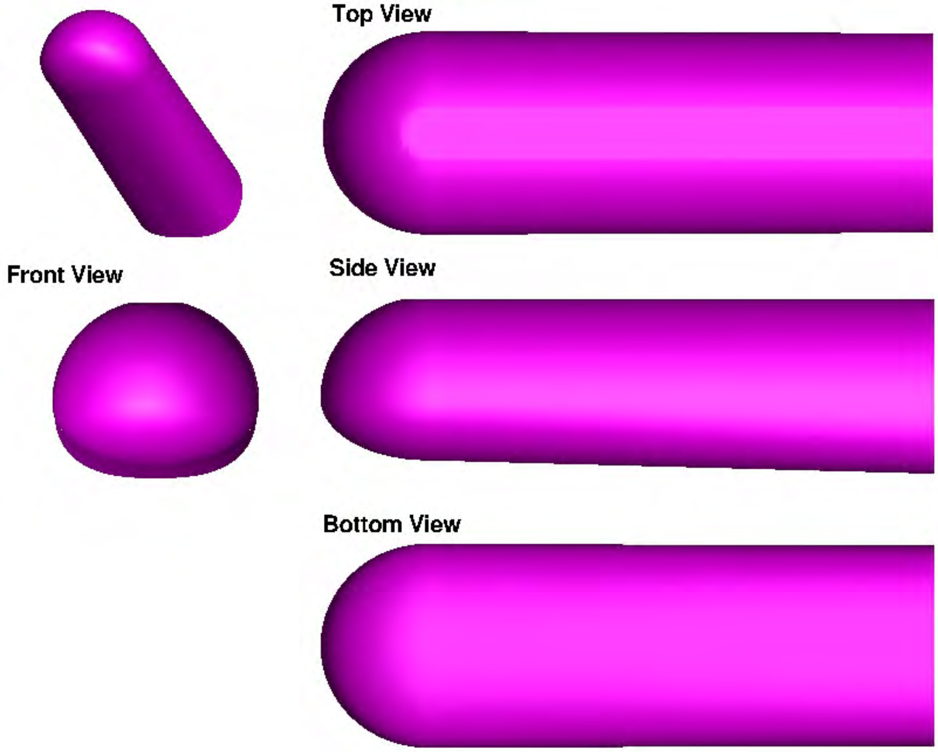

Figure 10. Schematic of COBRA-14888B Configuration

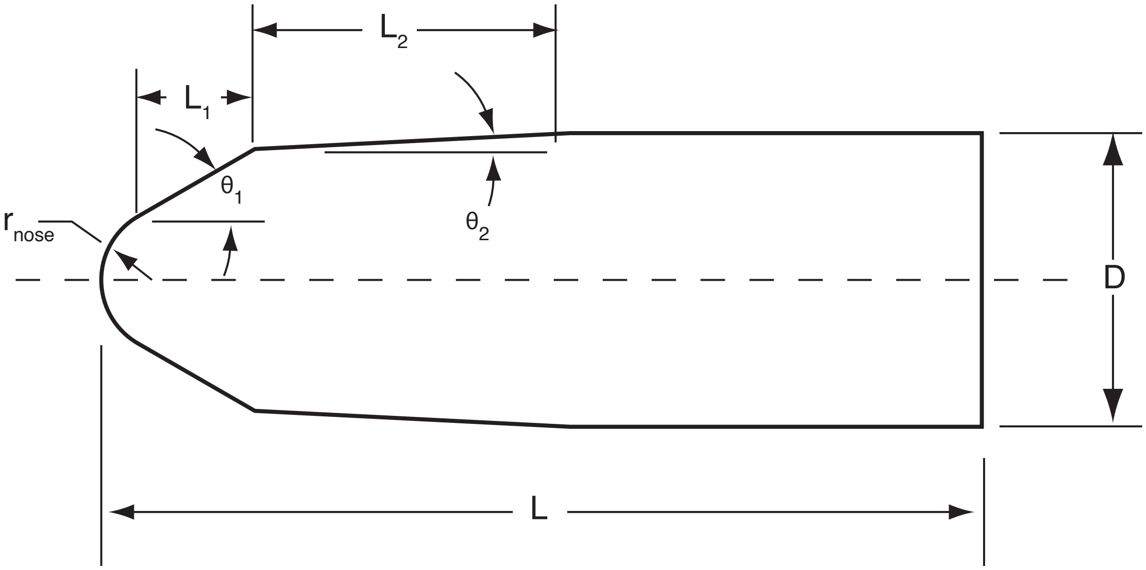

Figure 11. Hammerhead Geometry Definition

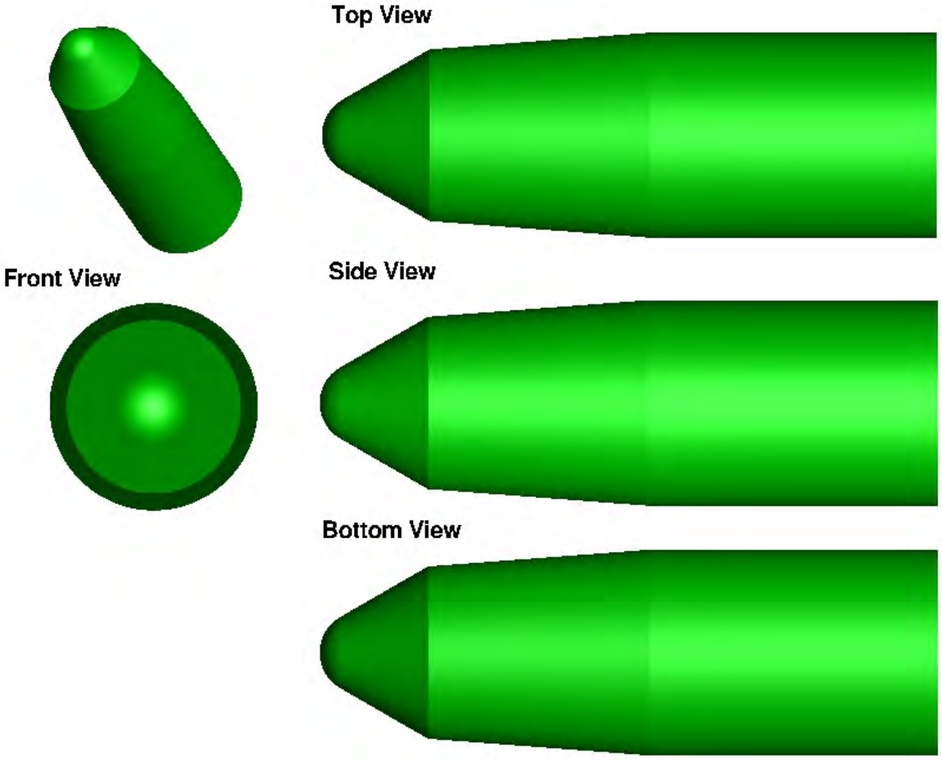

Figure 12. Schematic of Hammerhead-Sharp Configuration

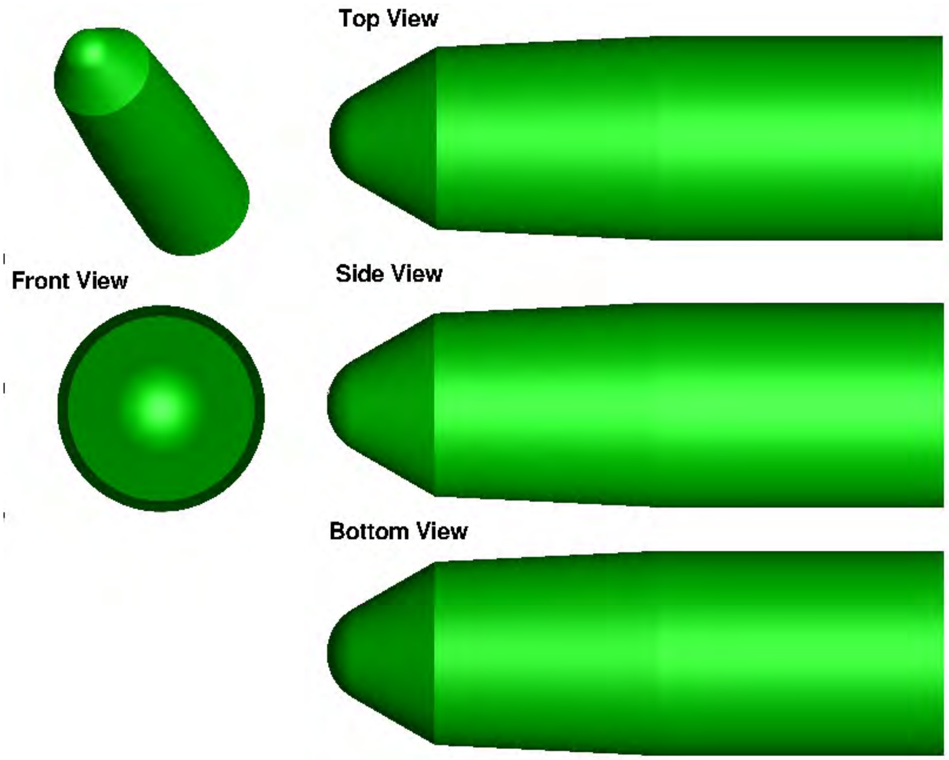

Figure 13. Schematic of Hammerhead-Nominal Configuration

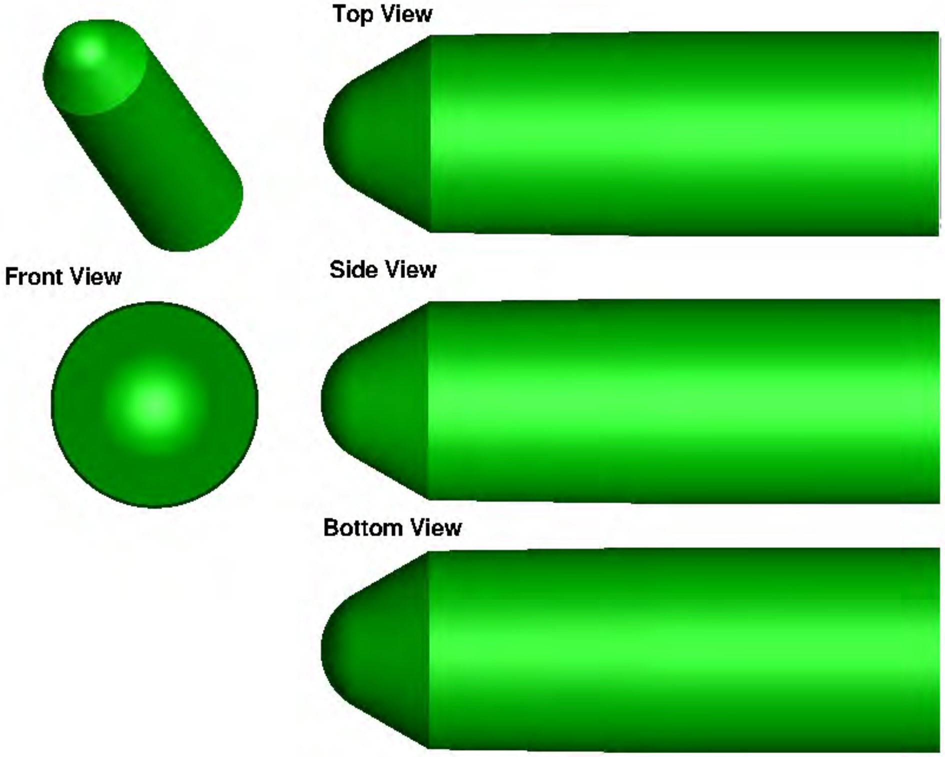

Figure 14. Schematic of Hammerhead-Blunt Configuration

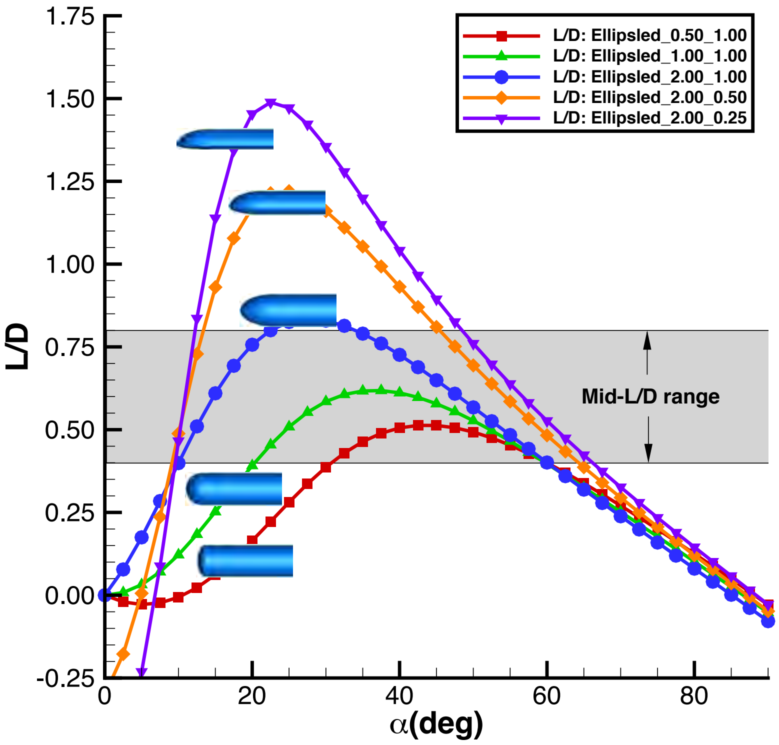

Figure 15. Ellipsled *L*/*D* vs. Angle-of-Attack

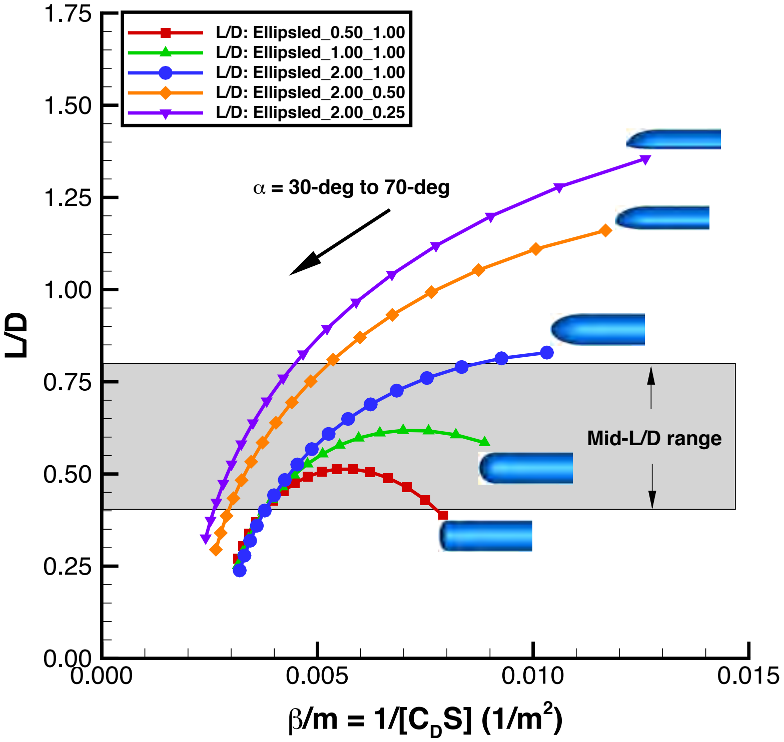

Figure 16. Ellipsled *L*/*D* vs. Reduced Ballistic Coefficient

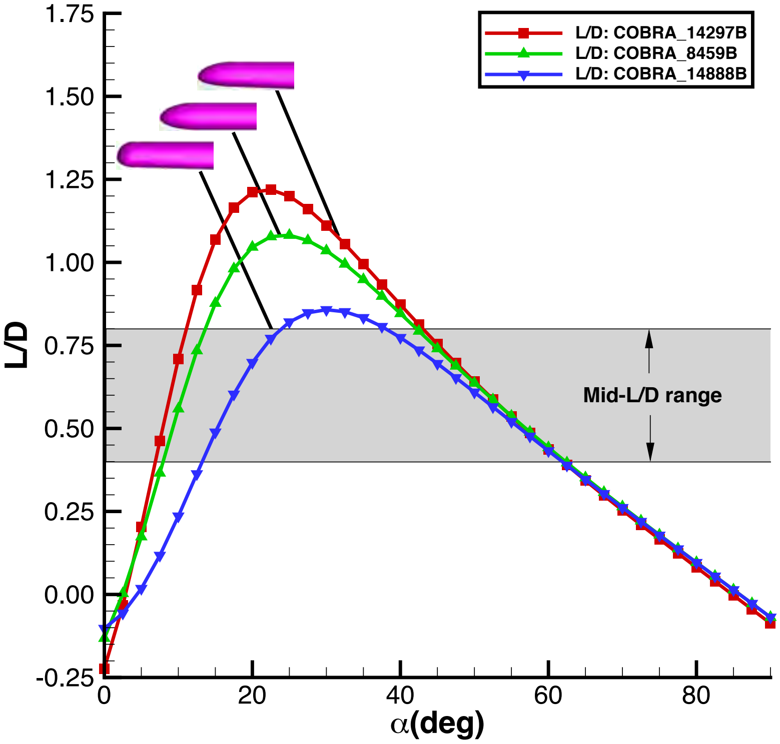

Figure 17. COBRA *L*/*D* vs. Angle-of-Attack

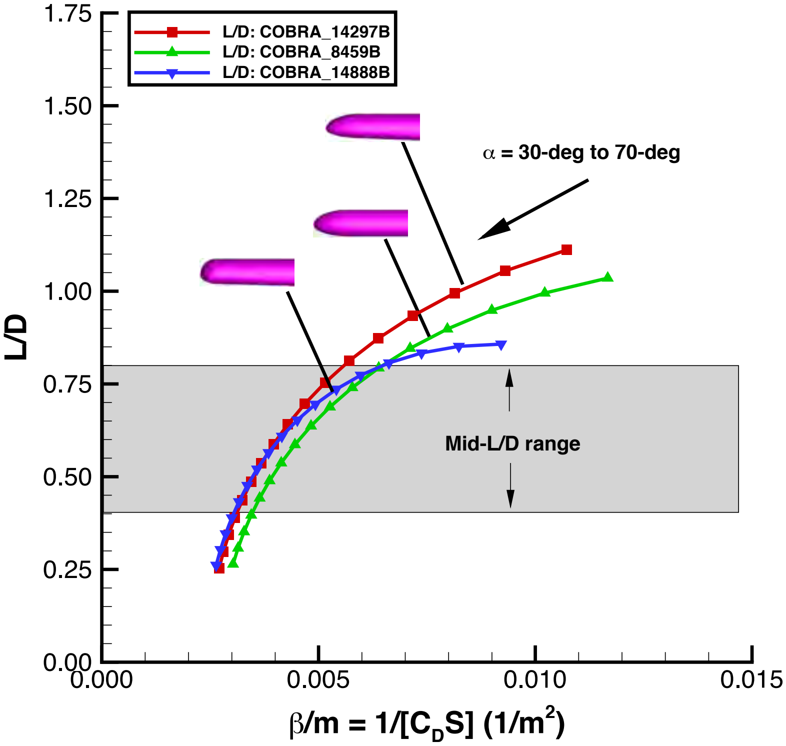

Figure 18. COBRA *L*/*D* vs. Reduced Ballistic Coefficient

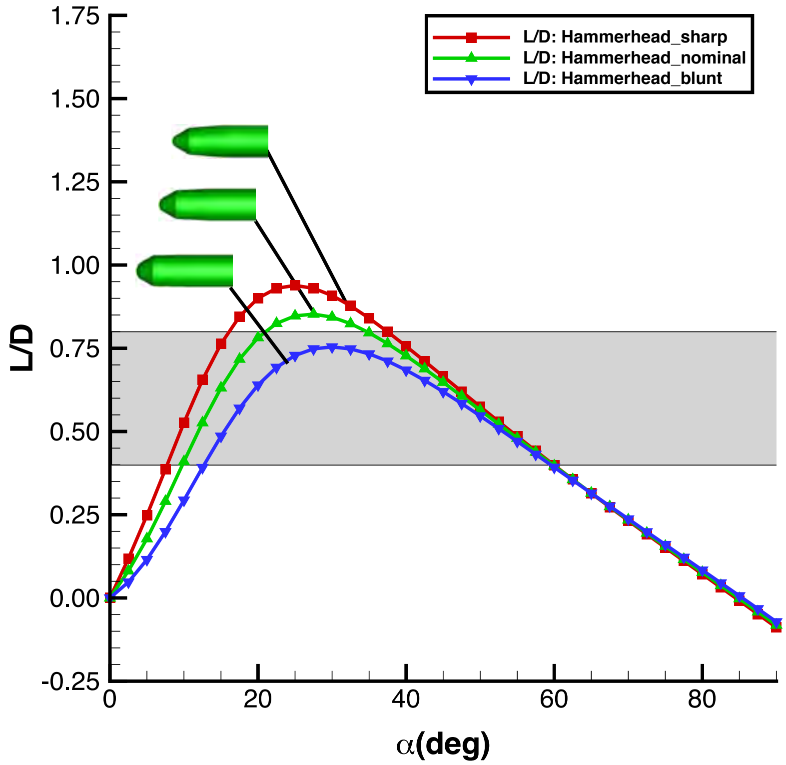

Figure 19. Hammerhead *L*/*D* vs. Angle-of-Attack

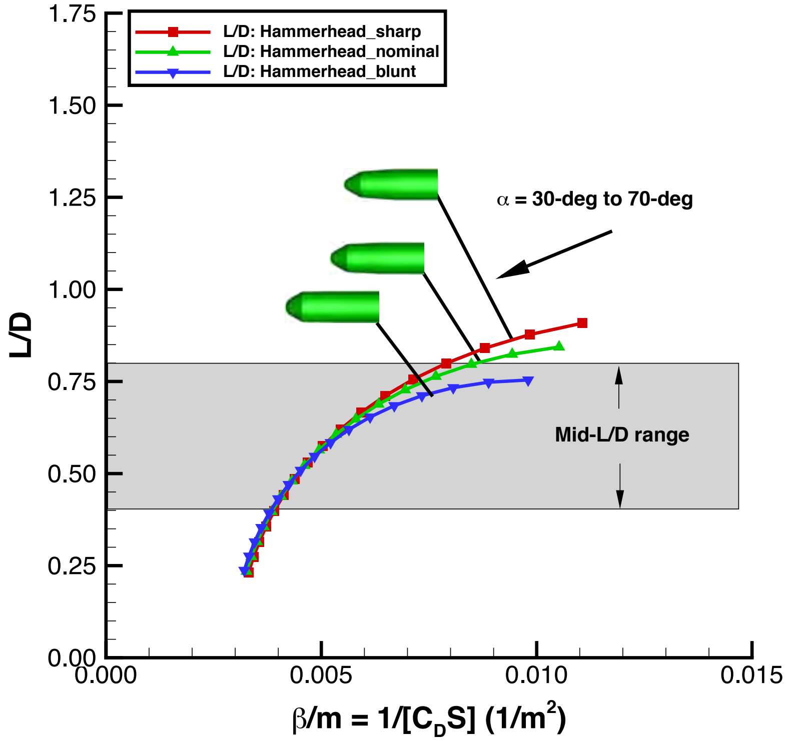

Figure 20. Hammerhead *L*/*D* vs. Reduced Ballistic Coefficient

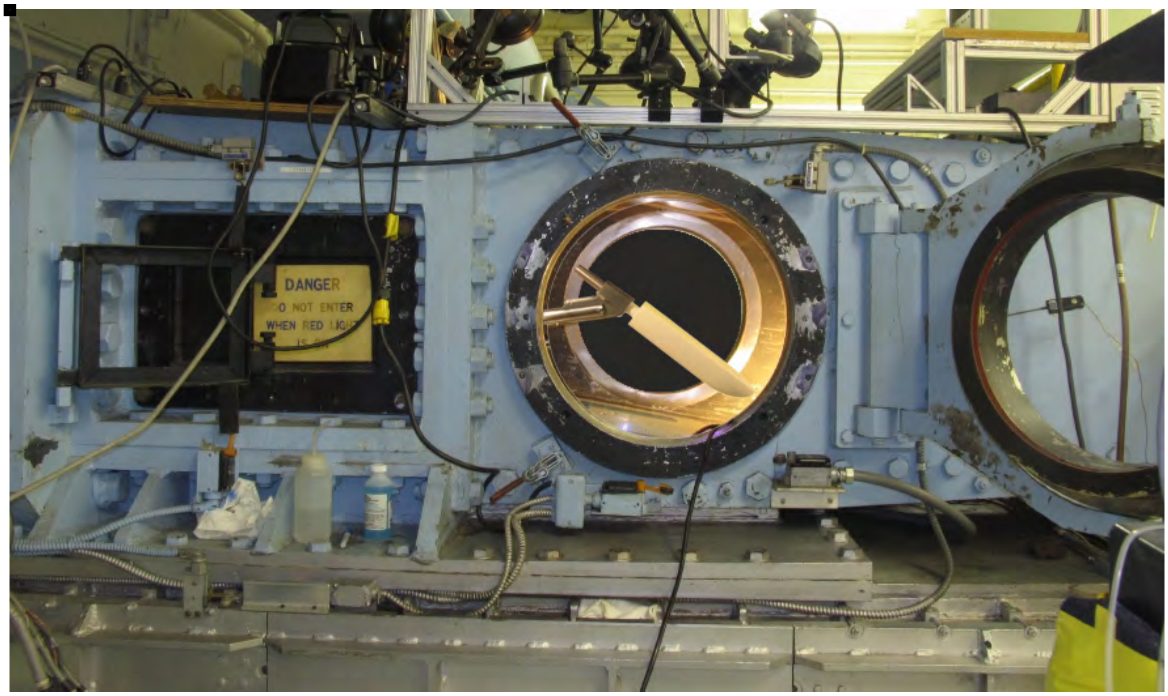

Figure 21. LaRC 20-Inch Mach 6 Air Tunnel

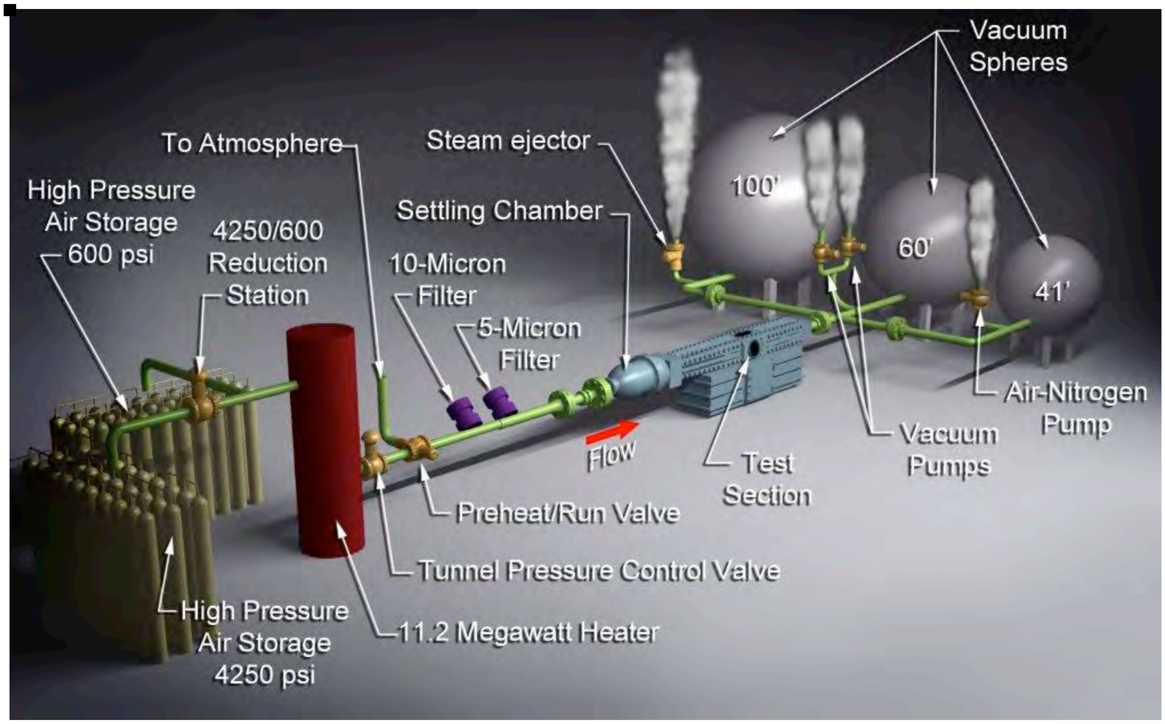

Figure 22. Schematic of LaRC 20-Inch Mach 6 Air Tunnel

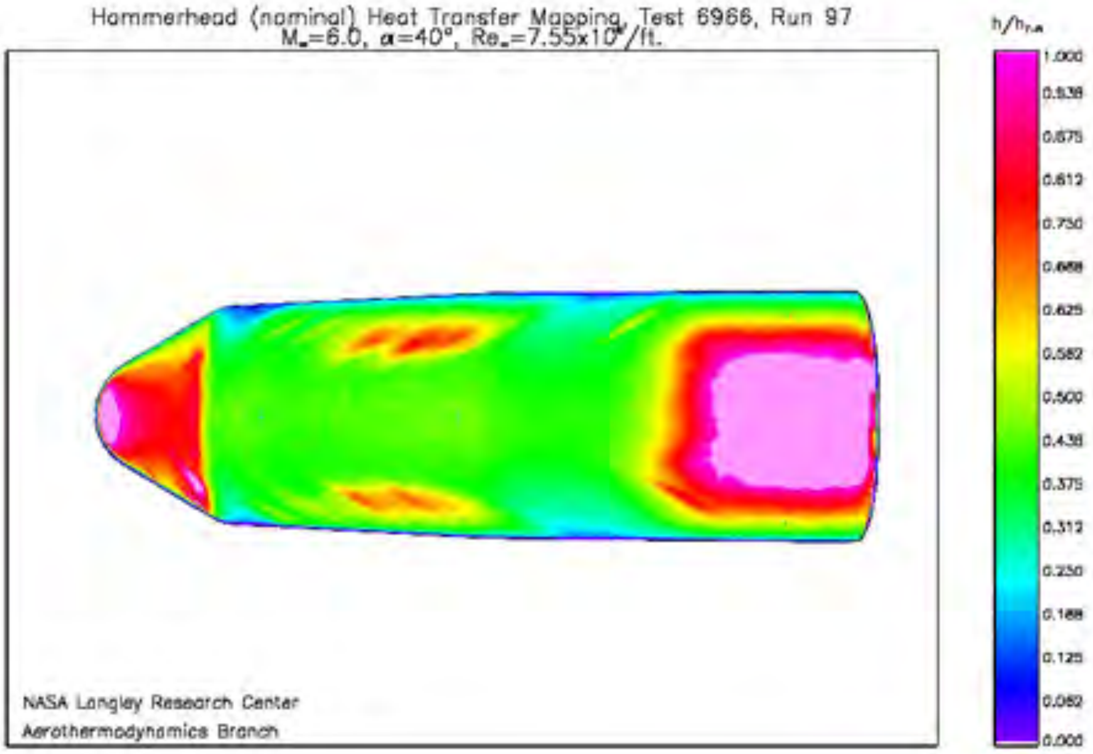

Figure 23. Sample 2-D Image Data from IHEAT

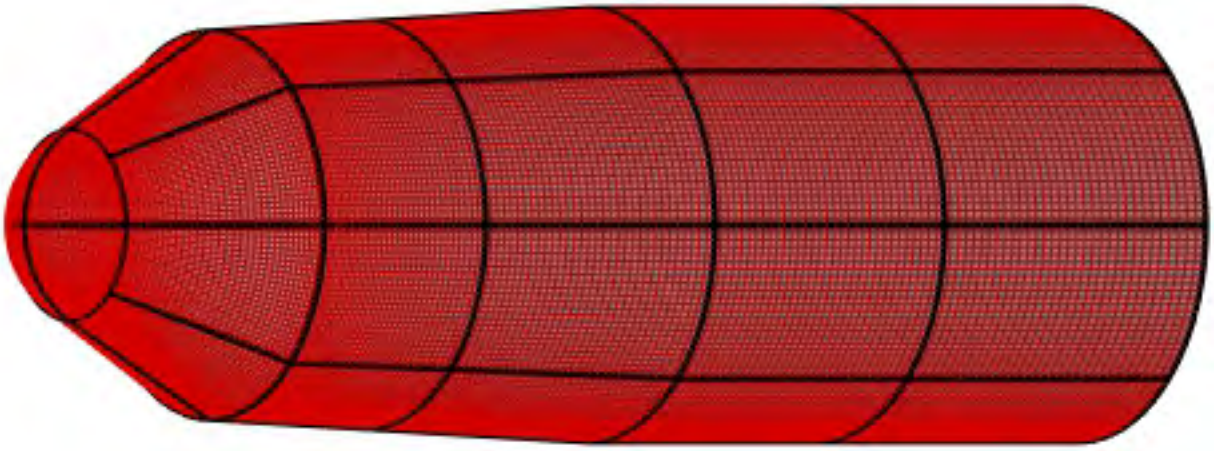

Figure 24. Sample 3-D Surface Geometry

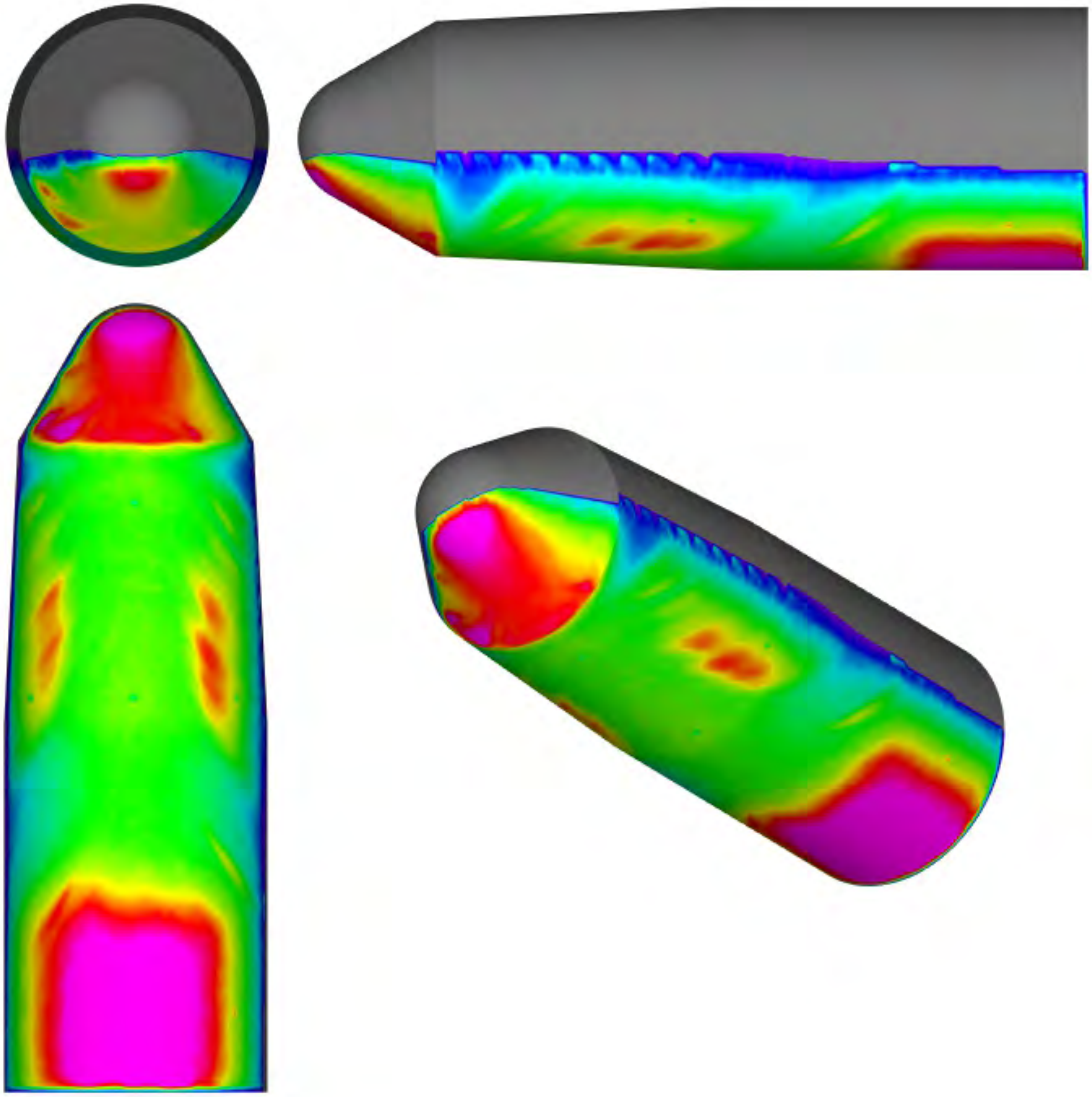

Figure 25. Sample Mapping of 2-D Image Data to 3-D Surface Geometry

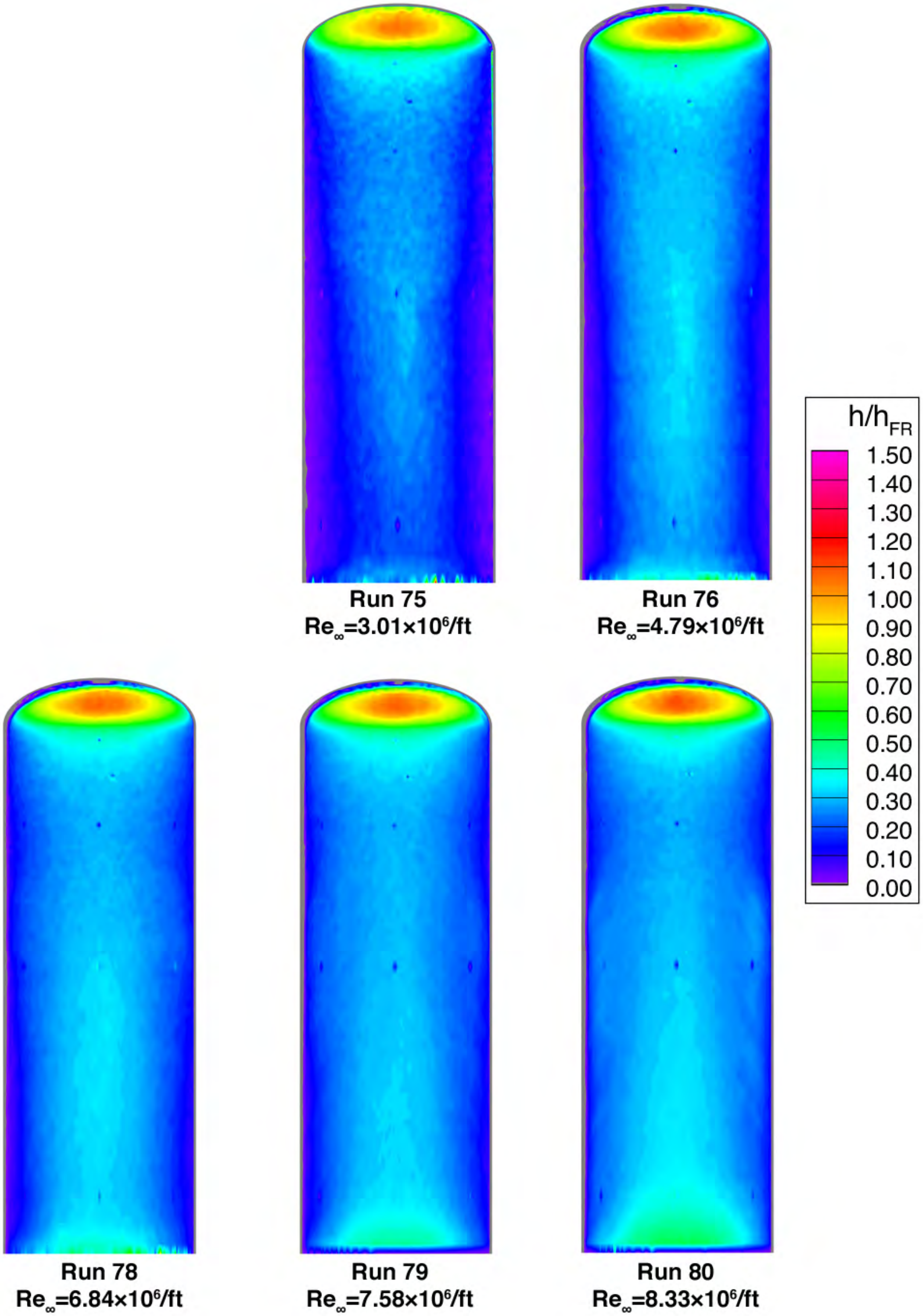

Run 75
Re_∞=3.01×10^6/ft

Run 76
Re_∞=4.79×10^6/ft

Run 78
Re_∞=6.84×10^6/ft

Run 79
Re_∞=7.58×10^6/ft

Run 80
Re_∞=8.33×10^6/ft

Figure 26. Reynolds Number Effects on Heating, Ellipsled-0.50-1.00, α = 30-deg

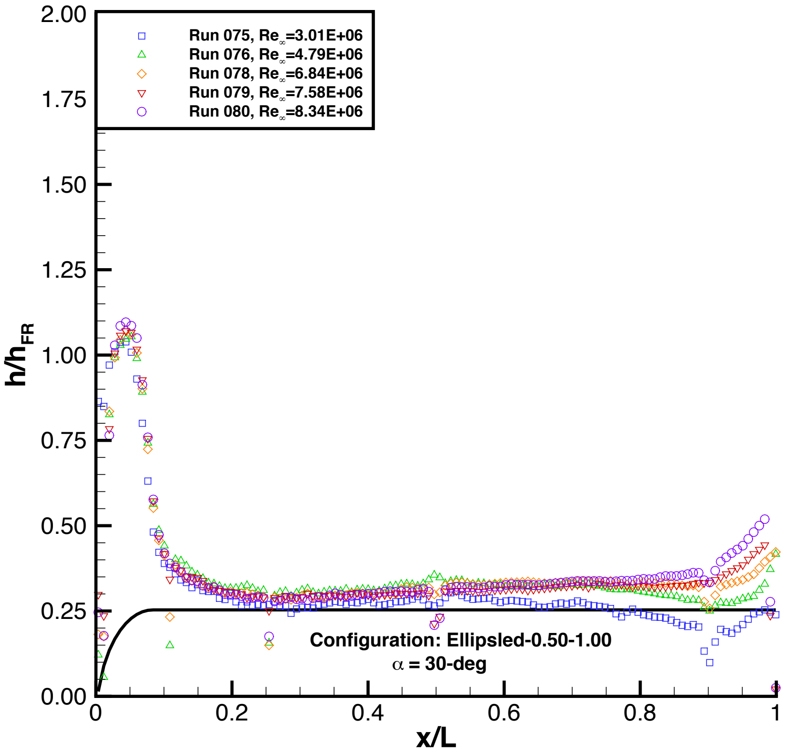

Figure 27. Centerline Heating, Ellipsled-0.50-1.00, α = 30-deg

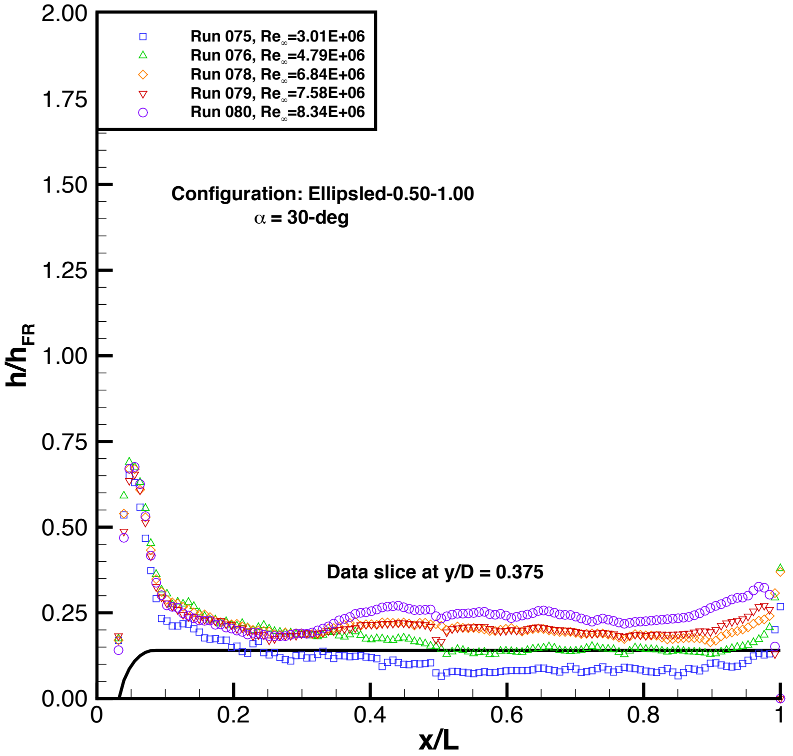

Figure 28. Off-Centerline Heating, Ellipsled-0.50-1.00, α = 30-deg

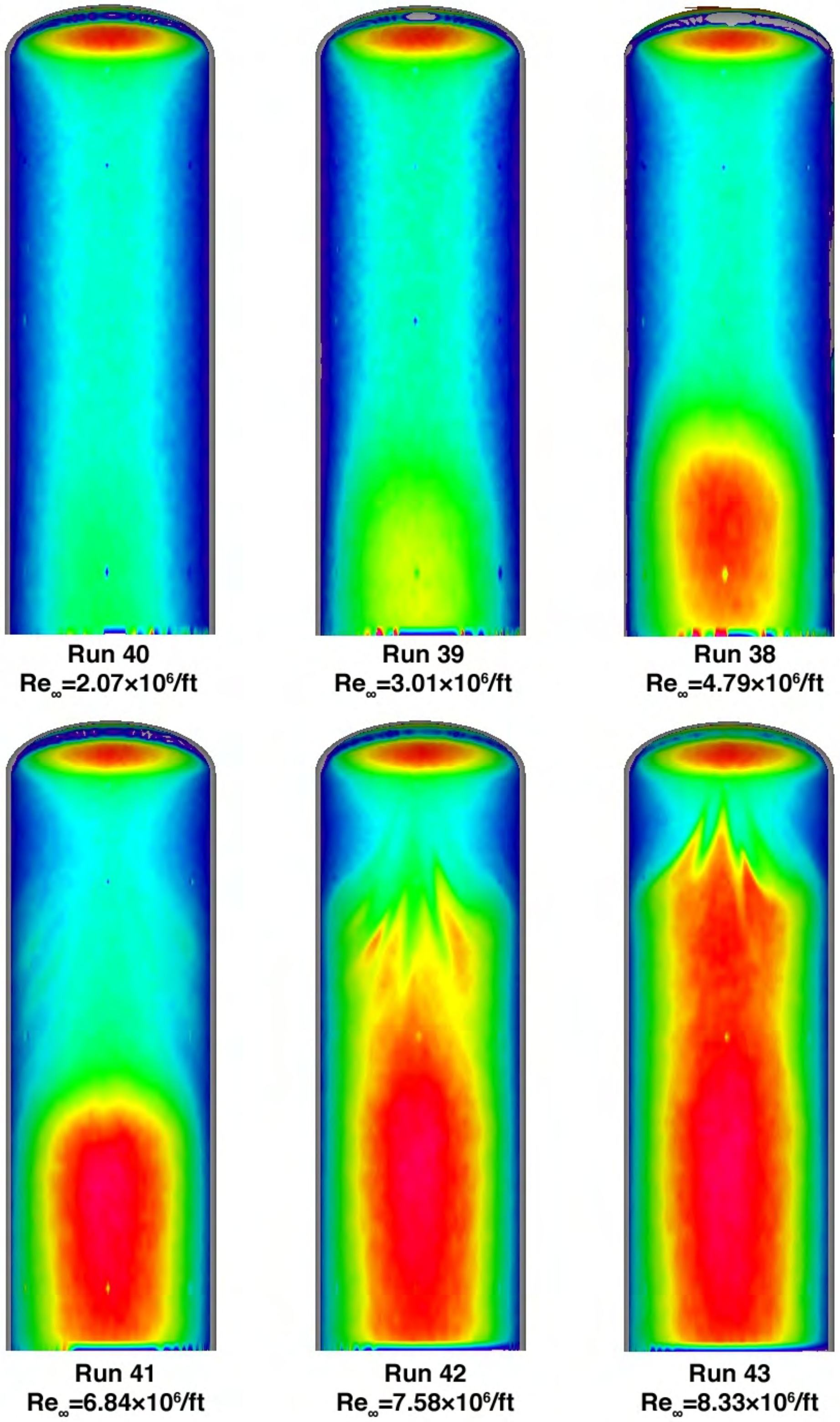

Run 40 Re_∞=2.07×10^6/ft

Run 39 Re_∞=3.01×10^6/ft

Run 38 Re_∞=4.79×10^6/ft

Run 41 Re_∞=6.84×10^6/ft

Run 42 Re_∞=7.58×10^6/ft

Run 43 Re_∞=8.33×10^6/ft

Figure 29. Reynolds Number Effects on Heating, Ellipsled-0.50-1.00, α = 40-deg

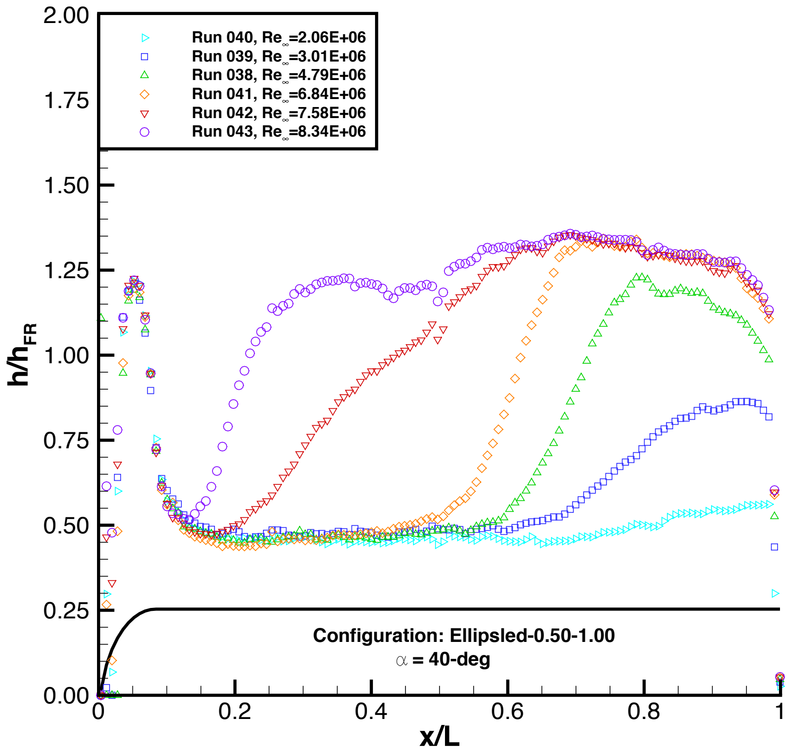

Figure 30. Centerline Heating, Ellipsled-0.50-1.00, α = 40-deg

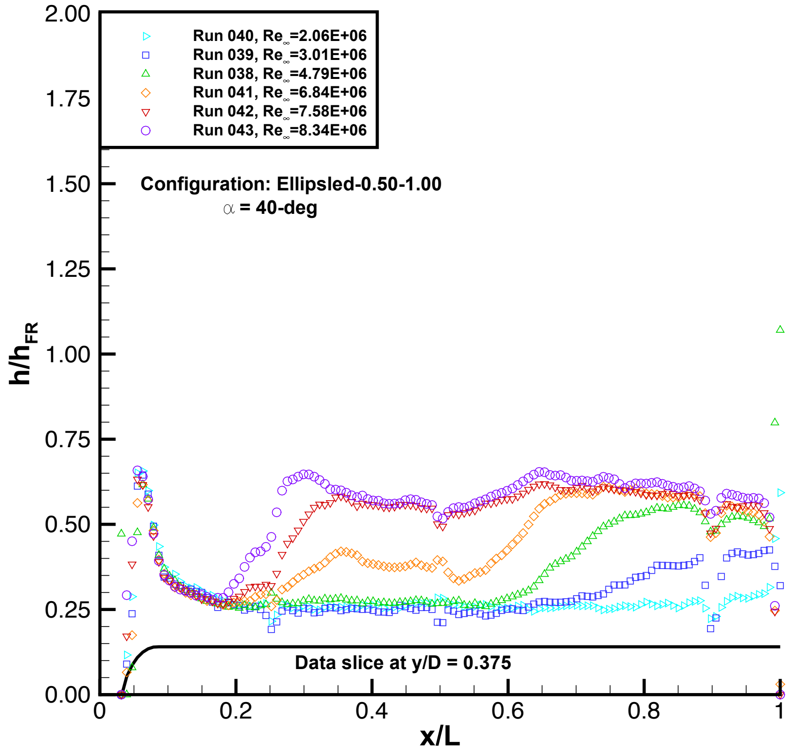

Figure 31. Off-Centerline Heating, Ellipsled-0.50-1.00, α = 40-deg

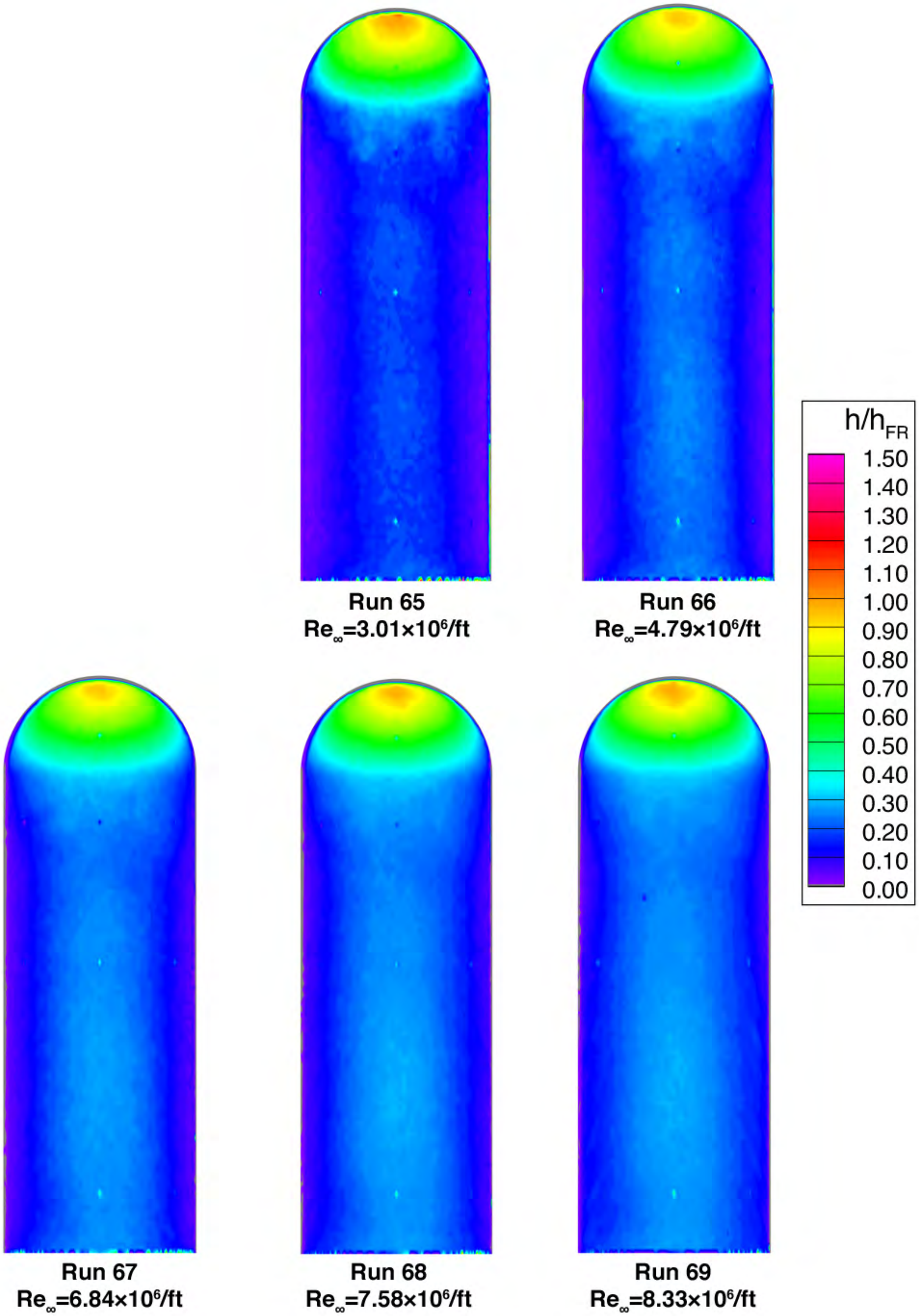

Run 65
$Re_\infty=3.01\times10^6$/ft

Run 66
$Re_\infty=4.79\times10^6$/ft

Run 67
$Re_\infty=6.84\times10^6$/ft

Run 68
$Re_\infty=7.58\times10^6$/ft

Run 69
$Re_\infty=8.33\times10^6$/ft

Figure 32. Reynolds Number Effects on Heating, Ellipsled-1.00-1.00, α = 30-deg

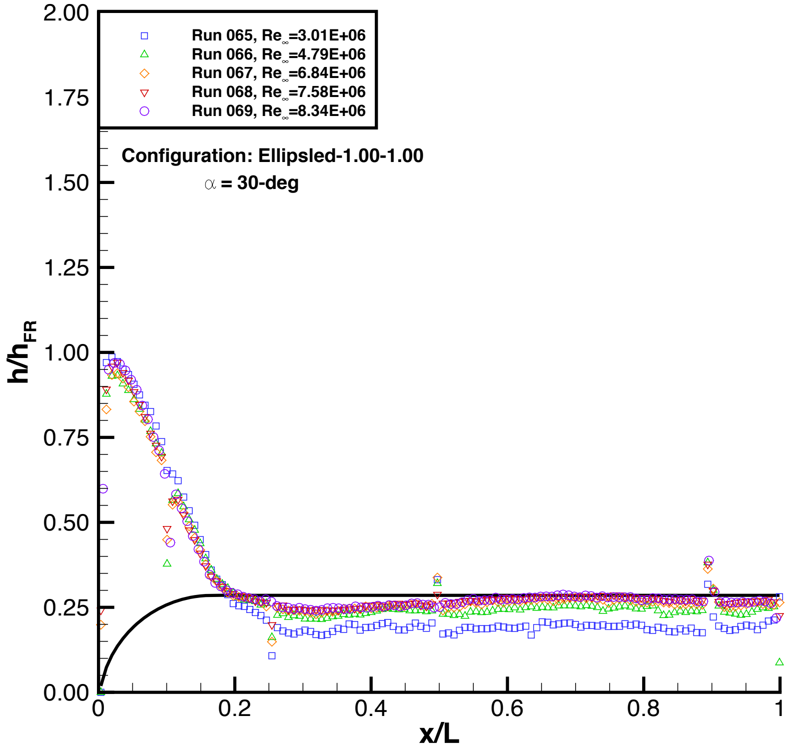

Figure 33. Centerline Heating, Ellipsled-1.00-1.00, α = 30-deg

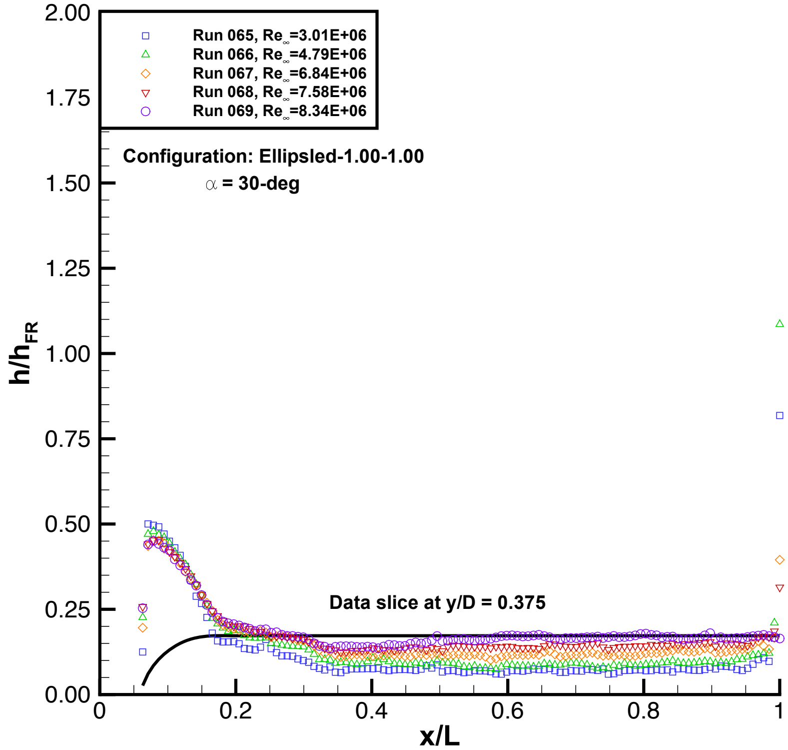

Figure 34. Off-Centerline Heating, Ellipsled-1.00-1.00, α = 30-deg

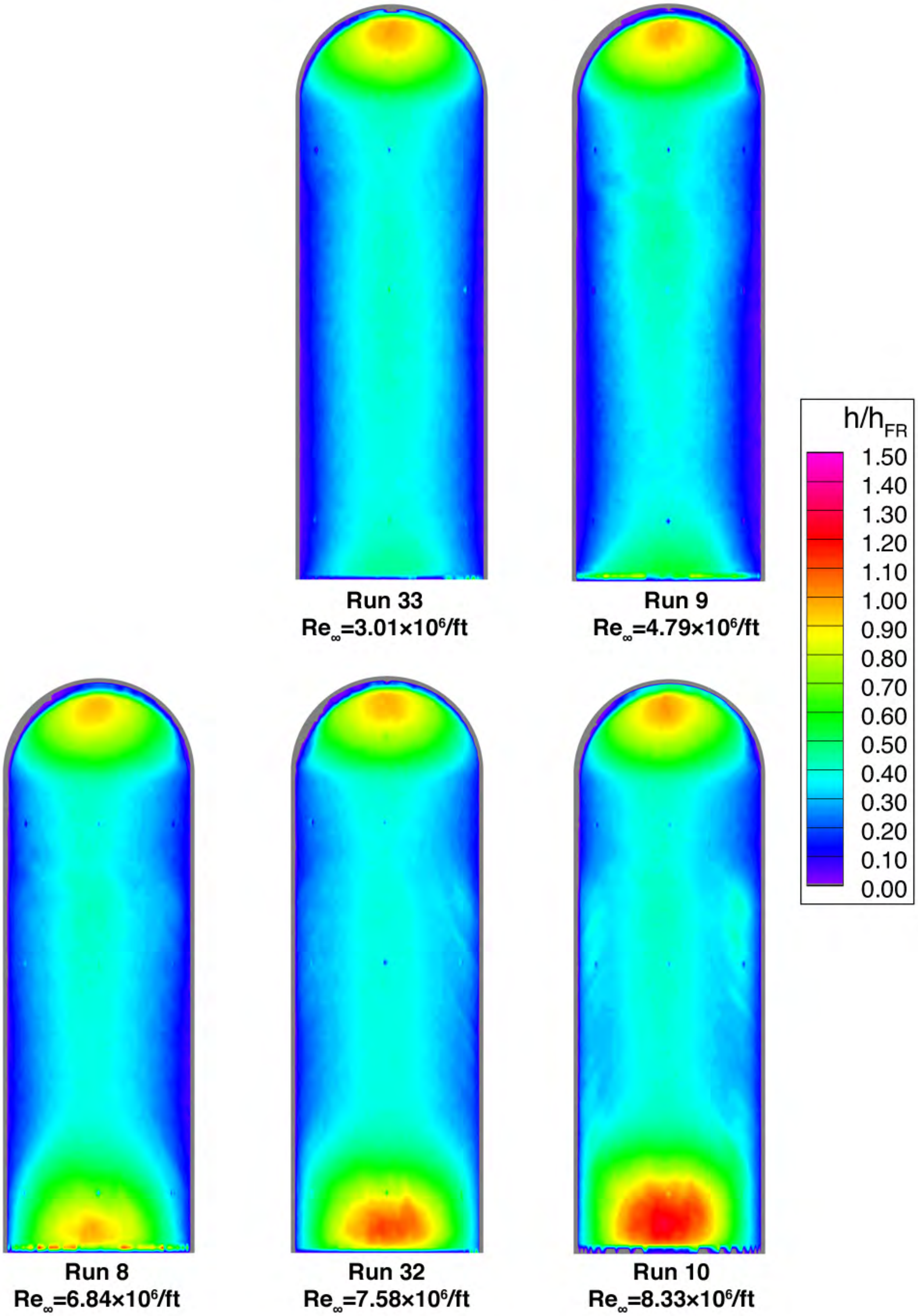

Run 33
$Re_\infty=3.01\times10^6$/ft

Run 9
$Re_\infty=4.79\times10^6$/ft

Run 8
$Re_\infty=6.84\times10^6$/ft

Run 32
$Re_\infty=7.58\times10^6$/ft

Run 10
$Re_\infty=8.33\times10^6$/ft

Figure 35. Reynolds Number Effects on Heating, Ellipsled-1.00-1.00, α = 40-deg

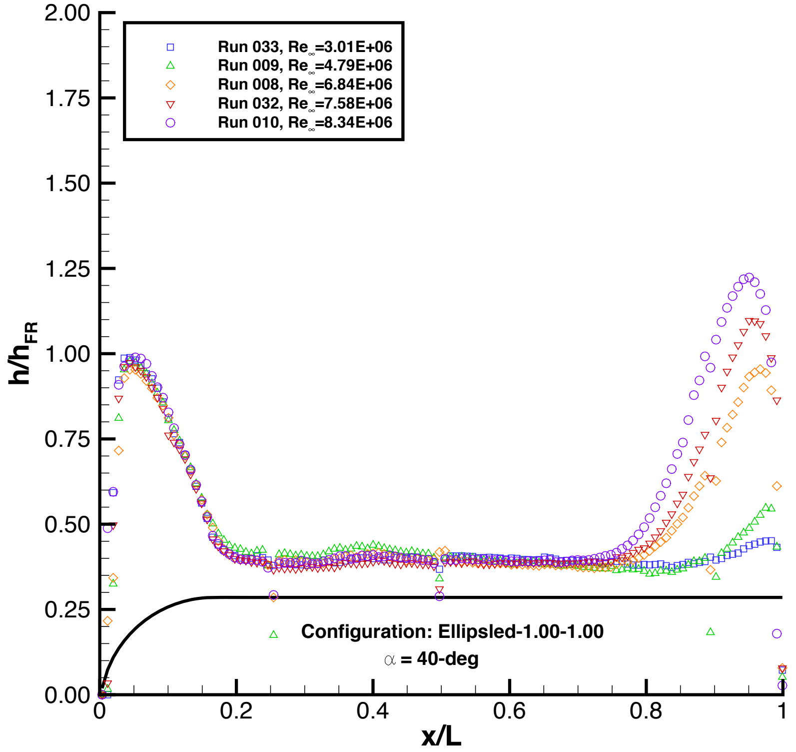

Figure 36. Centerline Heating, Ellipsled-1.00-1.00, α = 40-deg

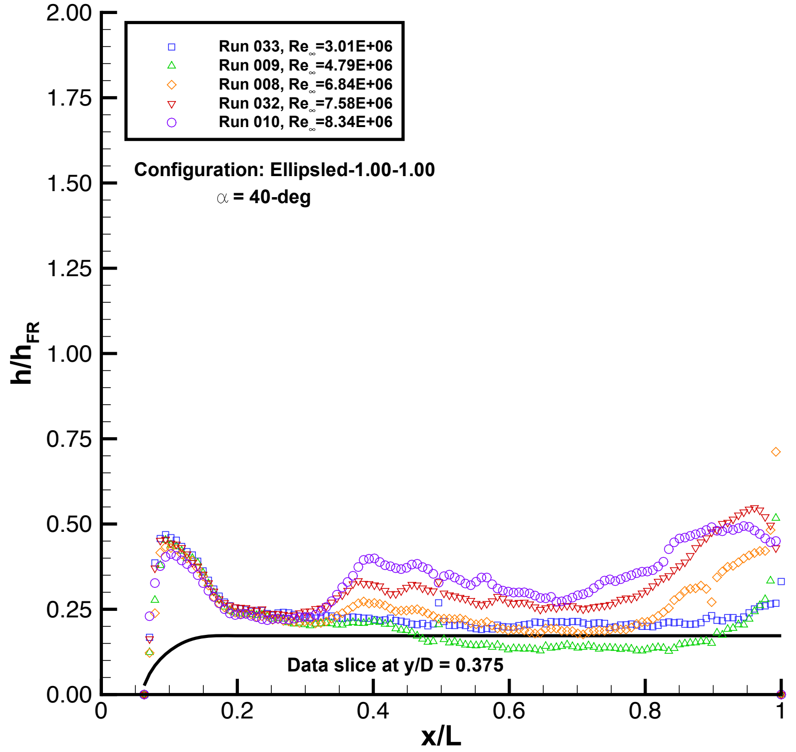

Figure 37. Off-Centerline Heating, Ellipsled-1.00-1.00, α = 40-deg

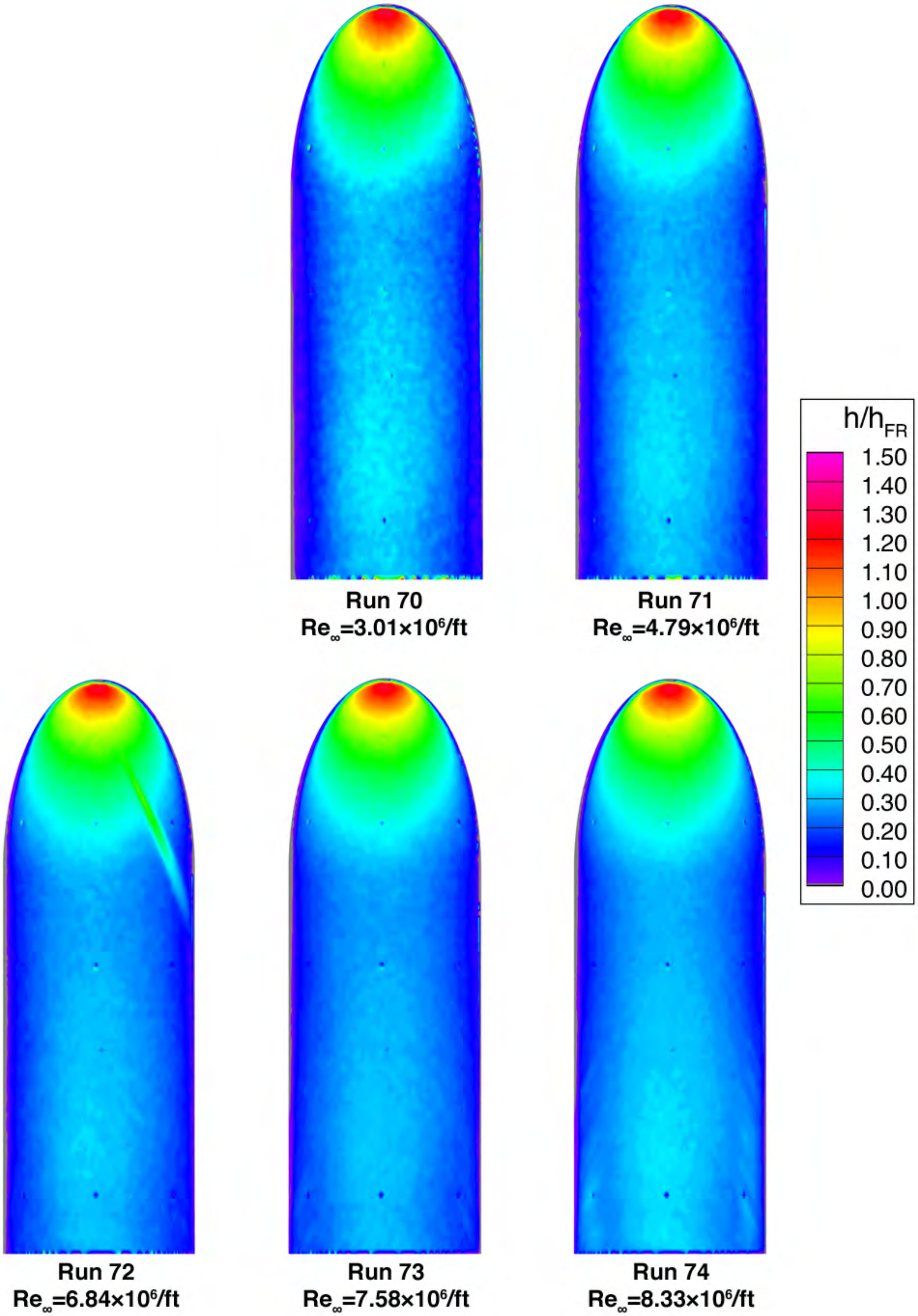

Run 70
Re_∞=3.01×10^6/ft

Run 71
Re_∞=4.79×10^6/ft

Run 72
Re_∞=6.84×10^6/ft

Run 73
Re_∞=7.58×10^6/ft

Run 74
Re_∞=8.33×10^6/ft

Figure 38. Reynolds Number Effects on Heating, Ellipsled-2.00-1.00, α = 30-deg

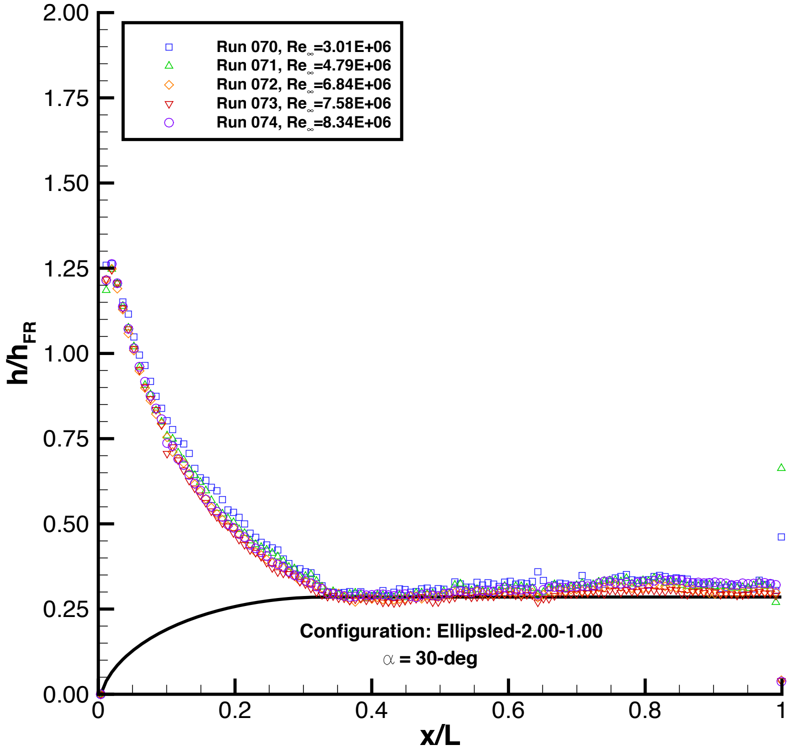

Figure 39. Centerline Heating, Ellipsled-2.00-1.00, α = 30-deg

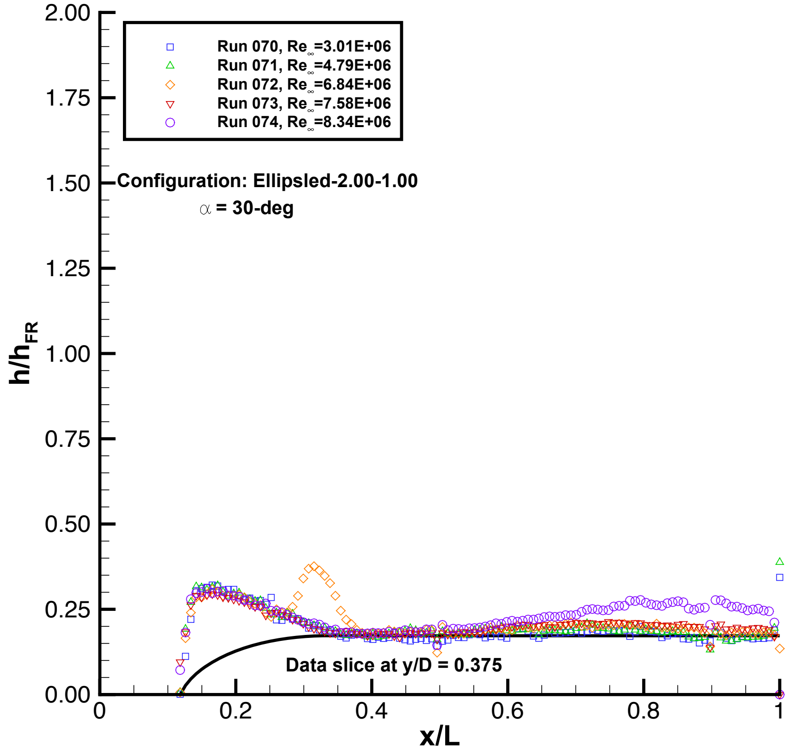

Figure 40. Off-Centerline Heating, Ellipsled-2.00-1.00, α = 30-deg

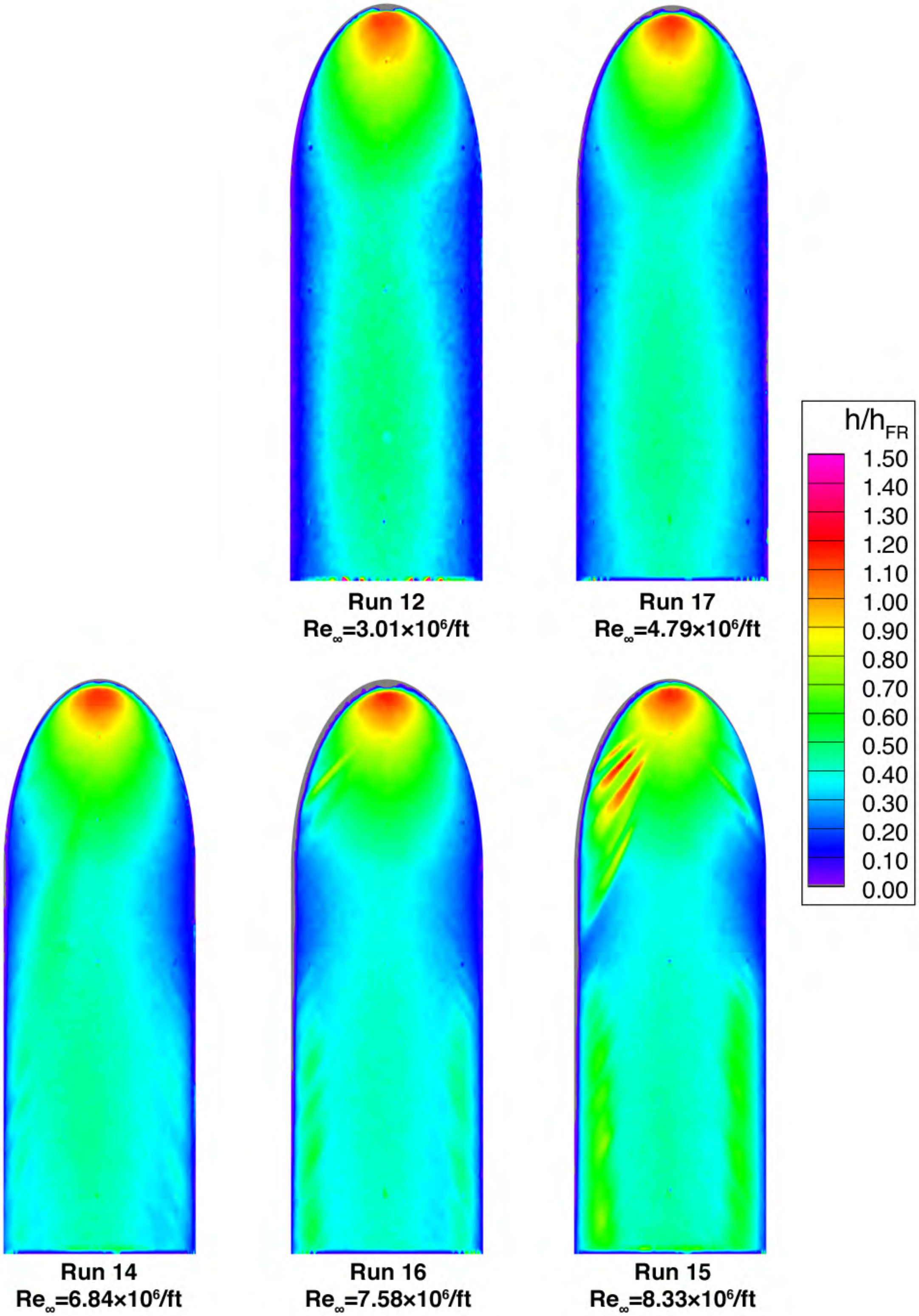

Run 12
$Re_\infty=3.01\times10^6$/ft

Run 17
$Re_\infty=4.79\times10^6$/ft

Run 14
$Re_\infty=6.84\times10^6$/ft

Run 16
$Re_\infty=7.58\times10^6$/ft

Run 15
$Re_\infty=8.33\times10^6$/ft

Figure 41. Reynolds Number Effects on Heating, Ellipsled-2.00-1.00, α = 40-deg

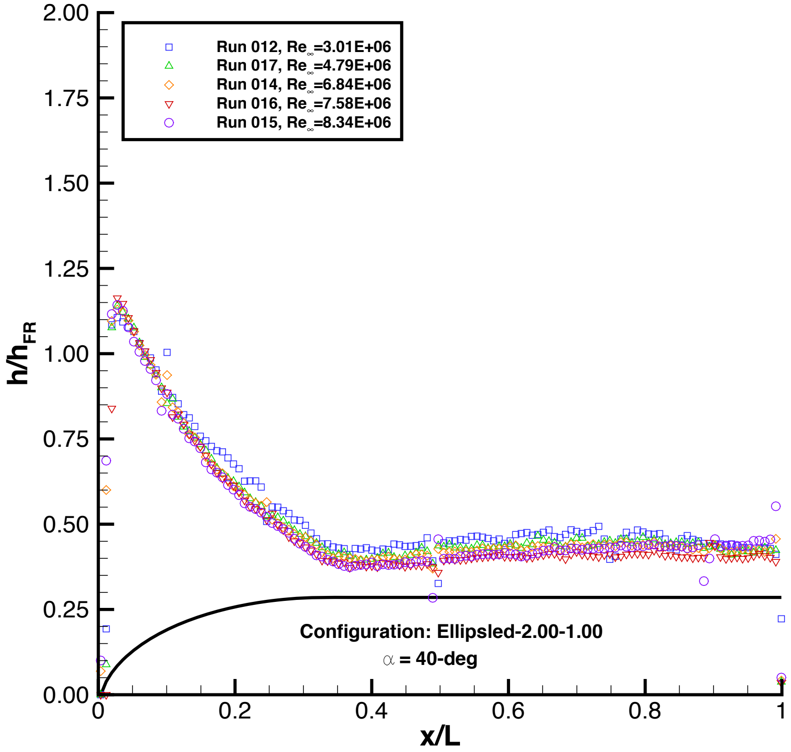

Figure 42. Centerline Heating, Ellipsled-2.00-1.00, α = 40-deg

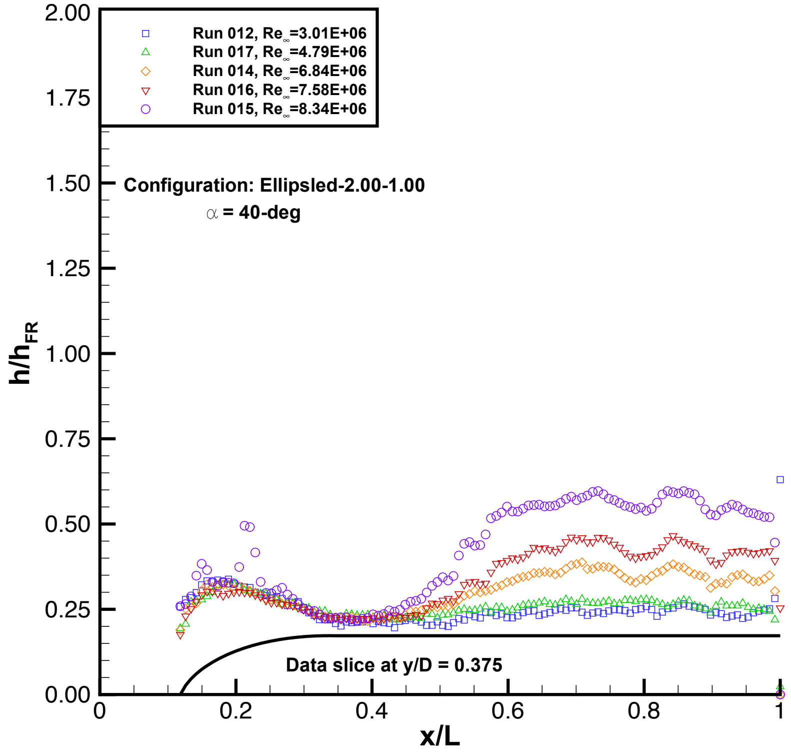

Figure 43. Off-Centerline Heating, Ellipsled-2.00-1.00, α = 40-deg

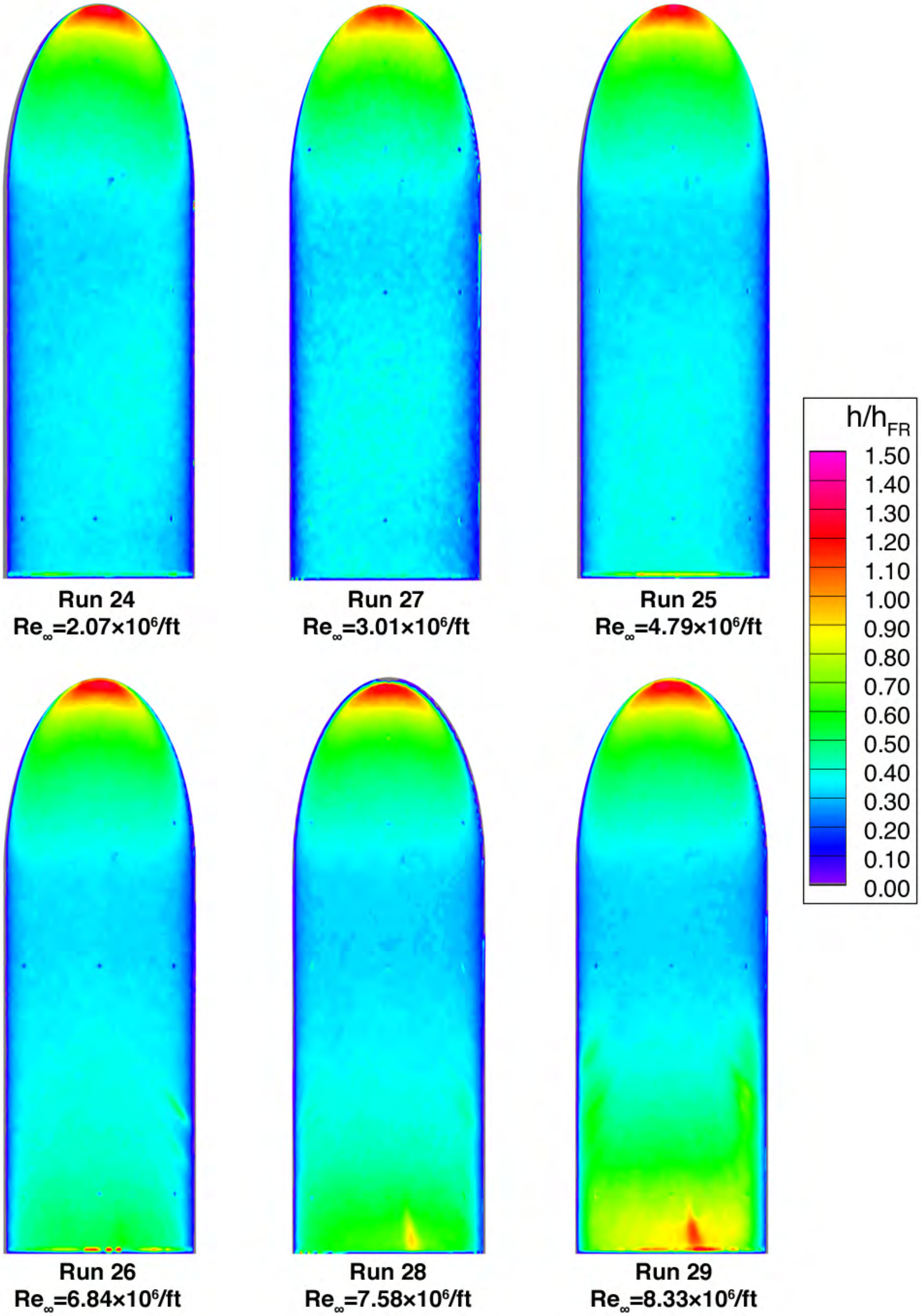
Run 24 $Re_\infty=2.07\times10^6$/ft

Run 27 $Re_\infty=3.01\times10^6$/ft

Run 25 $Re_\infty=4.79\times10^6$/ft

Run 26 $Re_\infty=6.84\times10^6$/ft

Run 28 $Re_\infty=7.58\times10^6$/ft

Run 29 $Re_\infty=8.33\times10^6$/ft

Figure 44. Reynolds Number Effects on Heating, Ellipsled-2.00-0.50, α = 40-deg

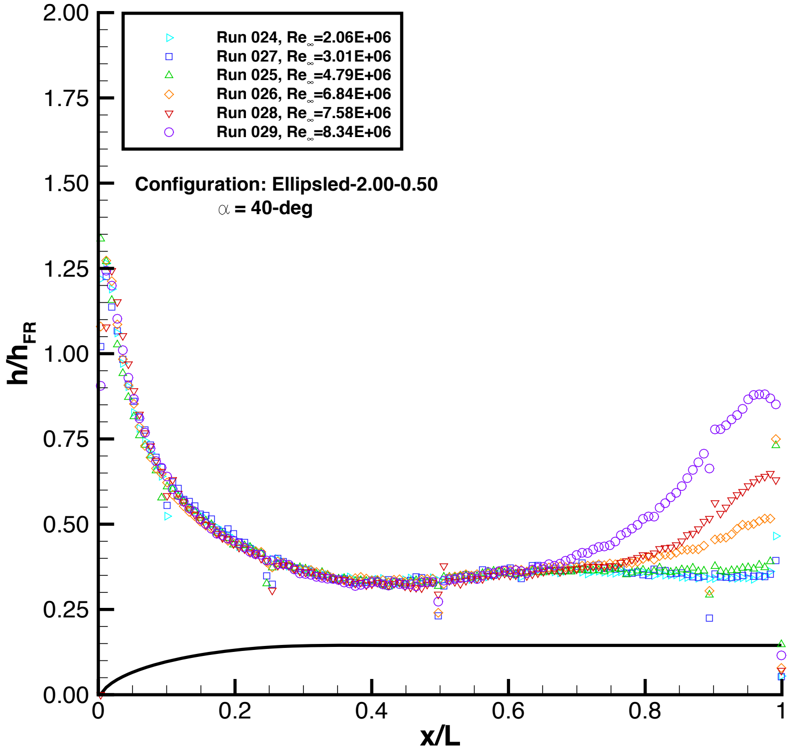

Figure 45. Centerline Heating, Ellipsled-2.00-0.50, α = 40-deg

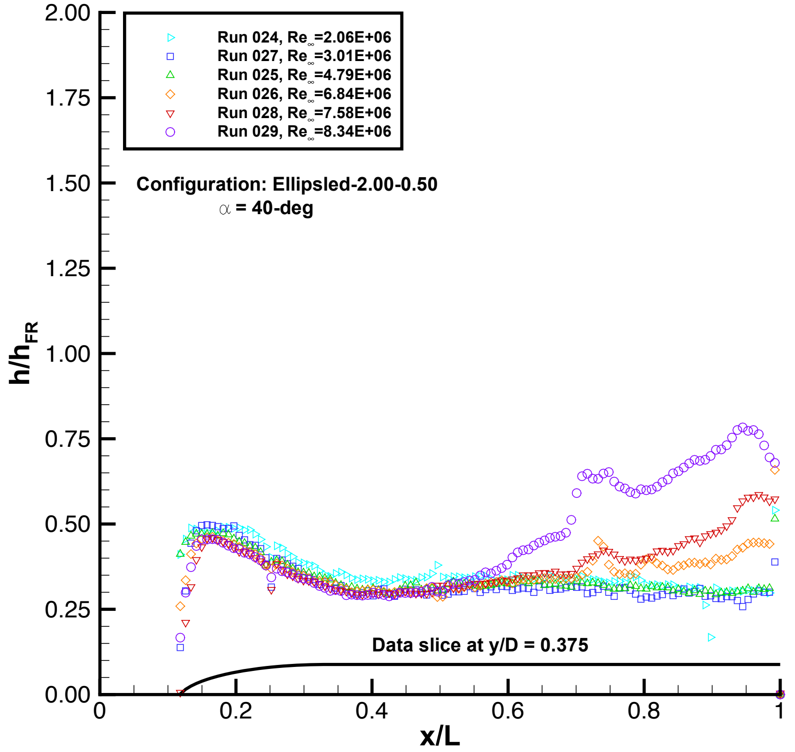

Figure 46. Off-Centerline Heating, Ellipsled-2.00-0.50, α = 40-deg

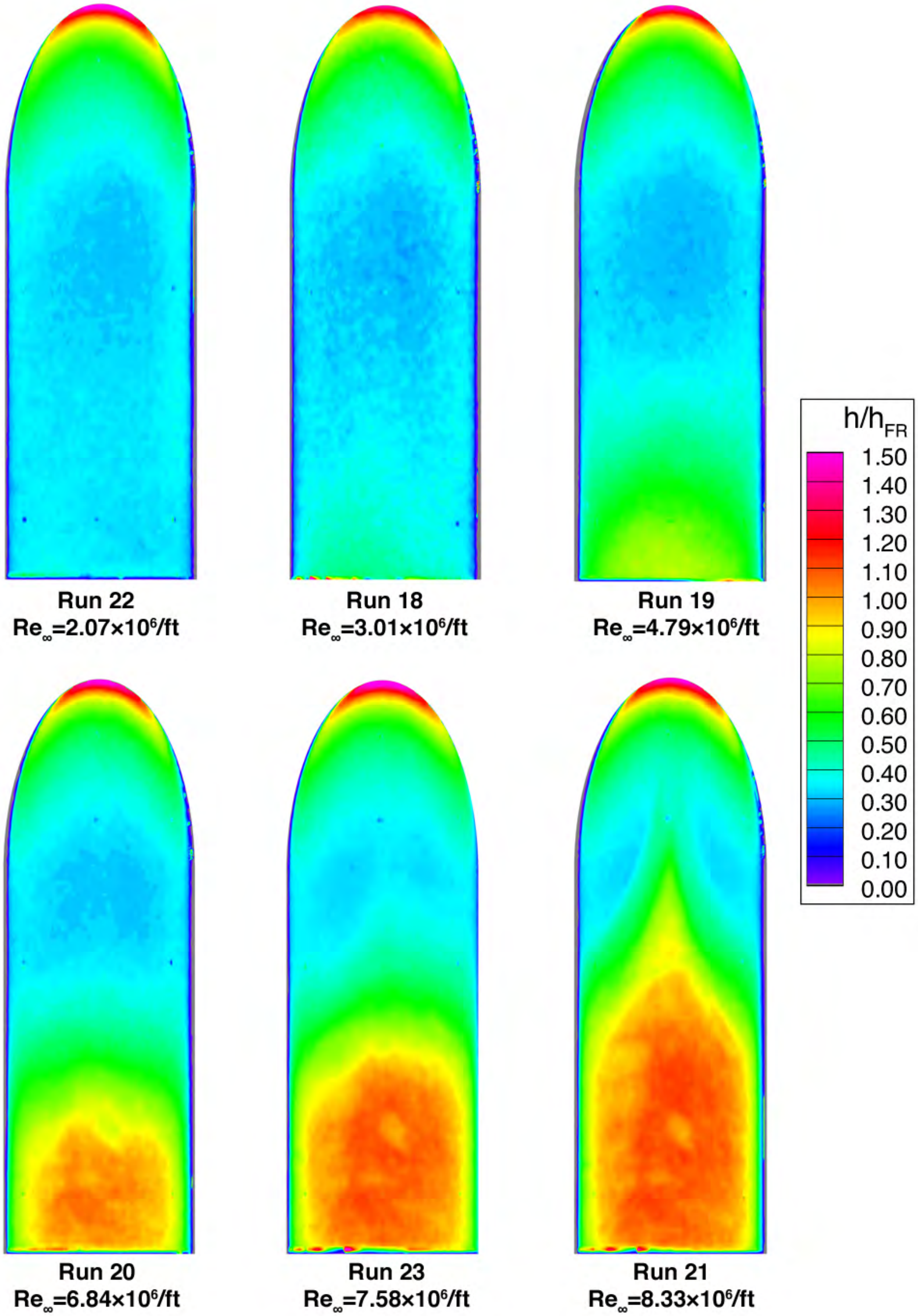
Run 22 $Re_\infty=2.07\times10^6$/ft

Run 18 $Re_\infty=3.01\times10^6$/ft

Run 19 $Re_\infty=4.79\times10^6$/ft

Run 20 $Re_\infty=6.84\times10^6$/ft

Run 23 $Re_\infty=7.58\times10^6$/ft

Run 21 $Re_\infty=8.33\times10^6$/ft

Figure 47. Reynolds Number Effects on Heating, Ellipsled-2.00-0.25, α = 40-deg

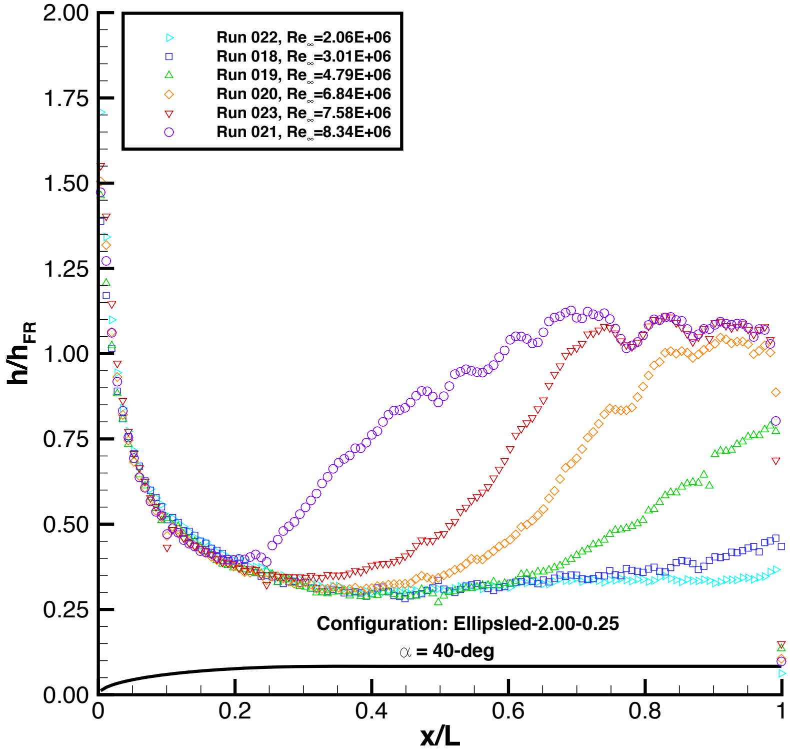

Figure 48. Centerline Heating, Ellipsled-2.00-0.25, α = 40-deg

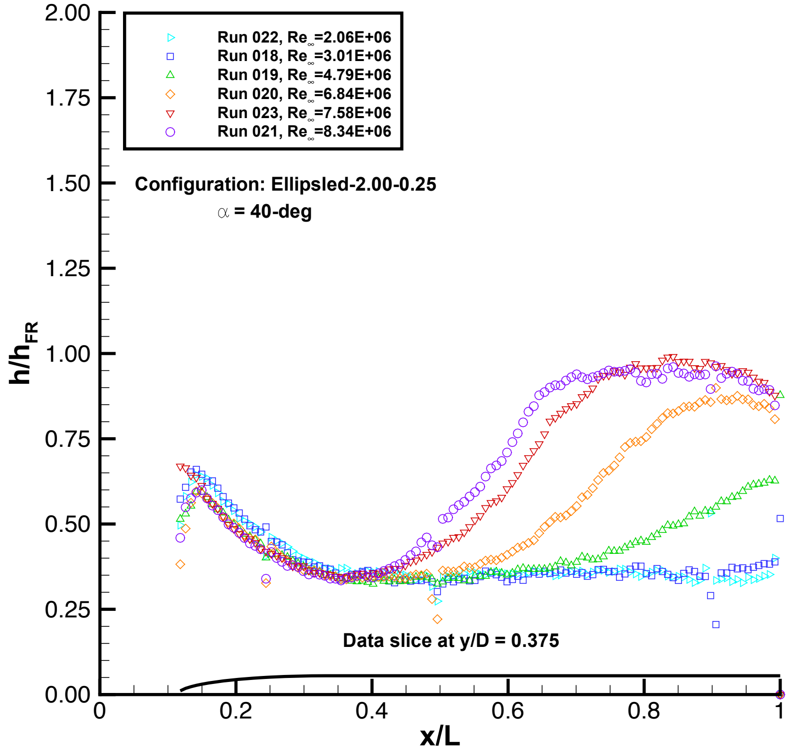

Figure 49. Off-Centerline Heating, Ellipsled-2.00-0.25, α = 40-deg

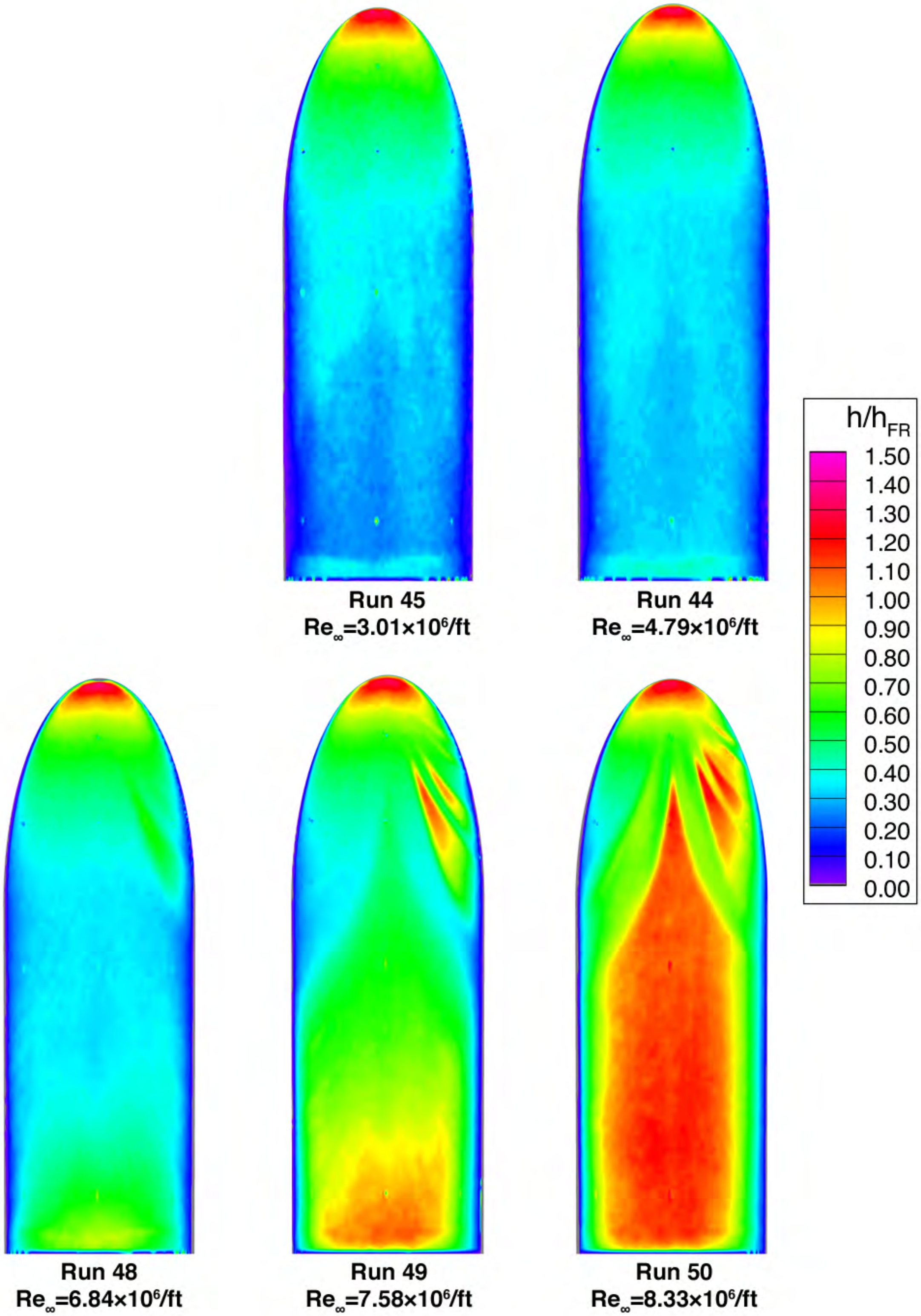
Run 45 Re$_\infty$=3.01×10^6/ft

Run 44 Re$_\infty$=4.79×10^6/ft

Run 48 Re$_\infty$=6.84×10^6/ft

Run 49 Re$_\infty$=7.58×10^6/ft

Run 50 Re$_\infty$=8.33×10^6/ft

Figure 50. Reynolds Number Effects on Heating, COBRA-14297B (Model C-1), α = 40-deg

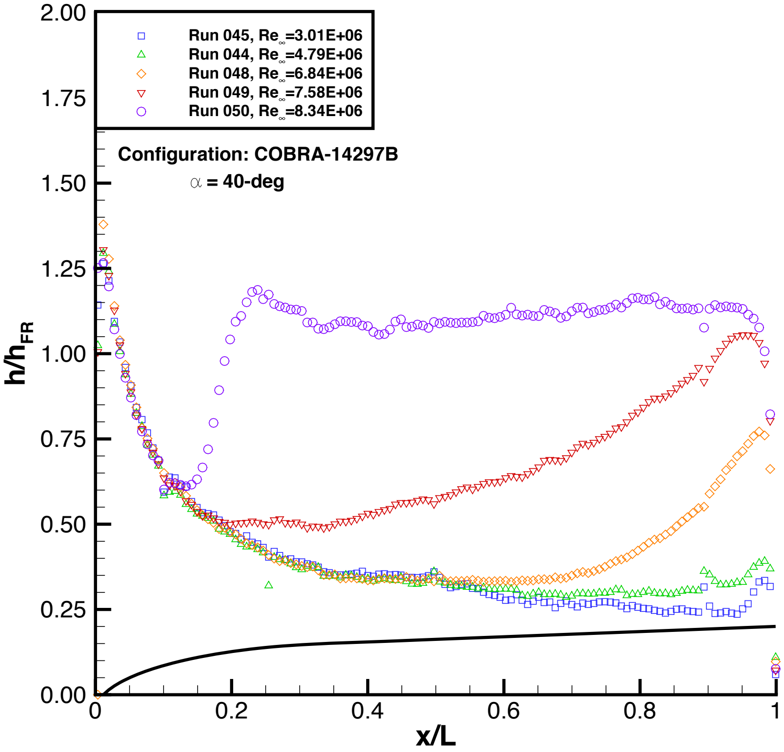

Figure 51. Centerline Heating, COBRA-14297B (Model C-1), α = 40-deg

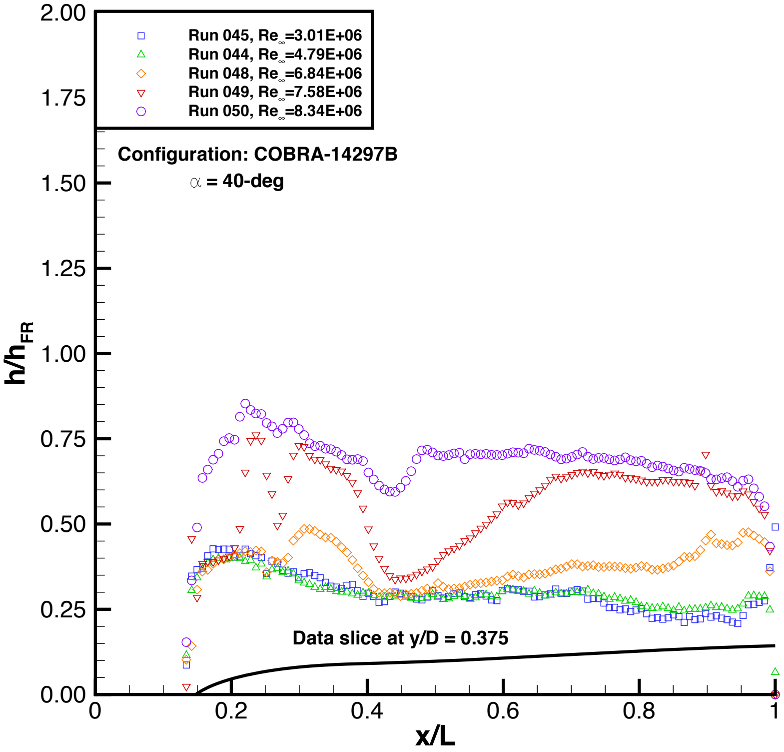

Figure 52. Off-Centerline Heating, COBRA-14297B (Model C-1), α = 40-deg

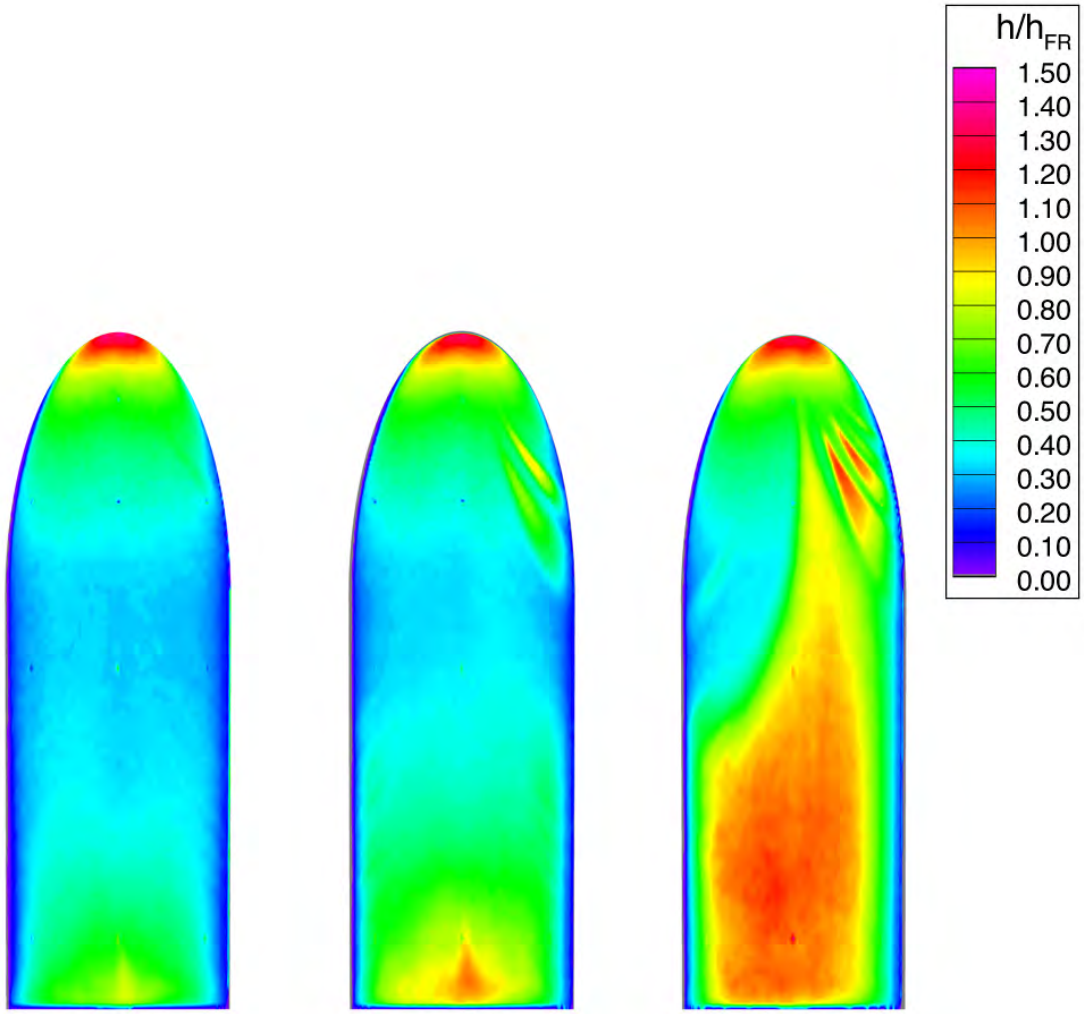

Run 110
Re_∞=6.84×10^6/ft

Run 111
Re_∞=7.58×10^6/ft

Run 112
Re_∞=8.33×10^6/ft

Figure 53. Reynolds Number Effects on Heating, COBRA-14297B (Model C-3), α = 40-deg

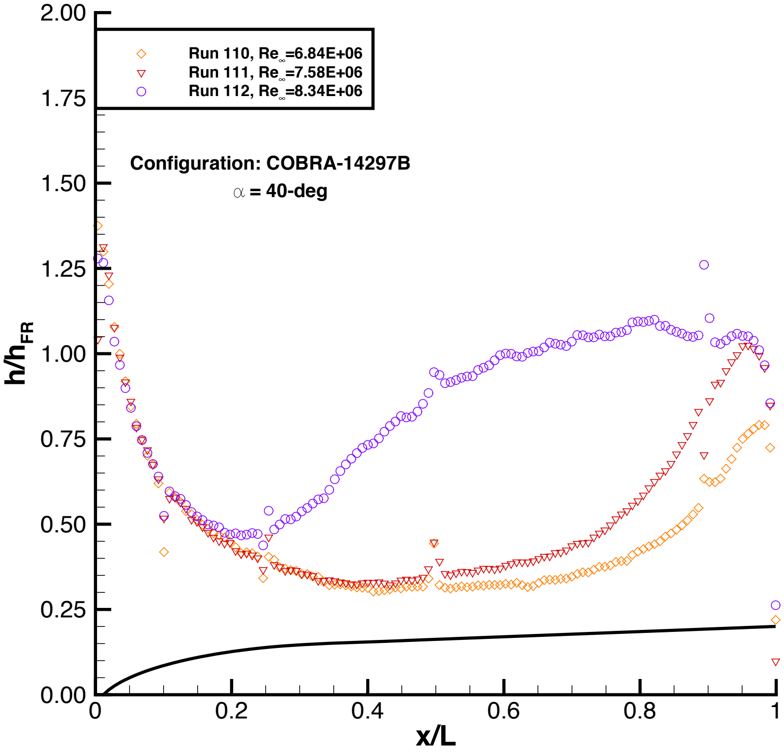

Figure 54. Centerline Heating, COBRA-14297B (Model C-3), α = 40-deg

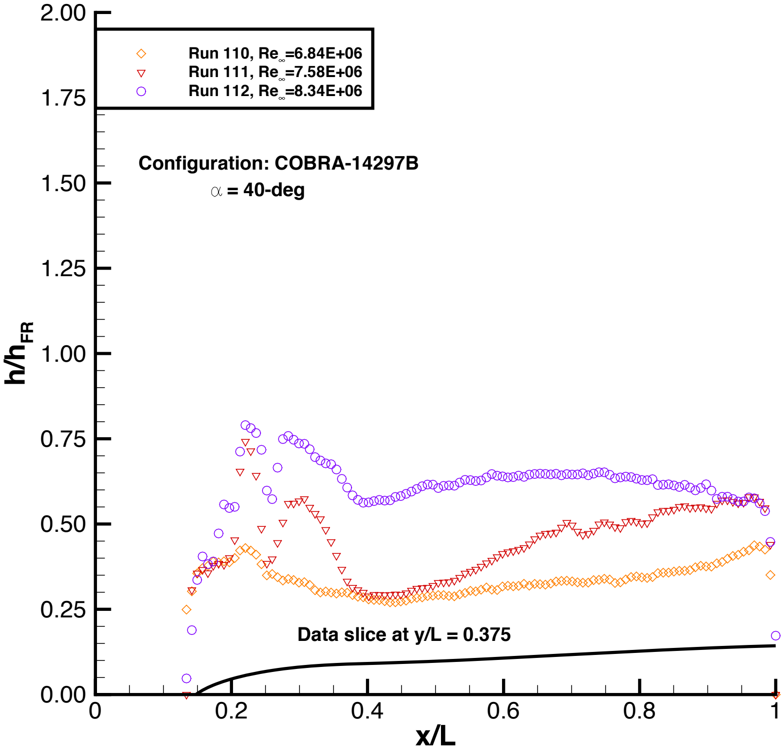

Figure 55. Off-Centerline Heating, COBRA-14297B (Model C-3), α = 40-deg

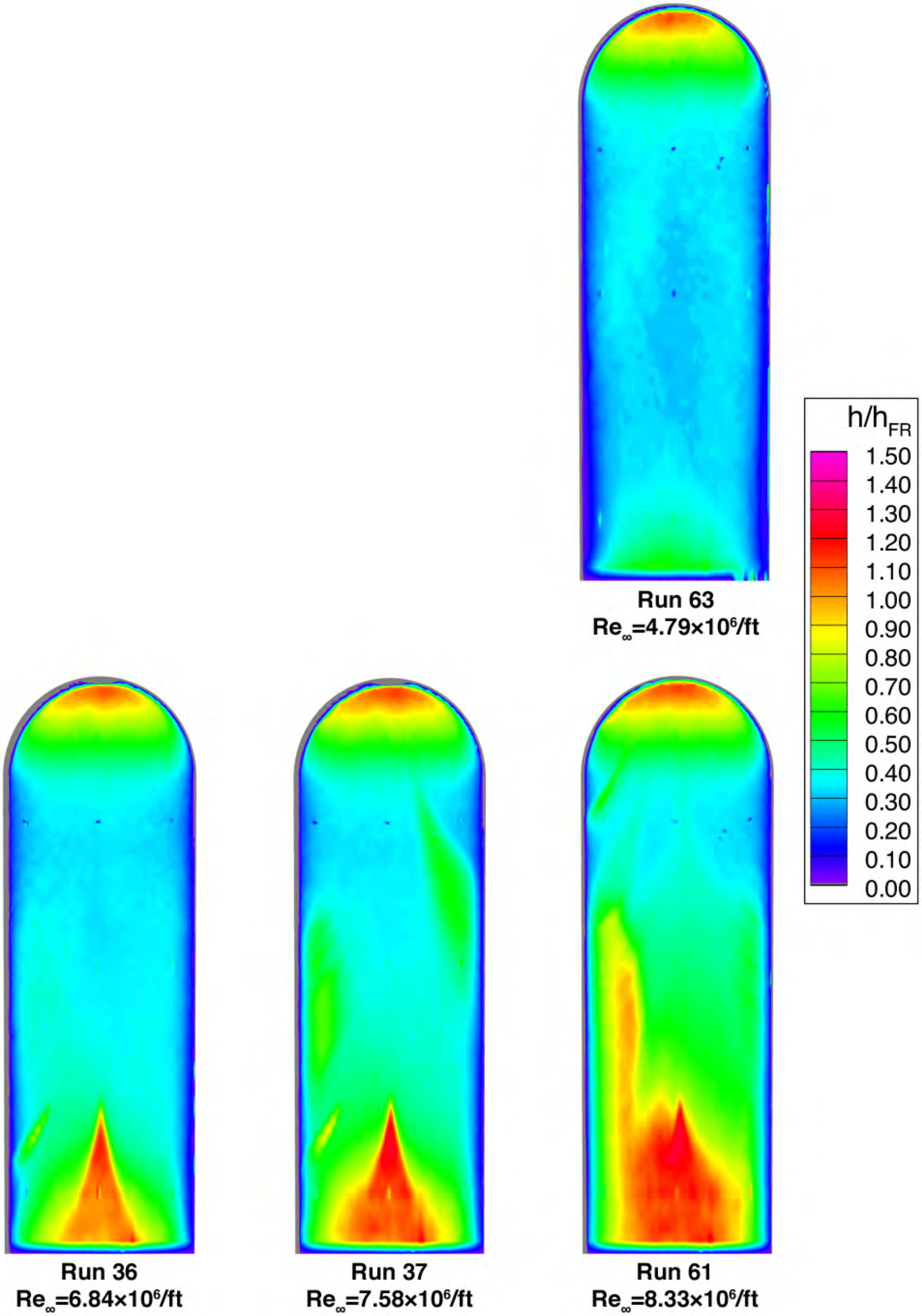

Run 63
Re$_\infty$=4.79×10^6/ft

Run 36
Re$_\infty$=6.84×10^6/ft

Run 37
Re$_\infty$=7.58×10^6/ft

Run 61
Re$_\infty$=8.33×10^6/ft

Figure 56. Reynolds Number Effects on Heating, COBRA-14888B (Model D-2), α = 40-deg

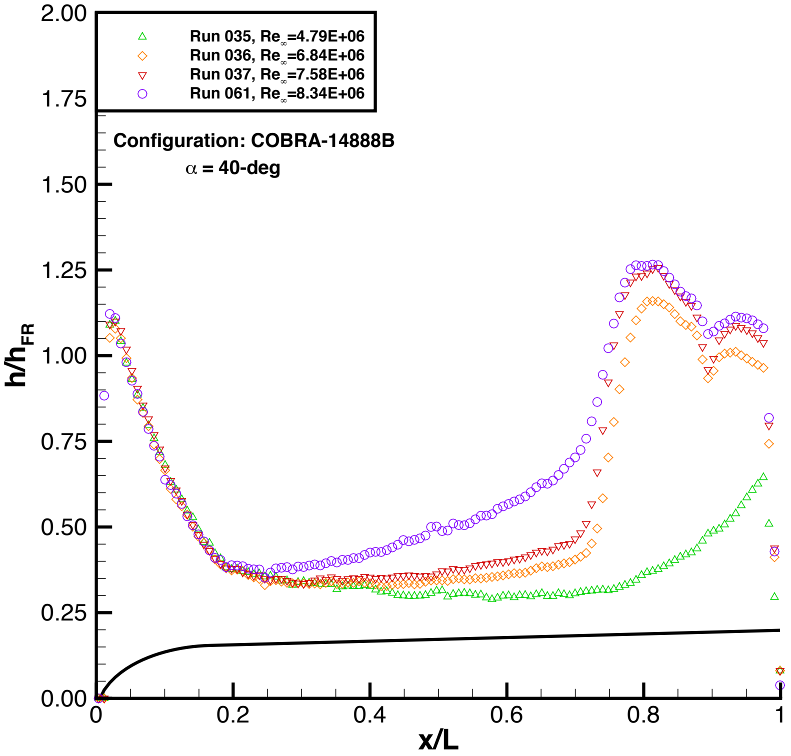

Figure 57. Centerline Heating, COBRA-14888B (Model D-2), α = 40-deg

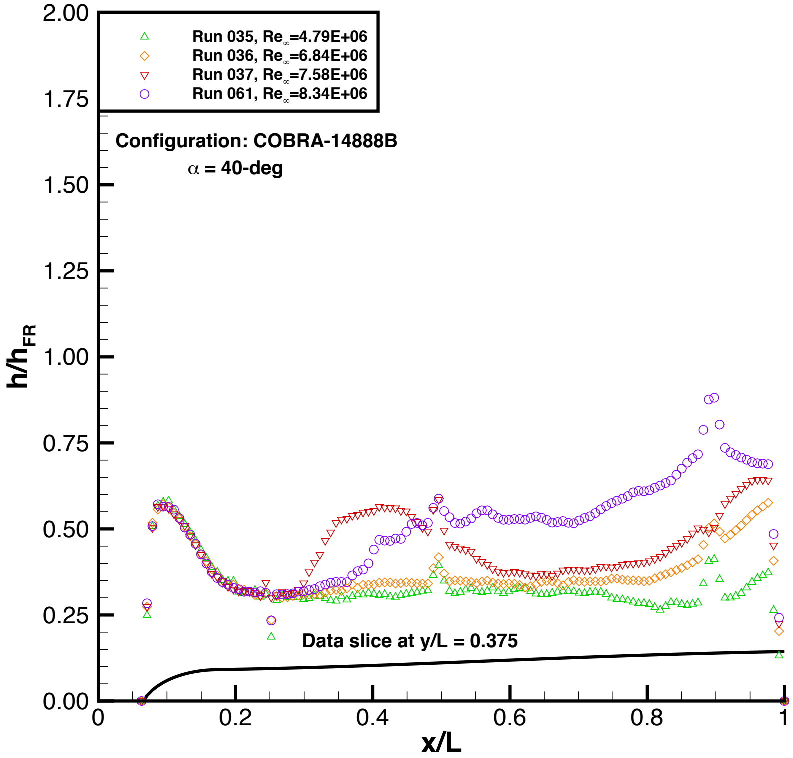

Figure 58. Off-Centerline Heating, COBRA-14888B (Model D-2), α = 40-deg

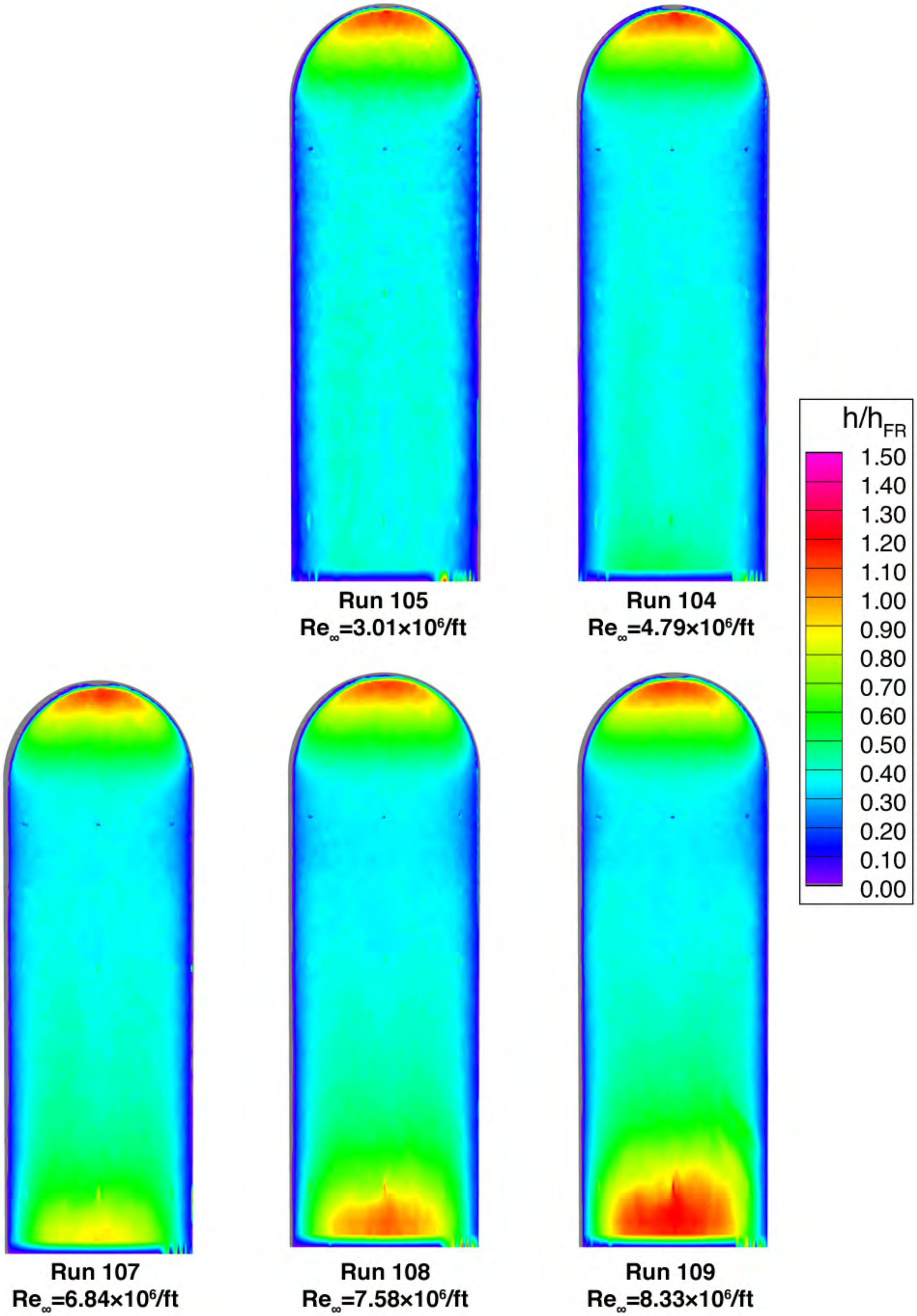

Run 105 $Re_\infty = 3.01 \times 10^6$/ft

Run 104 $Re_\infty = 4.79 \times 10^6$/ft

Run 107 $Re_\infty = 6.84 \times 10^6$/ft

Run 108 $Re_\infty = 7.58 \times 10^6$/ft

Run 109 $Re_\infty = 8.33 \times 10^6$/ft

Figure 59. Reynolds Number Effects on Heating, COBRA-14888B (Model D-3), α = 40-deg

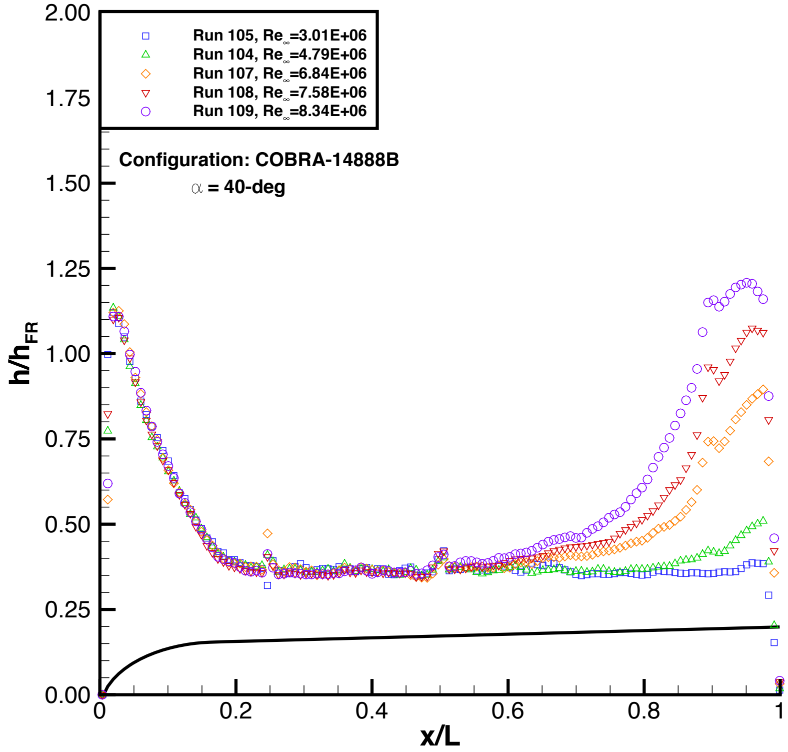

Figure 60. Centerline Heating, COBRA-14888B (Model D-3), α = 40-deg

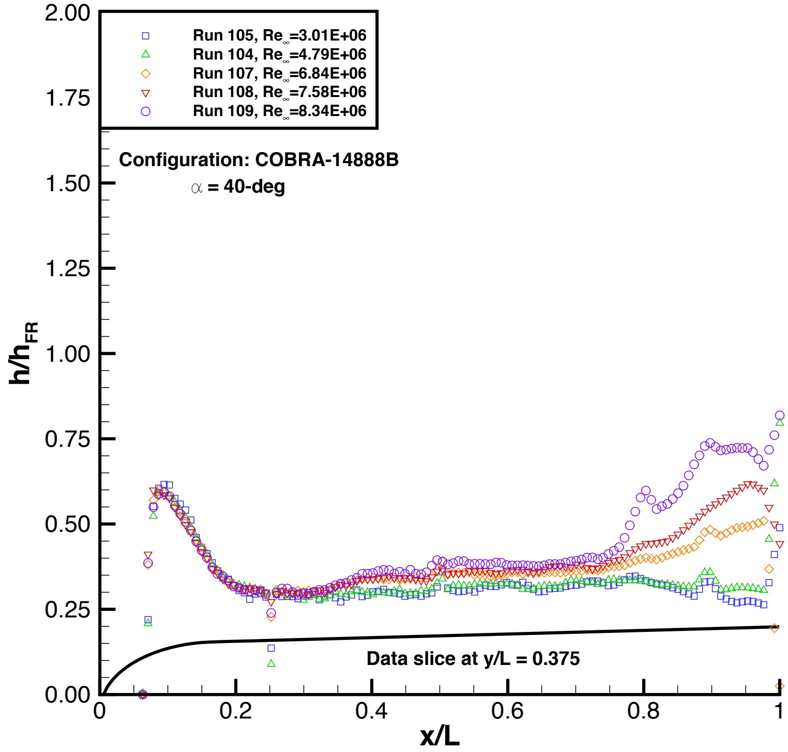

Figure 61. Off-Centerline Heating, COBRA-14888B (Model D-3), α = 40-deg

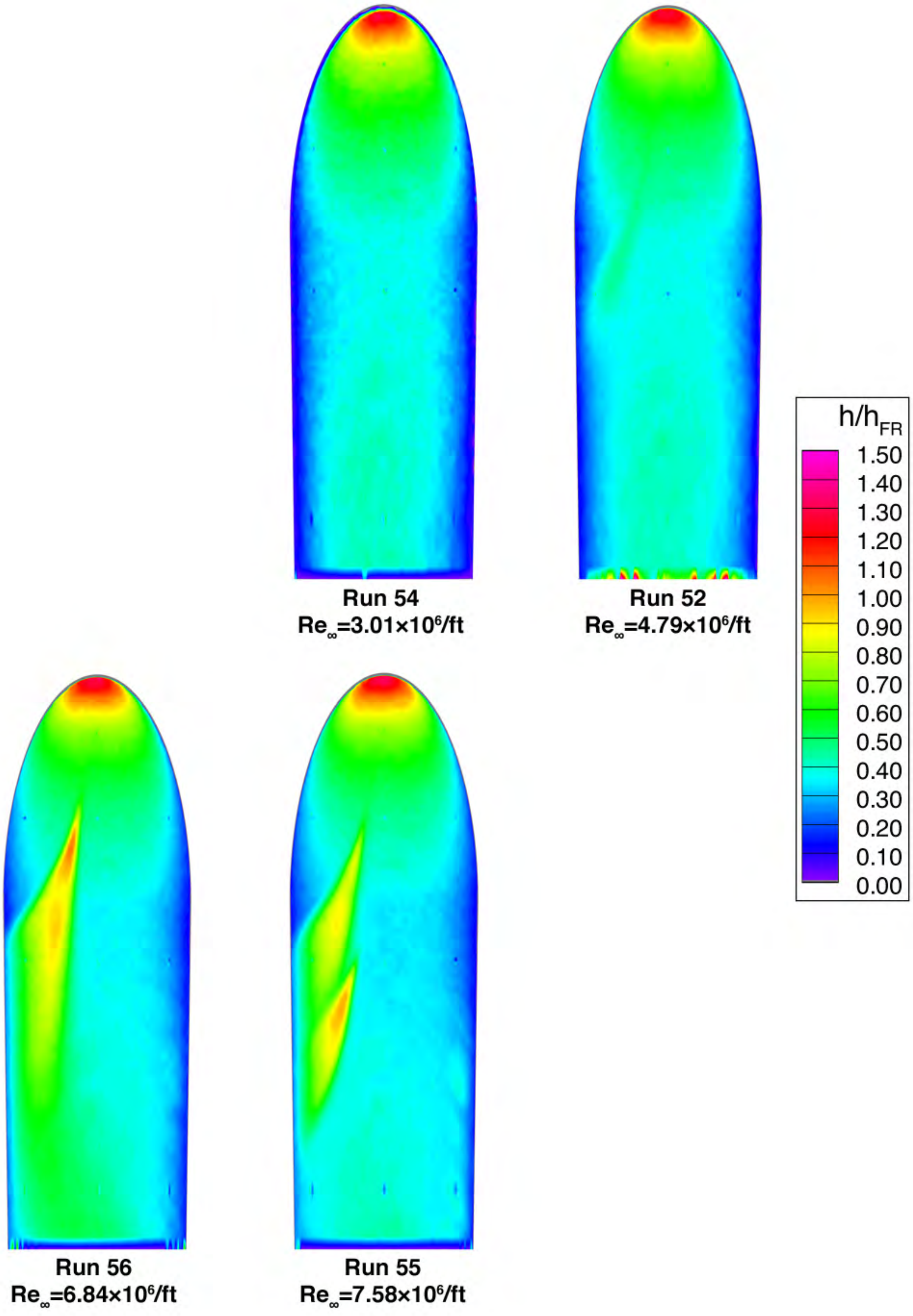

Figure 62. Reynolds Number Effects on Heating, COBRA-8459B (Model E-1), α = 40-deg

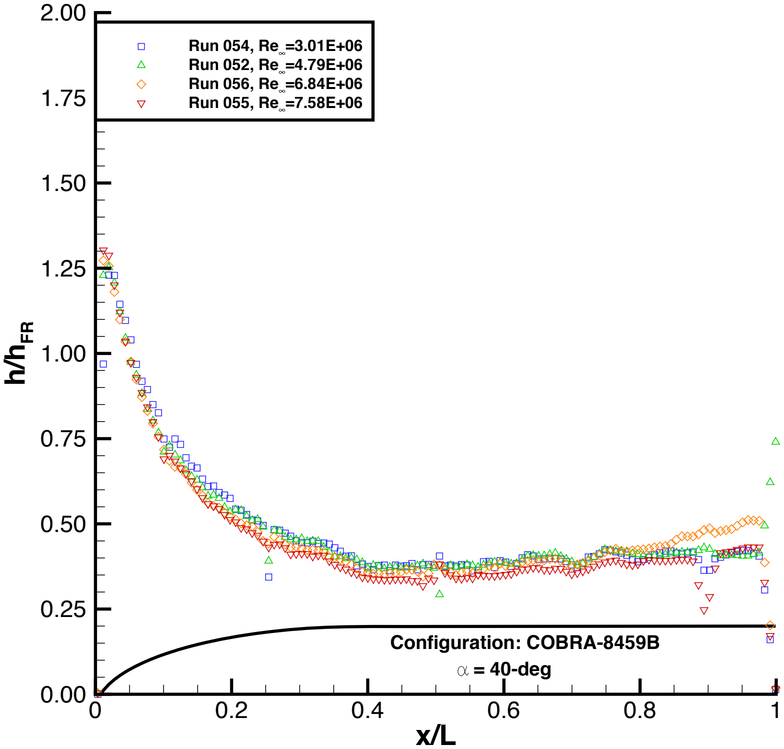

Figure 63. Centerline Heating, COBRA-8459B (Model E-1), α = 40-deg

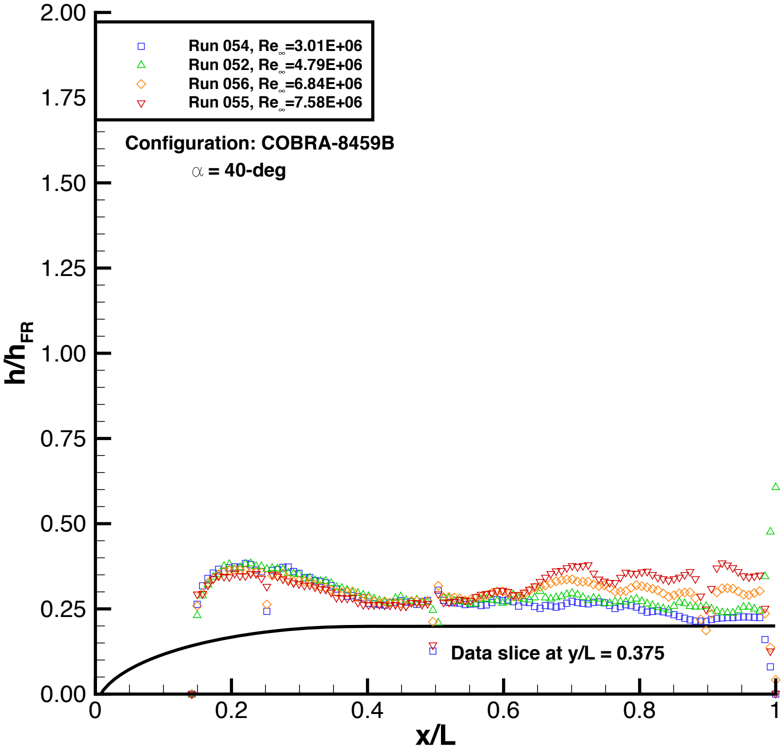

Figure 64. Off-Centerline Heating, COBRA-8459B (Model E-1), α = 40-deg

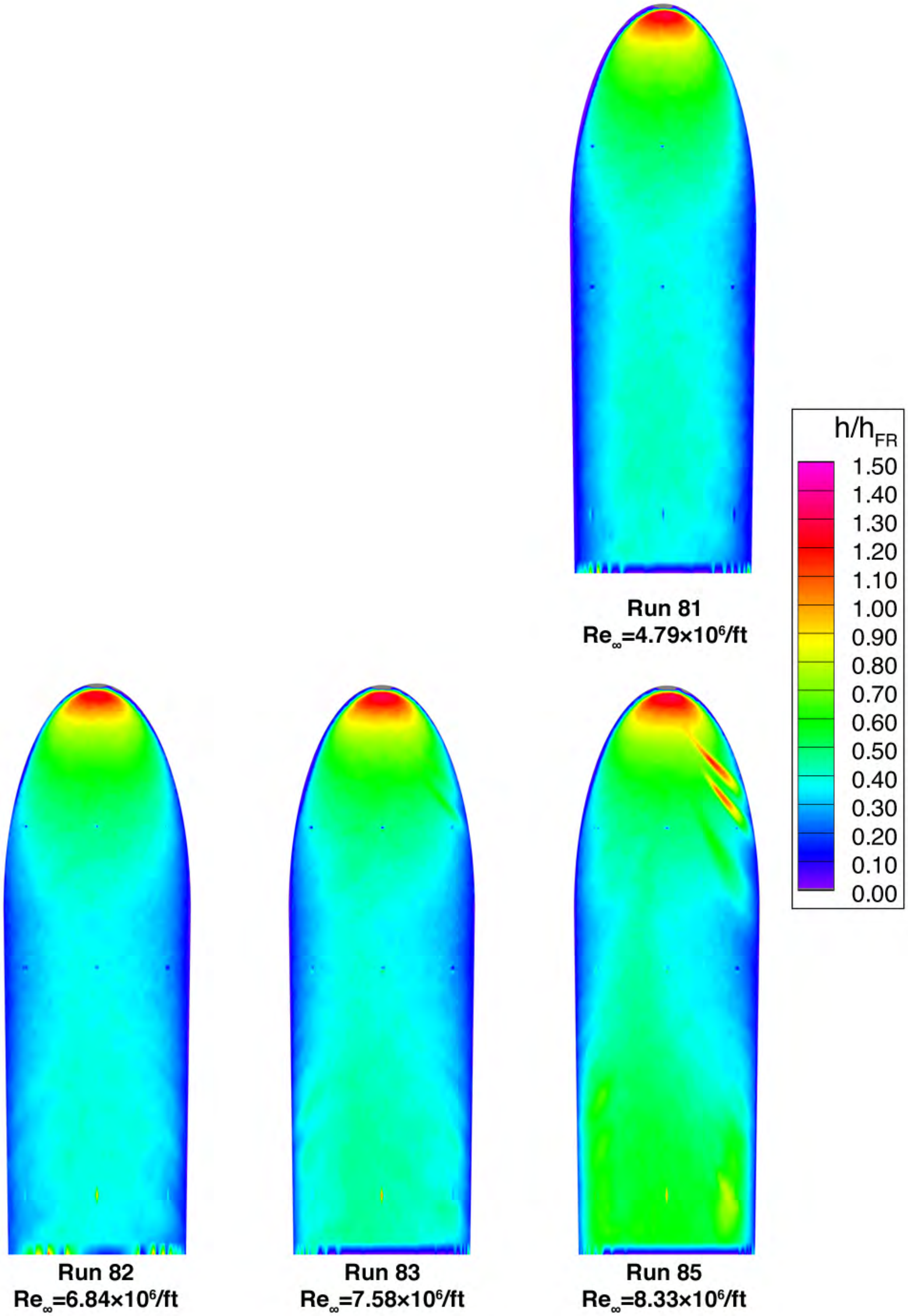

Run 81
Re_∞=4.79×10^6/ft

Run 82
Re_∞=6.84×10^6/ft

Run 83
Re_∞=7.58×10^6/ft

Run 85
Re_∞=8.33×10^6/ft

Figure 65. Reynolds Number Effects on Heating, COBRA-8459B (Model E-2), α = 40-deg

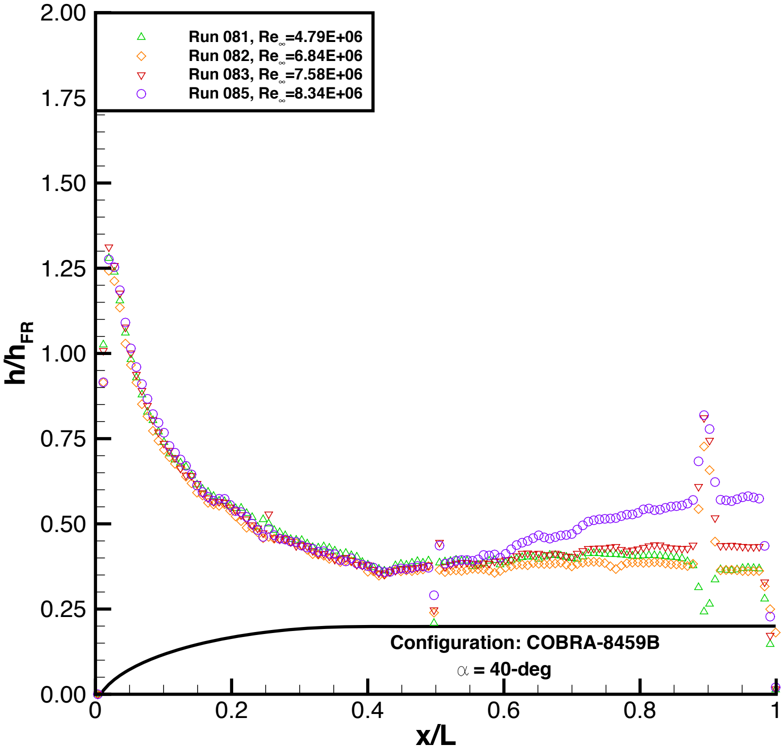

Figure 66. Centerline Heating, COBRA-8459B (Model E-2), α = 40-deg

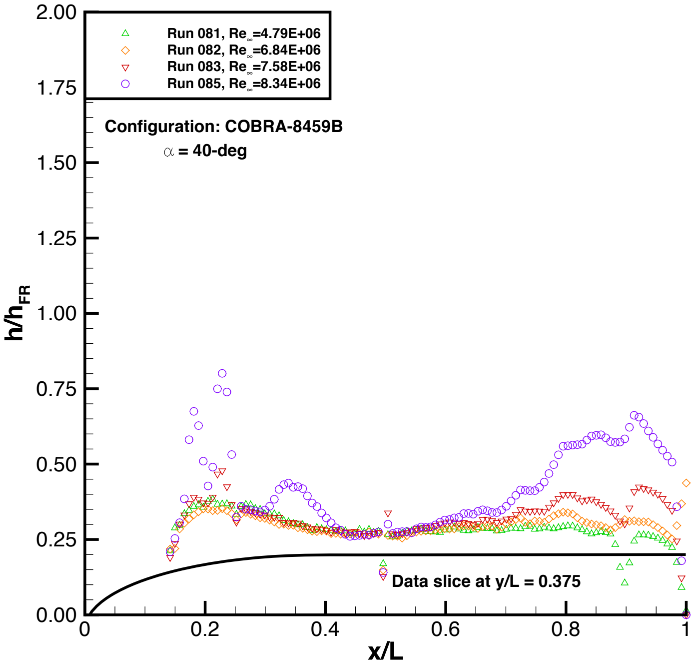

Figure 67. Off-Centerline Heating, COBRA-8459B (Model E-2), α = 40-deg

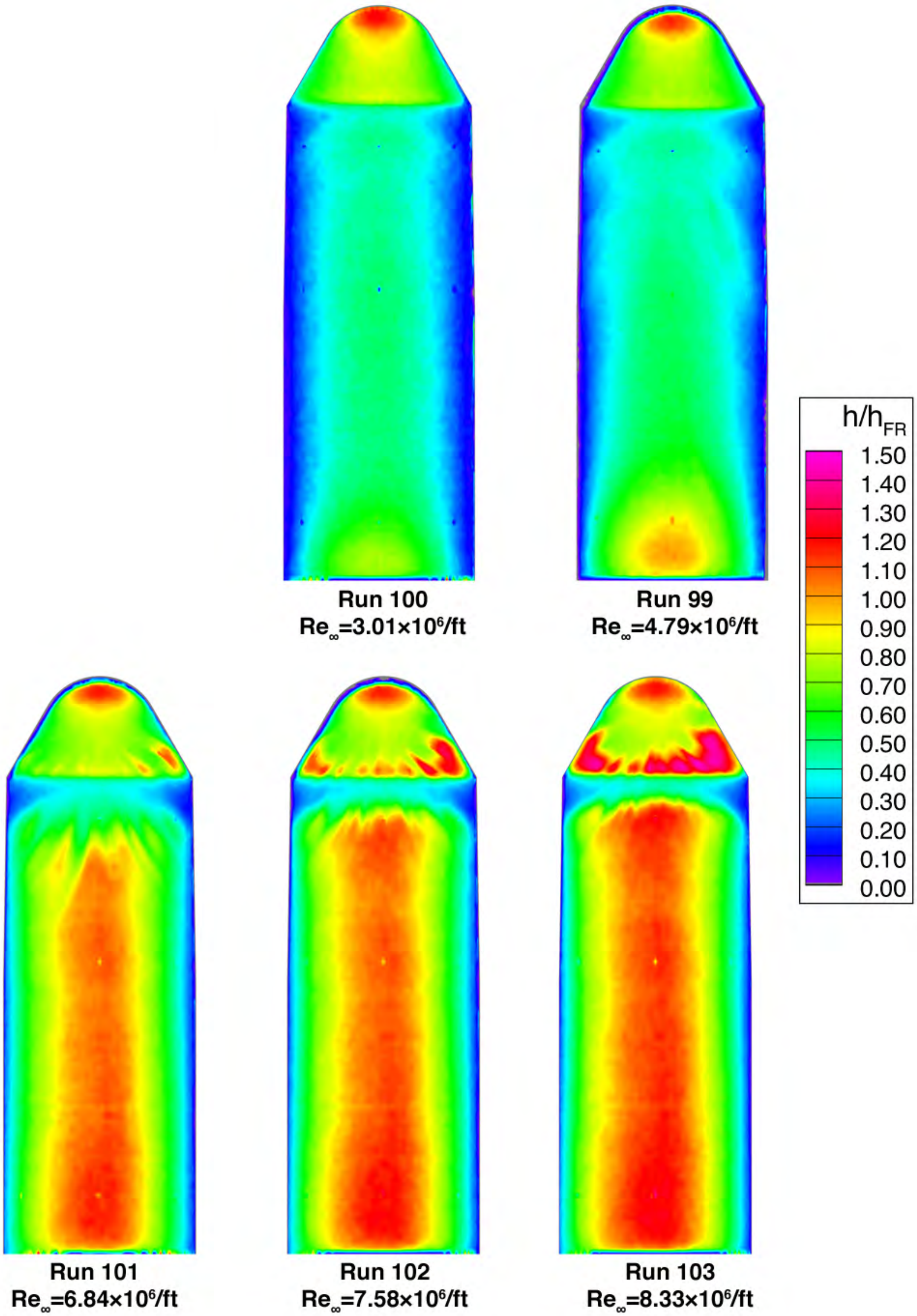

Figure 68. Reynolds Number Effects on Heating, Hammerhead-Blunt, α = 40-deg

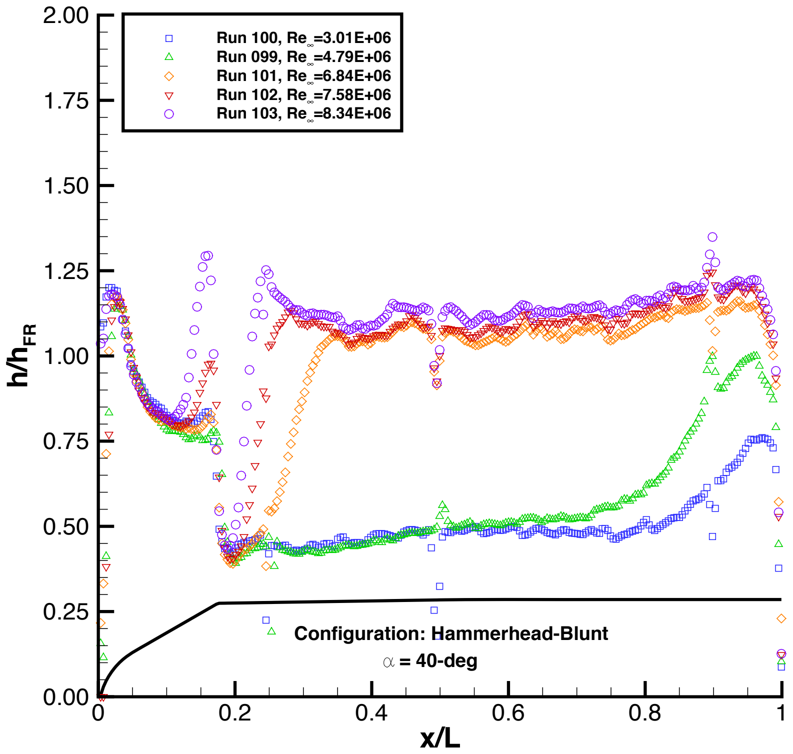

Figure 69. Centerline Heating, Hammerhead-Blunt, α = 40-deg

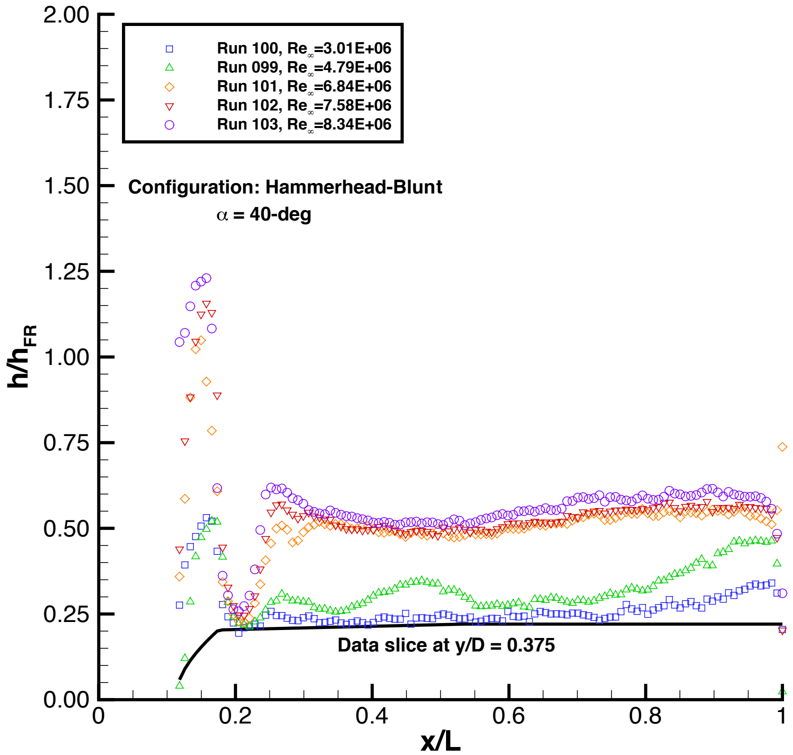

Figure 70. Off-Centerline Heating, Hammerhead-Blunt, α = 40-deg

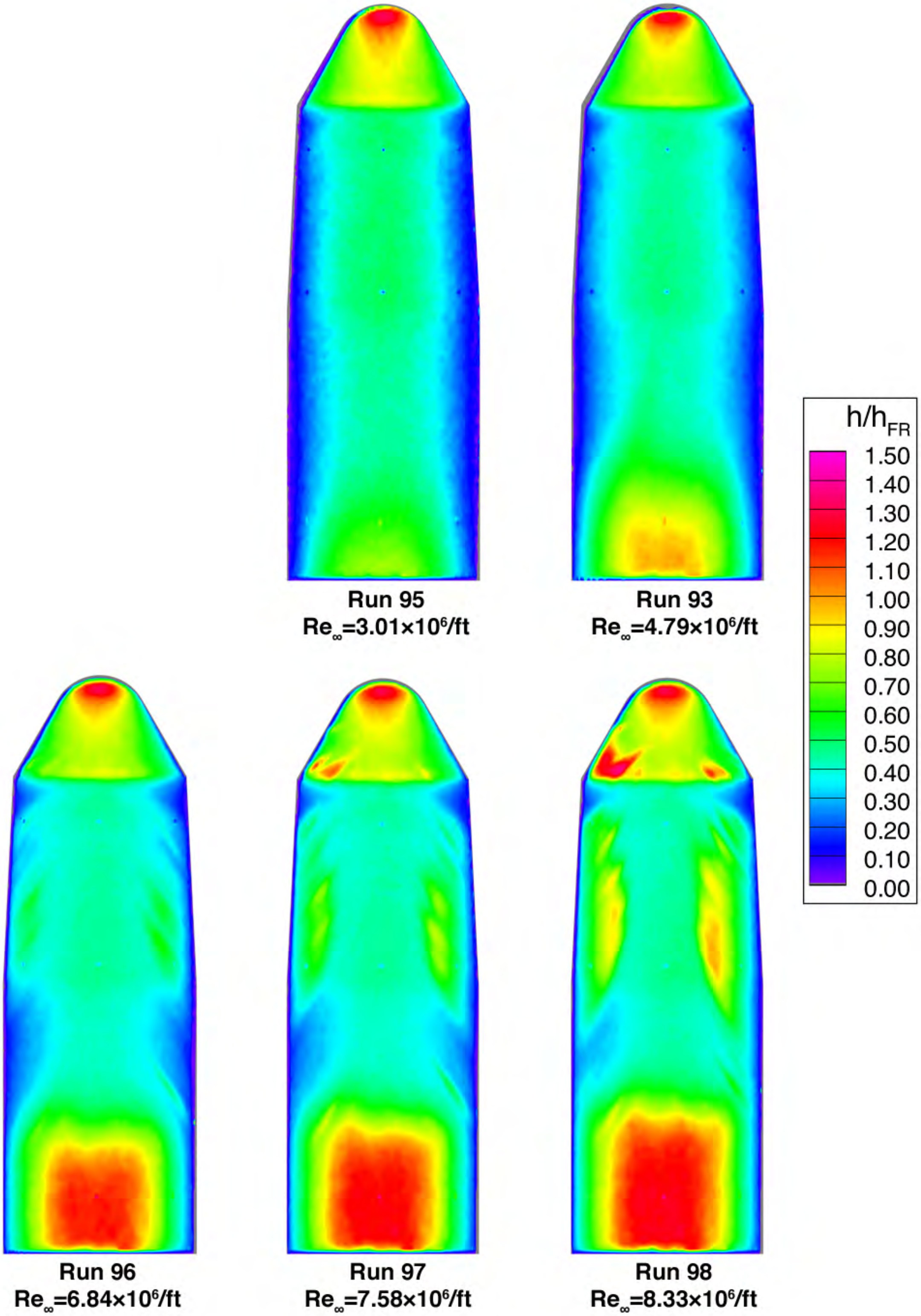

Run 95
$Re_\infty=3.01\times10^6$/ft

Run 93
$Re_\infty=4.79\times10^6$/ft

Run 96
$Re_\infty=6.84\times10^6$/ft

Run 97
$Re_\infty=7.58\times10^6$/ft

Run 98
$Re_\infty=8.33\times10^6$/ft

Figure 71. Reynolds Number Effects on Heating, Hammerhead-Nominal, α = 40-deg

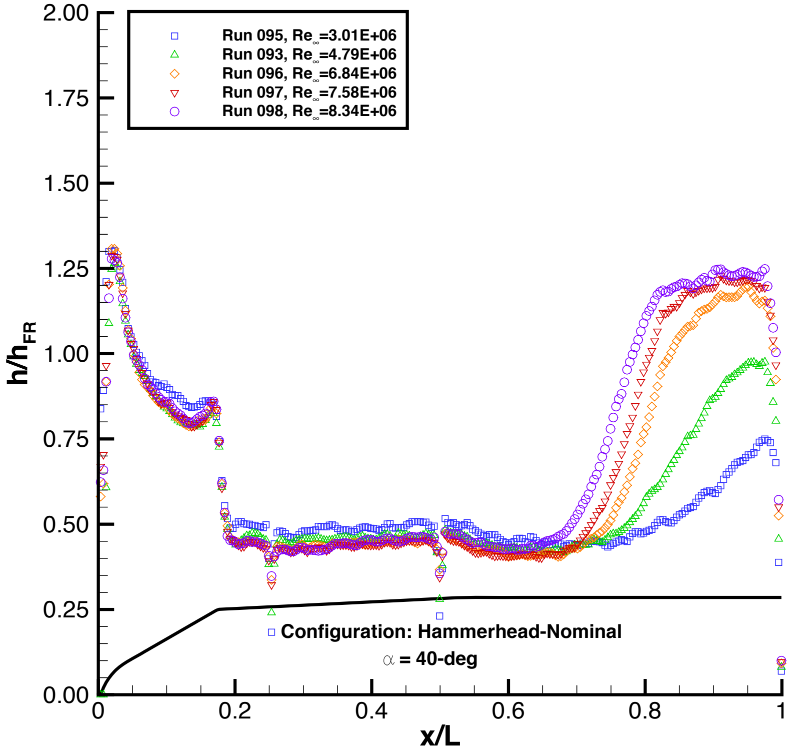

Figure 72. Centerline Heating, Hammerhead-Nominal, α = 40-deg

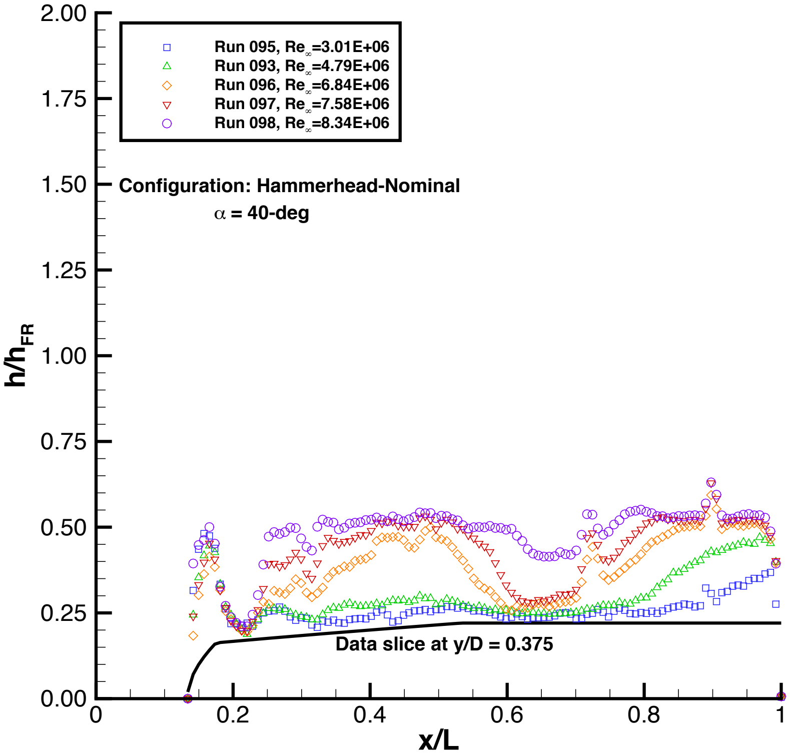

Figure 73. Off-Centerline Heating, Hammerhead-Nominal, α = 40-deg

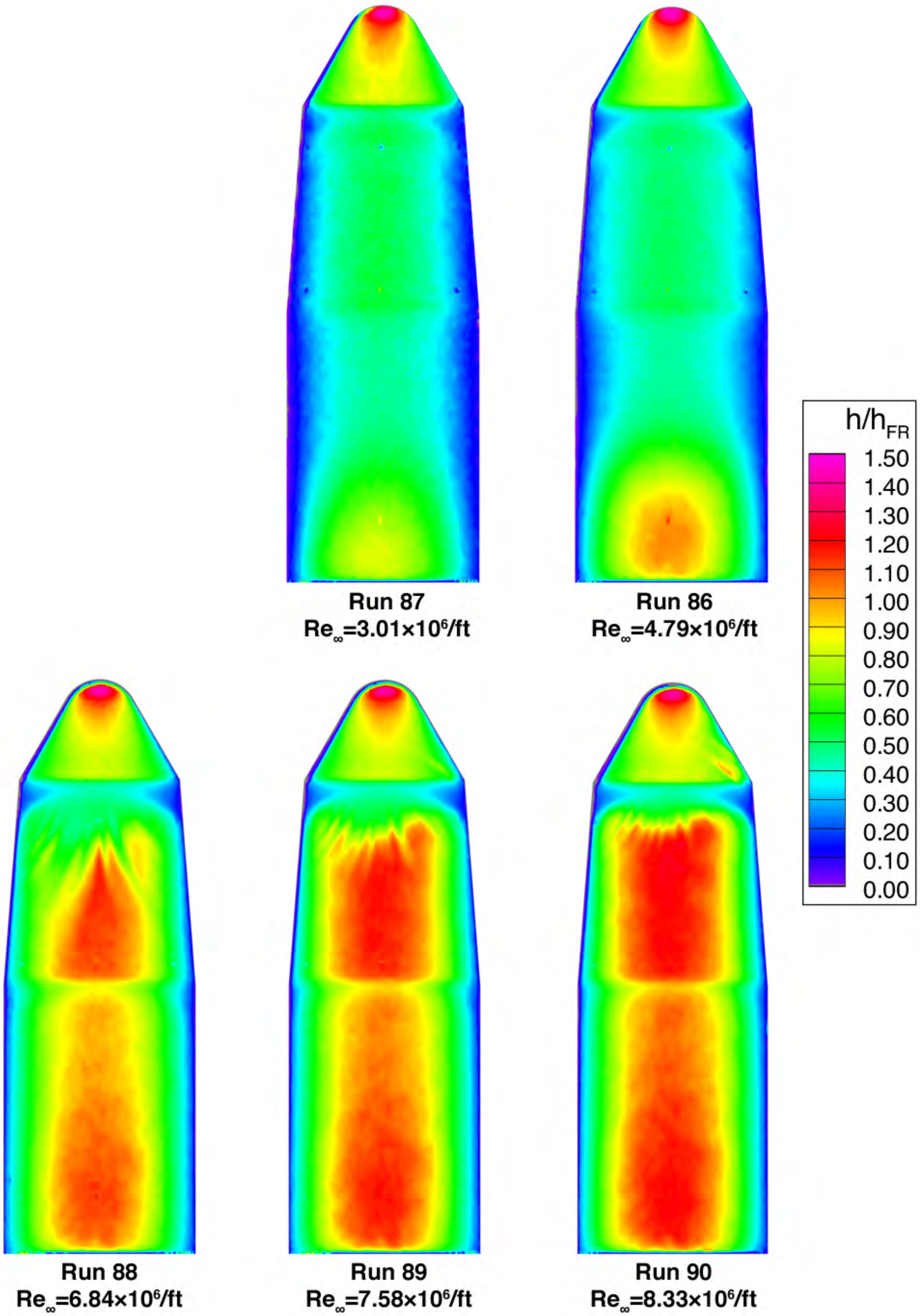

Run 87
$Re_\infty=3.01\times10^6/ft$

Run 86
$Re_\infty=4.79\times10^6/ft$

Run 88
$Re_\infty=6.84\times10^6/ft$

Run 89
$Re_\infty=7.58\times10^6/ft$

Run 90
$Re_\infty=8.33\times10^6/ft$

Figure 74. Reynolds Number Effects on Heating, Hammerhead-Sharp, α = 40-deg

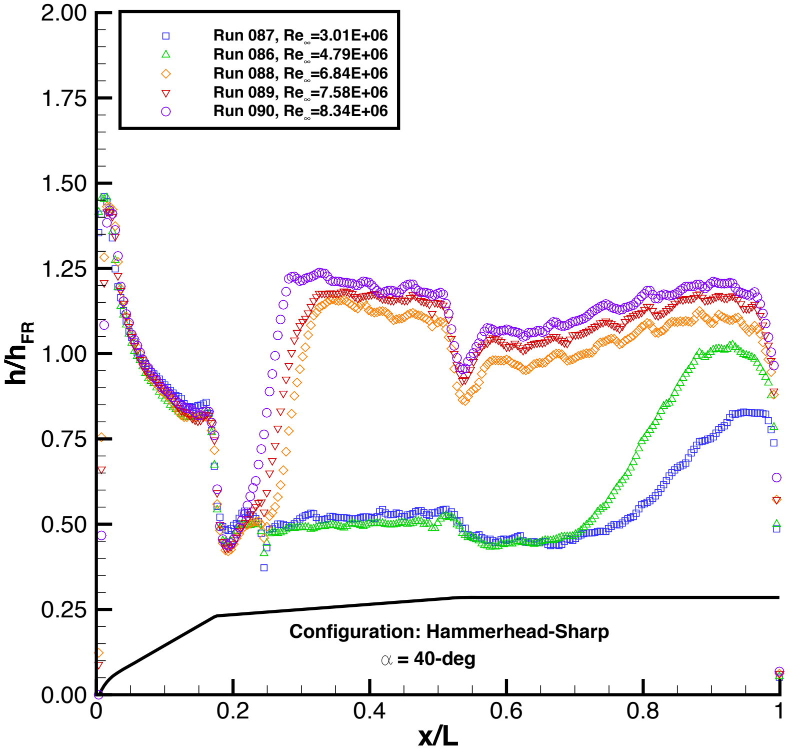

Figure 75. Centerline Heating, Hammerhead-Sharp, α = 40-deg

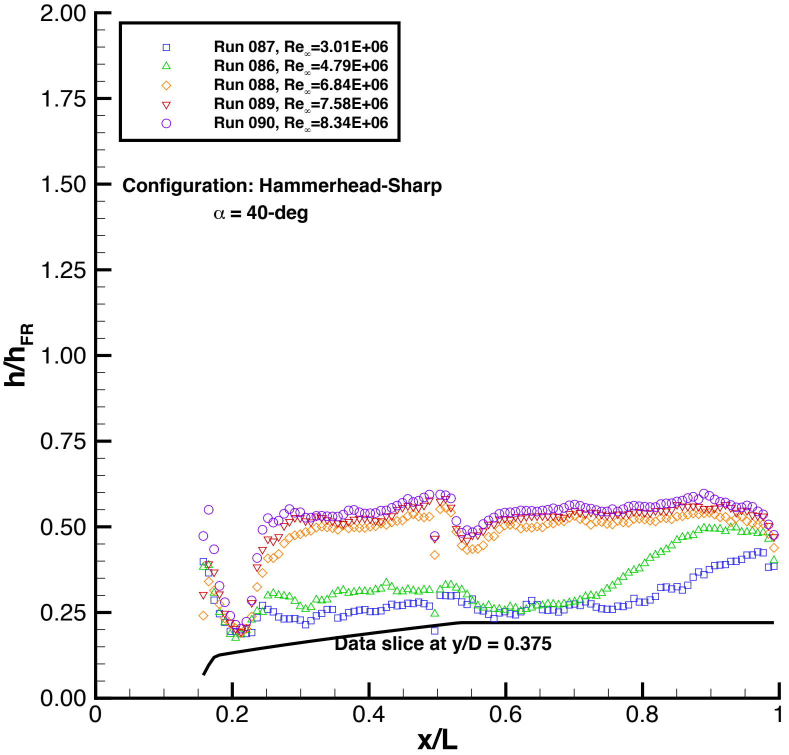

Figure 76. Off-Centerline Heating, Hammerhead-Sharp, α = 40-deg

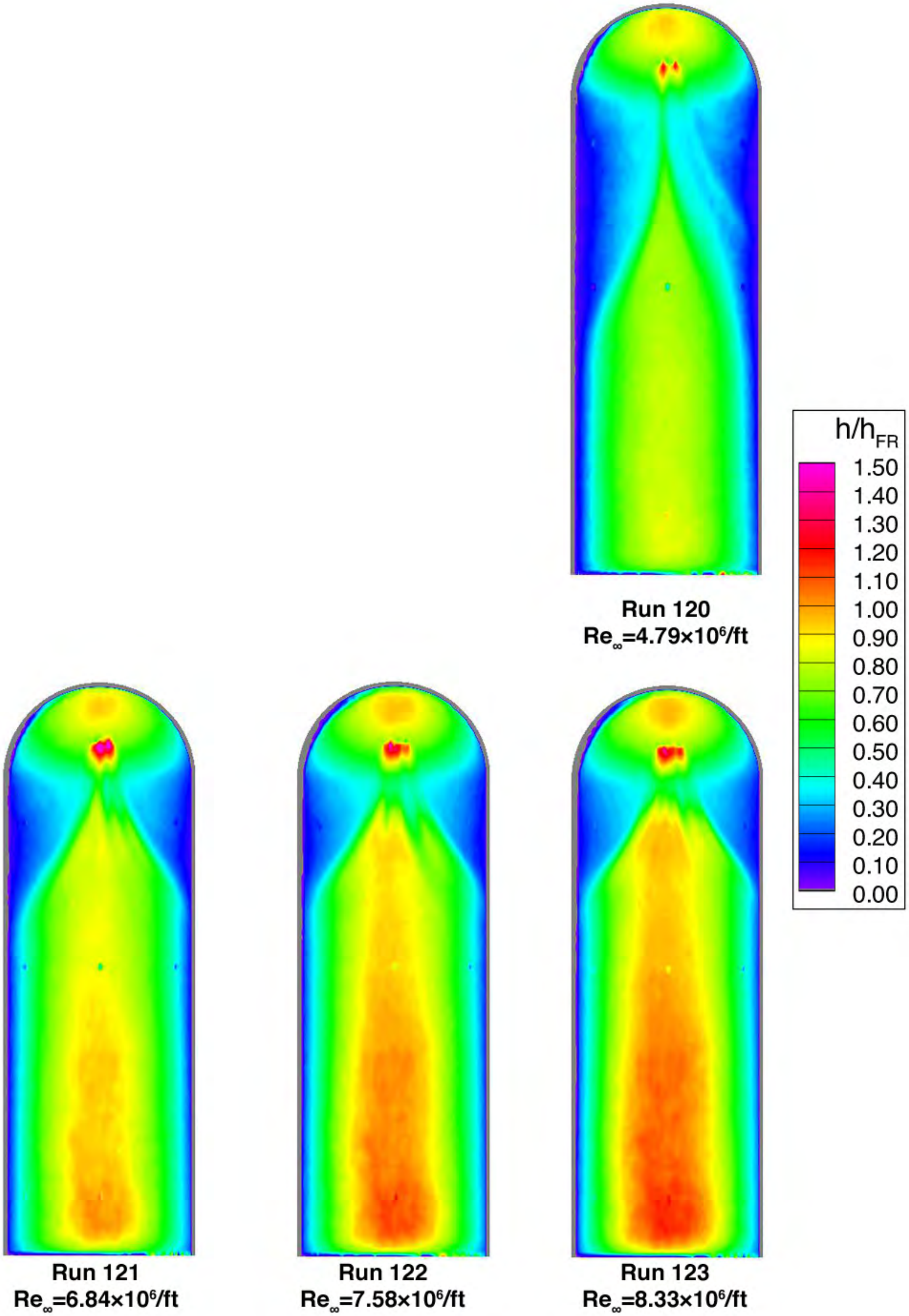

Run 120
Re$_\infty$=4.79×10^6/ft

Run 121
Re$_\infty$=6.84×10^6/ft

Run 122
Re$_\infty$=7.58×10^6/ft

Run 123
Re$_\infty$=8.33×10^6/ft

Figure 77. Reynolds Number Effects on Heating, Ellipsled-1.00-1.00, Trips at x/L=0.10, α = 40-deg

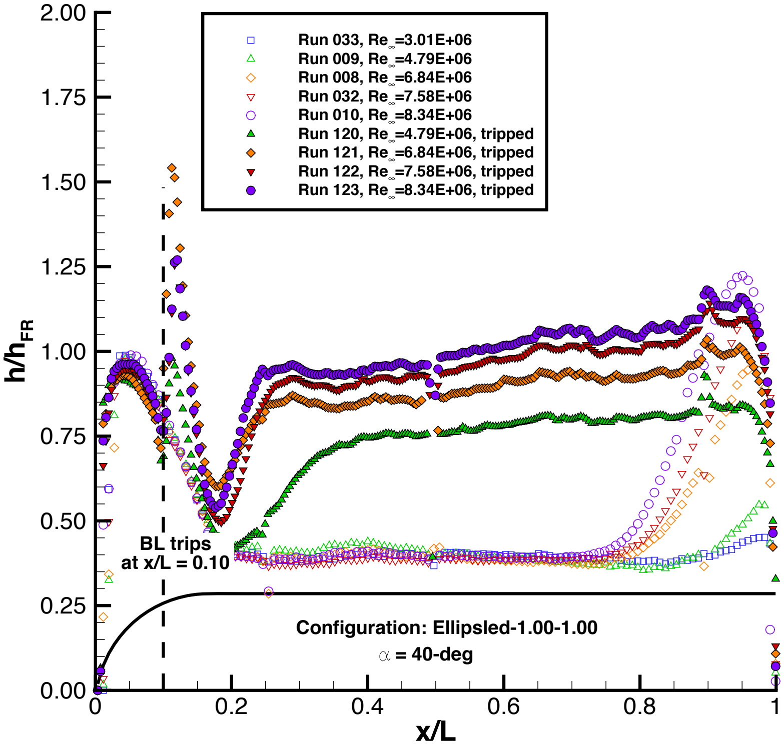

Figure 78. Centerline Heating, Ellipsled-1.00-1.00, Trips at x/L=0.10, α = 40-deg

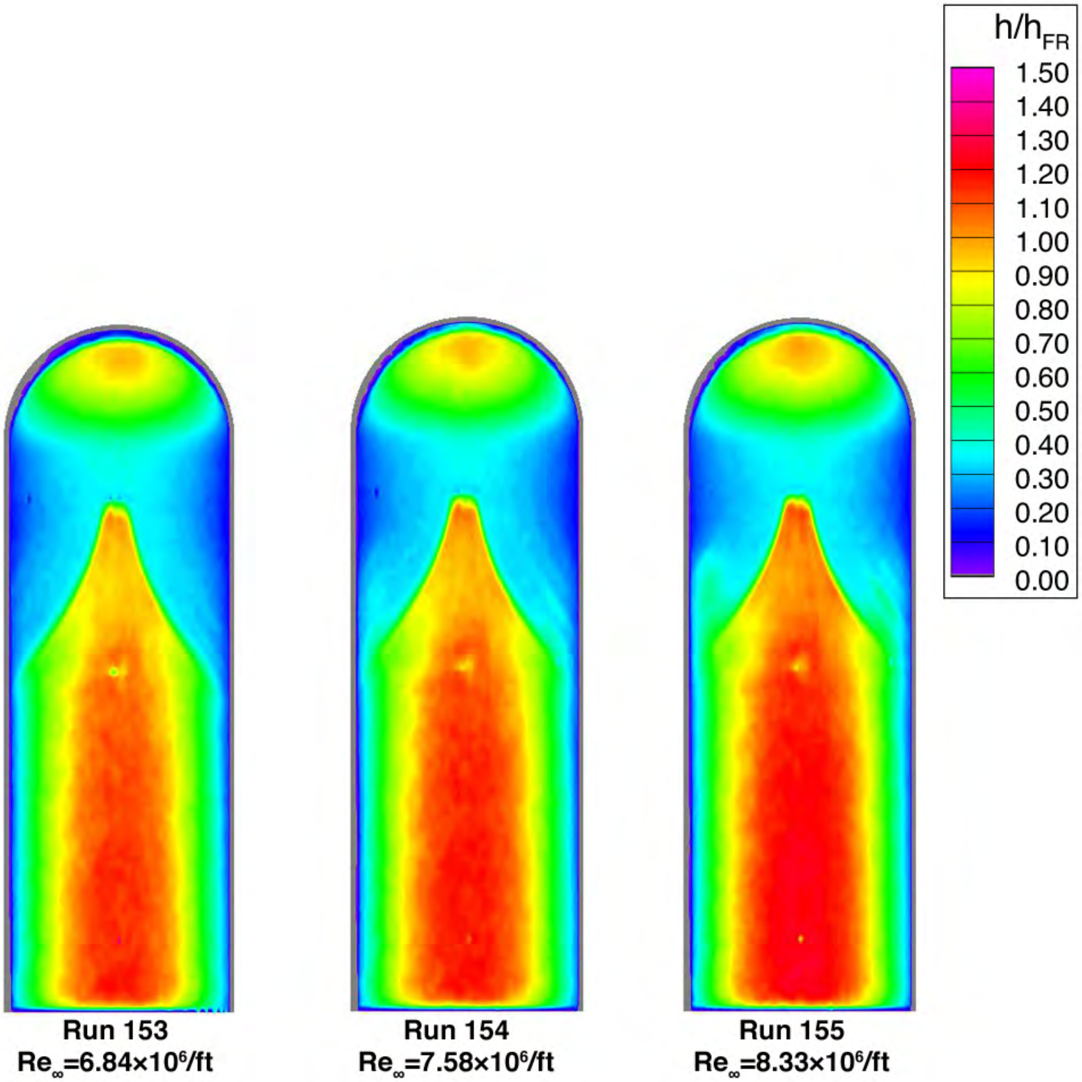

Figure 79. Reynolds Number Effects on Heating, Ellipsled-1.00-1.00, Trips at x/L=0.25, α = 40-deg

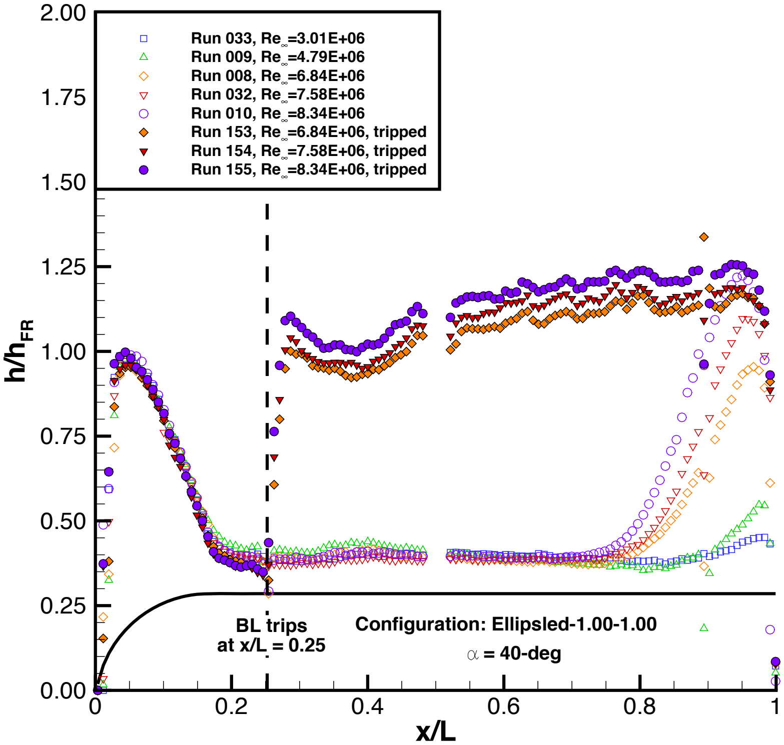

Figure 80. Centerline Heating, Ellipsled-1.00-1.00, Trips at x/L=0.25, α = 40-deg

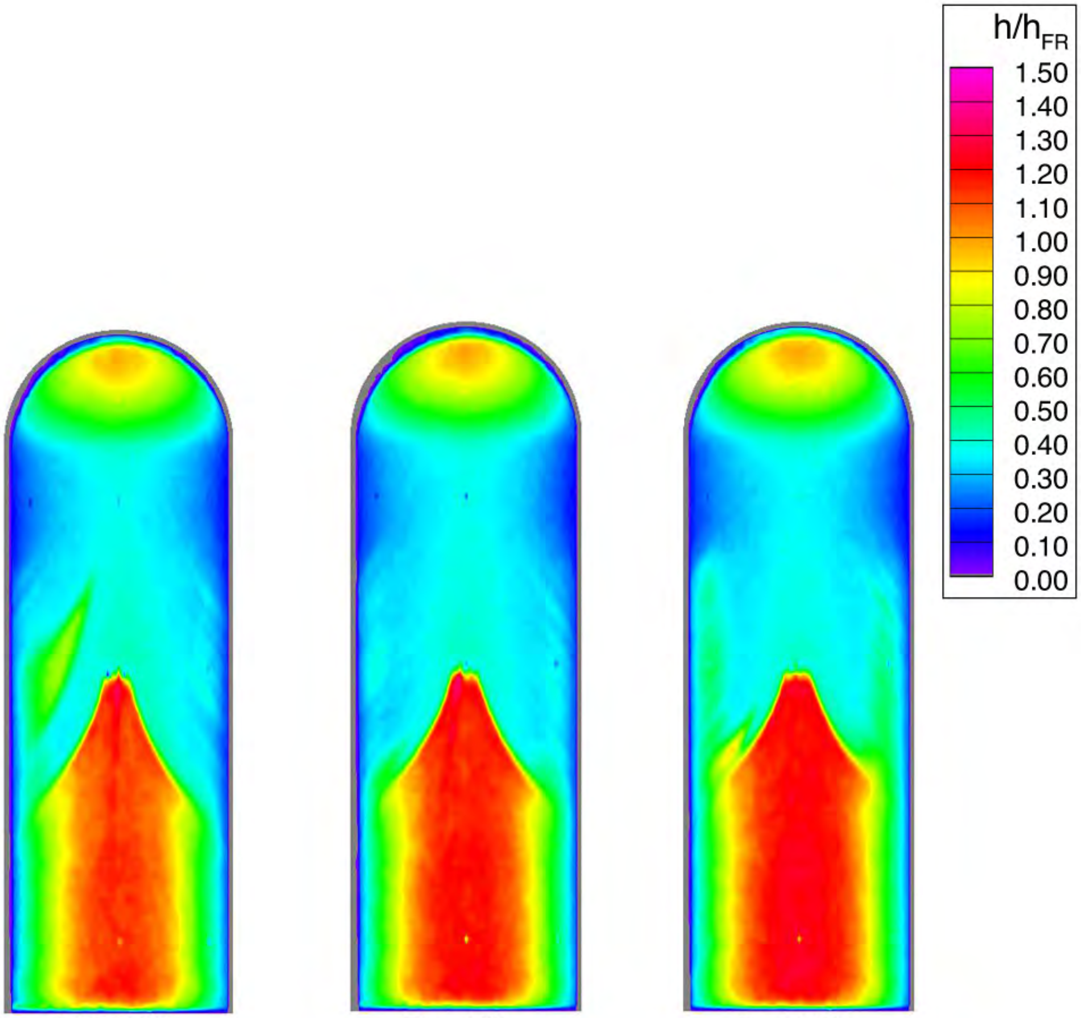

Run 150
Re$_\infty$=6.84×10^6/ft

Run 151
Re$_\infty$=7.58×10^6/ft

Run 152
Re$_\infty$=8.33×10^6/ft

Figure 81. Reynolds Number Effects on Heating, Ellipsled-1.00-1.00, Trips at x/L=0.50, α = 40-deg

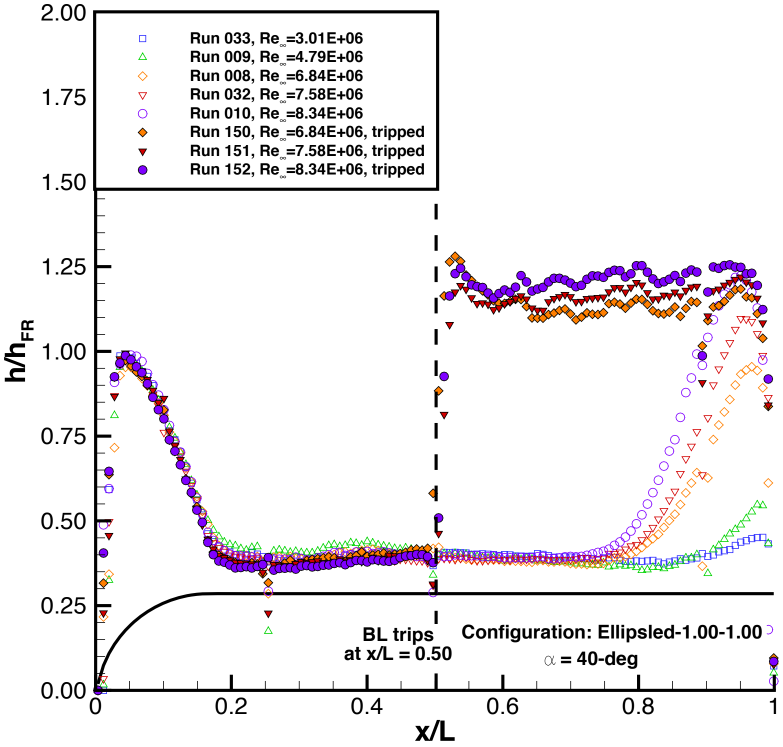

Figure 82. Centerline Heating, Ellipsled-1.00-1.00, Trips at x/L=0.50, α = 40-deg

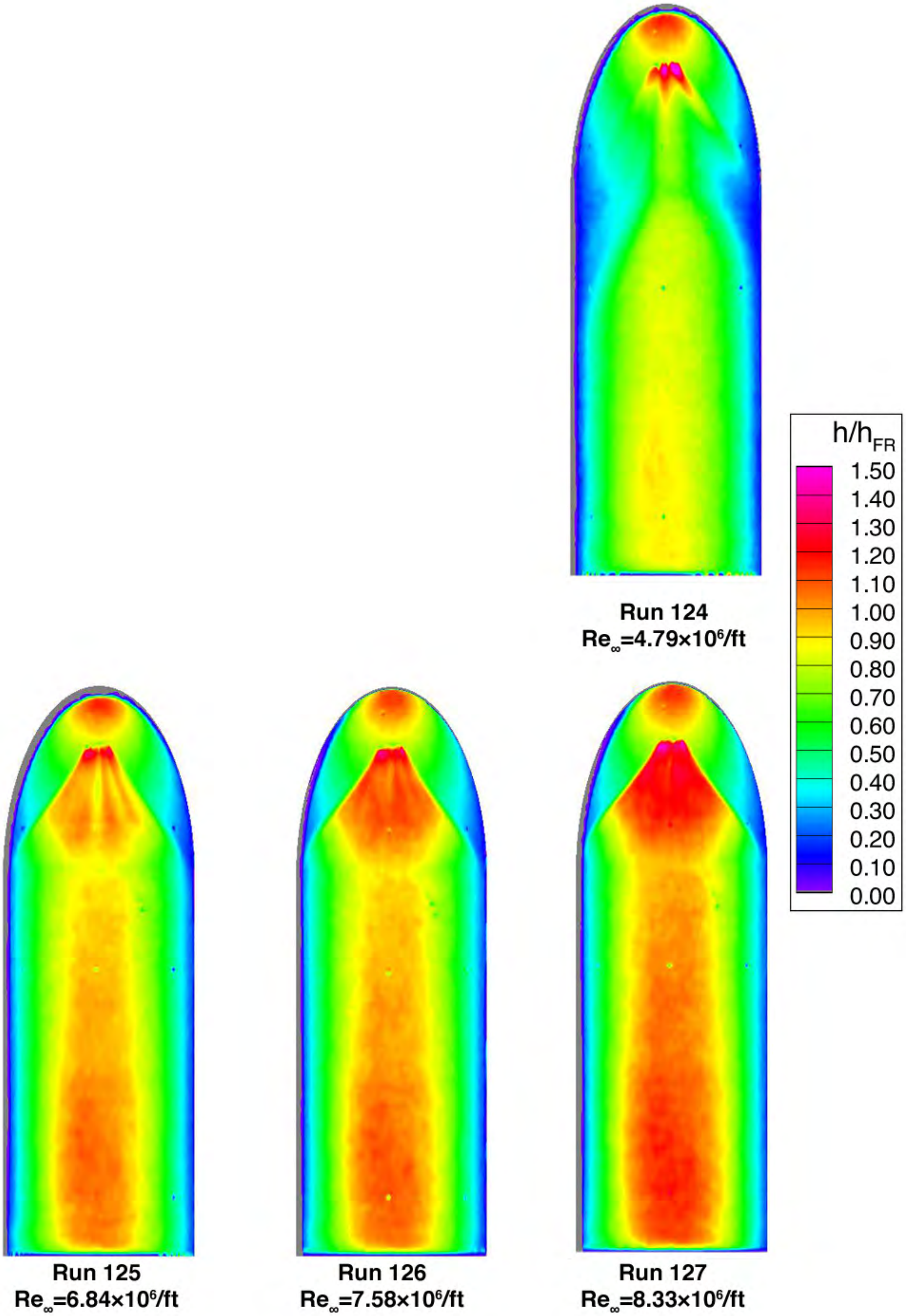

Run 124
Re_∞=4.79×10^6/ft

Run 125
Re_∞=6.84×10^6/ft

Run 126
Re_∞=7.58×10^6/ft

Run 127
Re_∞=8.33×10^6/ft

Figure 83. Reynolds Number Effects on Heating, Ellipsled-2.00-1.00, Trips at x/L=0.10, α = 40-deg

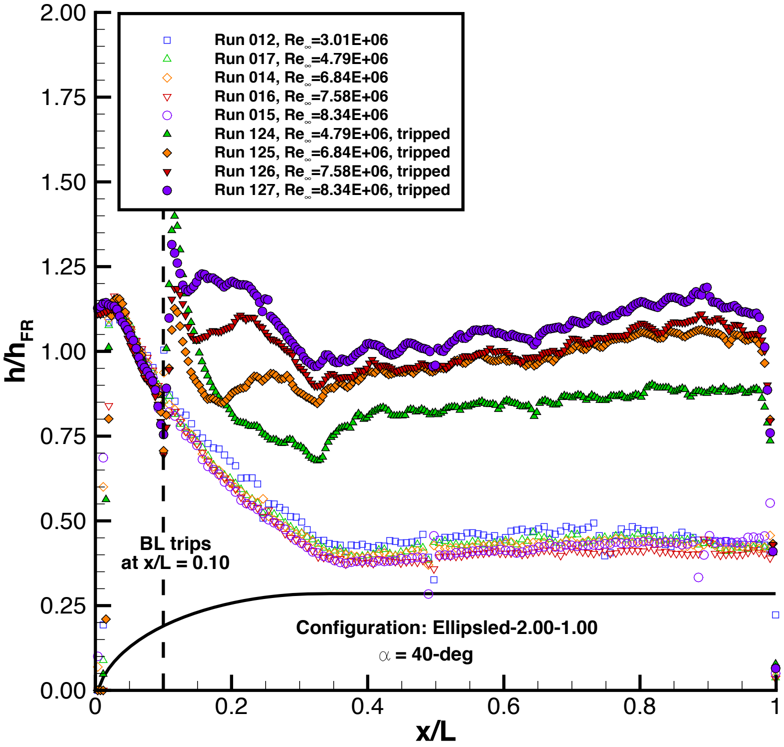

Figure 84. Centerline Heating, Ellipsled-2.00-1.00, Trips at x/L=0.10, α = 40-deg

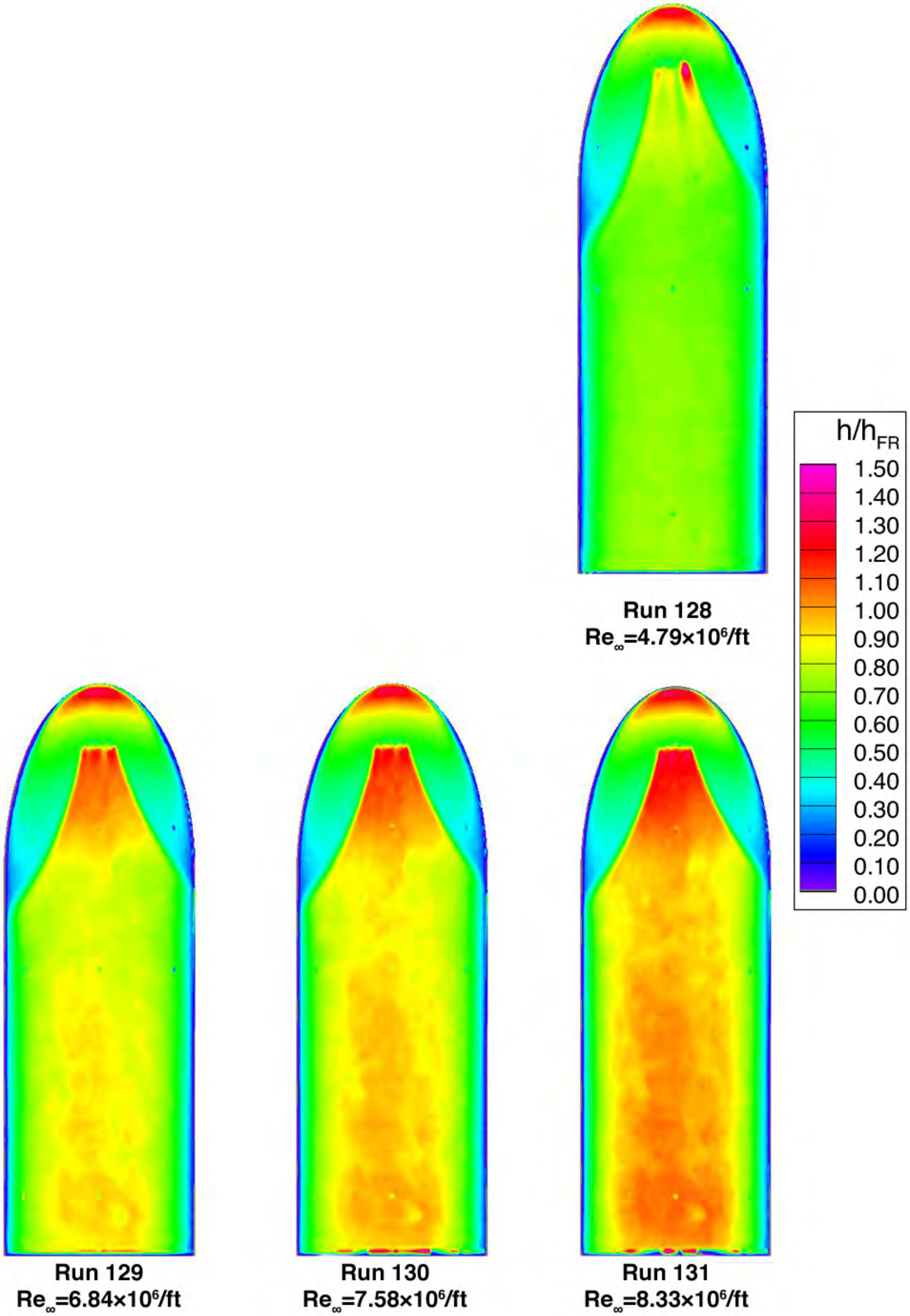

Run 128 $Re_\infty=4.79\times10^6$/ft

Run 129 $Re_\infty=6.84\times10^6$/ft

Run 130 $Re_\infty=7.58\times10^6$/ft

Run 131 $Re_\infty=8.33\times10^6$/ft

Figure 85. Reynolds Number Effects on Heating, Ellipsled-2.00-0.50, Trips at x/L=0.10, α = 40-deg

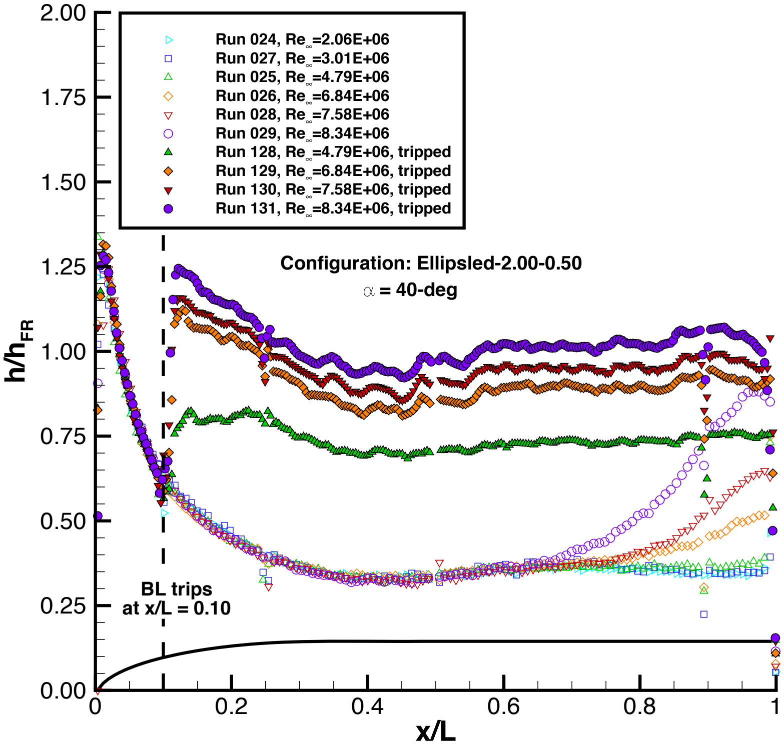

Figure 86. Centerline Heating, Ellipsled-2.00-0.50, Trips at x/L=0.10, α = 40-deg

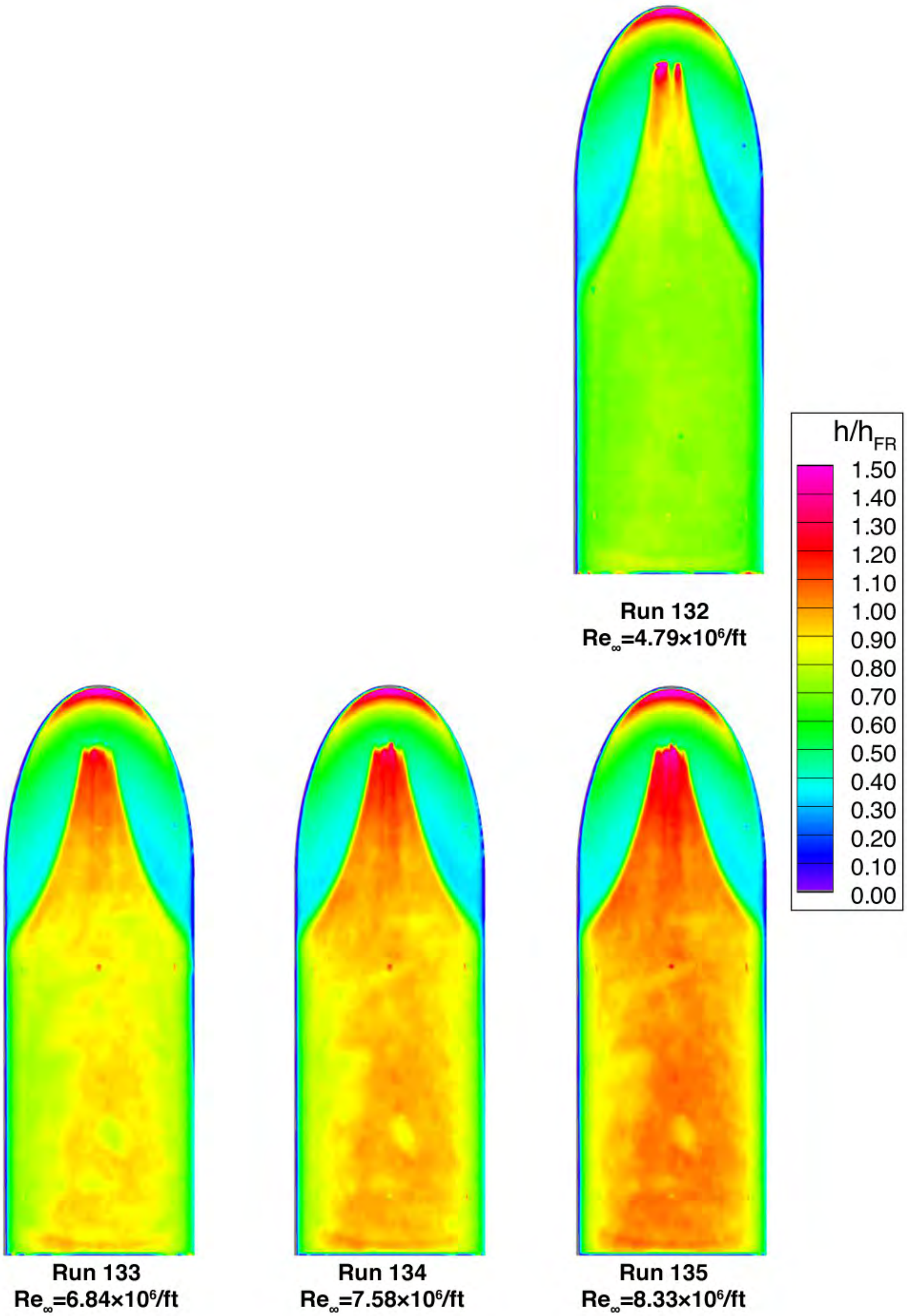

Run 132
$Re_{\infty}=4.79\times10^{6}$/ft

Run 133
$Re_{\infty}=6.84\times10^{6}$/ft

Run 134
$Re_{\infty}=7.58\times10^{6}$/ft

Run 135
$Re_{\infty}=8.33\times10^{6}$/ft

Figure 87. Reynolds Number Effects on Heating, Ellipsled-2.00-0.25, Trips at x/L=0.10, α = 40-deg

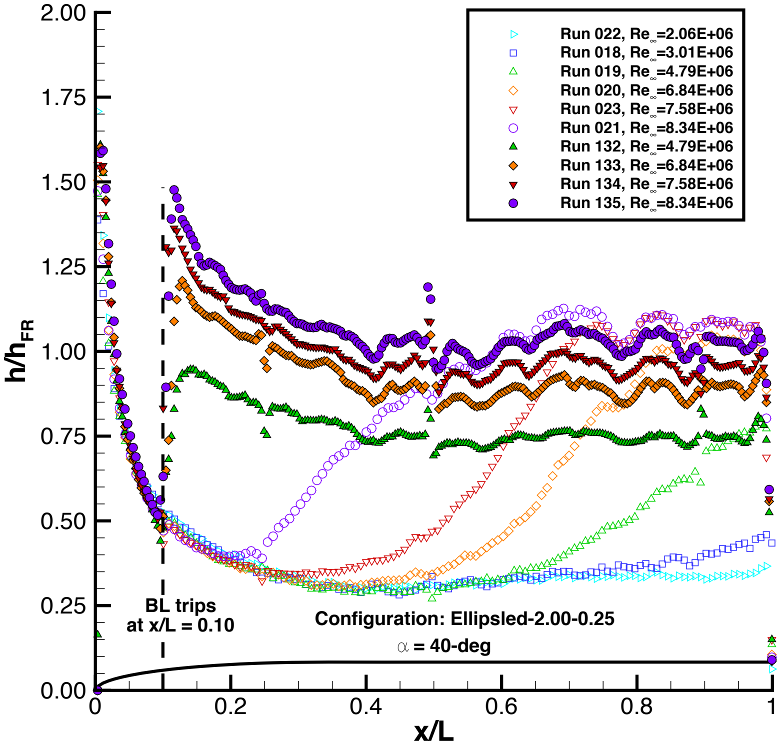

Figure 88. Centerline Heating, Ellipsled-2.00-0.25, Trips at x/L=0.10, α = 40-deg

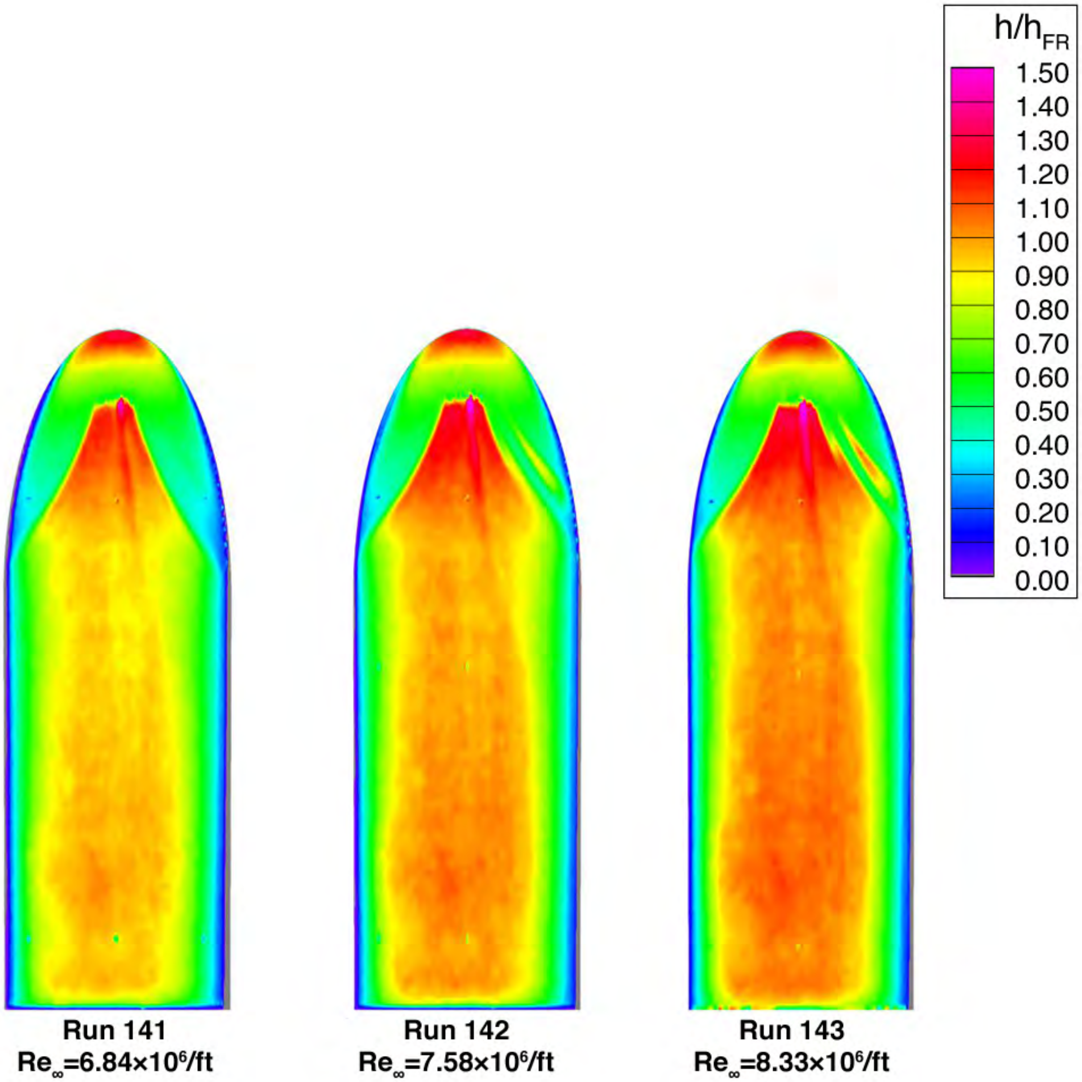

Run 141
$Re_\infty=6.84\times10^6$/ft

Run 142
$Re_\infty=7.58\times10^6$/ft

Run 143
$Re_\infty=8.33\times10^6$/ft

Figure 89. Reynolds Number Effects on Heating, COBRA-14297B, Trips at x/L=0.10, α = 40-deg

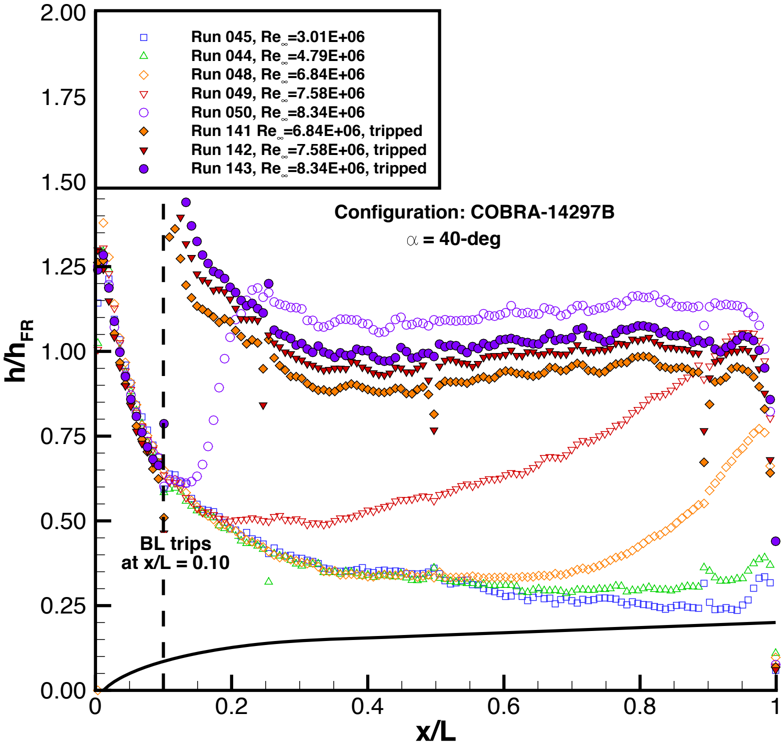

Figure 90. Centerline Heating, COBRA-14297B, Trips at x/L=0.10, α = 40-deg

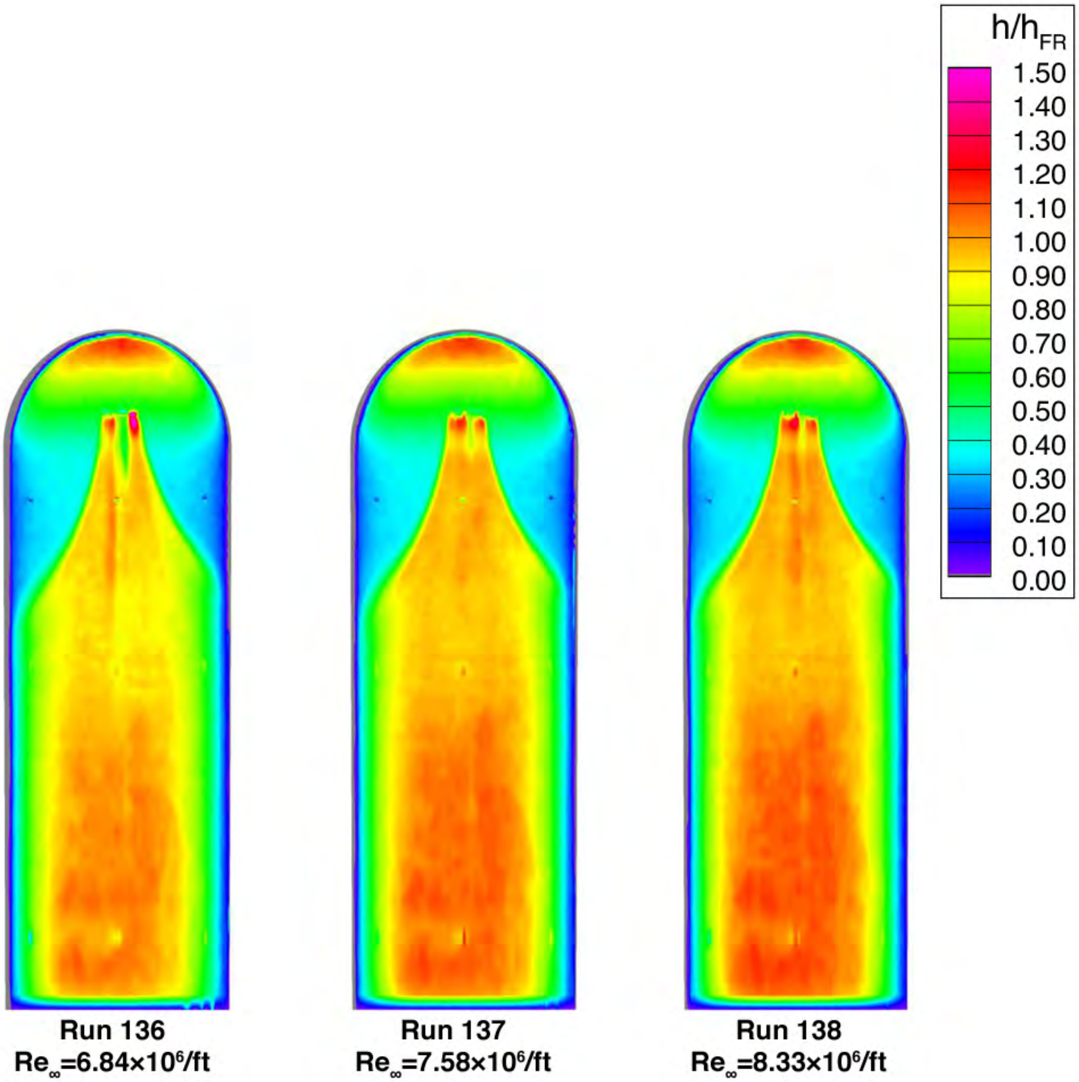

Figure 91. Reynolds Number Effects on Heating, COBRA-14888B, Trips at x/L=0.10, α = 40-deg

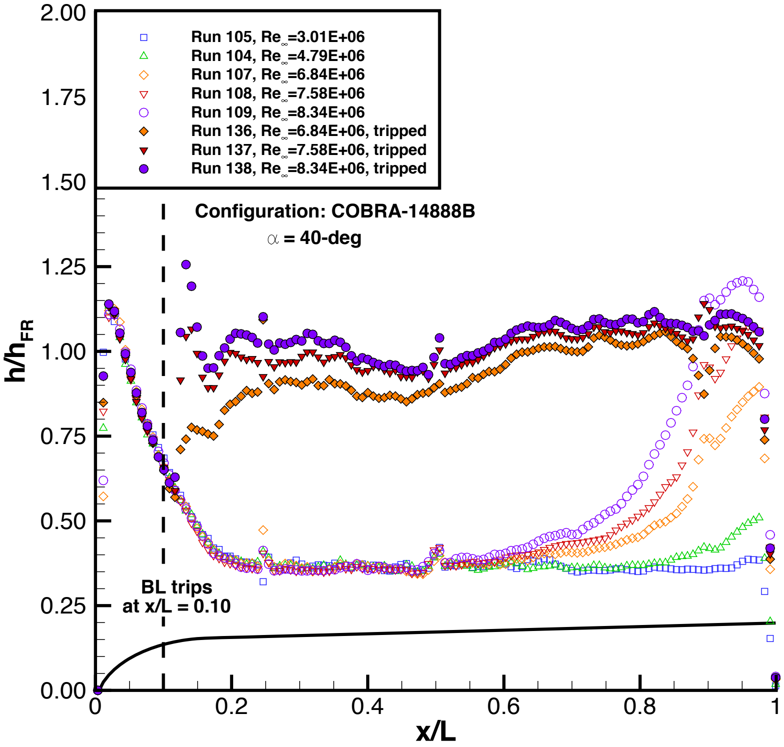

Figure 92. Centerline Heating, COBRA-14888B, Trips at x/L=0.10, α = 40-deg

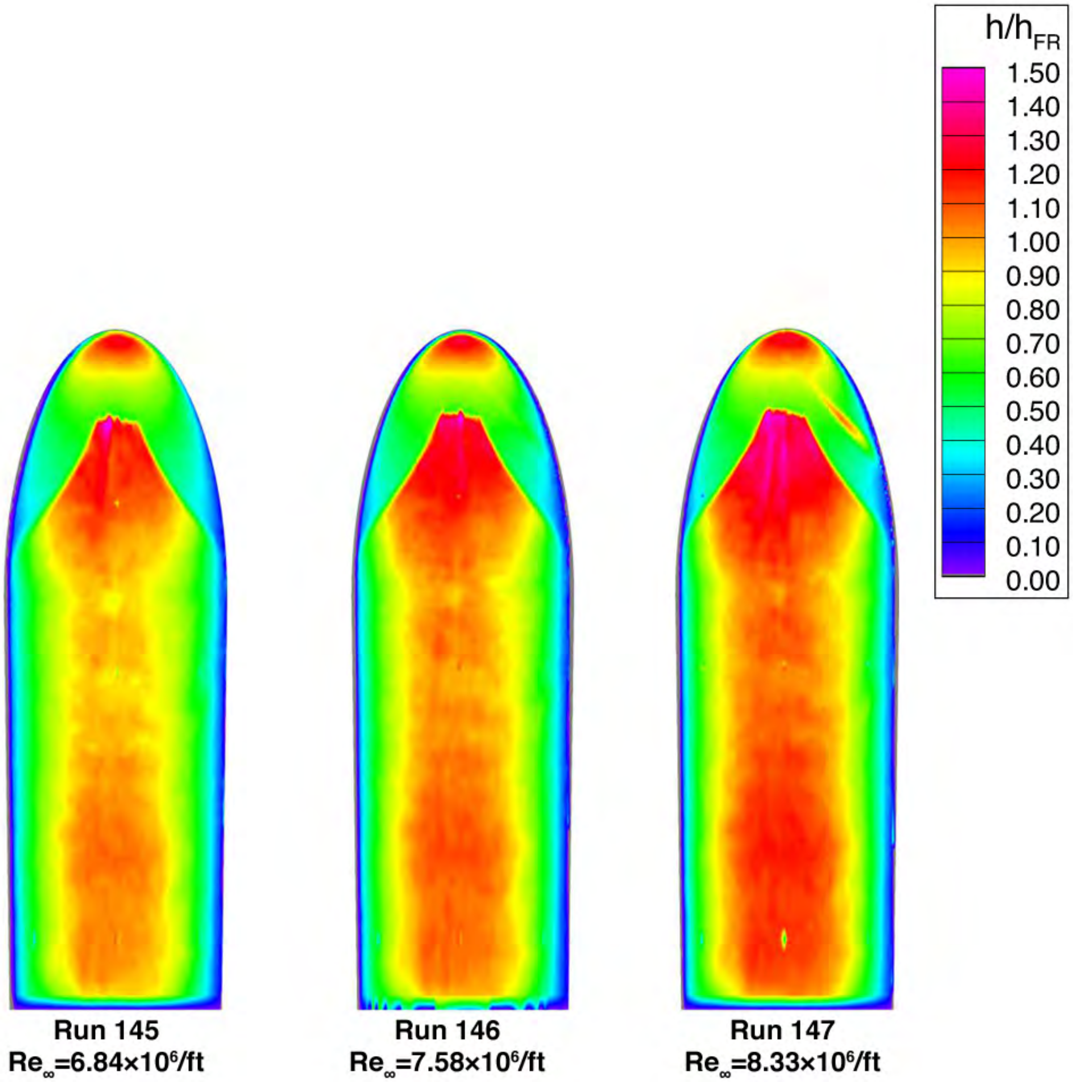

Run 145
$Re_\infty=6.84\times10^6$/ft

Run 146
$Re_\infty=7.58\times10^6$/ft

Run 147
$Re_\infty=8.33\times10^6$/ft

Figure 93. Reynolds Number Effects on Heating, COBRA-8459B, Trips at x/L=0.10, α = 40-deg

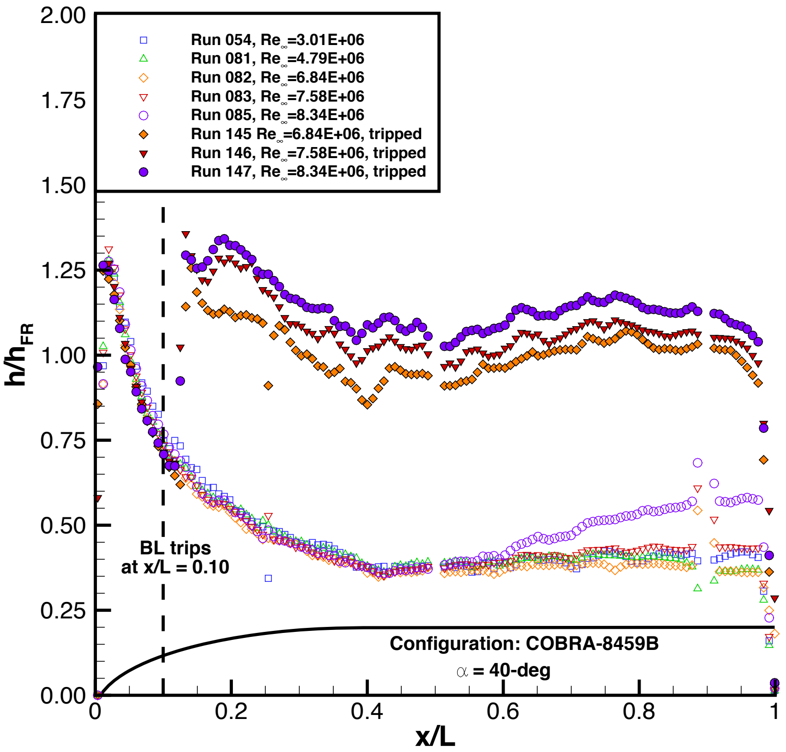

Figure 94. Centerline Heating, COBRA-8459B, Trips at x/L=0.10, α = 40-deg

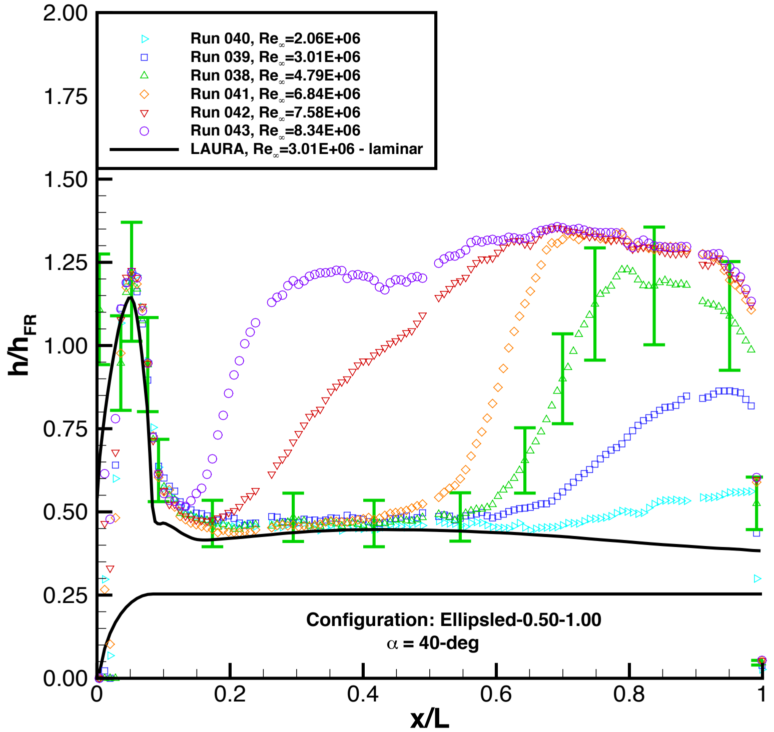

Figure 95. Ellipsled-0.50-1.00 Data vs. Laminar Predictions, α = 40-deg

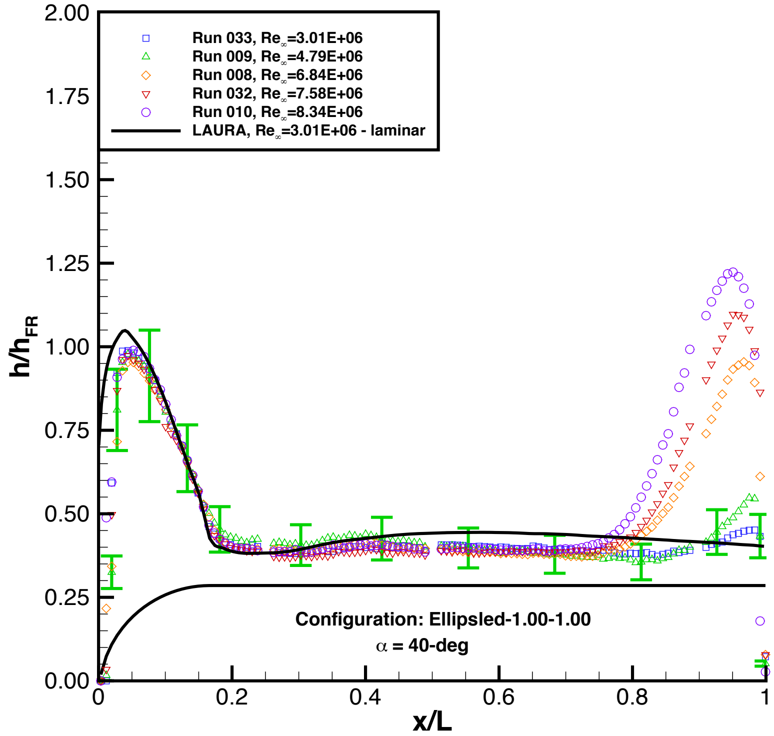

Figure 96. Ellipsled-1.00-1.00 Data vs. Laminar Predictions, α = 40-deg

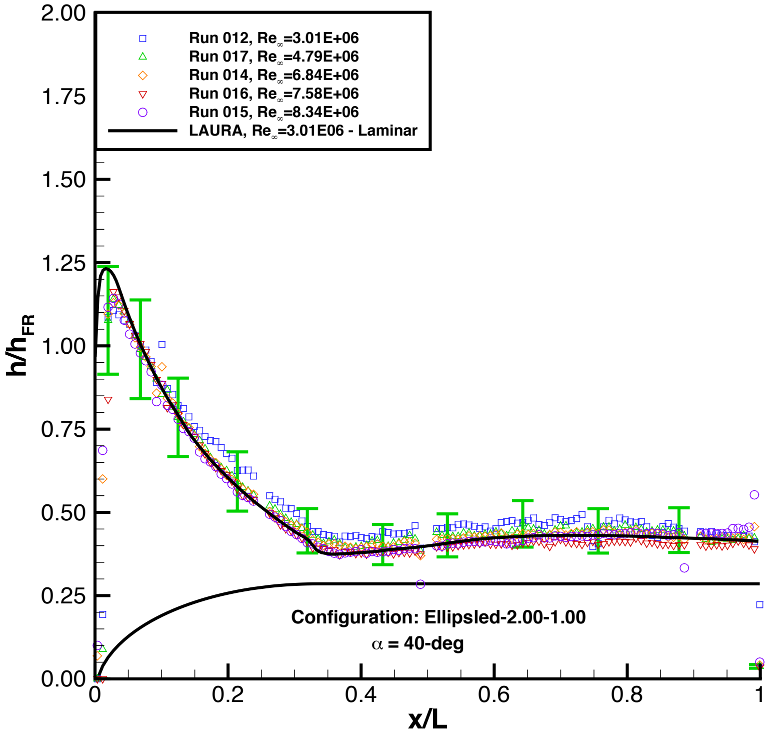

Figure 97. Ellipsled-2.00-1.00 Data vs. Laminar Predictions, α = 40-deg

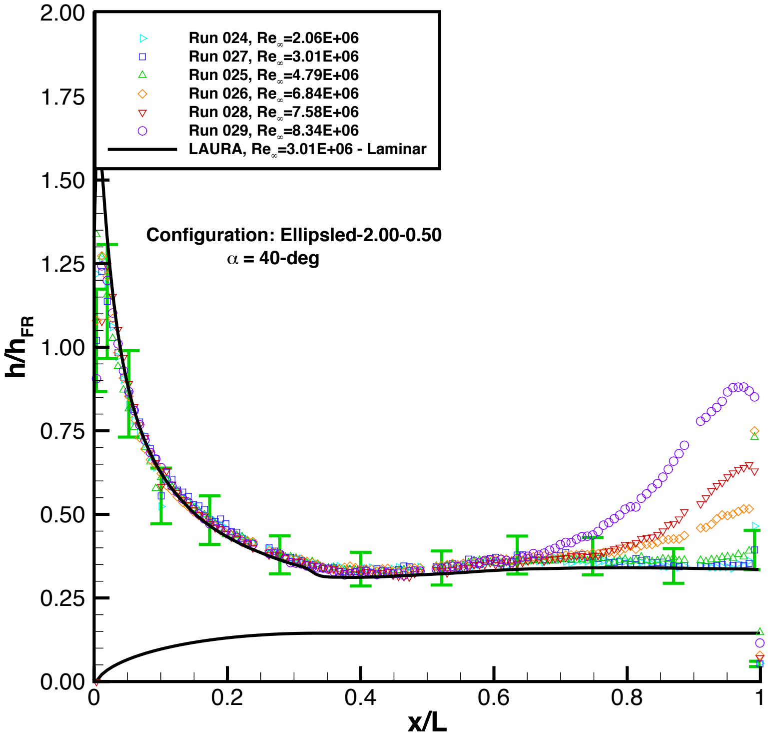

Figure 98. Ellipsled-2.00-0.50 Data vs. Laminar Predictions, α = 40-deg

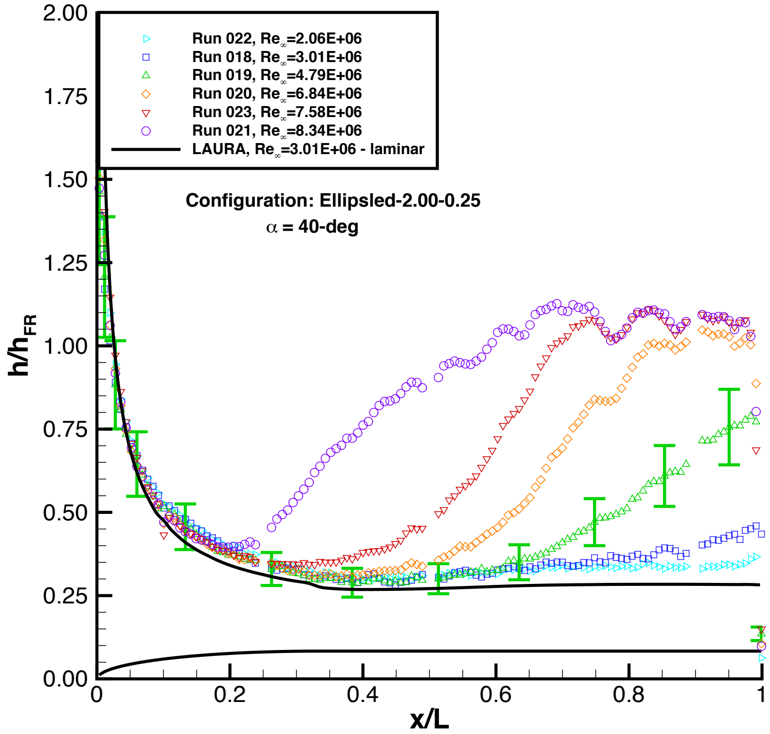

Figure 99. Ellipsled-2.00-0.25 Data vs. Laminar Predictions, α = 40-deg

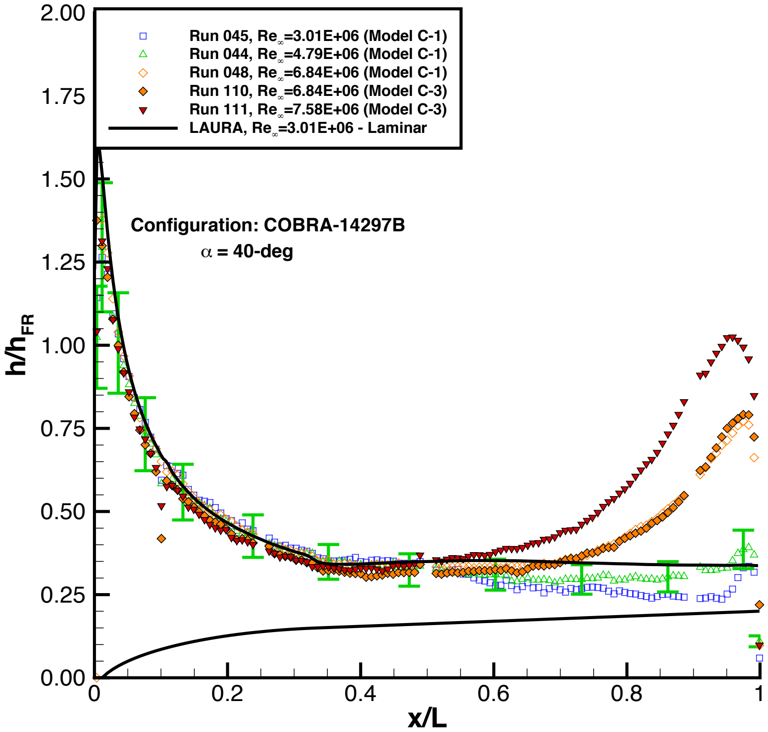

Figure 100. COBRA-14297B Data vs. Laminar Predictions, α = 40-deg

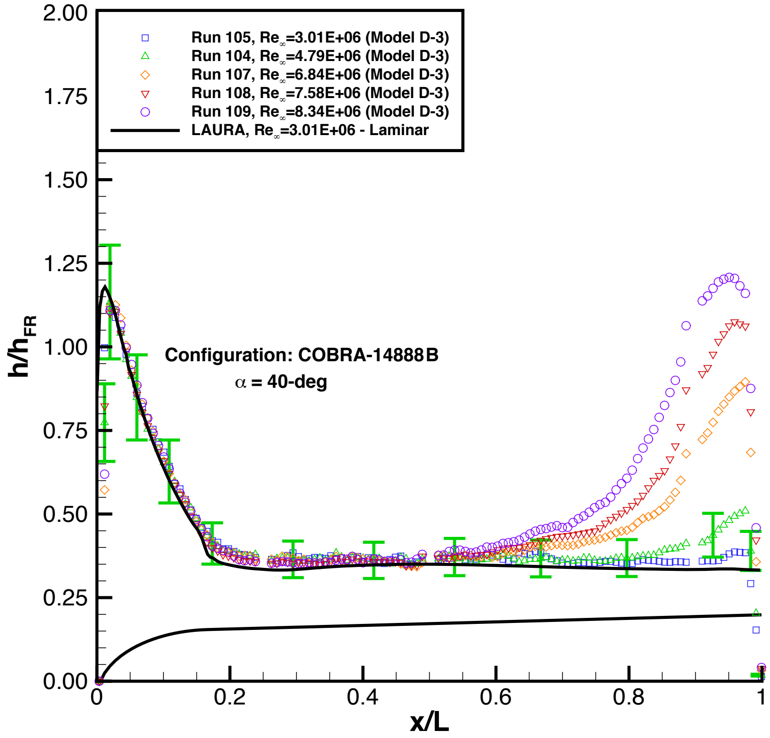

Figure 101. COBRA-14888B Data vs. Laminar Predictions, α = 40-deg

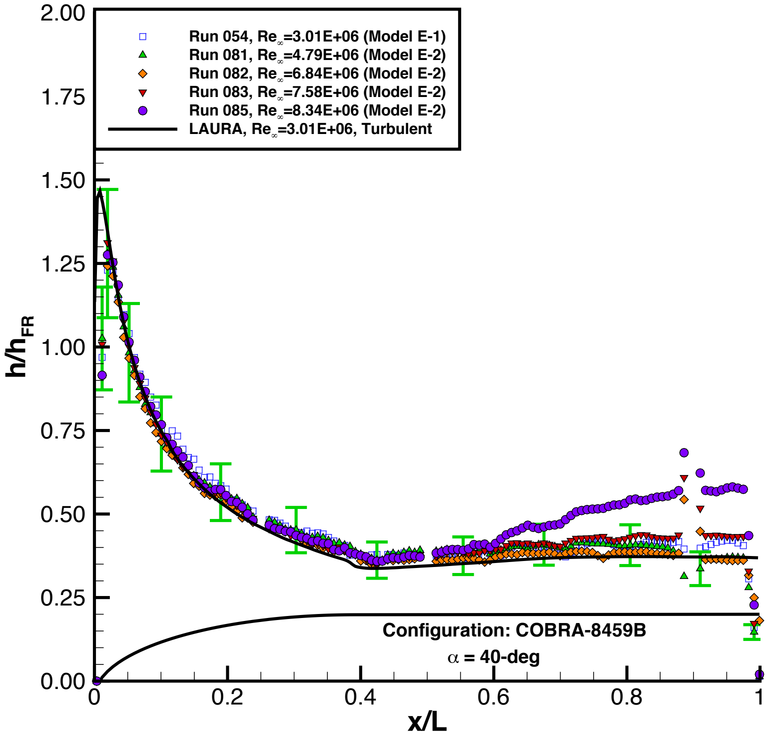

Figure 102. COBRA-8459B Data vs. Laminar Predictions, α = 40-deg

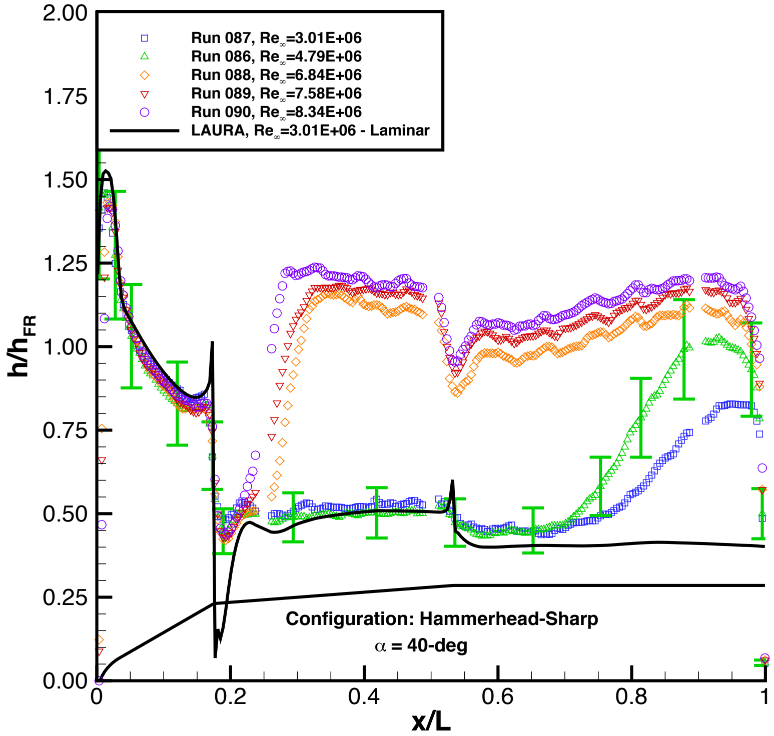

Figure 103. Hammerhead-Sharp Data vs. Laminar Predictions, α = 40-deg

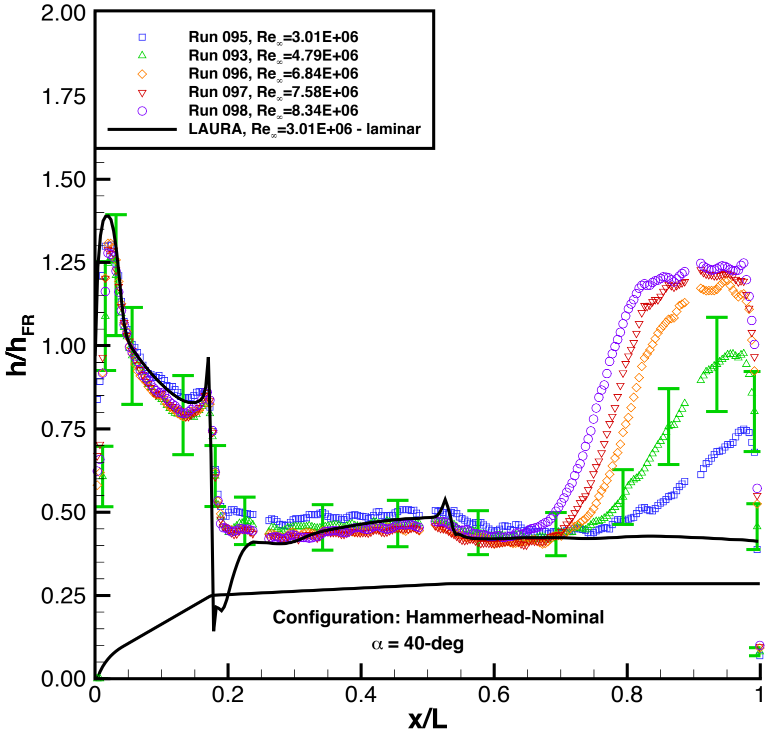

Figure 104. Hammerhead-Nominal Data vs. Laminar Predictions, α = 40-deg

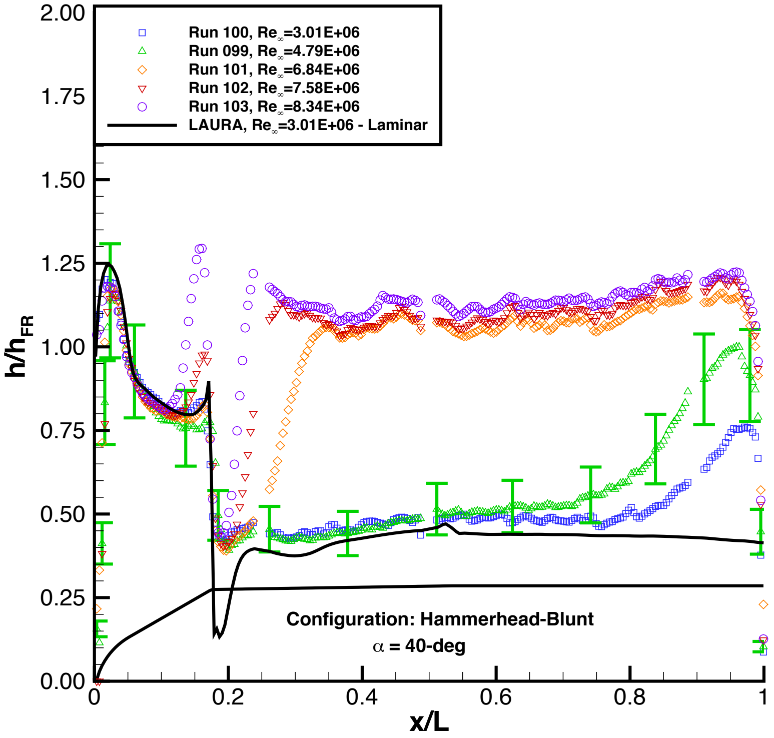

Figure 105. Hammerhead-Blunt Data vs. Laminar Predictions, α = 40-deg

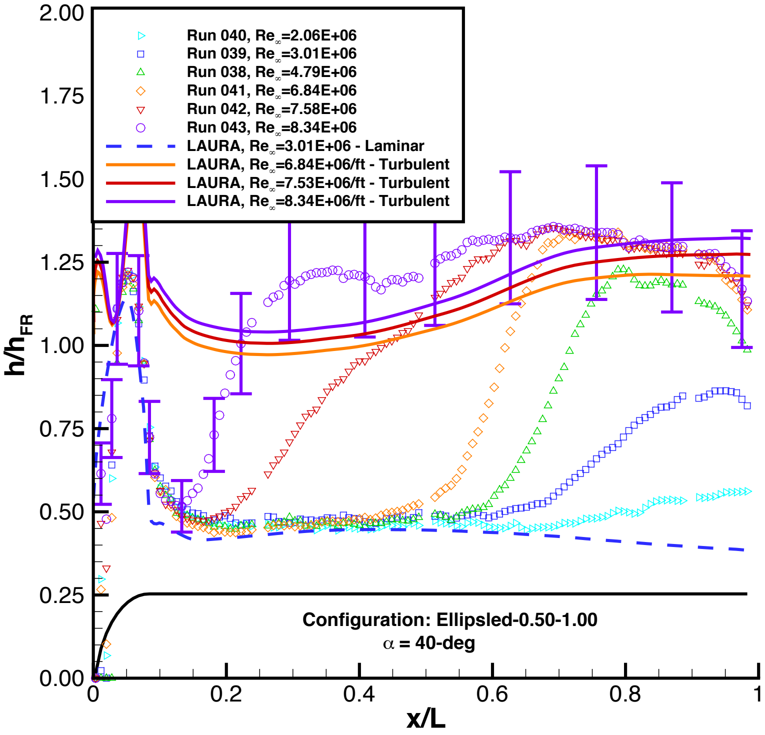

Figure 106. Ellipsled-0.50-1.00 Data vs. Turbulent Predictions, α = 40-deg

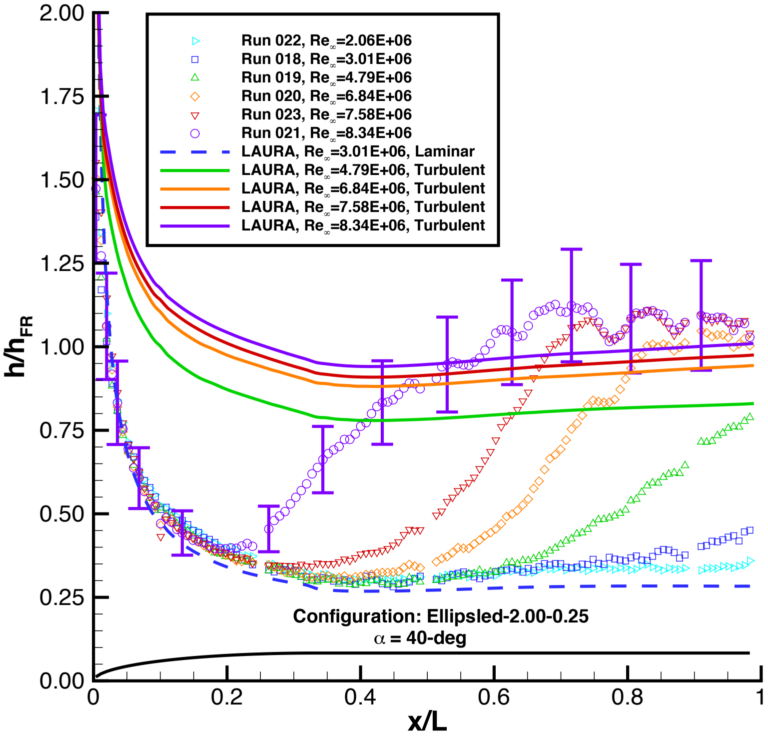

Figure 107. Ellipsled-2.00-0.25 Data vs. Turbulent Predictions, α = 40-deg

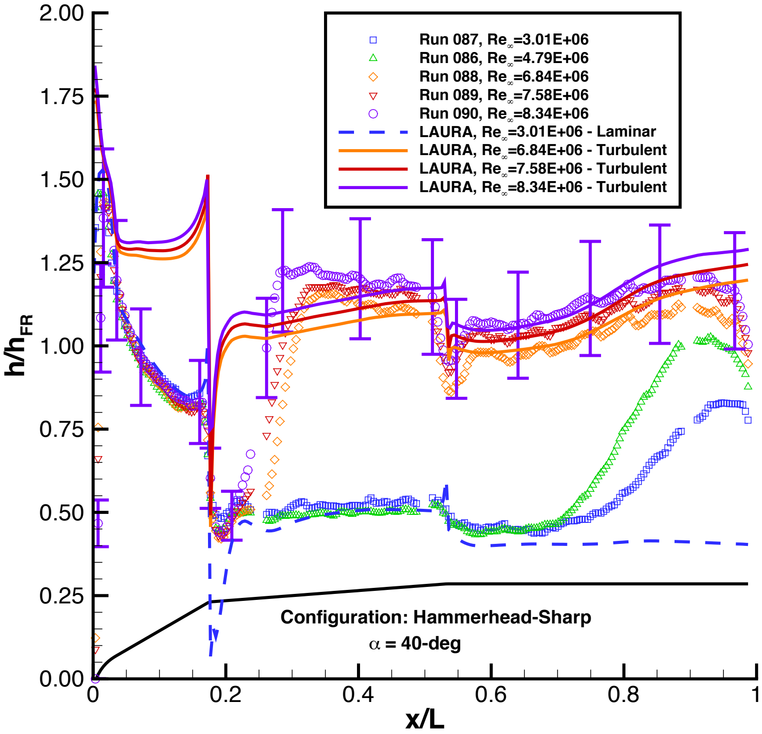

Figure 108. Hammerhead-Sharp Data vs. Turbulent Predictions, α = 40-deg

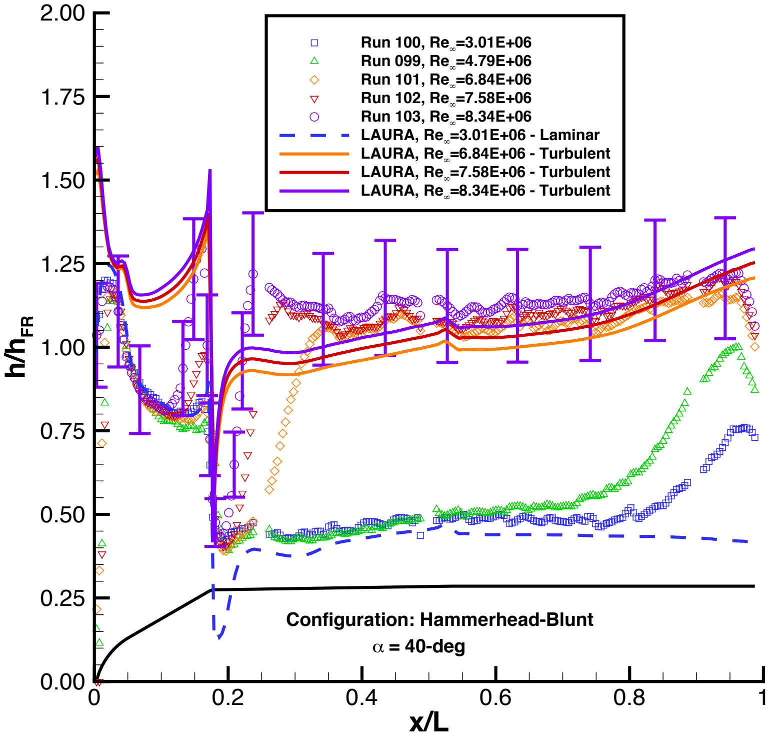

Figure 109. Hammerhead-Blunt Data vs. Turbulent Predictions, α = 40-deg

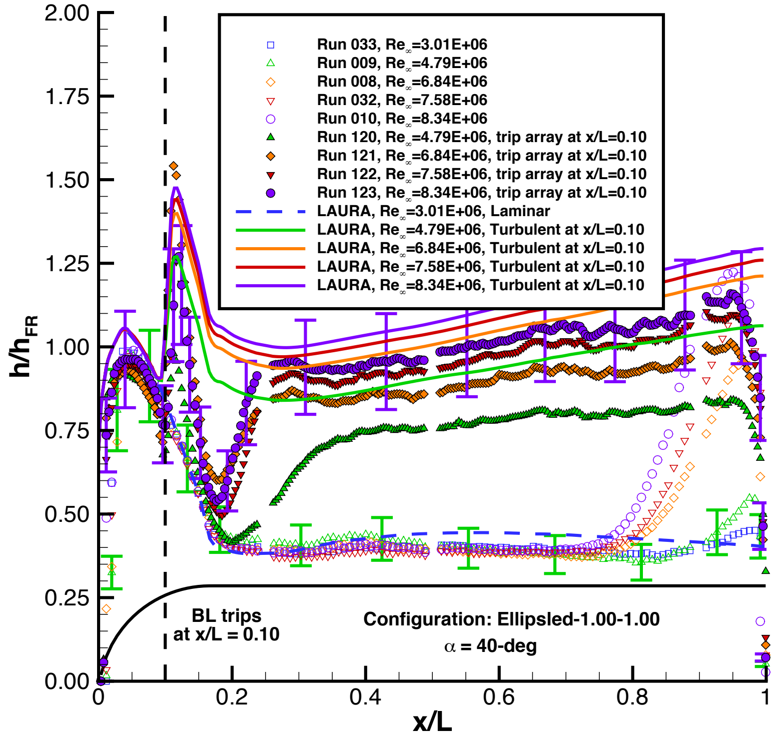

Figure 110. Ellipsled-1.00-1.00 Data vs. Predictions, Tripped at *x*/*L*=0.10 α = 40-deg

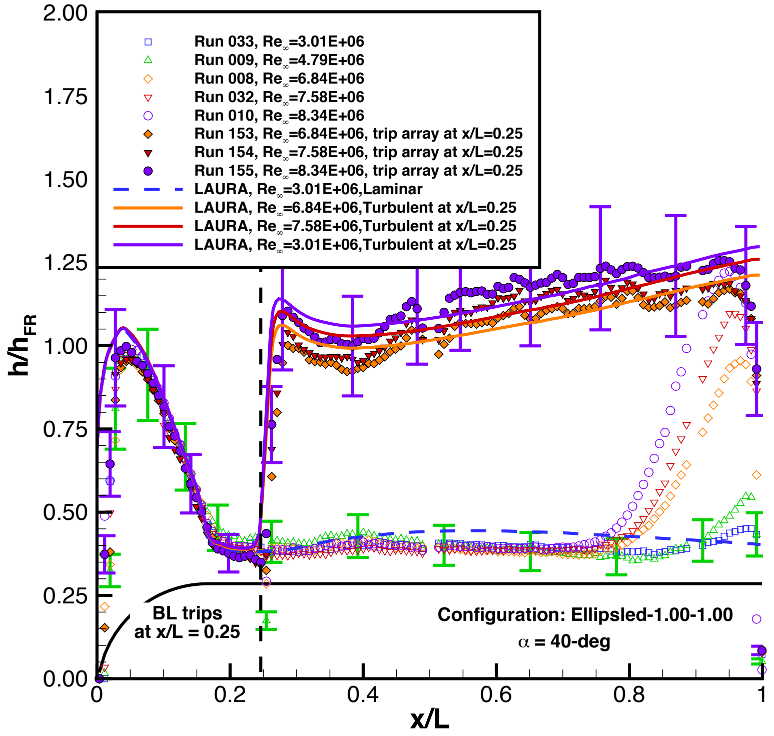

Figure 111. Ellipsled-1.00-1.00 Data vs. Predictions, Tripped at *x*/*L* =0.25 α = 40-deg

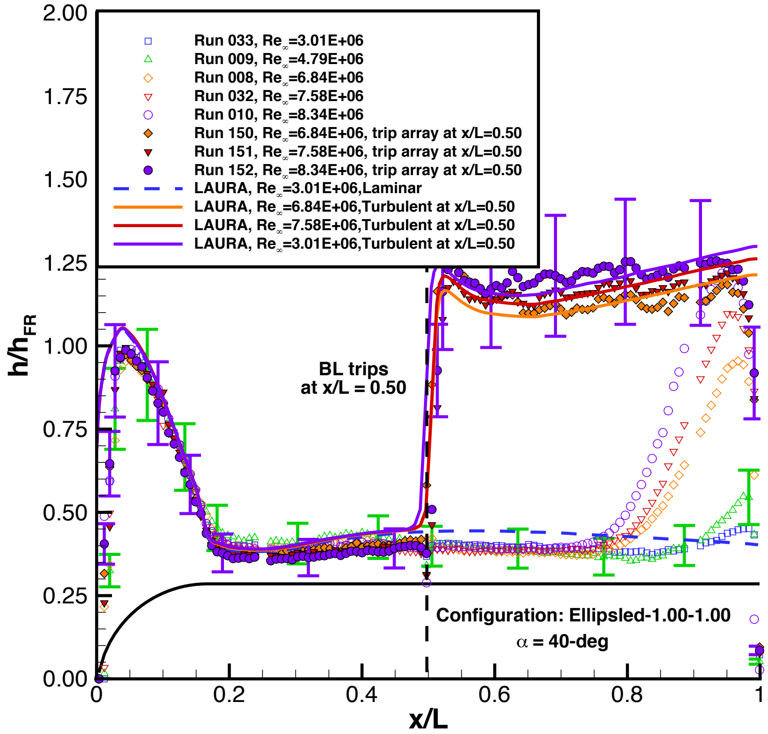

Figure 112. Ellipsled-1.00-1.00 Data vs. Predictions, Tripped at *x*/*L* =0.50 α = 40-deg

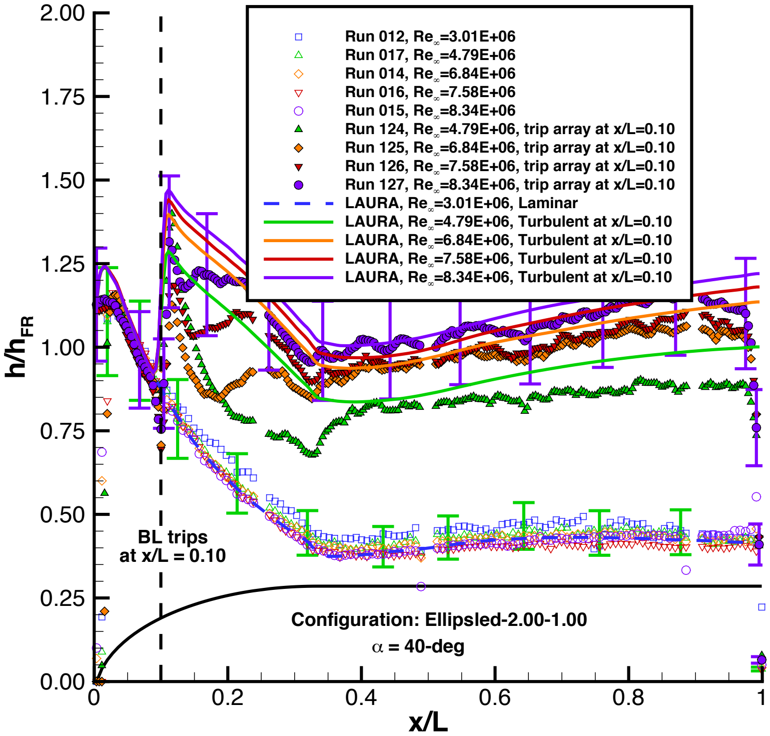

Figure 113. Ellipsled-2.00-1.00 Data vs. Predictions, Tripped at *x*/*L* =0.10 α = 40-deg

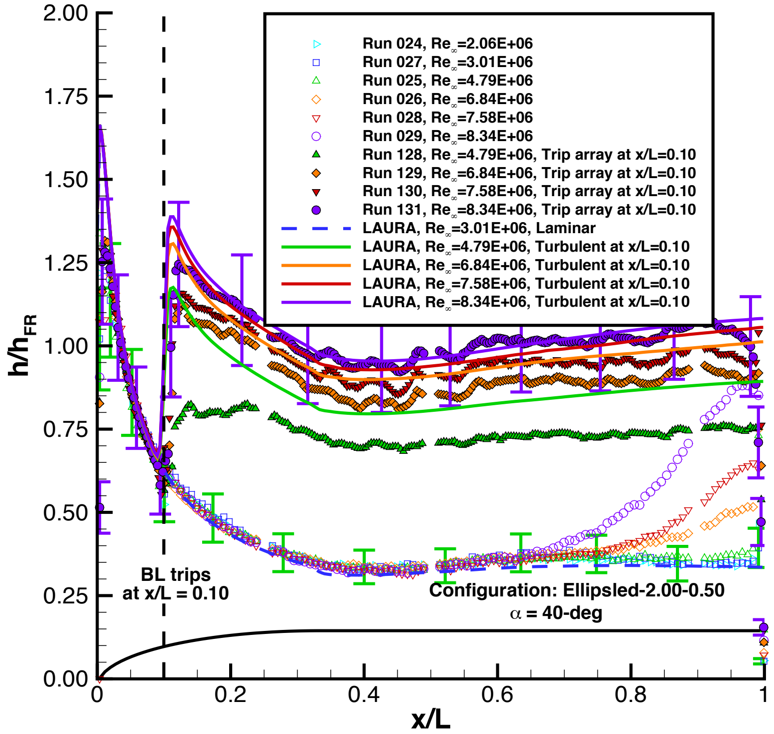

Figure 114. Ellipsled-2.00-0.50 Data vs. Predictions, Tripped at *x*/*L* =0.50 α = 40-deg

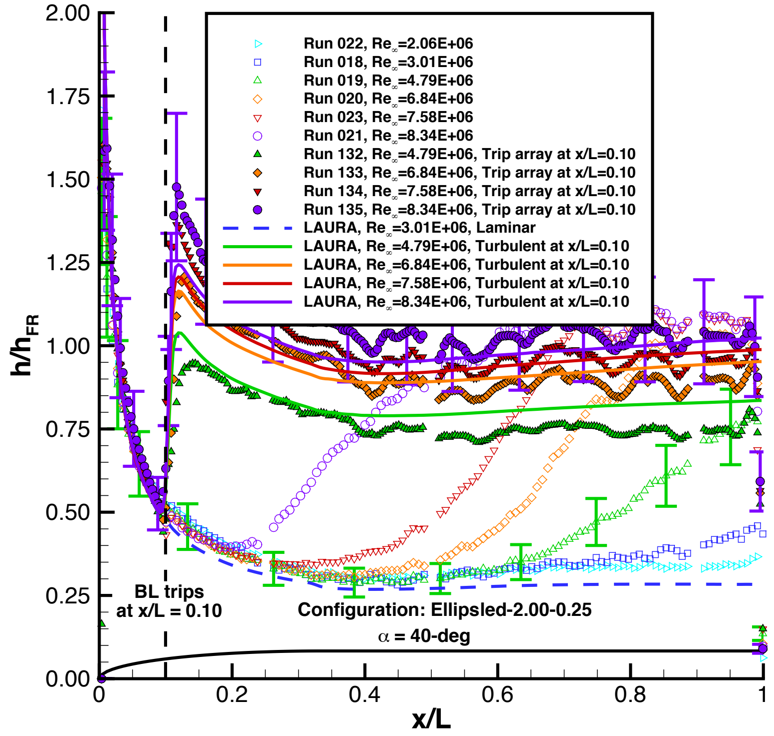

Figure 115. Ellipsled-2.00-0.25 Data vs. Predictions, Tripped at *x*/*L* =0.10 α = 40-deg

Appendix A. Ellipsled Global Image Heating Data

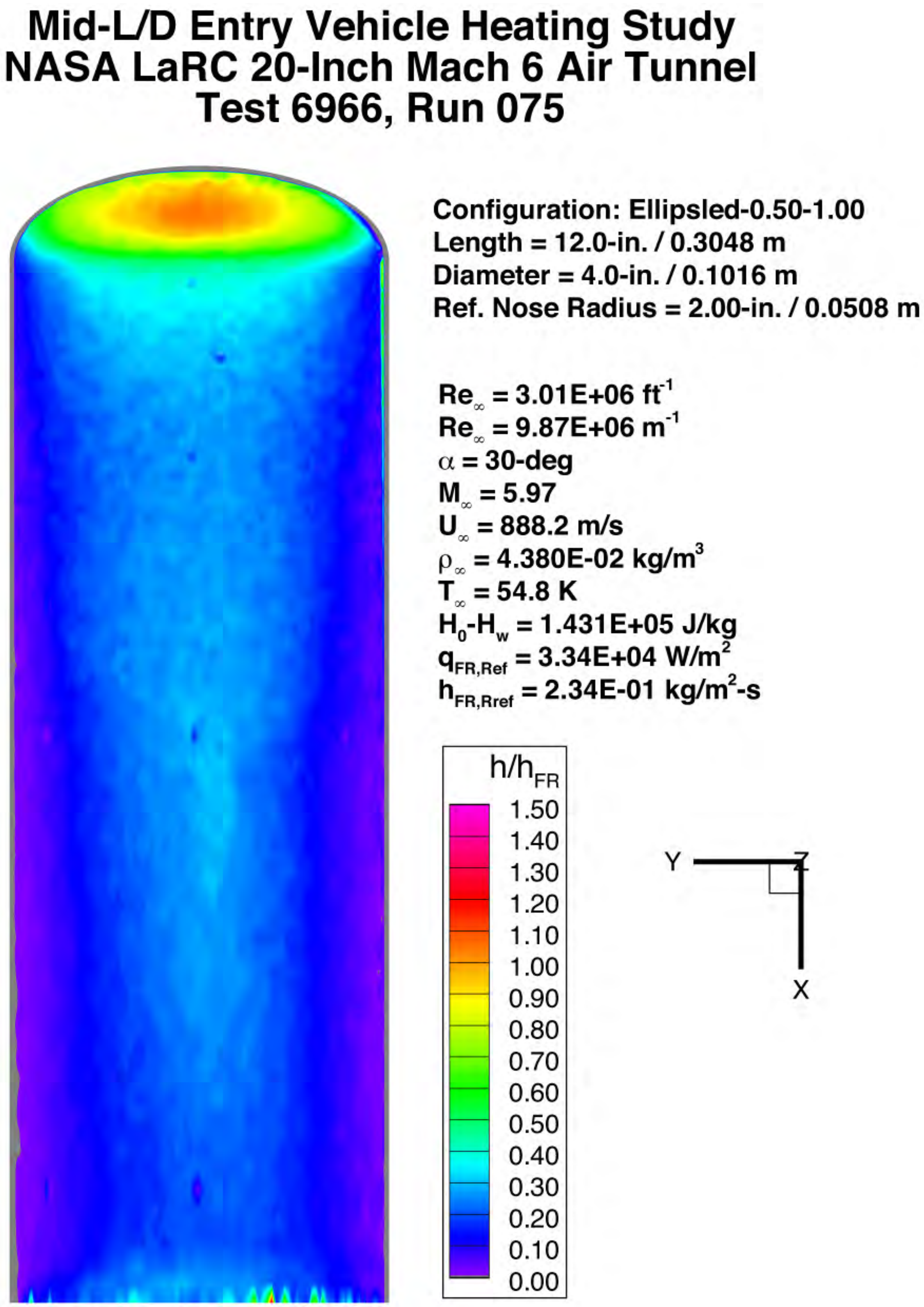

Figure 116. Run 075 Heating Data, Ellipsled-0.50-1.00, Re_∞=3.01×10^6/ft

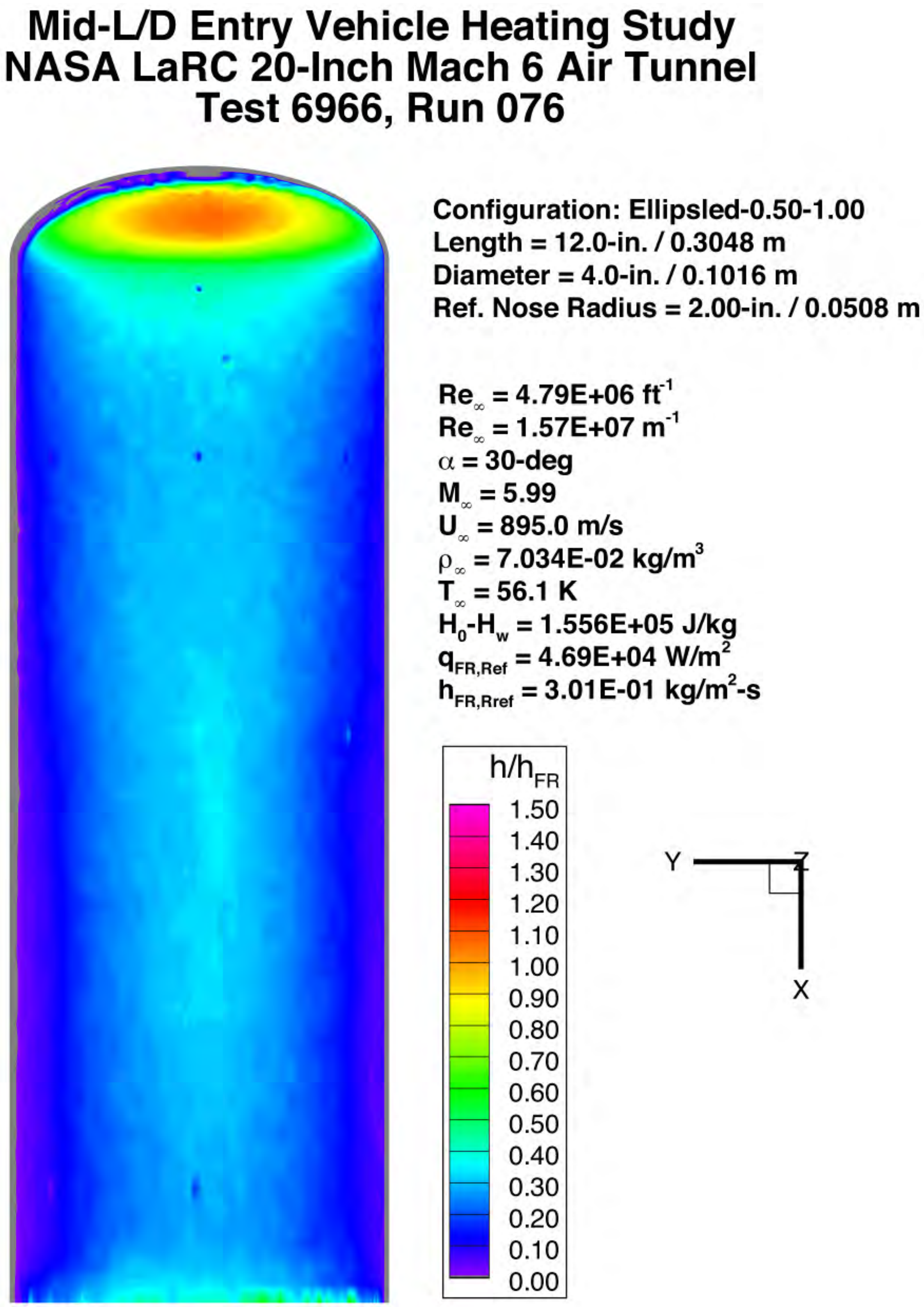

Figure 117. Run 076 Heating Data, Ellipsled-0.50-1.00, Re_∞=4.79×10^6/ft

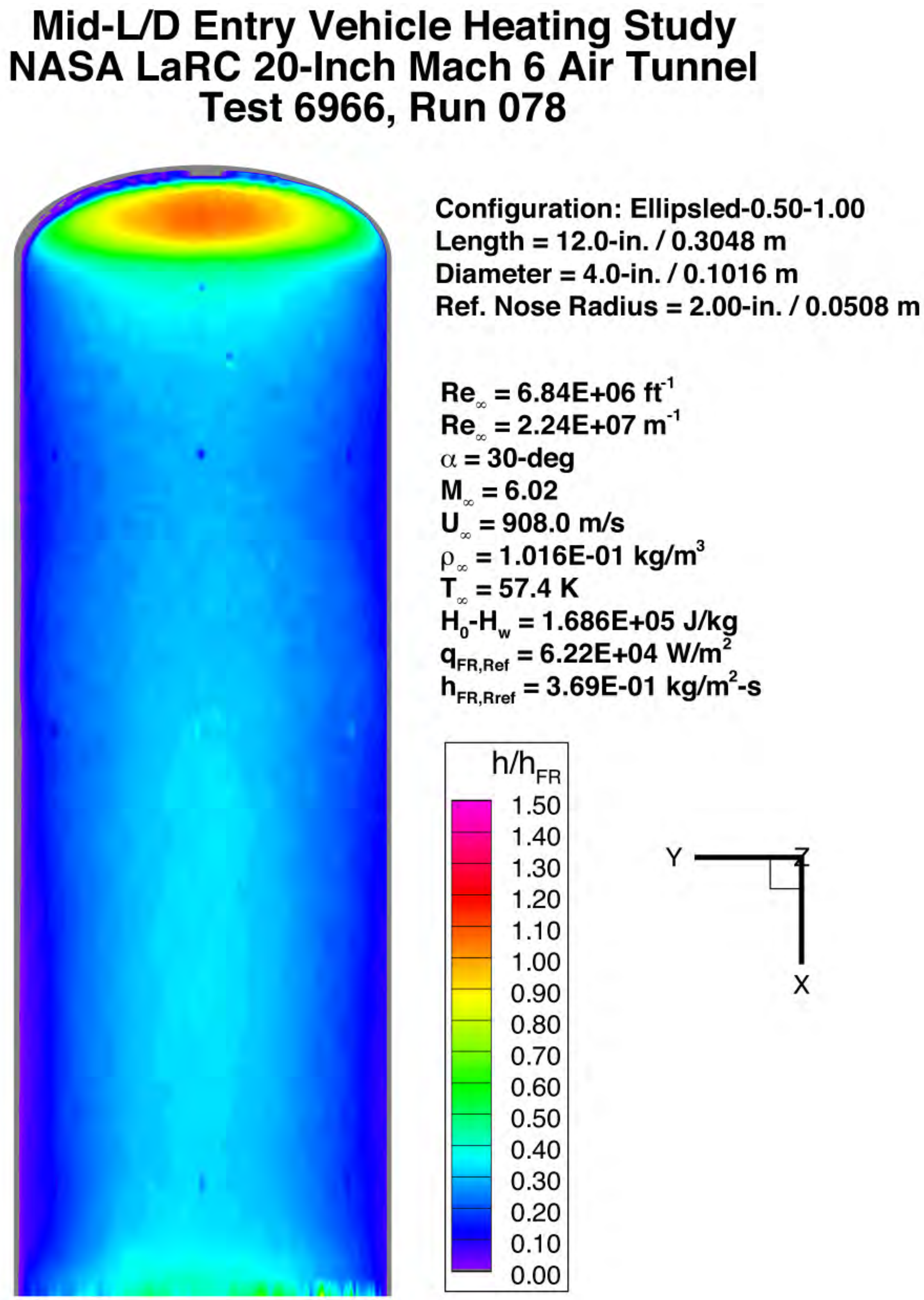

Mid-L/D Entry Vehicle Heating Study
NASA LaRC 20-Inch Mach 6 Air Tunnel
Test 6966, Run 078

Configuration: Ellipsled-0.50-1.00
Length = 12.0-in. / 0.3048 m
Diameter = 4.0-in. / 0.1016 m
Ref. Nose Radius = 2.00-in. / 0.0508 m

Re_∞ = 6.84E+06 ft^{-1}
Re_∞ = 2.24E+07 m^{-1}
α = 30-deg
M_∞ = 6.02
U_∞ = 908.0 m/s
ρ_∞ = 1.016E-01 kg/m^3
T_∞ = 57.4 K
H_0-H_w = 1.686E+05 J/kg
$q_{FR,Ref}$ = 6.22E+04 W/m^2
$h_{FR,Rref}$ = 3.69E-01 kg/m^2-s

Figure 118. Run 078 Heating Data, Ellipsled-0.50-1.00, $Re_\infty=6.84\times10^6$/ft

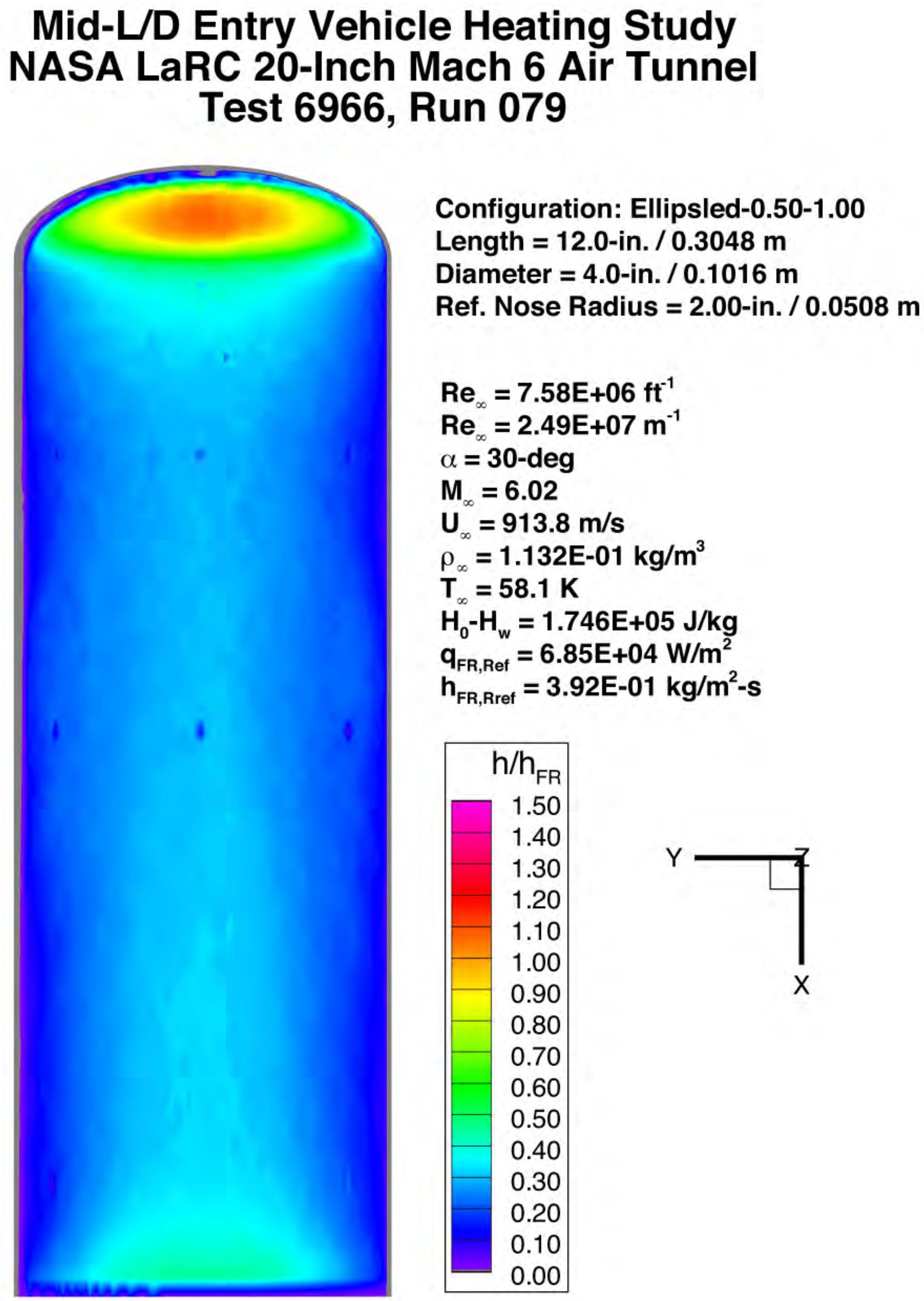

Mid-L/D Entry Vehicle Heating Study
NASA LaRC 20-Inch Mach 6 Air Tunnel
Test 6966, Run 079

Configuration: Ellipsled-0.50-1.00
Length = 12.0-in. / 0.3048 m
Diameter = 4.0-in. / 0.1016 m
Ref. Nose Radius = 2.00-in. / 0.0508 m

Re_∞ = 7.58E+06 ft^{-1}
Re_∞ = 2.49E+07 m^{-1}
α = 30-deg
M_∞ = 6.02
U_∞ = 913.8 m/s
ρ_∞ = 1.132E-01 kg/m^3
T_∞ = 58.1 K
H_0-H_w = 1.746E+05 J/kg
$q_{FR,Ref}$ = 6.85E+04 W/m^2
$h_{FR,Rref}$ = 3.92E-01 kg/m^2-s

Figure 119. Run 079 Heating Data, Ellipsled-0.50-1.00, Re_∞=7.58×10^6/ft

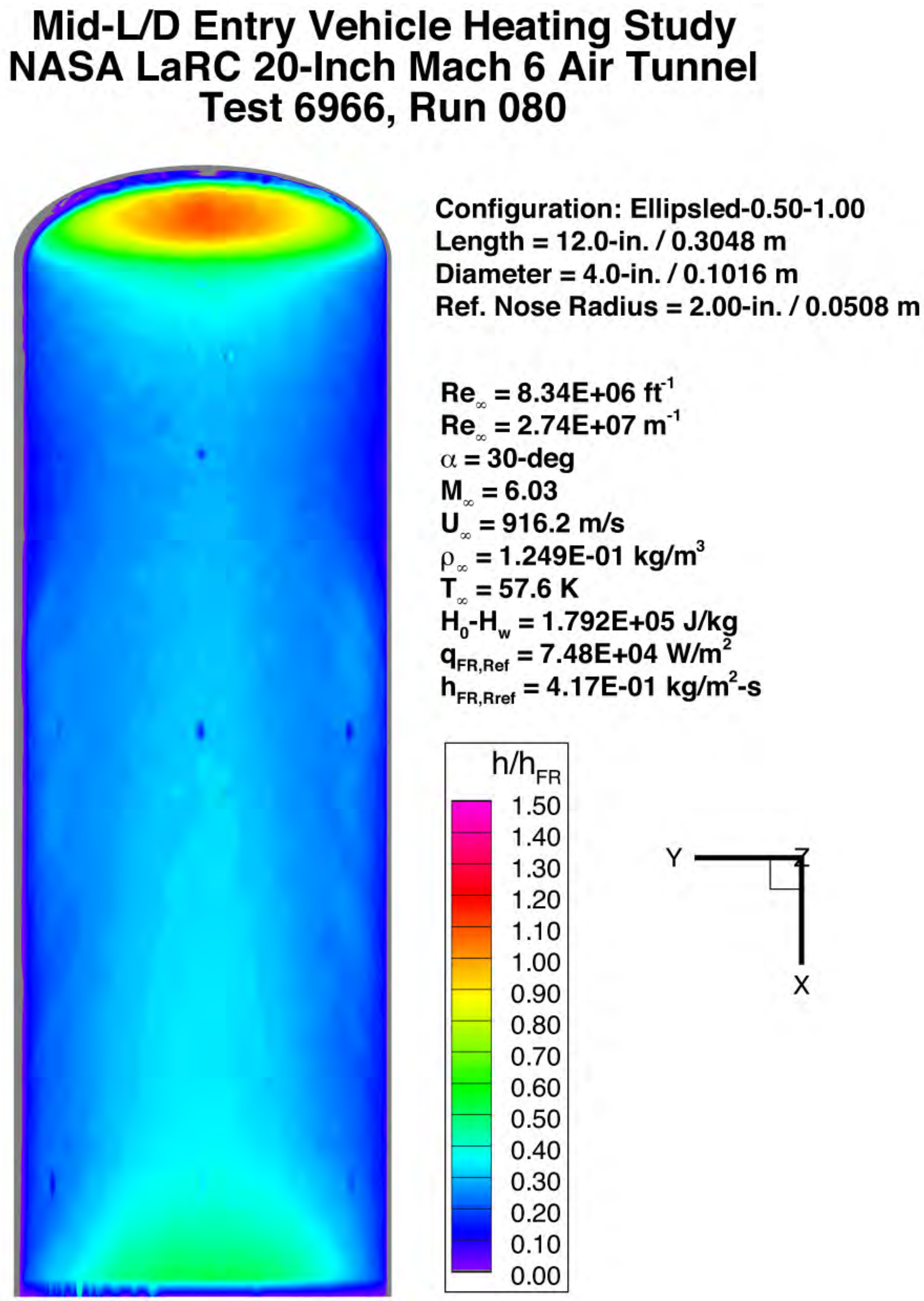

Figure 120. Run 080 Heating Data, Ellipsled-0.50-1.00, $Re_\infty=8.34\times10^6$/ft

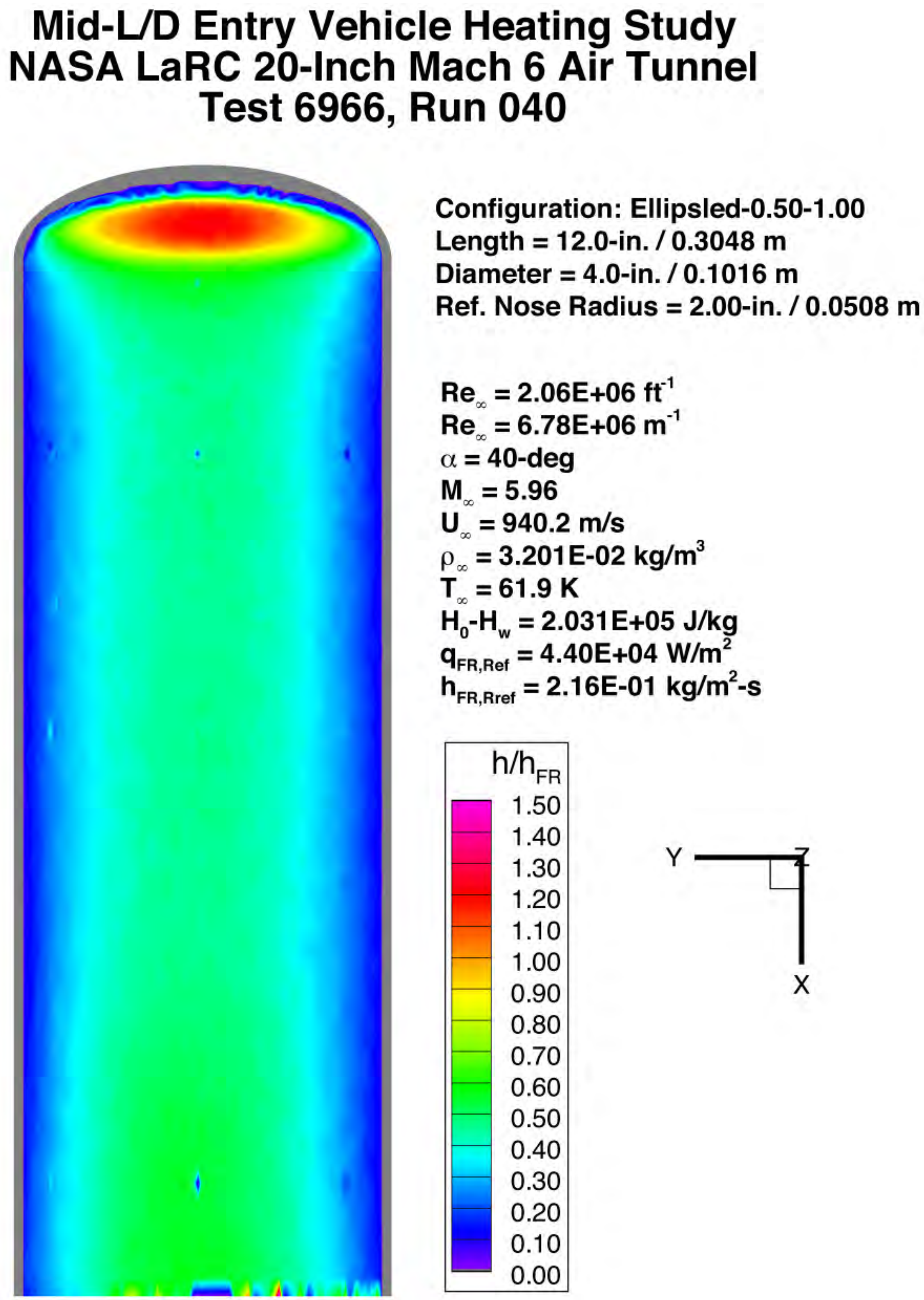

Figure 121. Run 040 Heating Data, Ellipsled-0.50-1.00, Re_∞=2.06×10^6/ft

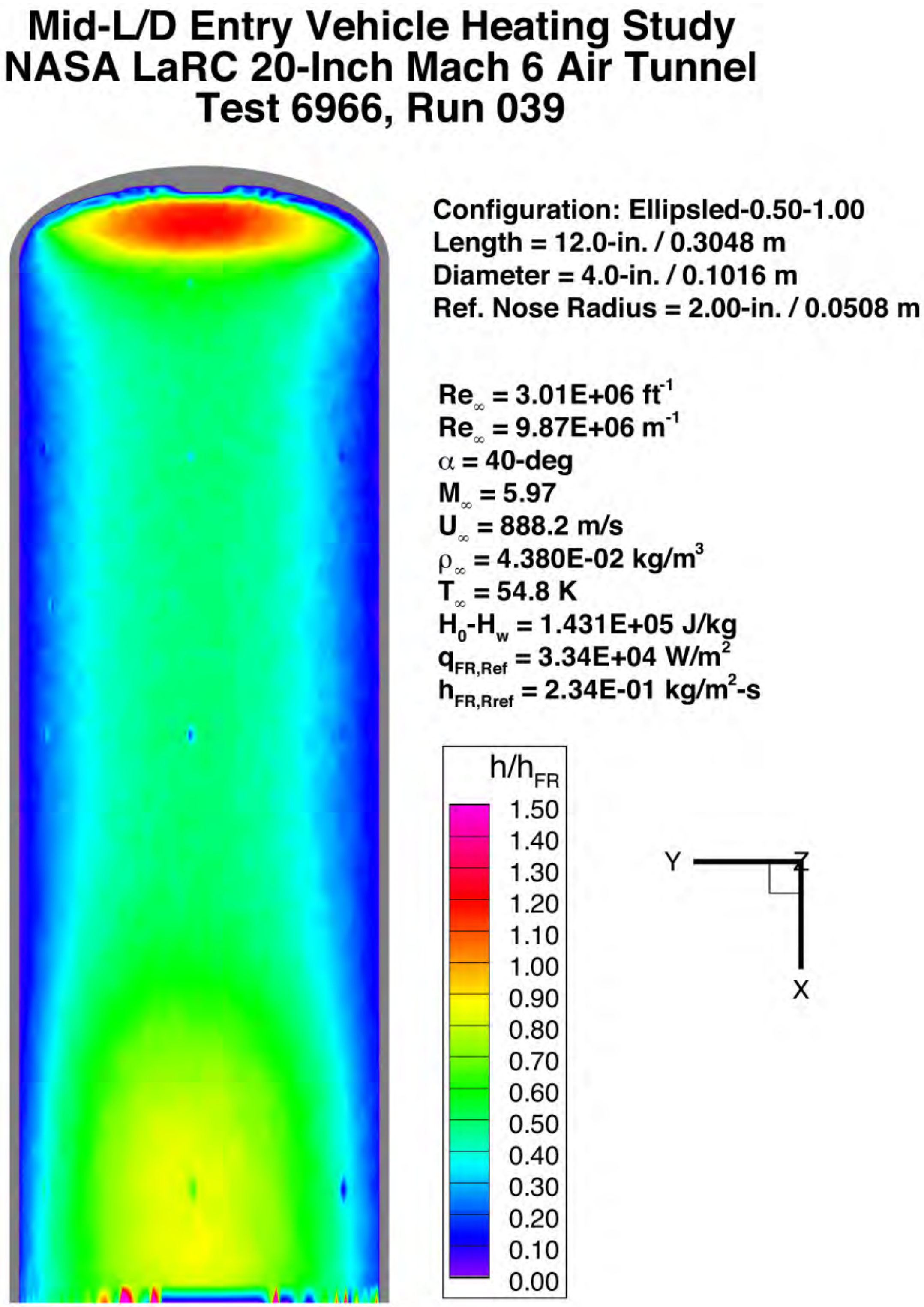

Figure 122. Run 039 Heating Data, Ellipsled-0.50-1.00, Re_∞=3.01×10^6/ft

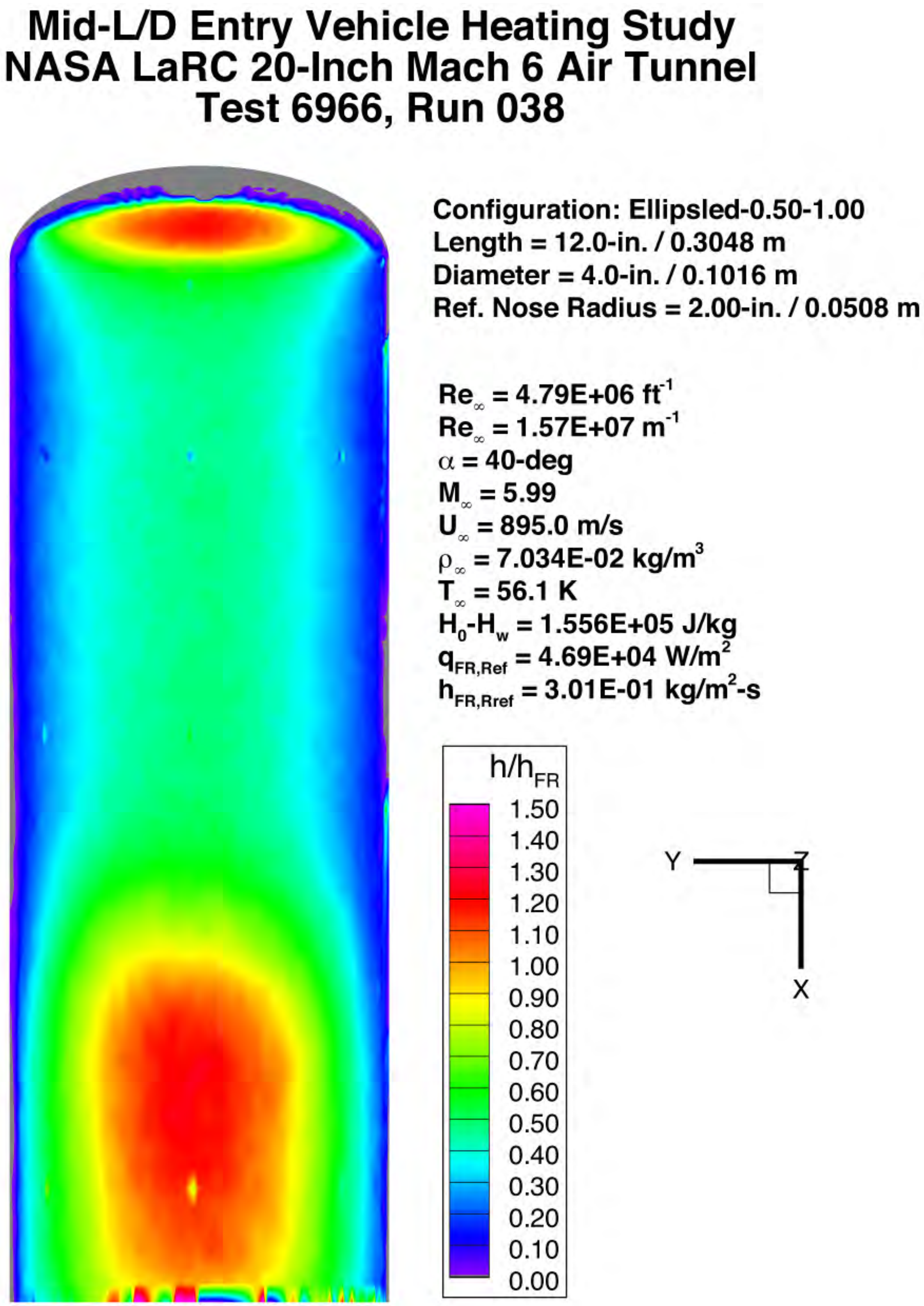

Figure 123. Run 038 Heating Data, Ellipsled-0.50-1.00, Re_∞=4.79×10^6/ft

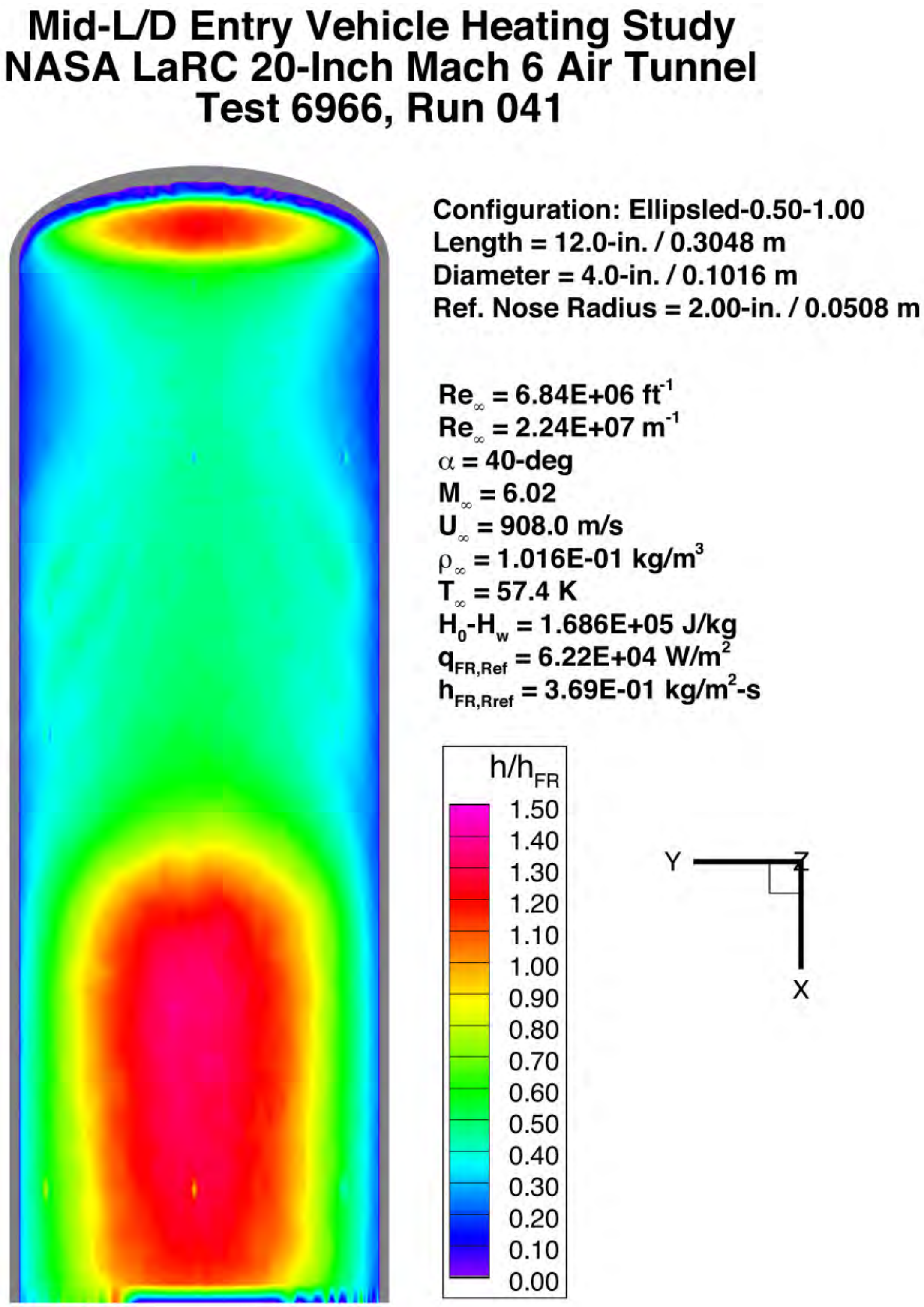

Figure 124. Run 041 Heating Data, Ellipsled-0.50-1.00, Re$_\infty$=6.84×10^6/ft

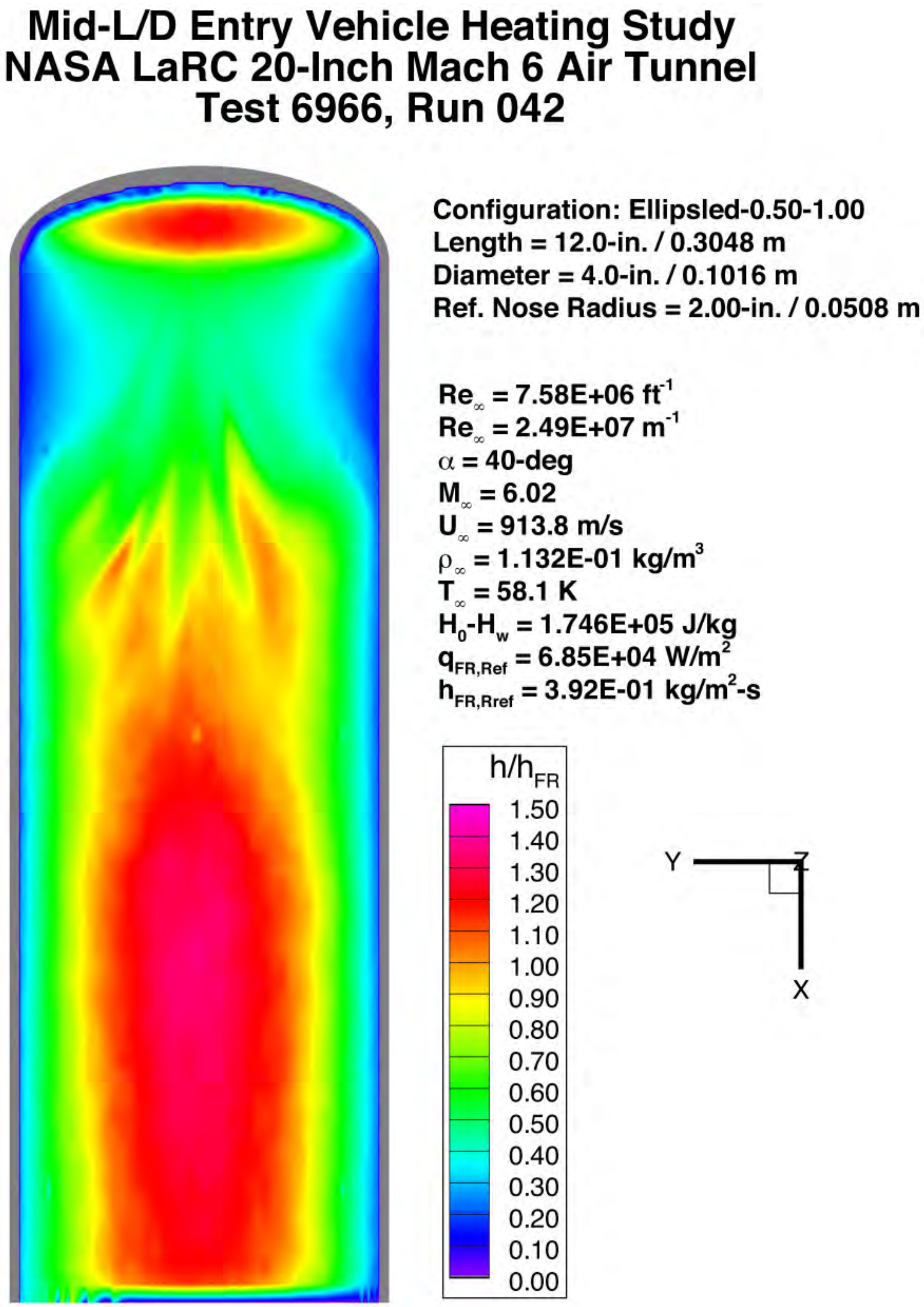

Figure 125. Run 042 Heating Data, Ellipsled-0.50-1.00, Re_∞=7.58×10^6/ft

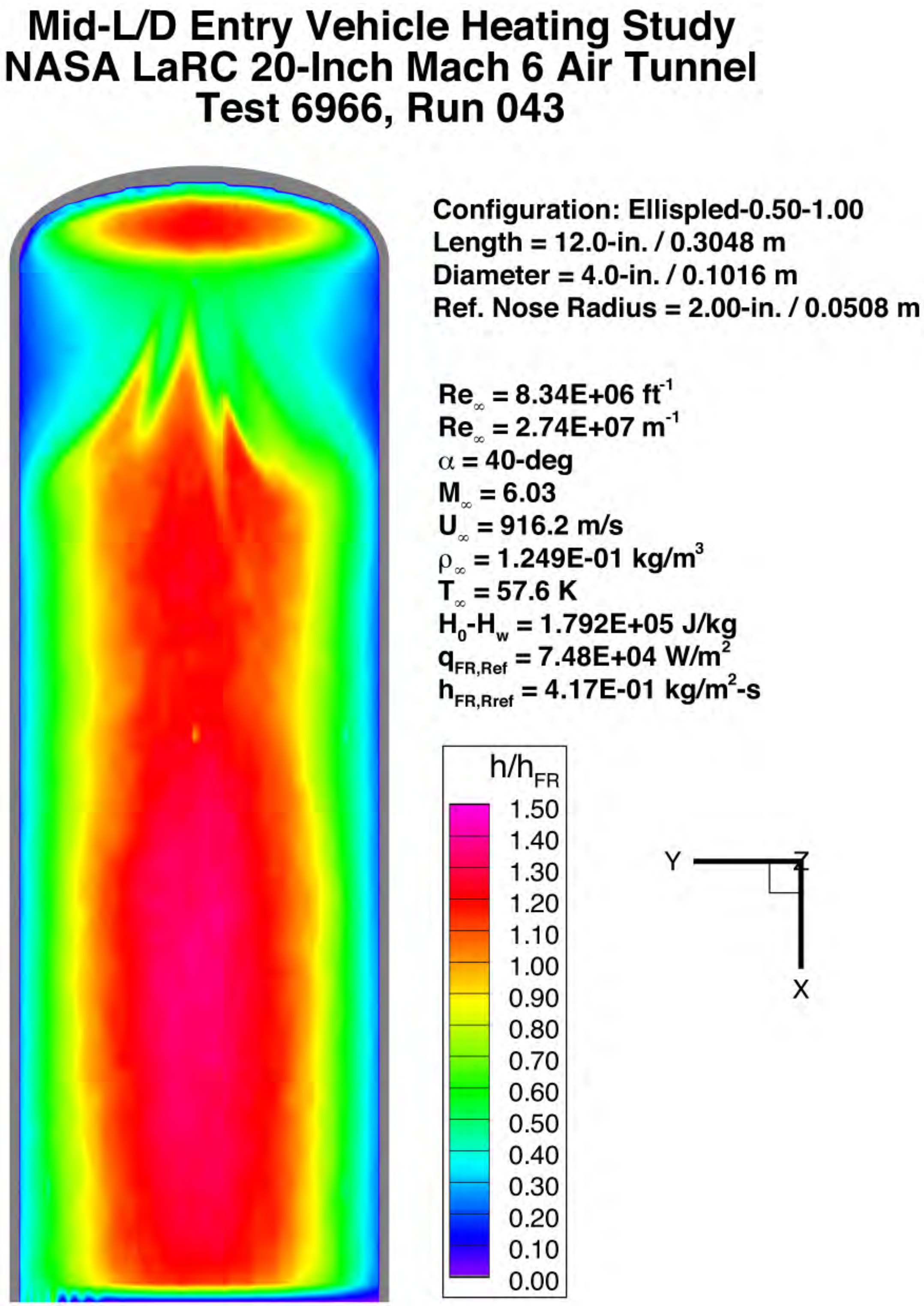

Figure 126. Run 043 Heating Data, Ellipsled-0.50-1.00, Re_∞=8.34×10^6/ft

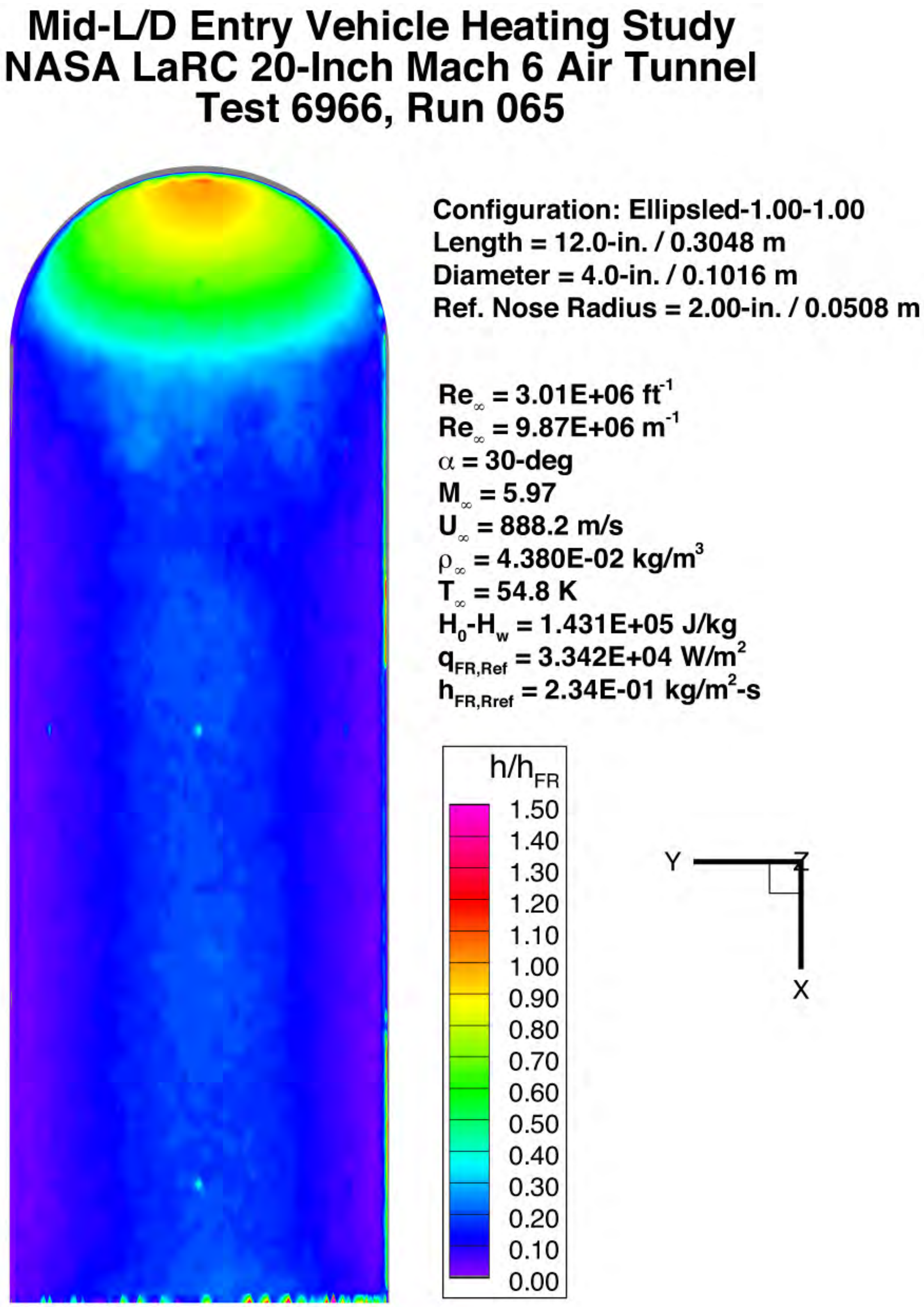

Figure 127. Run 065 Heating Data, Ellipsled-1.00-1.00, $Re_\infty=3.01\times10^6$/ft

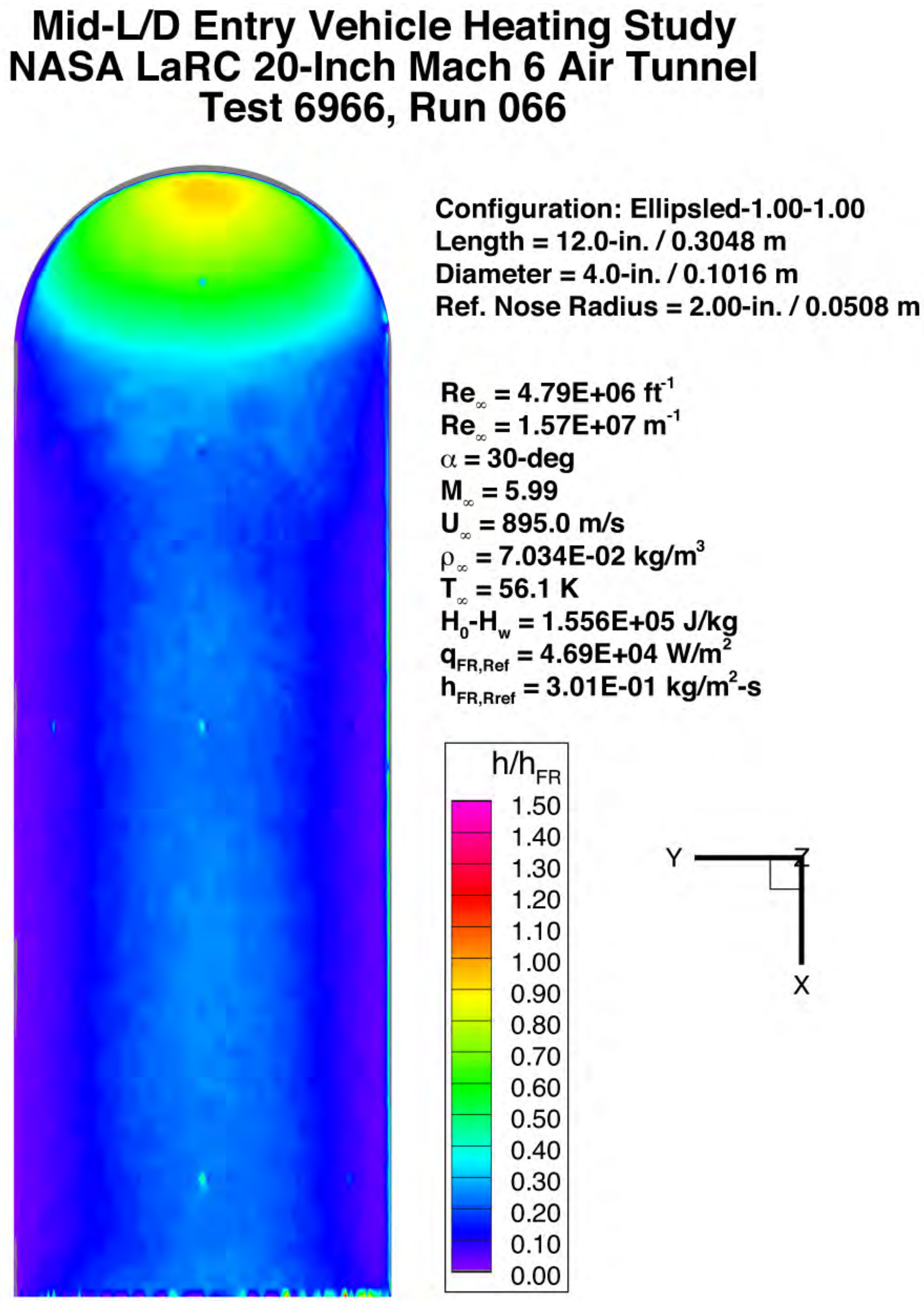

Figure 128. Run 066 Heating Data, Ellipsled-1.00-1.00, Re_∞=4.79×10^6/ft

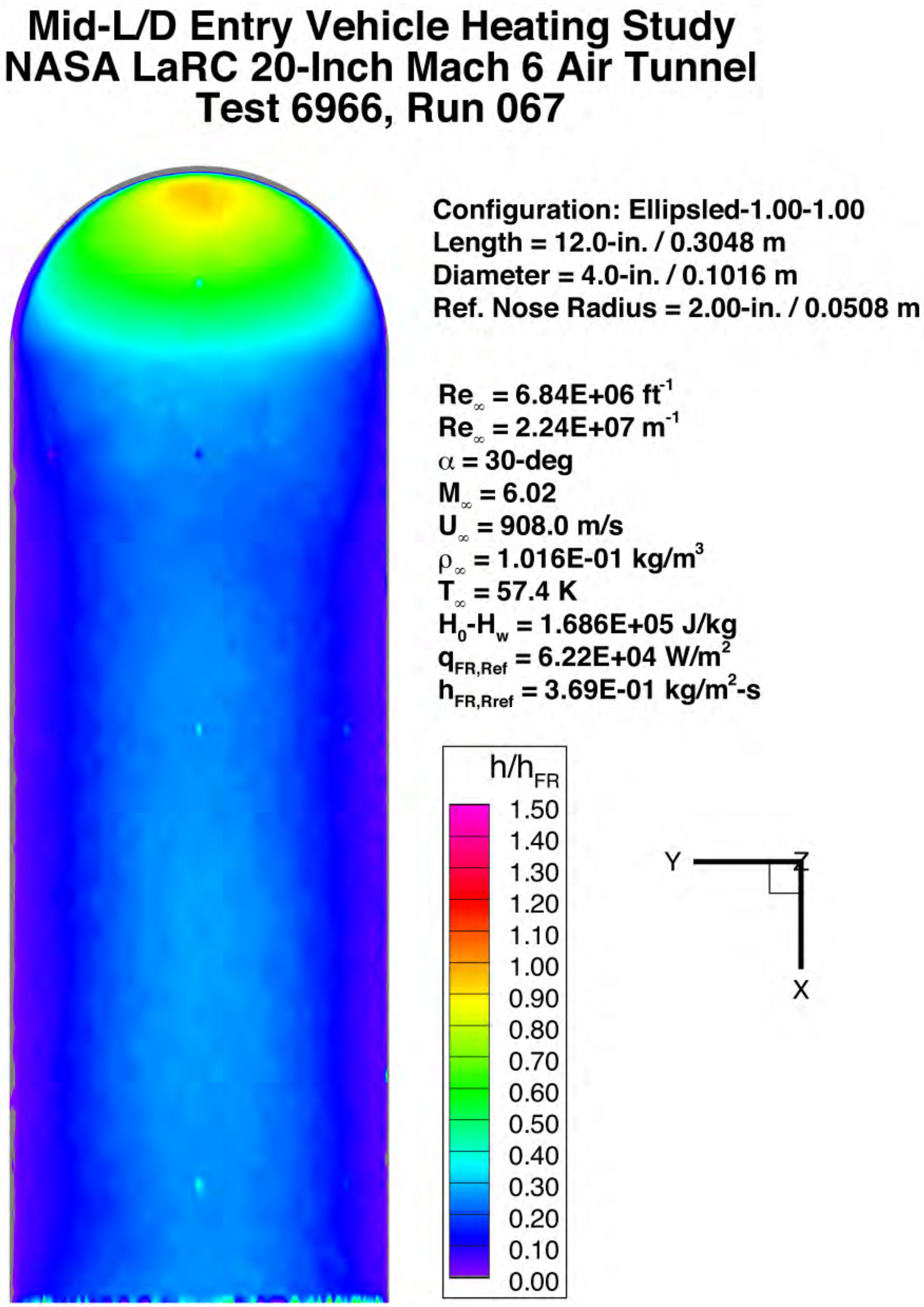

Figure 129. Run 067 Heating Data, Ellipsled-1.00-1.00, Re_∞=6.84×10^6/ft

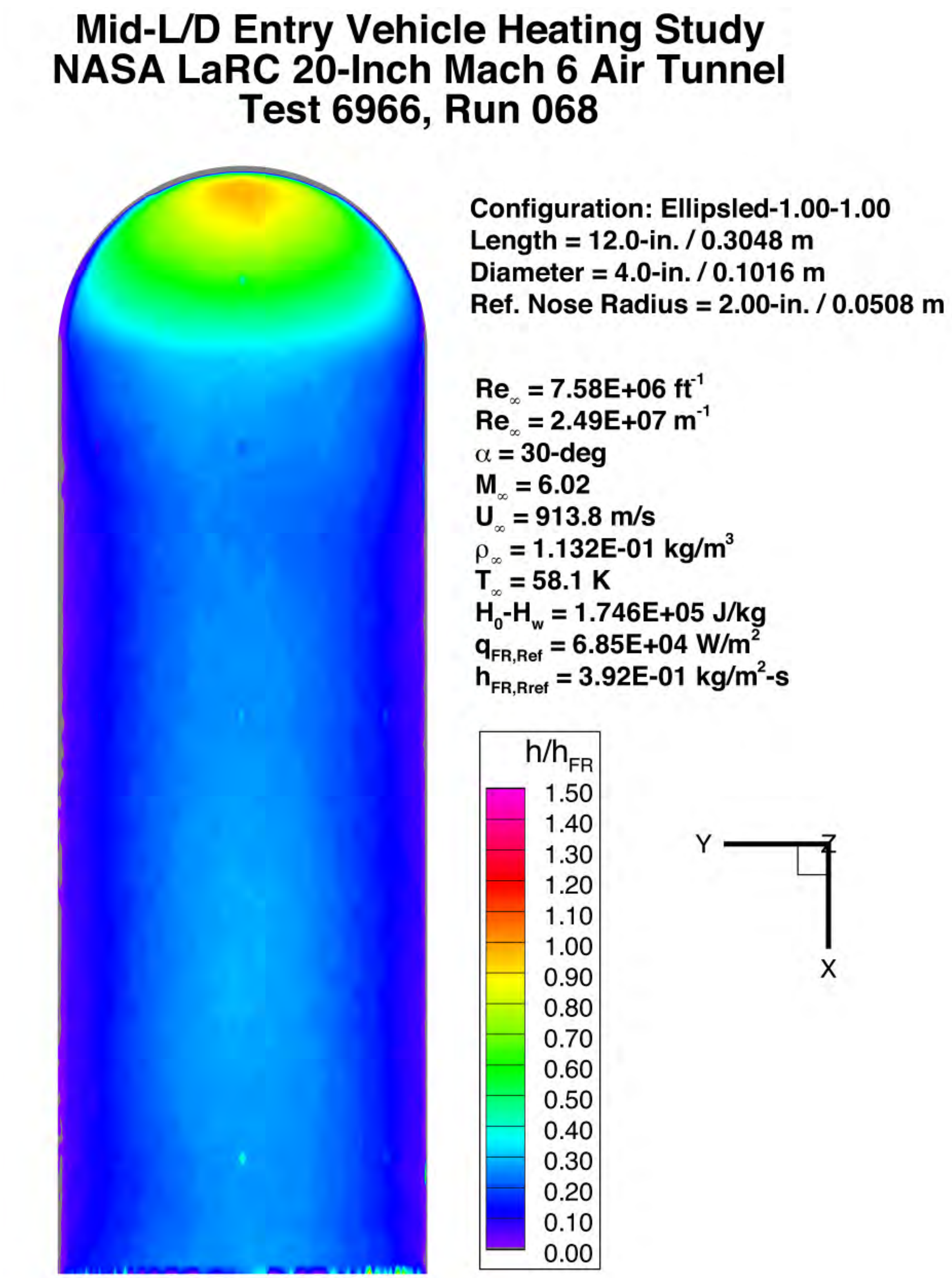

Figure 130. Run 068 Heating Data, Ellipsled-1.00-1.00, Re_∞=7.58×10^6/ft

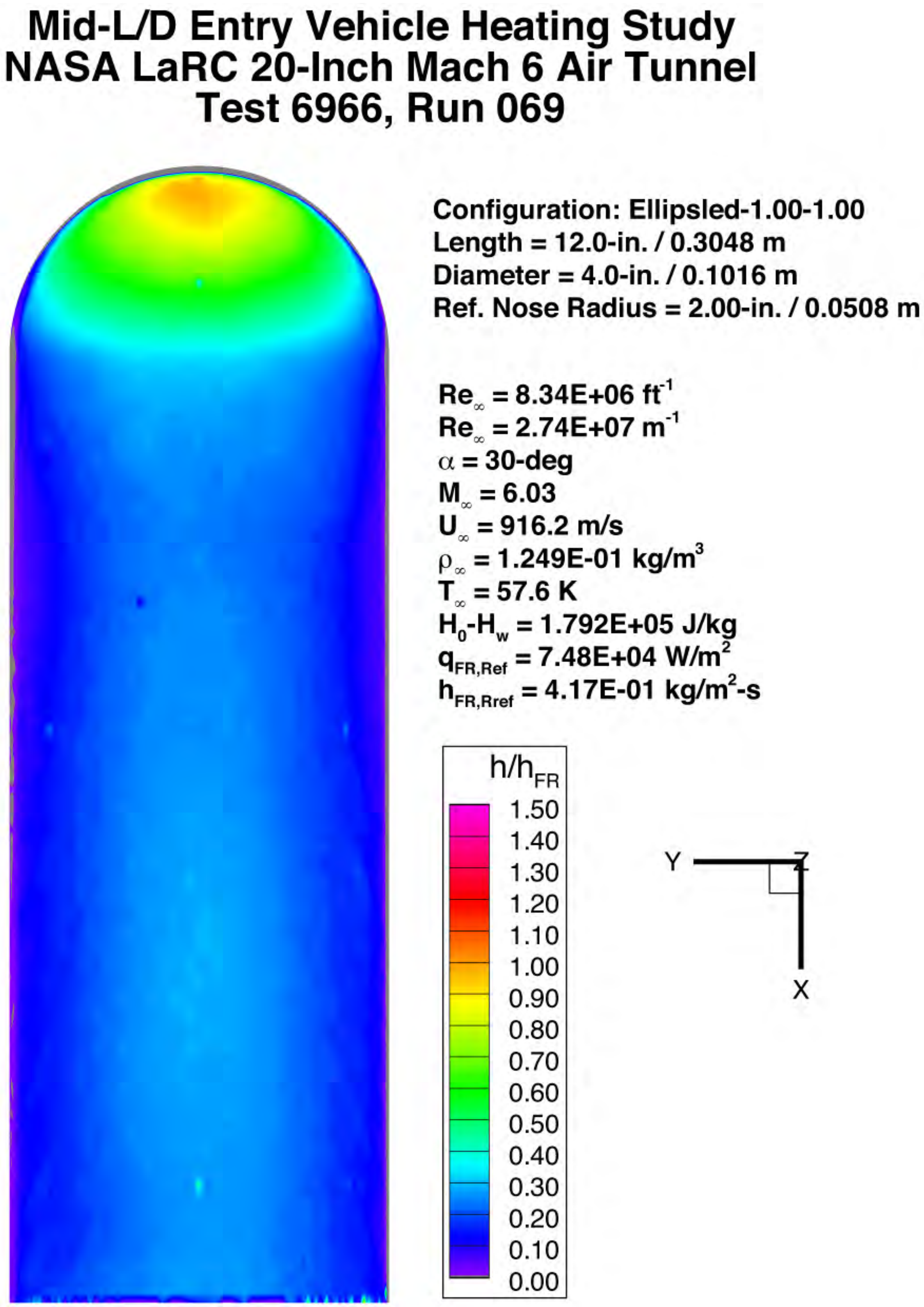

Figure 131. Run 069 Heating Data, Ellipsled-1.00-1.00, Re_∞=8.34×10^6/ft

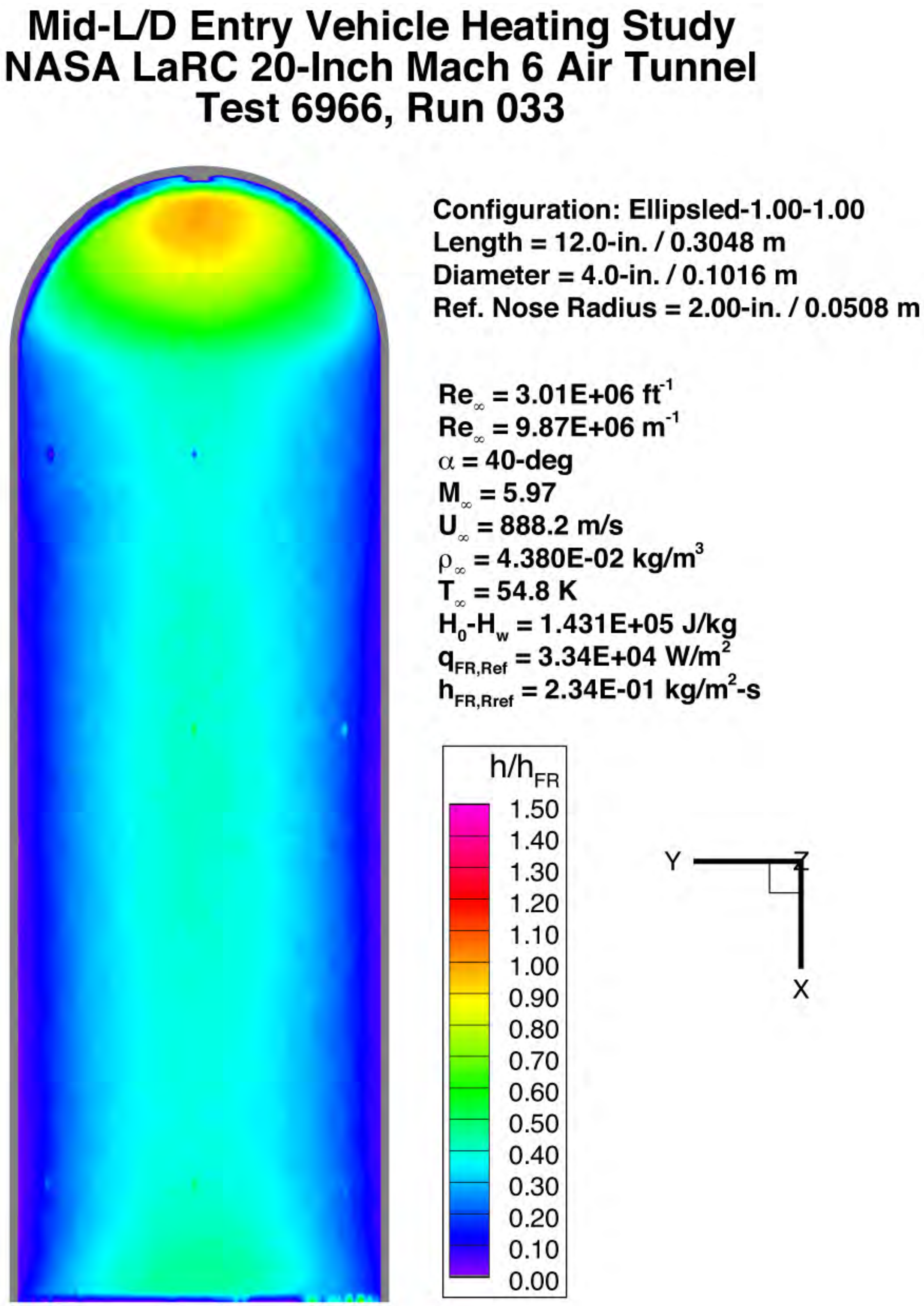

Figure 132. Run 033 Heating Data, Ellipsled-1.00-1.00, Re_∞=3.01×10^6/ft

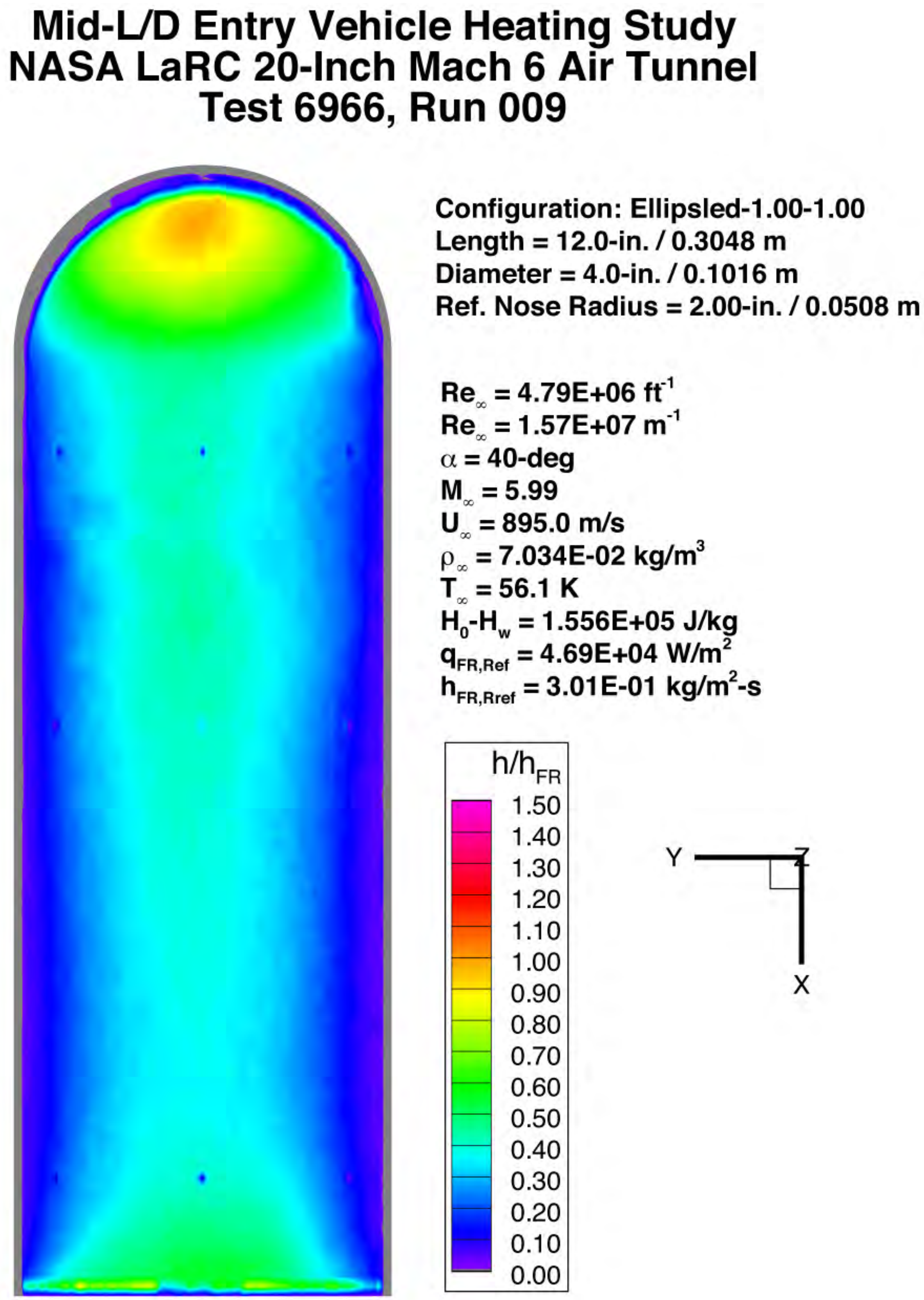

Figure 133. Run 009 Heating Data, Ellipsled-1.00-1.00, $Re_\infty=4.79\times10^6$/ft

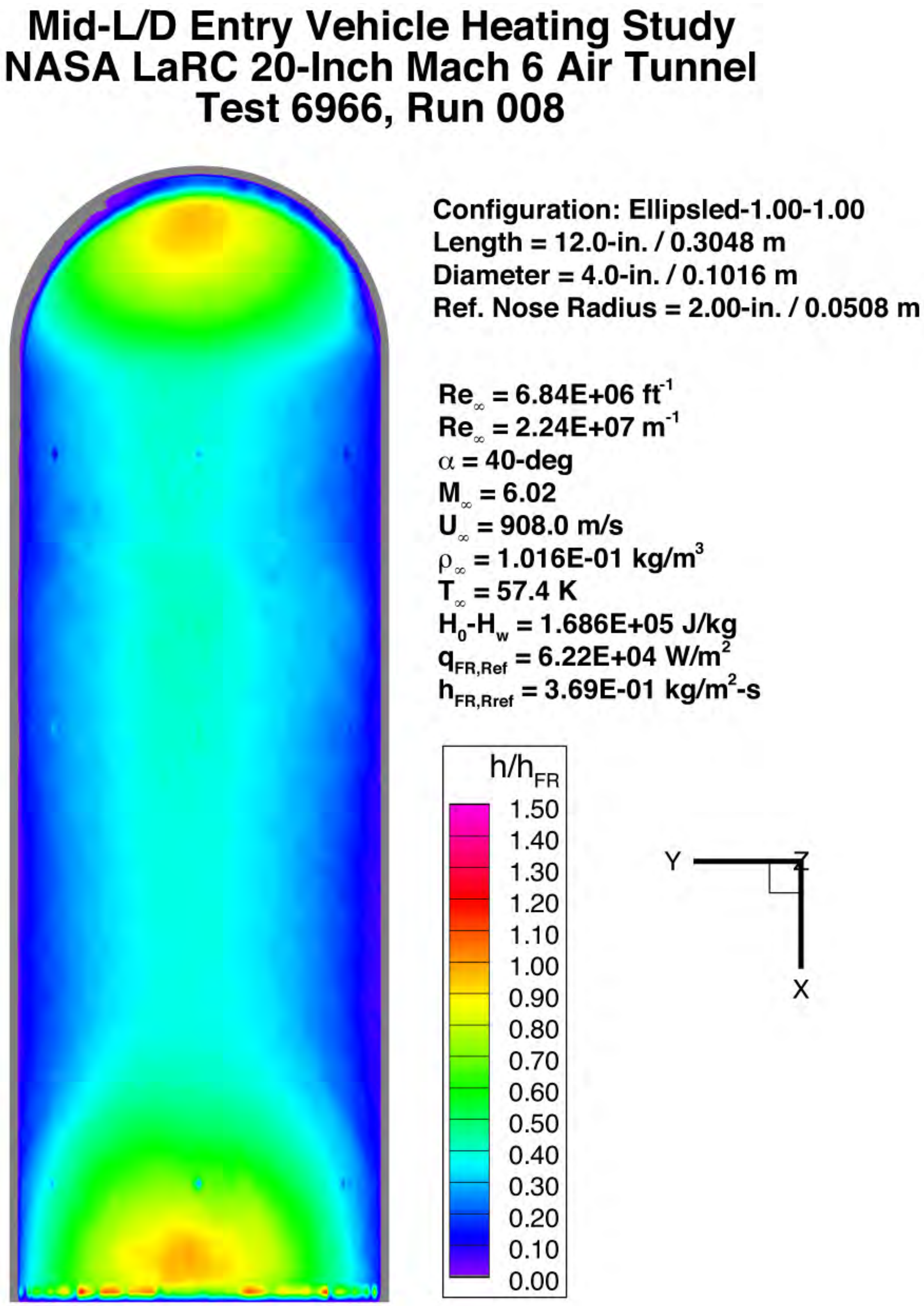

Figure 134. Run 008 Heating Data, Ellipsled-1.00-1.00, Re_∞=6.84×10^6/ft

Mid-L/D Entry Vehicle Heating Study
NASA LaRC 20-Inch Mach 6 Air Tunnel
Test 6966, Run 032

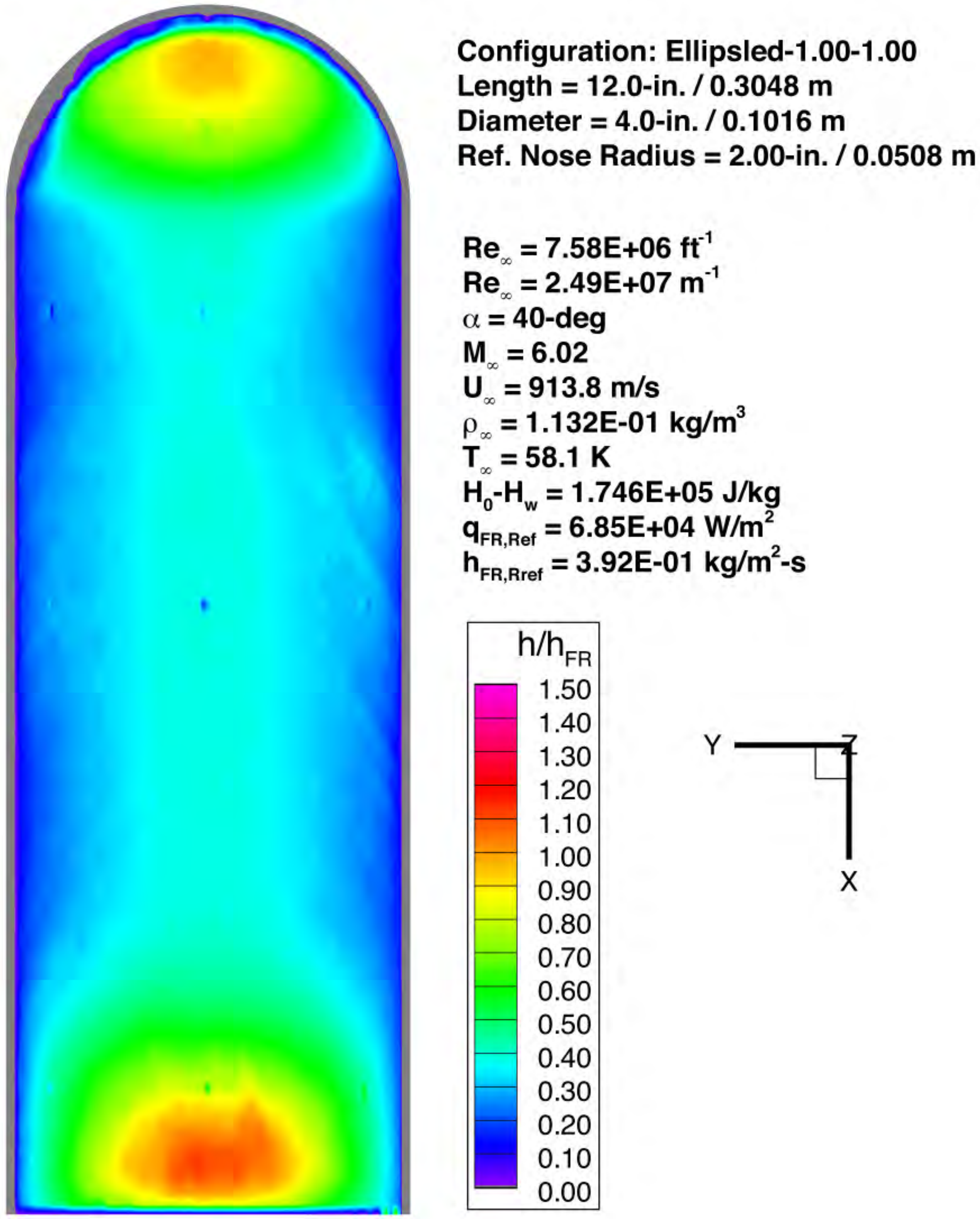

Configuration: Ellipsled-1.00-1.00
Length = 12.0-in. / 0.3048 m
Diameter = 4.0-in. / 0.1016 m
Ref. Nose Radius = 2.00-in. / 0.0508 m

$Re_\infty = 7.58E{+}06\ ft^{-1}$
$Re_\infty = 2.49E{+}07\ m^{-1}$
$\alpha = 40\text{-deg}$
$M_\infty = 6.02$
$U_\infty = 913.8\ m/s$
$\rho_\infty = 1.132E{-}01\ kg/m^3$
$T_\infty = 58.1\ K$
$H_0\text{-}H_w = 1.746E{+}05\ J/kg$
$q_{FR,Ref} = 6.85E{+}04\ W/m^2$
$h_{FR,Rref} = 3.92E{-}01\ kg/m^2\text{-}s$

Figure 135. Run 032 Heating Data, Ellipsled-1.00-1.00, $Re_\infty = 7.58\times10^6$/ft

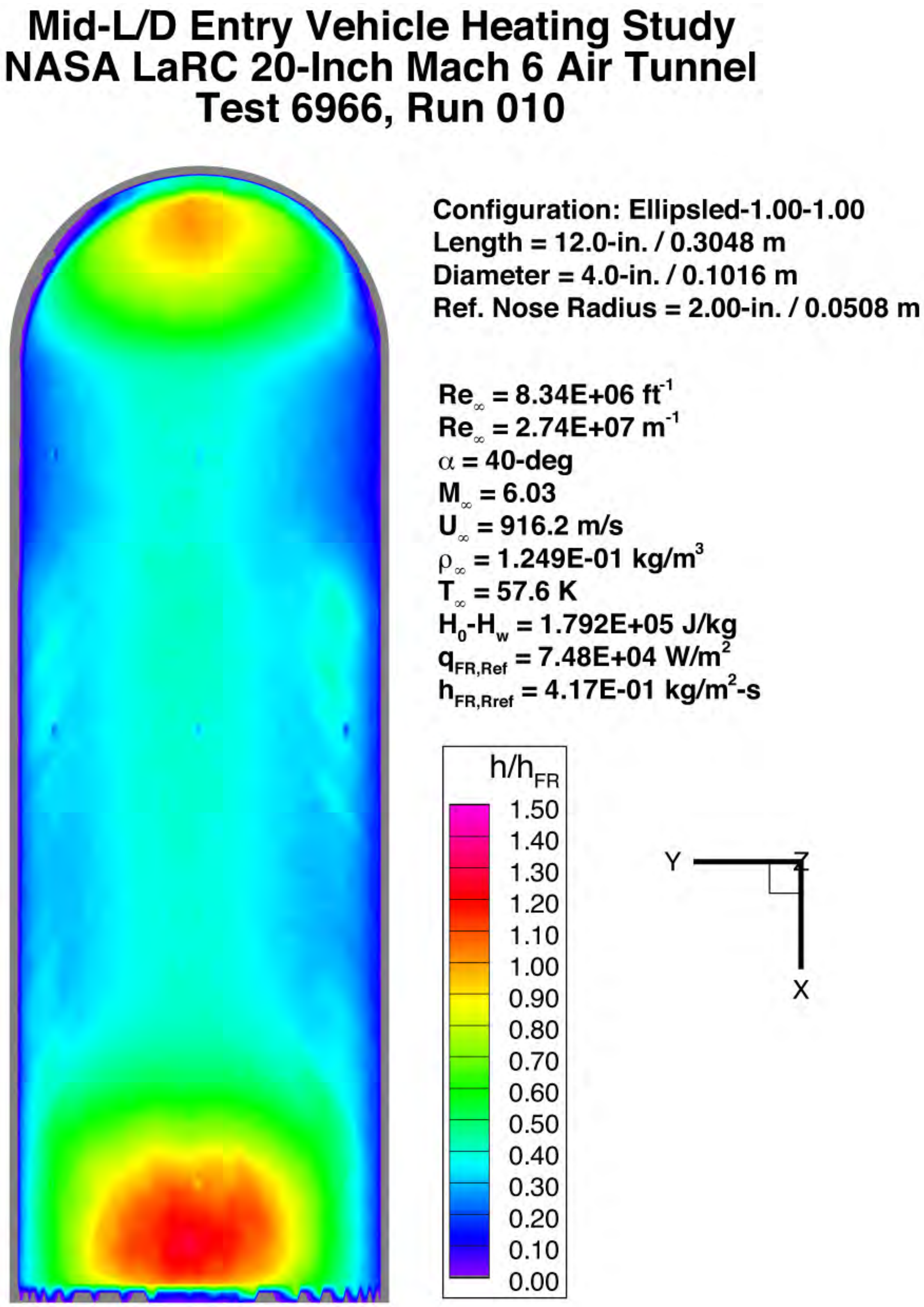

Figure 136. Run 010 Heating Data, Ellipsled-1.00-1.00, Re_∞=8.34×10^6/ft

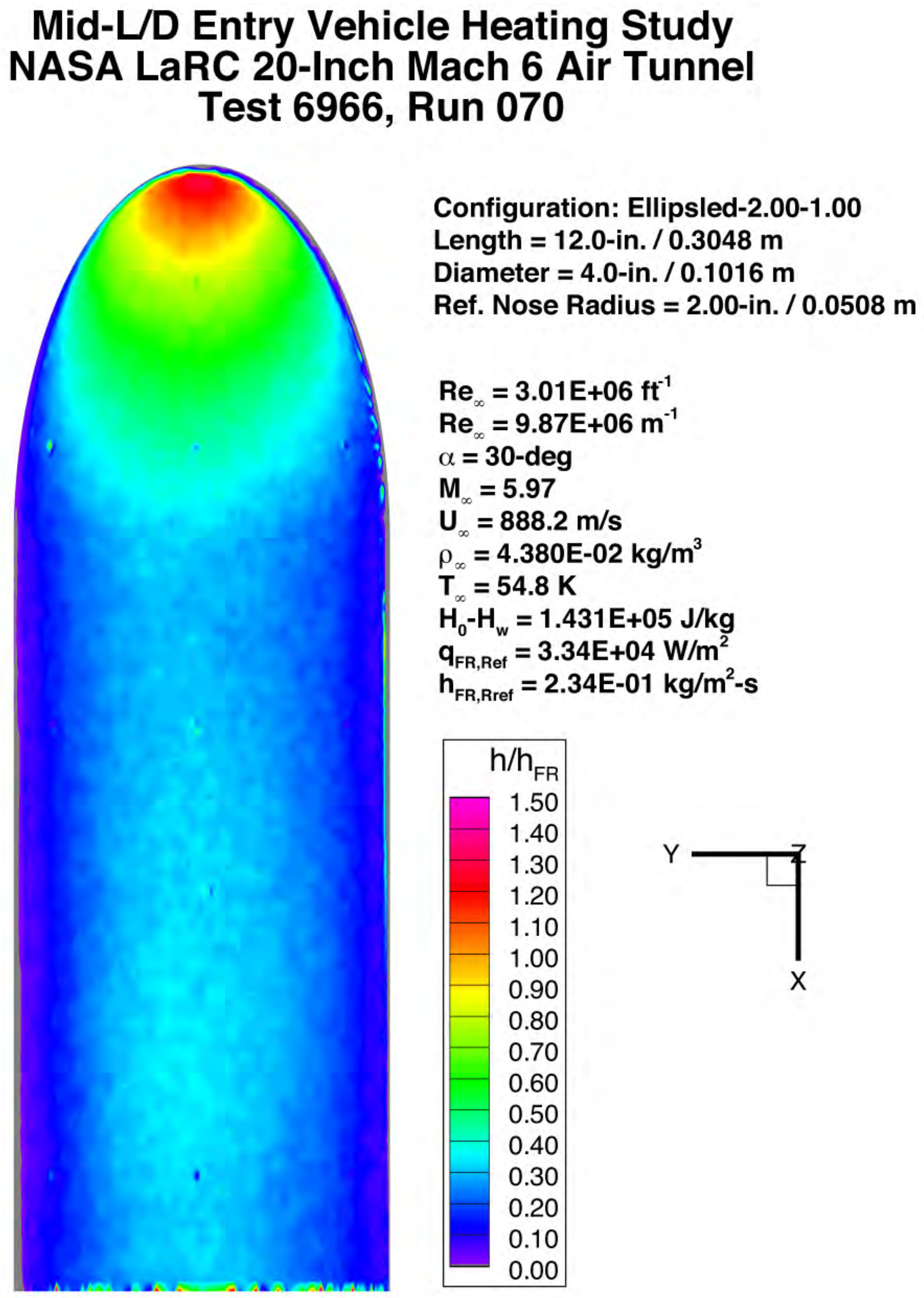

Figure 137. Run 070 Heating Data, Ellipsled-2.00-1.00, $Re_\infty=3.01\times10^6$/ft

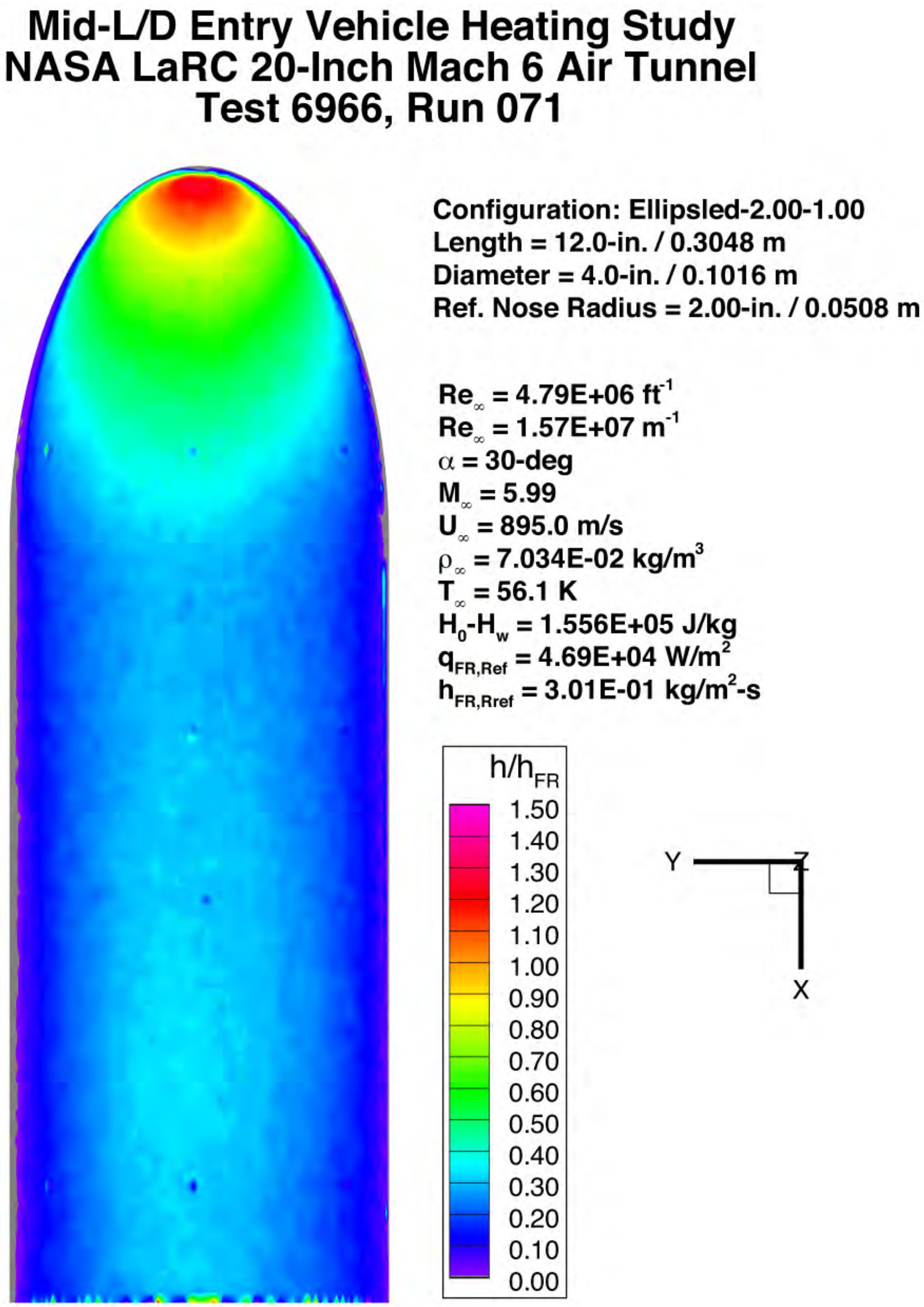

Figure 138. Run 071 Heating Data, Ellipsled-2.00-1.00, Re∞=4.79×10⁶/ft

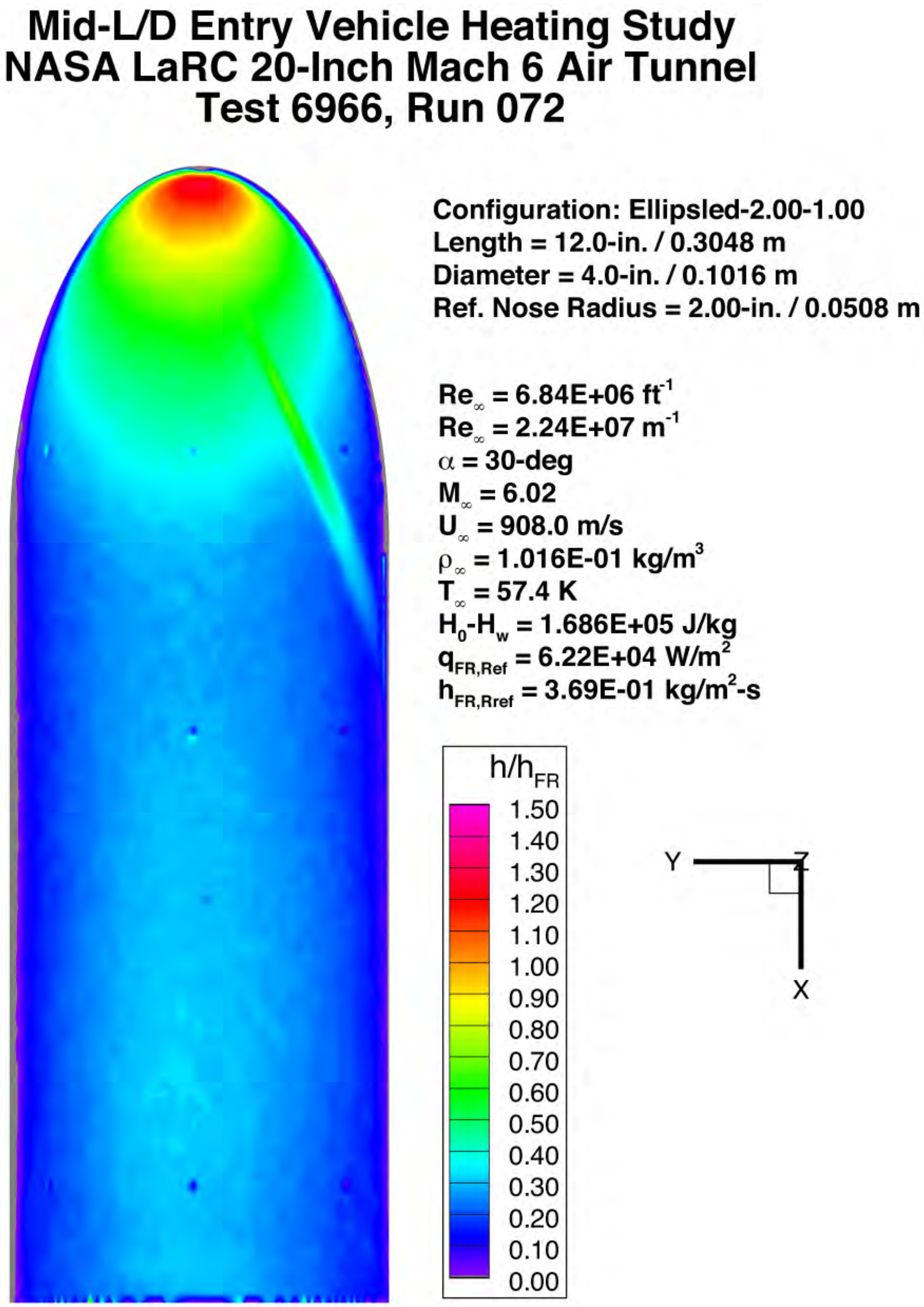

Figure 139. Run 072 Heating Data, Ellipsled-2.00-1.00, Re_∞=6.84×10^6/ft

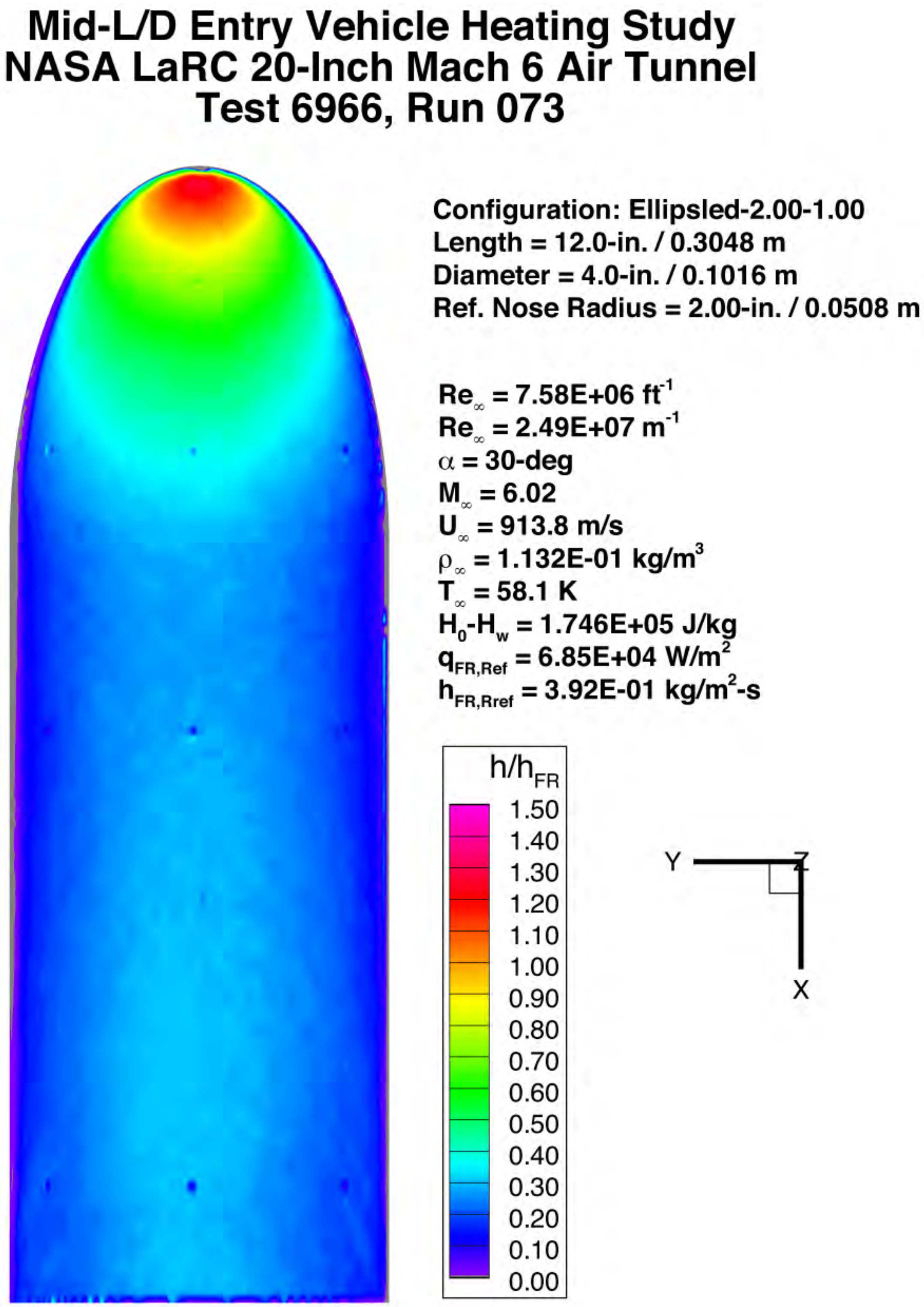

Figure 140. Run 073 Heating Data, Ellipsled-2.00-1.00, Re$_\infty$=7.58×10^6/ft

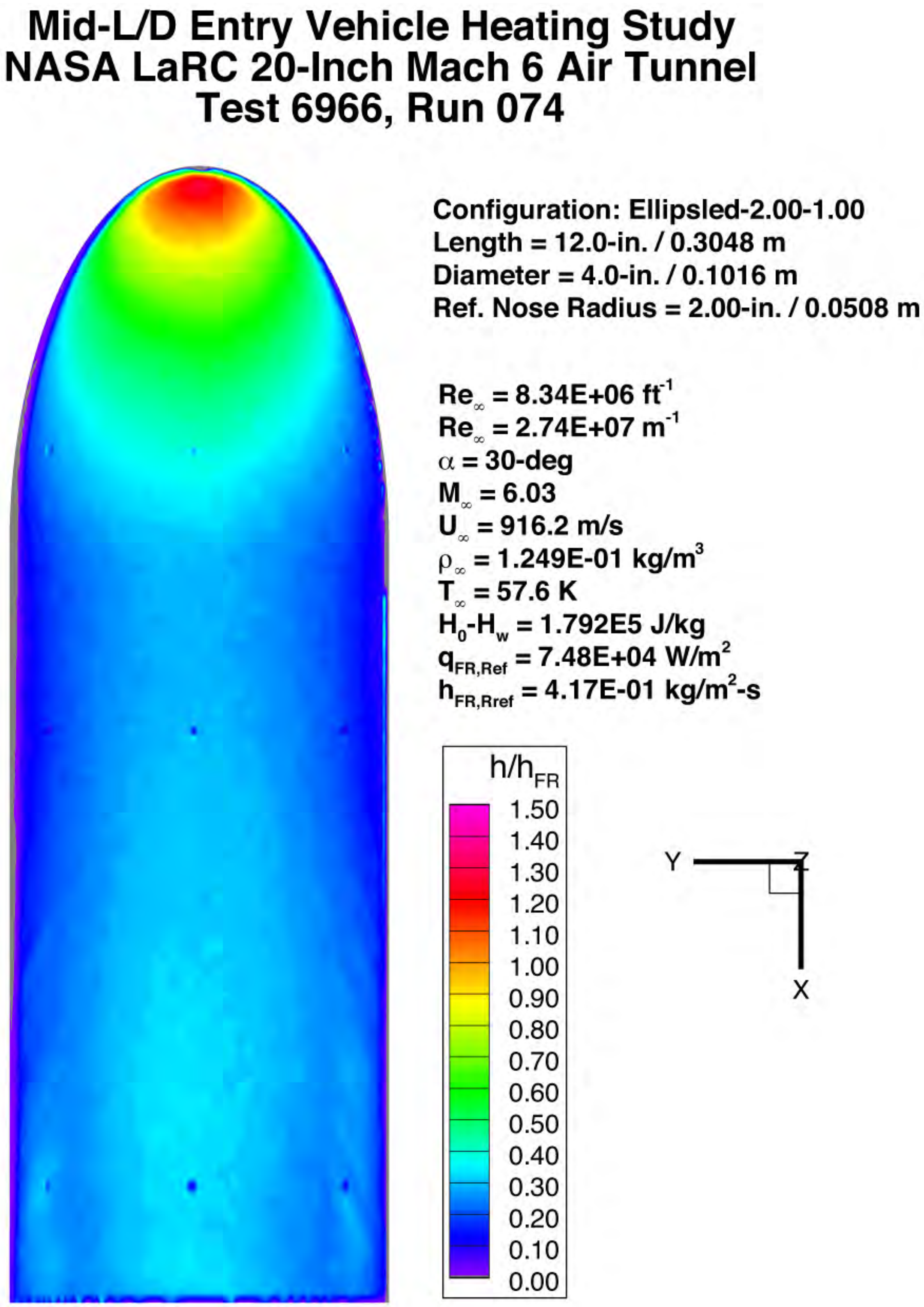

Figure 141. Run 074 Heating Data, Ellipsled-2.00-1.00, Re_∞=8.34×10^6/ft

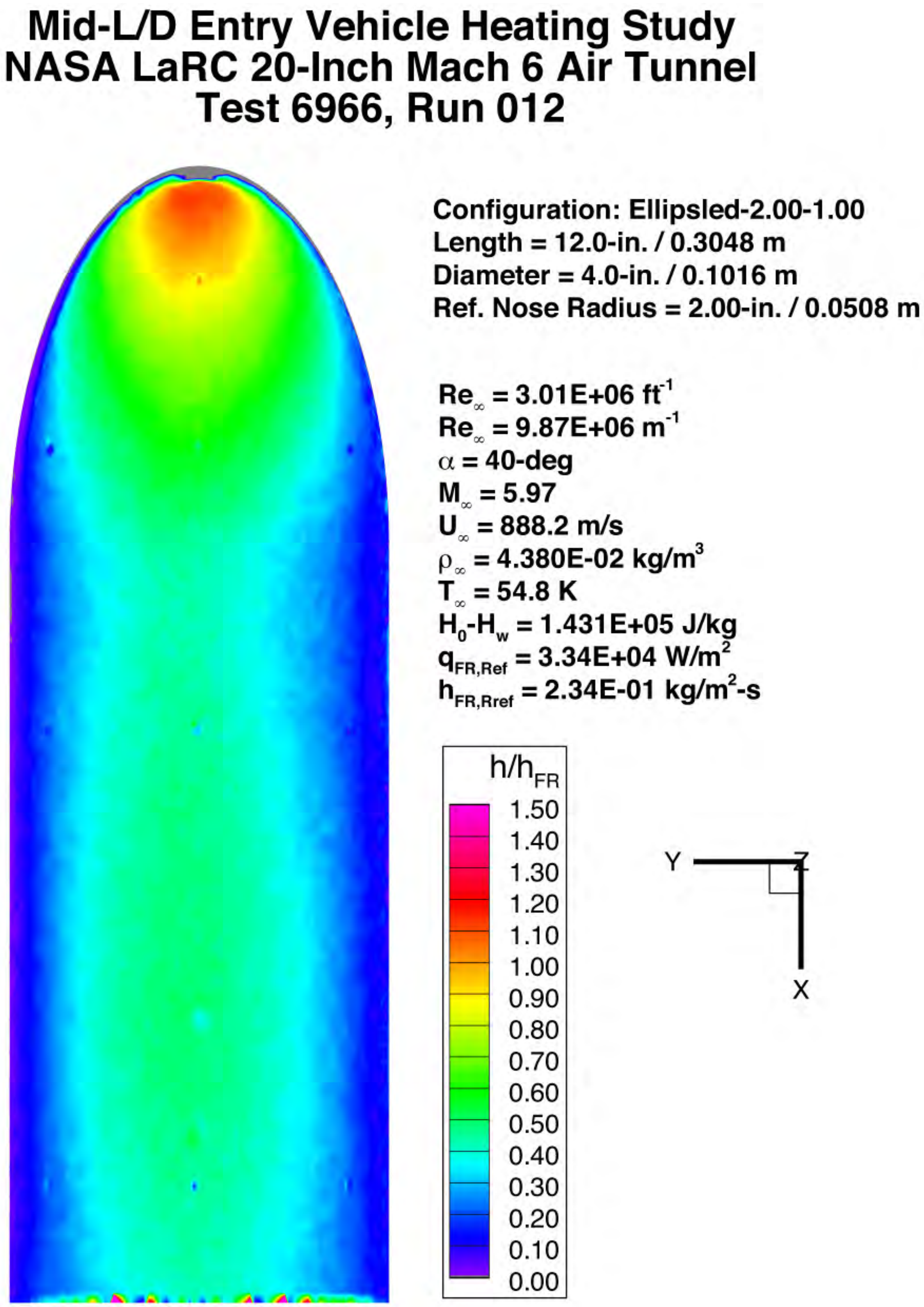

Figure 142. Run 012 Heating Data, Ellipsled-2.00-1.00, Re_∞=3.01×10^6/ft

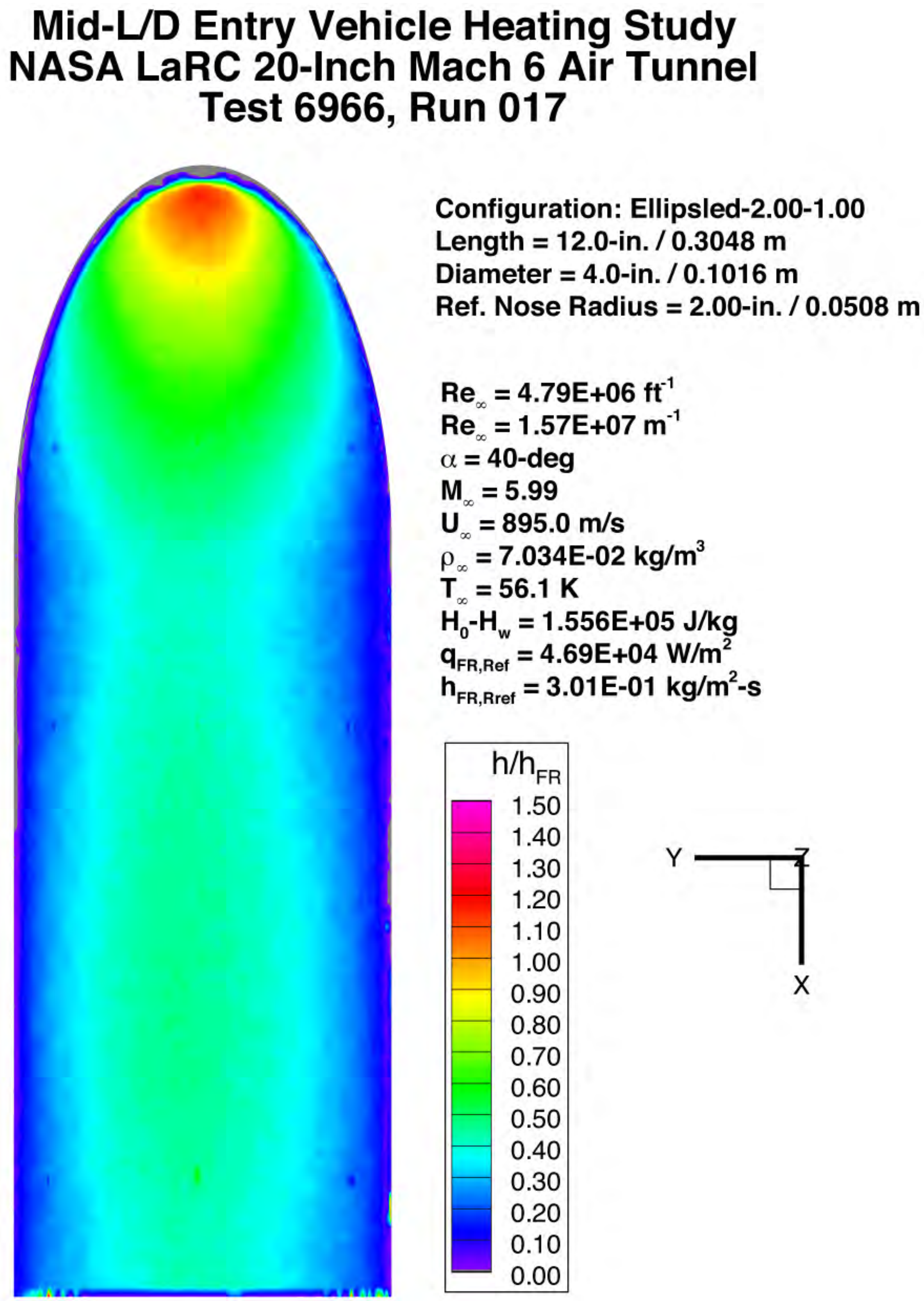

Figure 143. Run 017 Heating Data, Ellipsled-2.00-1.00, Re_∞=4.79×10^6/ft

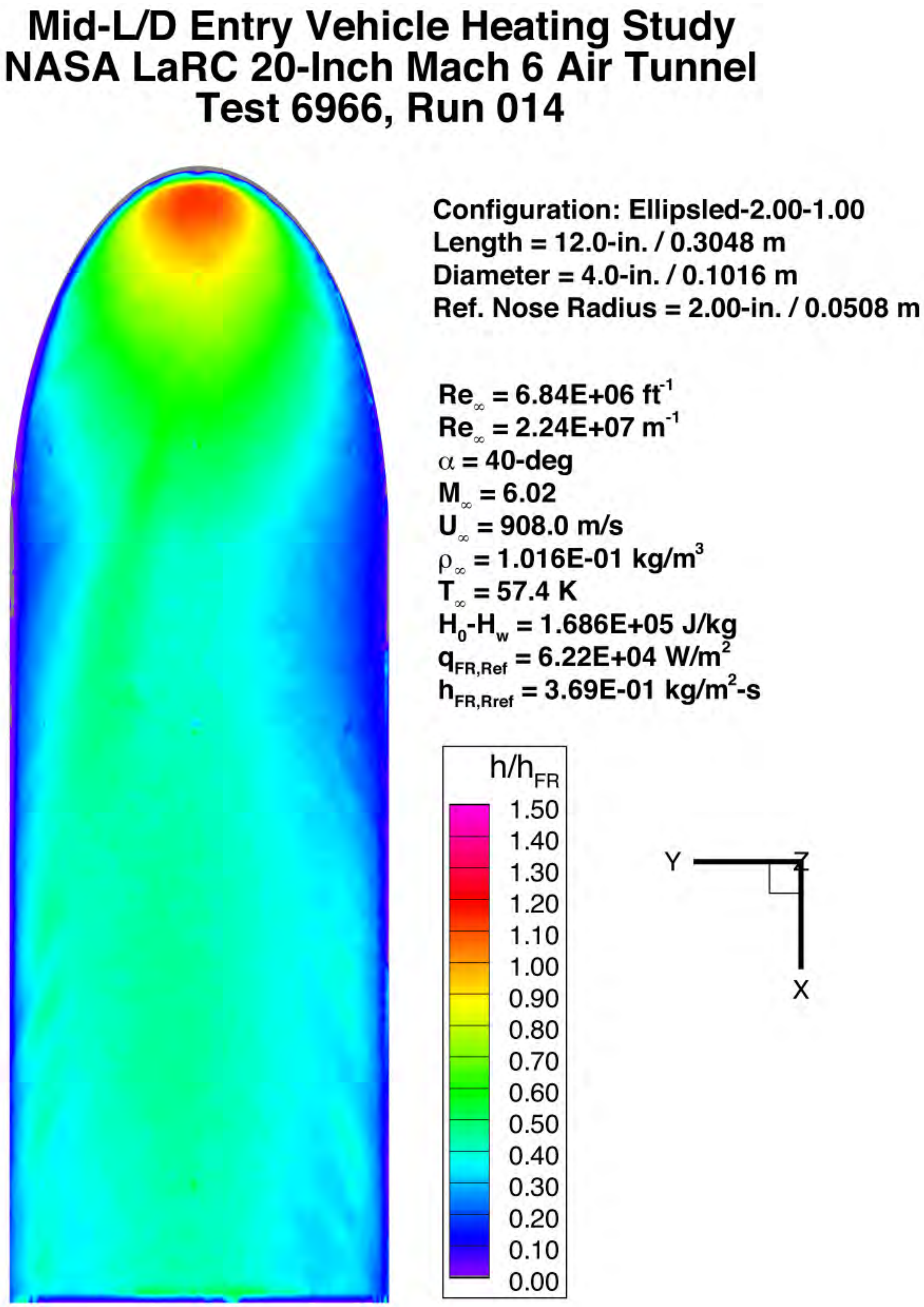

Figure 144. Run 014 Heating Data, Ellipsled-2.00-1.00, $Re_\infty=6.84\times10^6$/ft

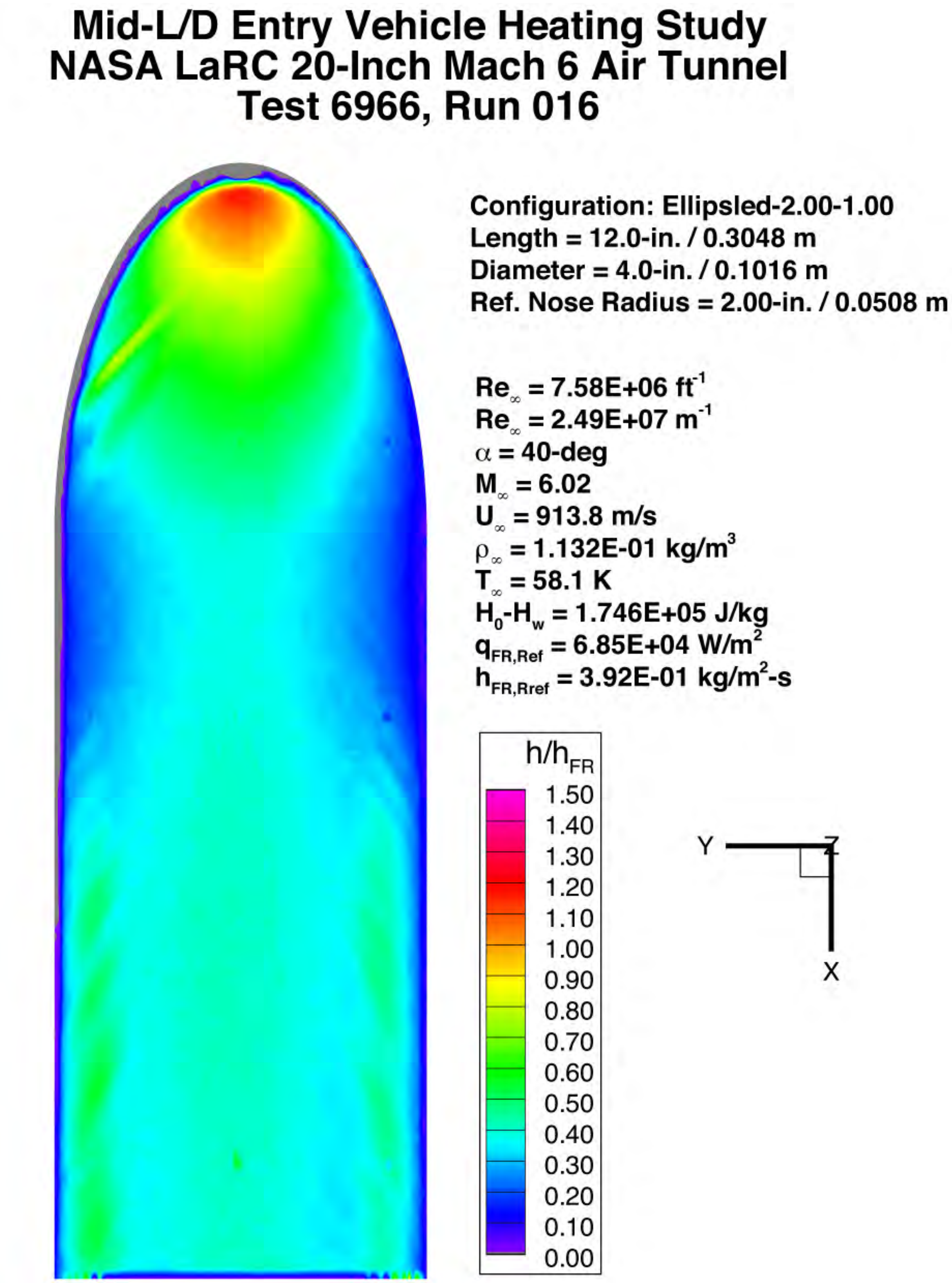

Figure 145. Run 016 Heating Data, Ellipsled-2.00-1.00, Re$_\infty$=7.58×10^6/ft

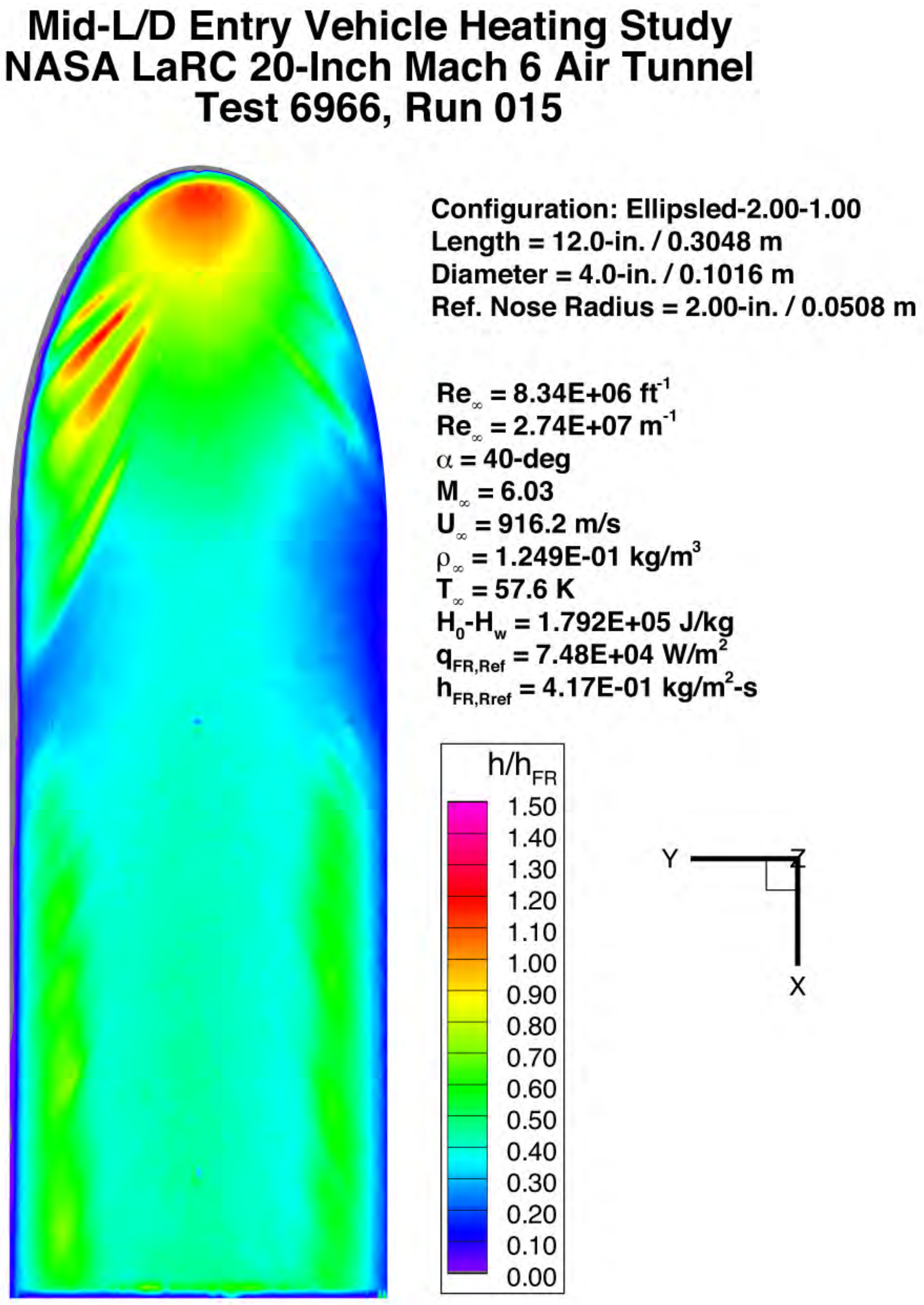

Figure 146. Run 015 Heating Data, Ellipsled-2.00-1.00, Re_∞=8.34×10^6/ft

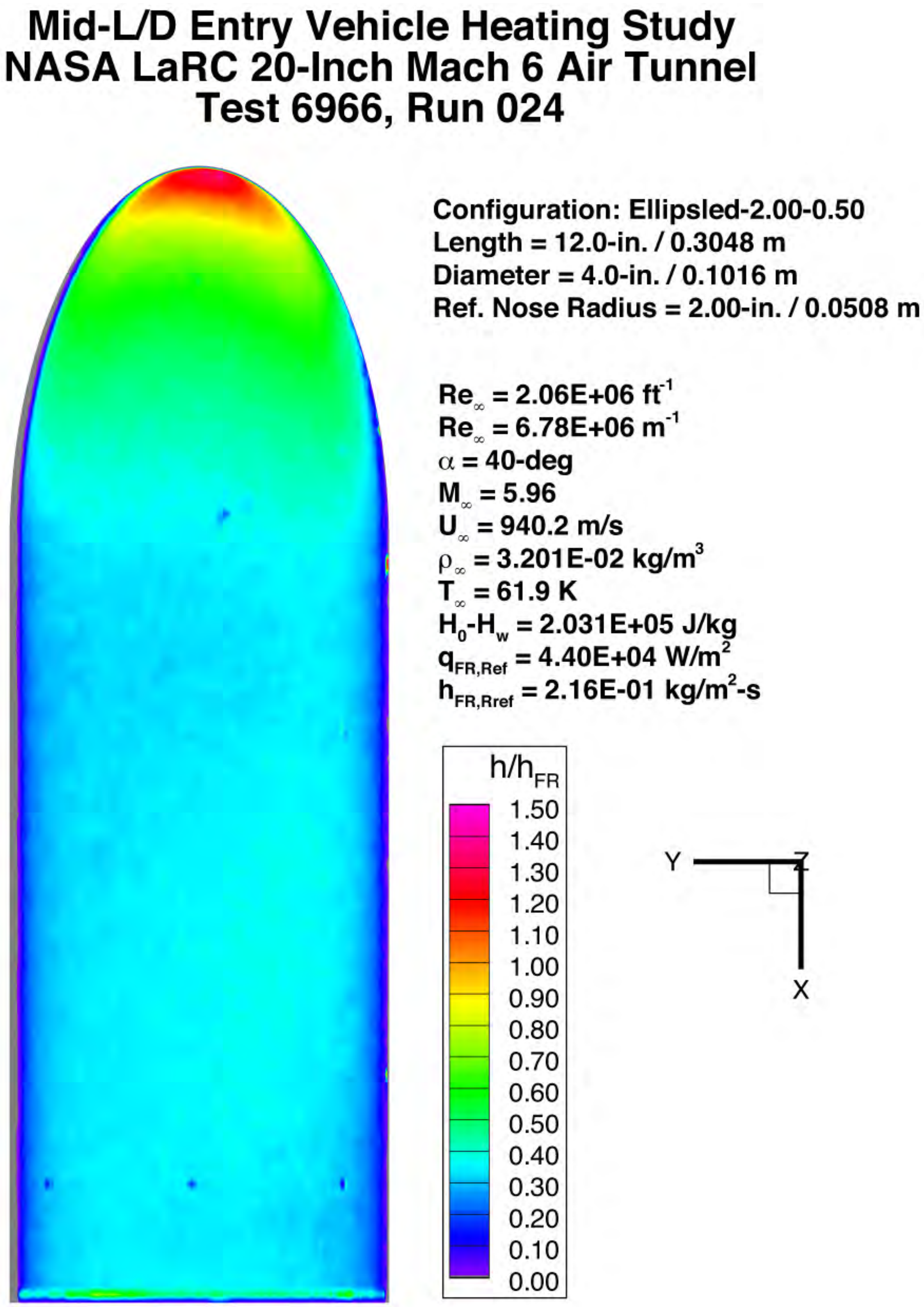

Figure 147. Run 024 Heating Data, Ellipsled-2.00-0.50, Re_∞=2.06×10^6/ft

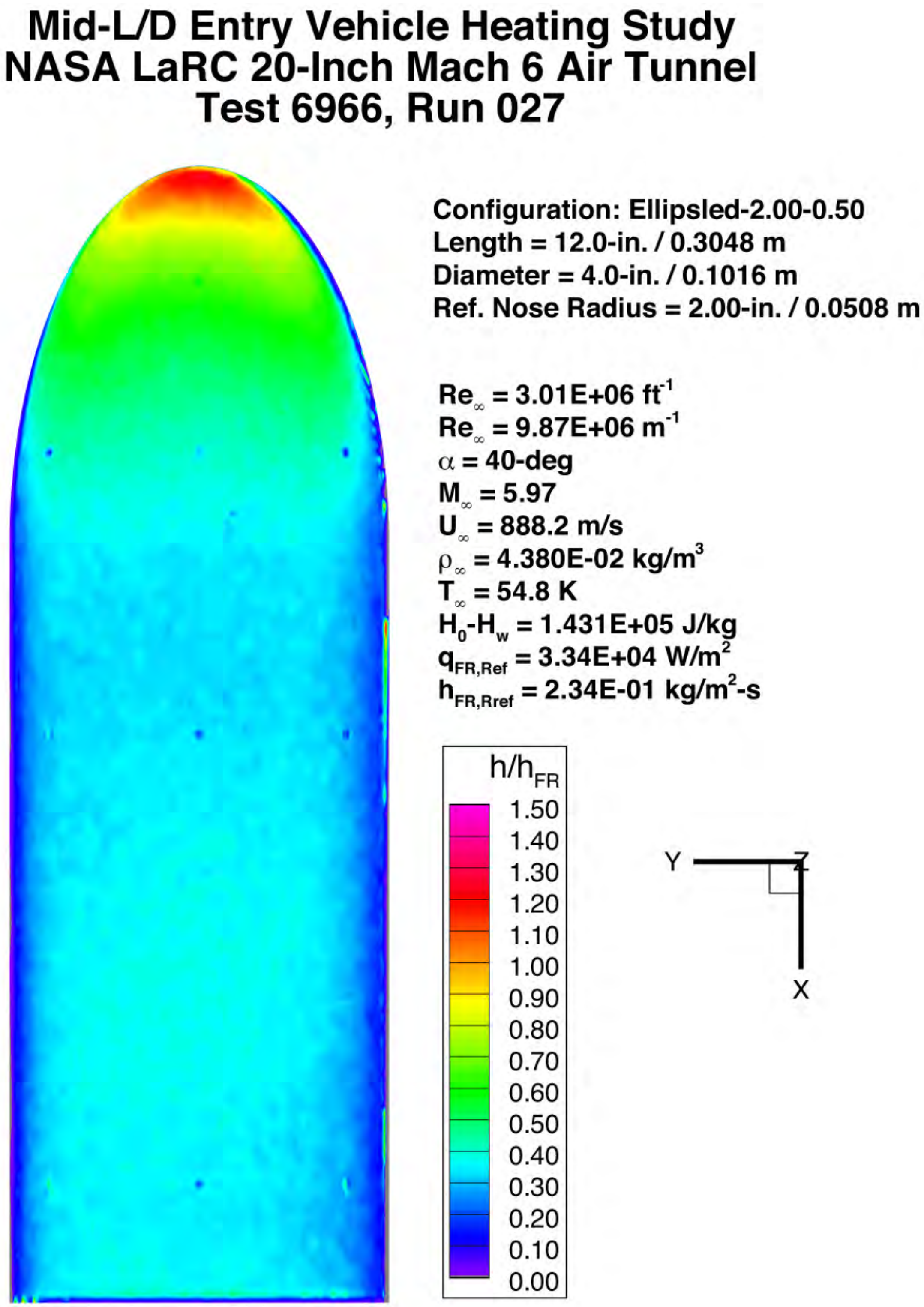

Figure 148. Run 027 Heating Data, Ellipsled-2.00-0.50, Re_∞=3.01×10^6/ft

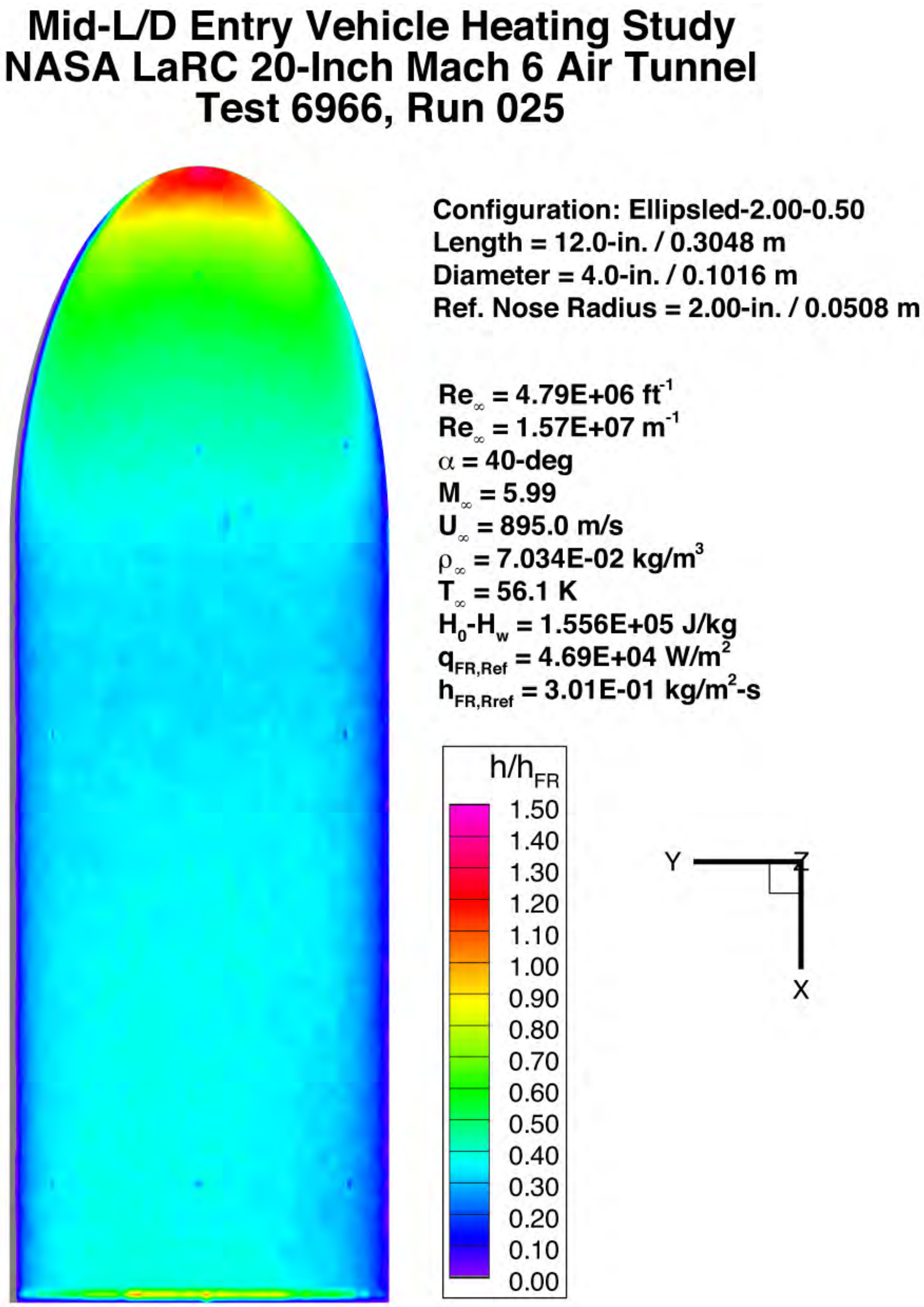

Figure 149. Run 025 Heating Data, Ellipsled-2.00-0.50, Re_∞=4.79×10^6/ft

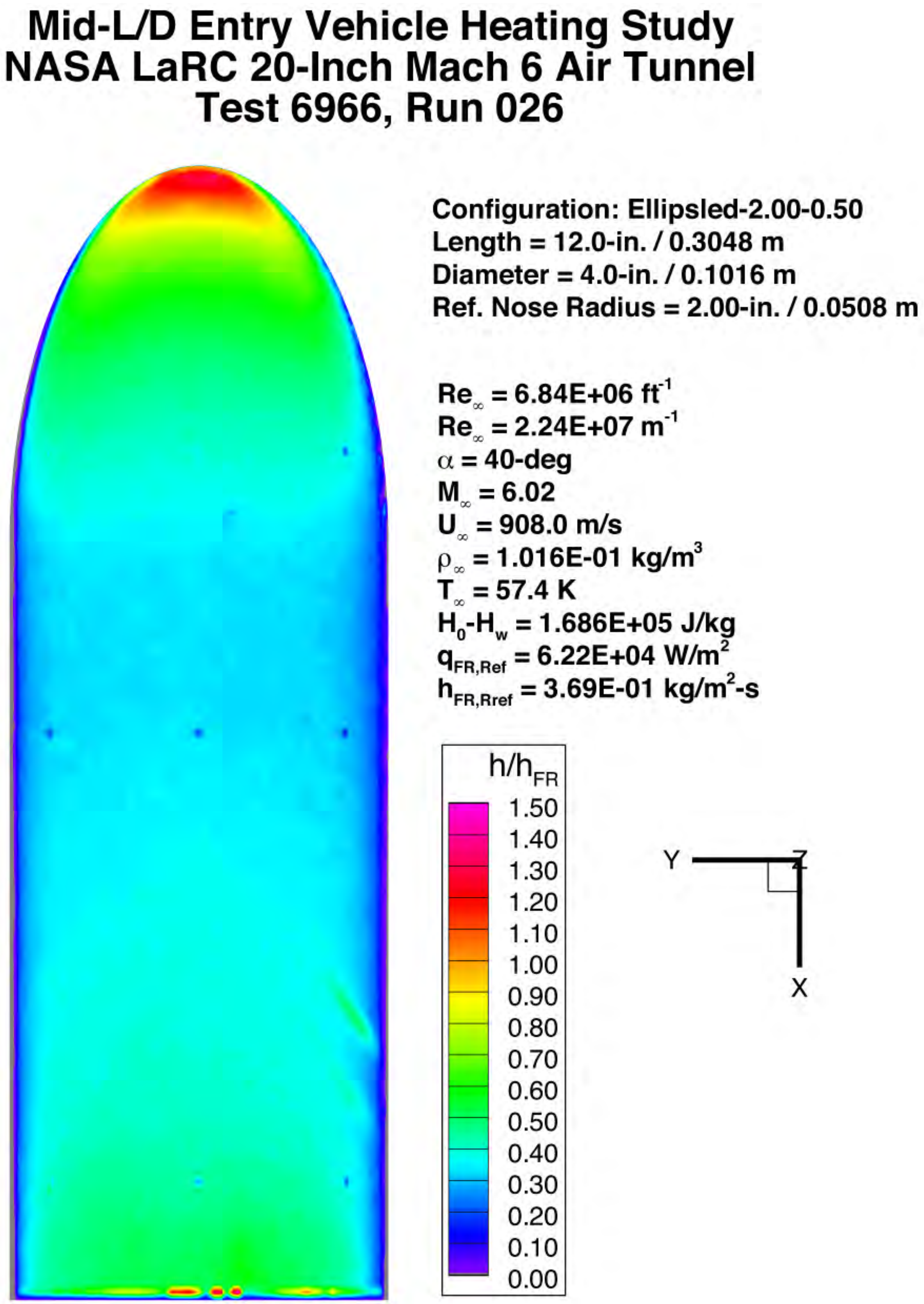

Figure 150. Run 026 Heating Data, Ellipsled-2.00-0.50, $Re_\infty = 6.84 \times 10^6$/ft

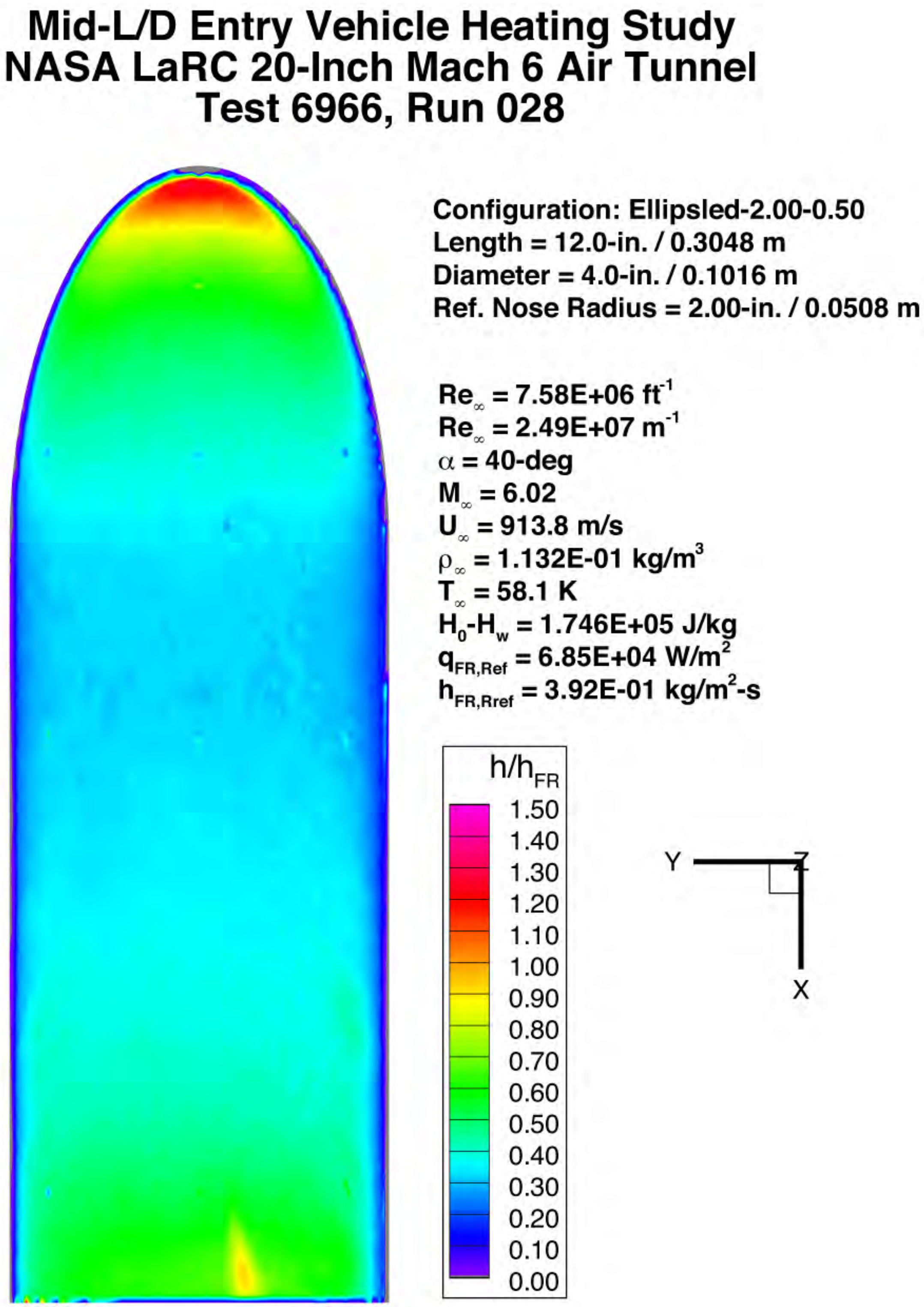

Figure 151. Run 028 Heating Data, Ellipsled-2.00-0.50, Re_∞=7.58×10^6/ft

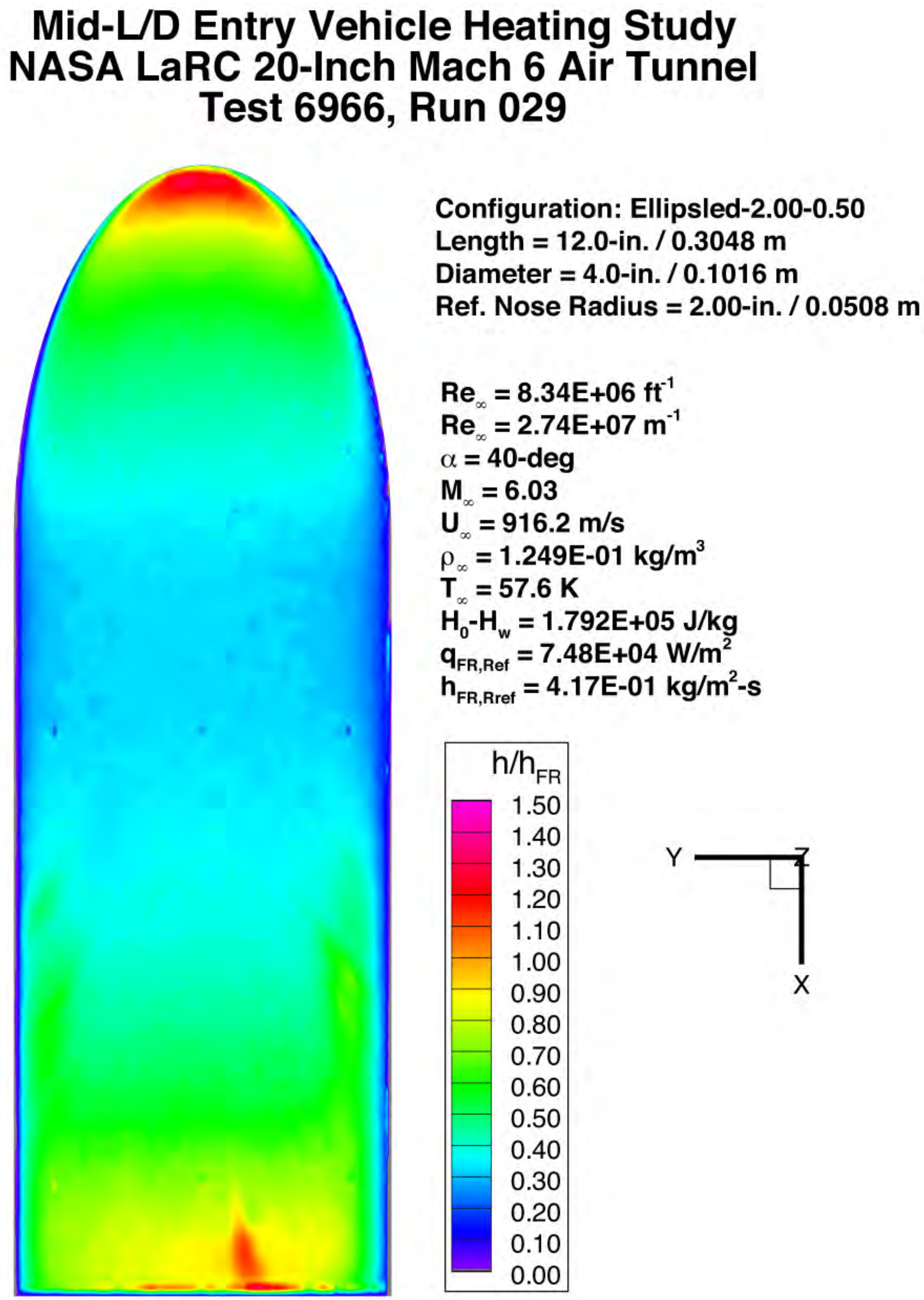

Mid-L/D Entry Vehicle Heating Study
NASA LaRC 20-Inch Mach 6 Air Tunnel
Test 6966, Run 029

Configuration: Ellipsled-2.00-0.50
Length = 12.0-in. / 0.3048 m
Diameter = 4.0-in. / 0.1016 m
Ref. Nose Radius = 2.00-in. / 0.0508 m

Re_∞ = 8.34E+06 ft^{-1}
Re_∞ = 2.74E+07 m^{-1}
α = 40-deg
M_∞ = 6.03
U_∞ = 916.2 m/s
ρ_∞ = 1.249E-01 kg/m^3
T_∞ = 57.6 K
H_0-H_w = 1.792E+05 J/kg
$q_{FR,Ref}$ = 7.48E+04 W/m^2
$h_{FR,Rref}$ = 4.17E-01 kg/m^2-s

Figure 152. Run 029 Heating Data, Ellipsled-2.00-0.50, $Re_\infty = 8.34\times10^6$/ft

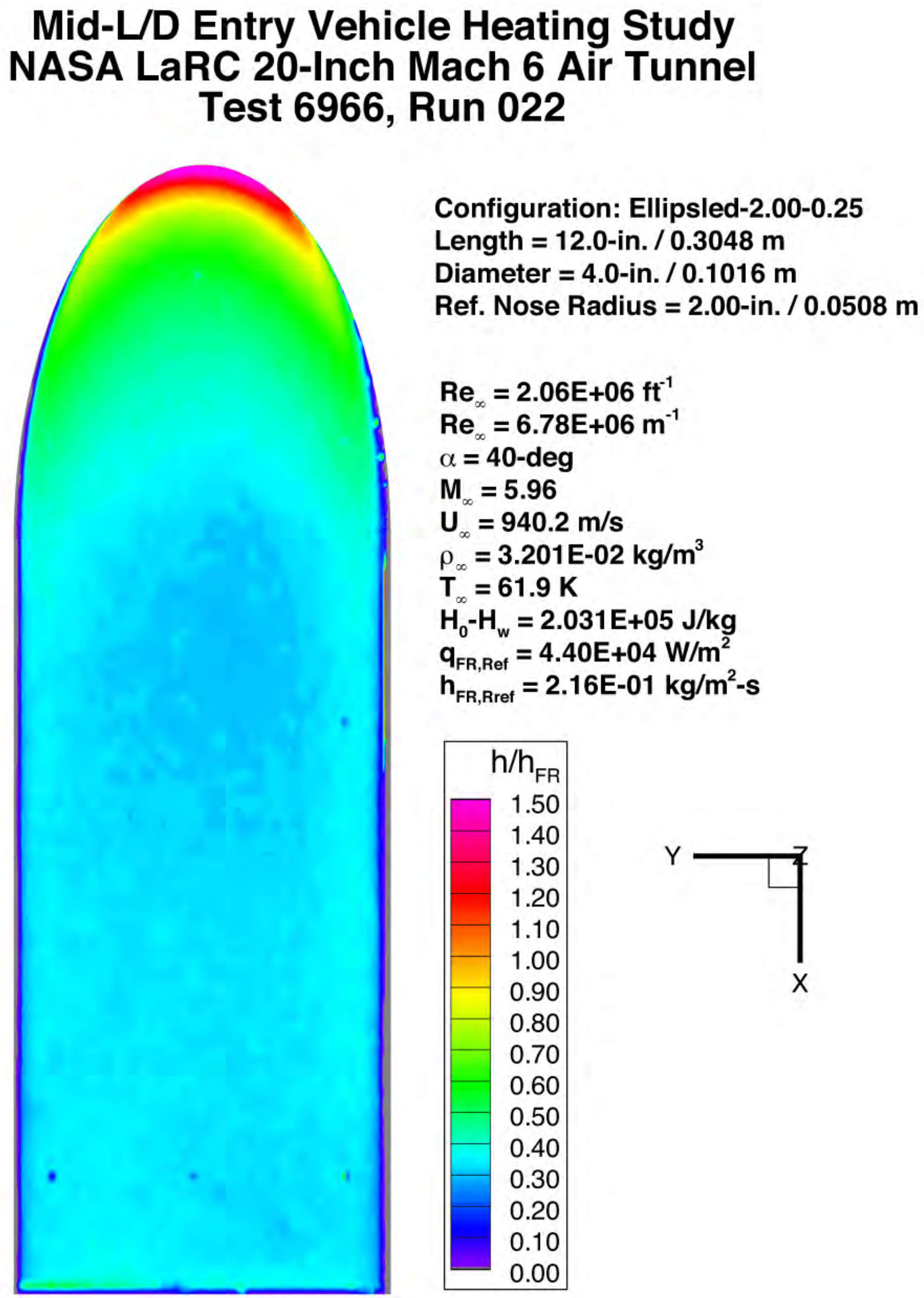

Figure 153. Run 022 Heating Data, Ellipsled-2.00-0.25, $Re_\infty=2.06\times10^6$/ft

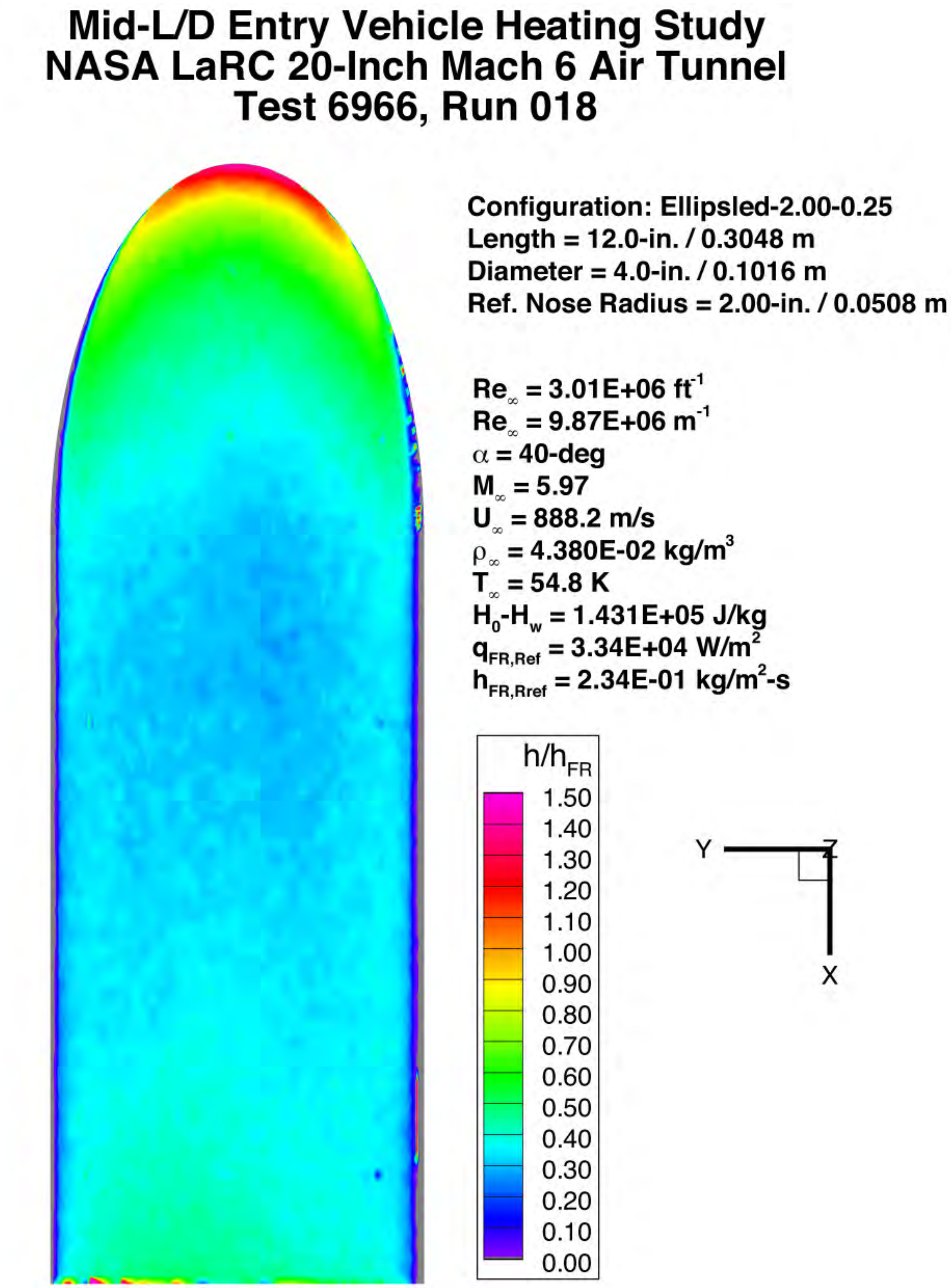

Figure 154. Run 018 Heating Data, Ellipsled-2.00-0.25, $Re_\infty = 3.01 \times 10^6$/ft

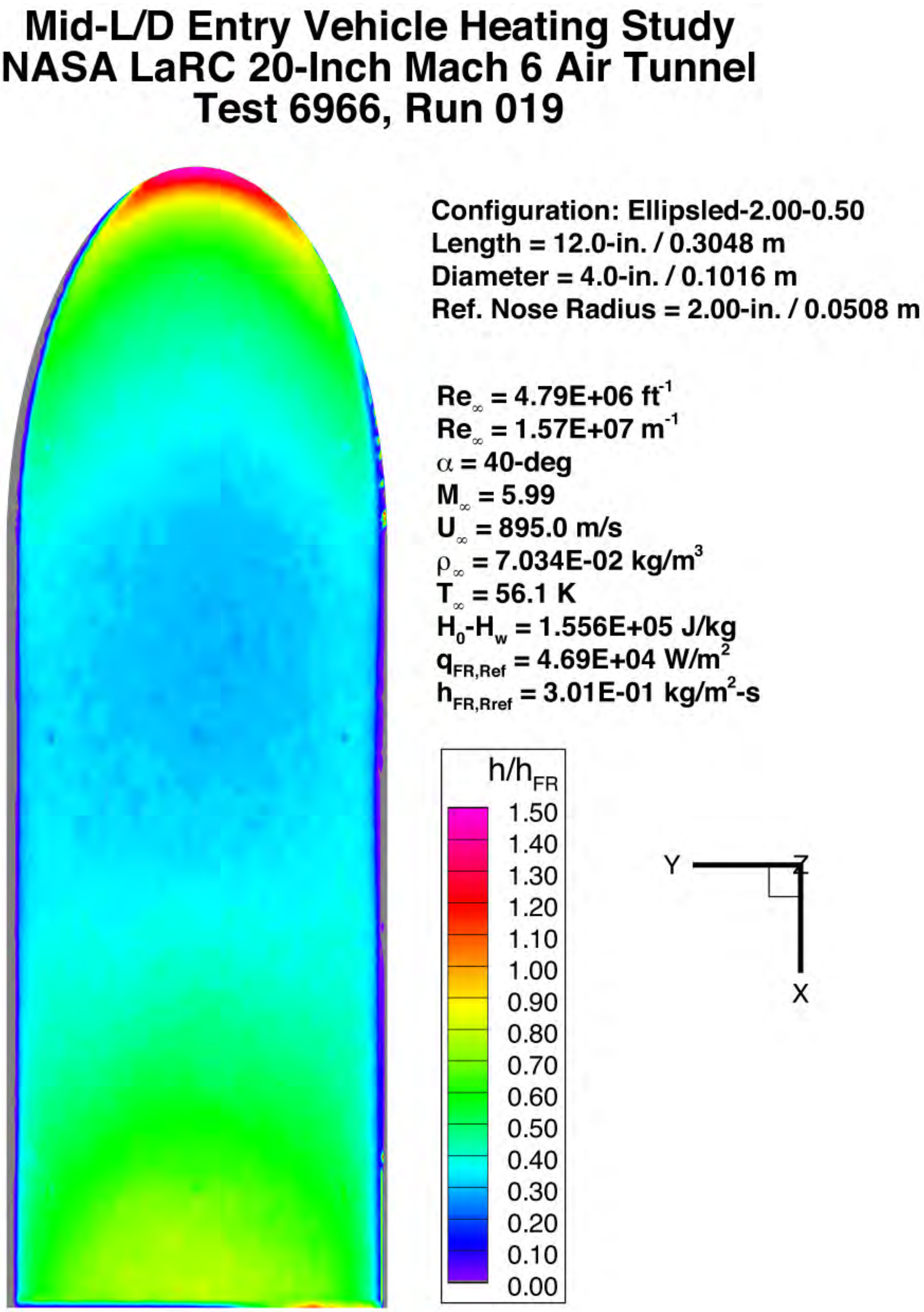

Mid-L/D Entry Vehicle Heating Study
NASA LaRC 20-Inch Mach 6 Air Tunnel
Test 6966, Run 019

Configuration: Ellipsled-2.00-0.50
Length = 12.0-in. / 0.3048 m
Diameter = 4.0-in. / 0.1016 m
Ref. Nose Radius = 2.00-in. / 0.0508 m

$Re_\infty = 4.79E+06\ ft^{-1}$
$Re_\infty = 1.57E+07\ m^{-1}$
$\alpha = 40$-deg
$M_\infty = 5.99$
$U_\infty = 895.0$ m/s
$\rho_\infty = 7.034E-02\ kg/m^3$
$T_\infty = 56.1$ K
$H_0-H_w = 1.556E+05$ J/kg
$q_{FR,Ref} = 4.69E+04\ W/m^2$
$h_{FR,Rref} = 3.01E-01\ kg/m^2$-s

Figure 155. Run 019 Heating Data, Ellipsled-2.00-0.25, $Re_\infty=4.79\times10^6$/ft

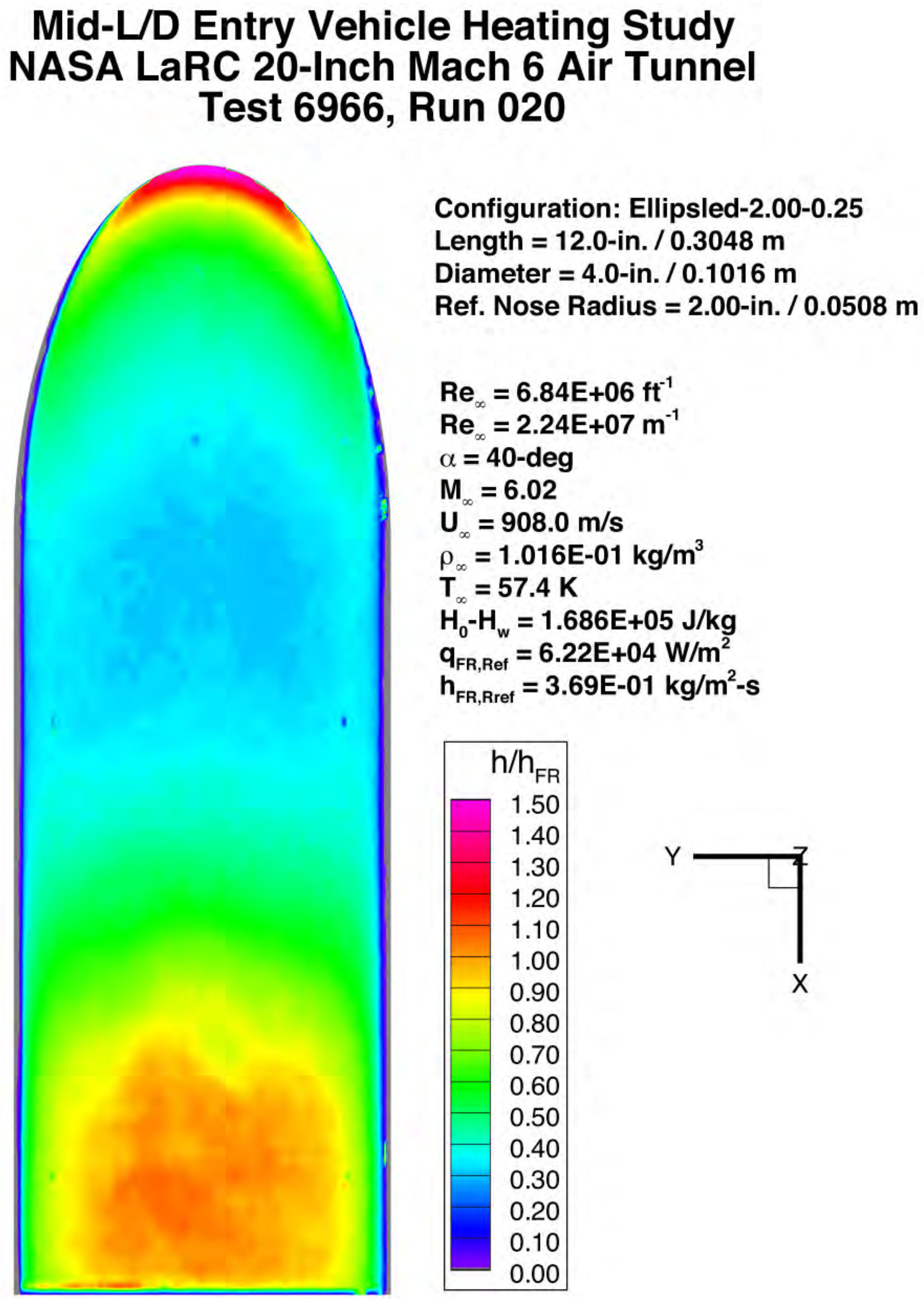

Figure 156. Run 020 Heating Data, Ellipsled-2.00-0.25, Re_∞=6.84×10^6/ft

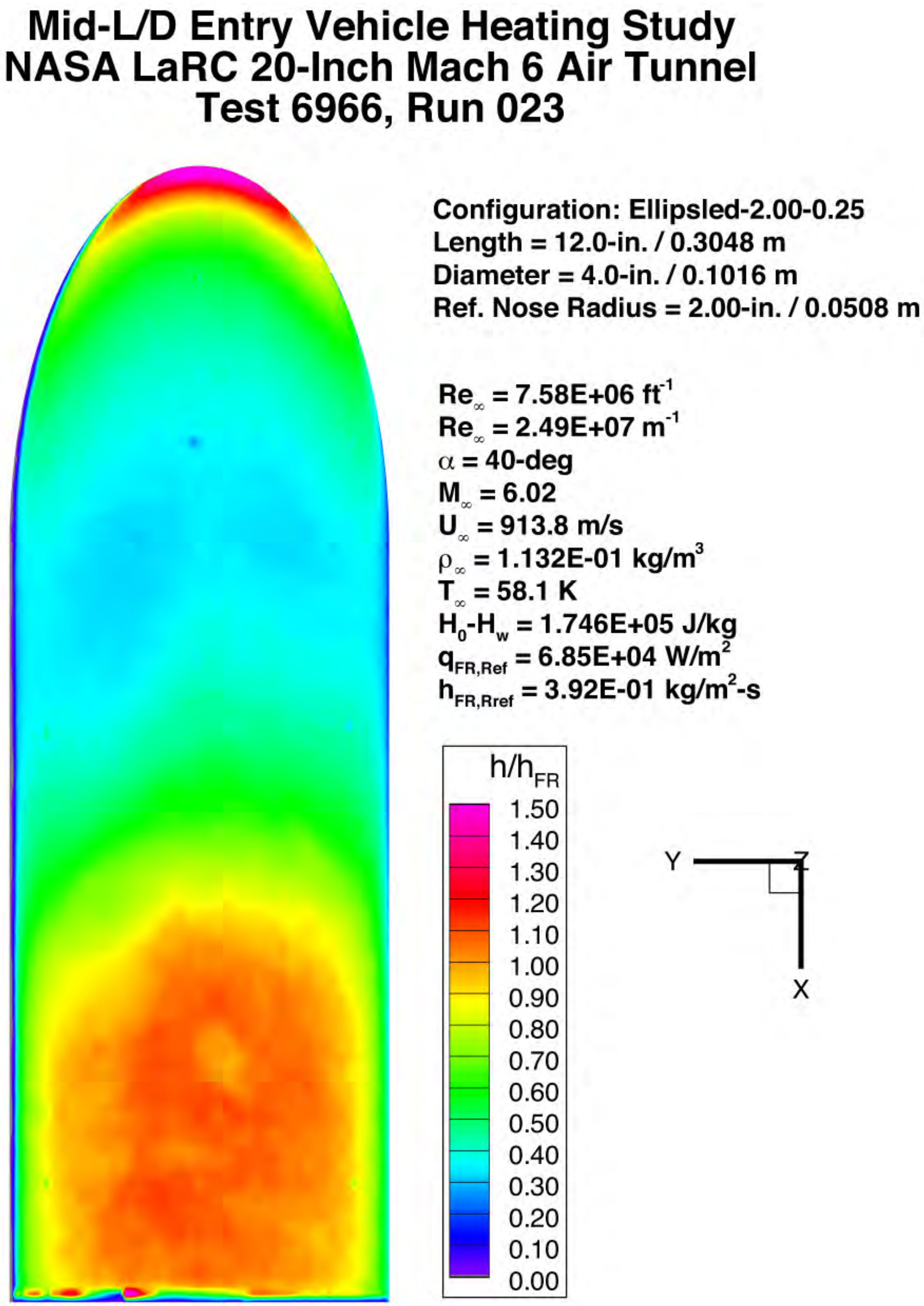

Figure 157. Run 023 Heating Data, Ellipsled-2.00-0.25, $Re_\infty = 7.58 \times 10^6$/ft

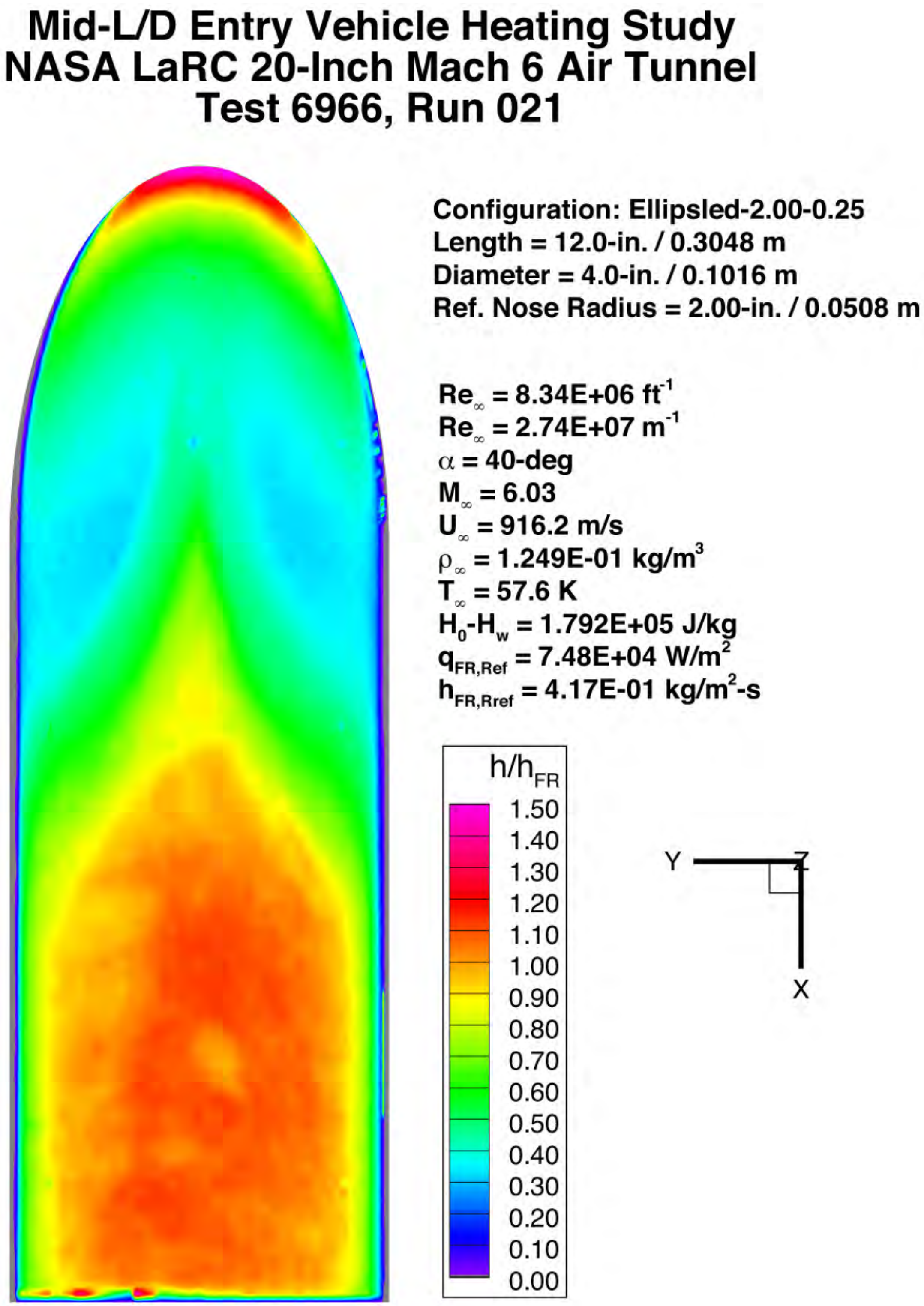

Figure 158. Run 021 Heating Data, Ellipsled-2.00-0.25, $Re_\infty=8.34\times10^6$/ft

Appendix B. COBRA Global Image Heating Data

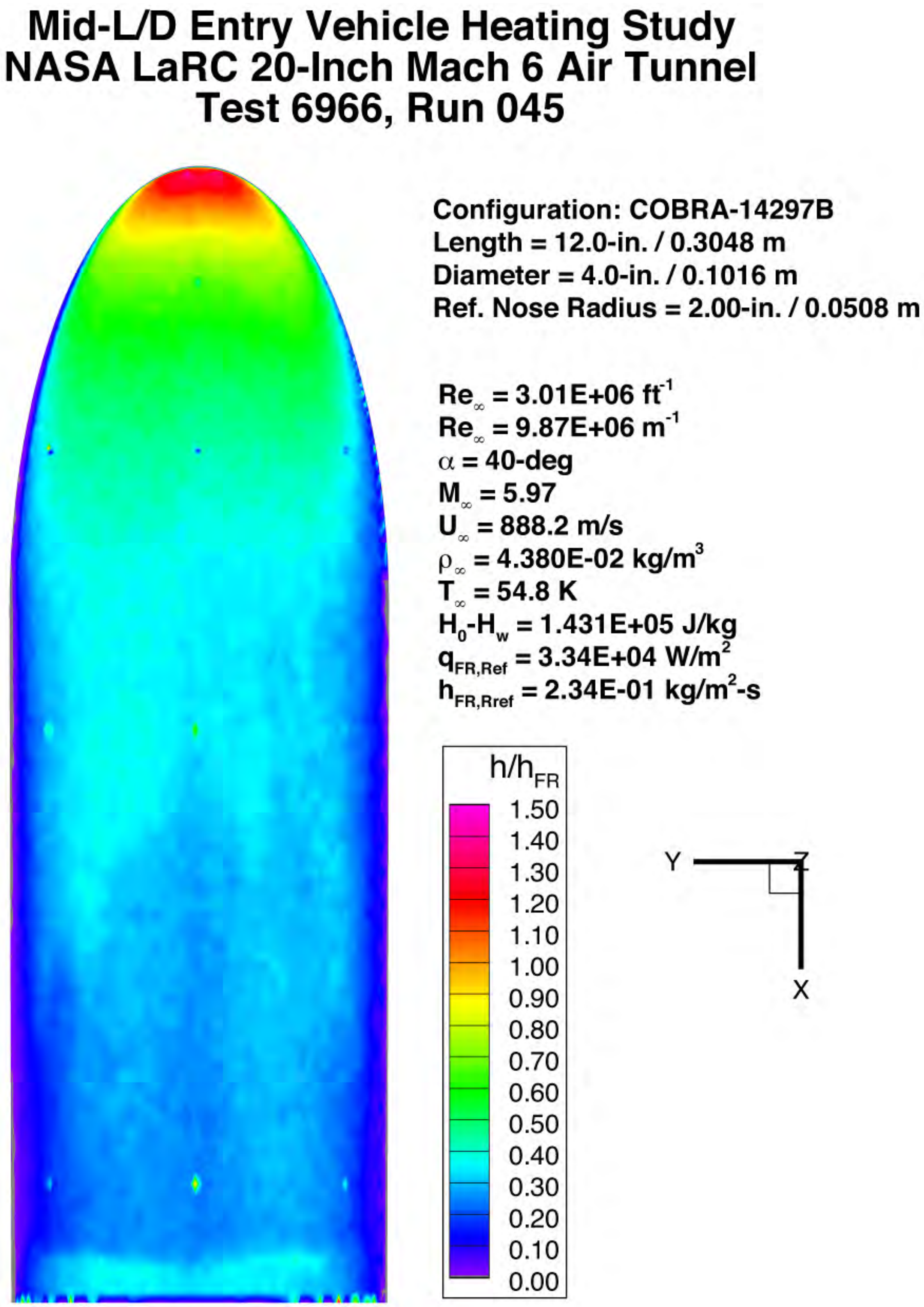

Figure 159. Run 045 Heating Data, COBRA-14297B (Model C-1), Re_∞=3.01×10^6/ft

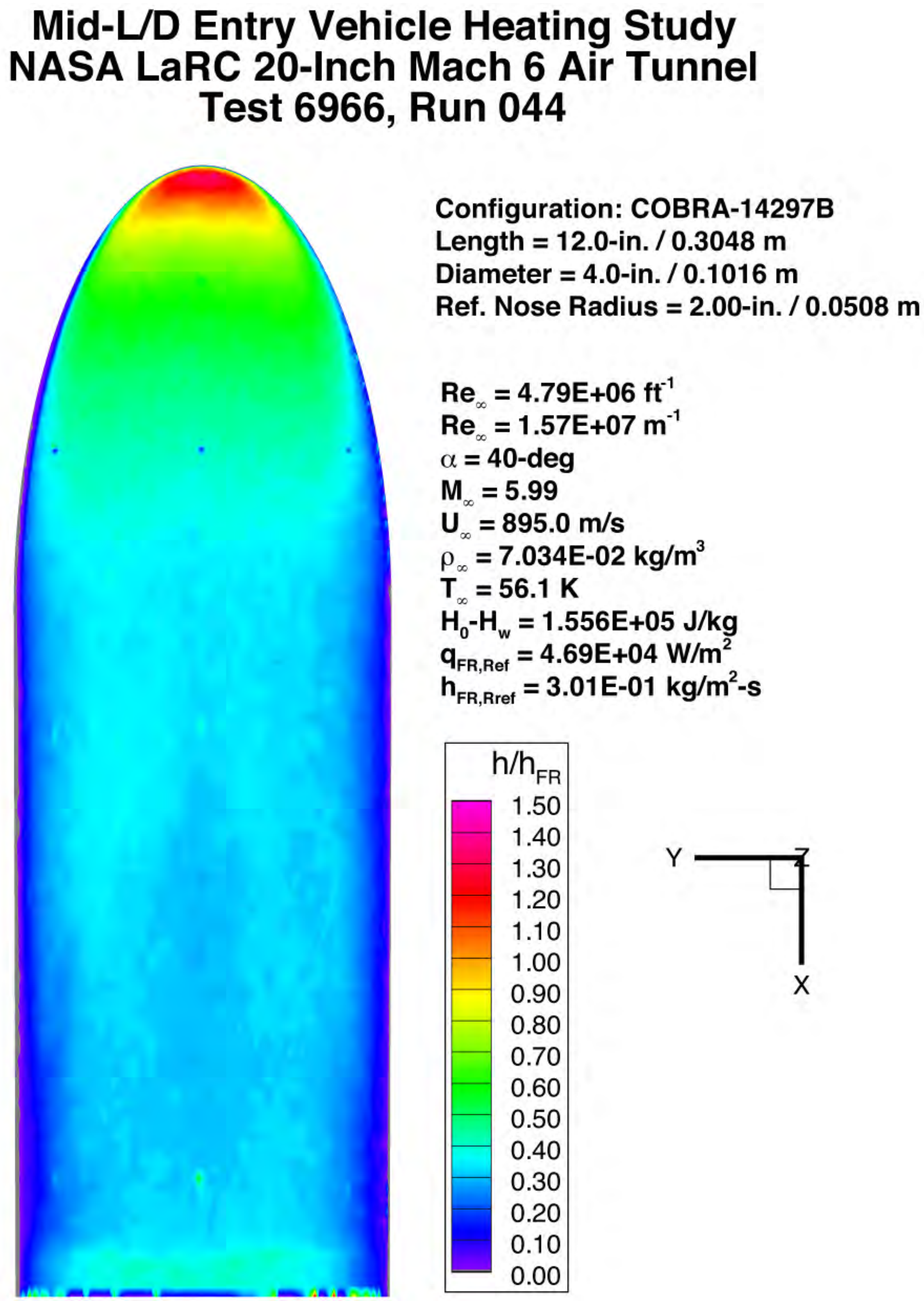

Mid-L/D Entry Vehicle Heating Study
NASA LaRC 20-Inch Mach 6 Air Tunnel
Test 6966, Run 044

Configuration: COBRA-14297B
Length = 12.0-in. / 0.3048 m
Diameter = 4.0-in. / 0.1016 m
Ref. Nose Radius = 2.00-in. / 0.0508 m

$Re_\infty = 4.79E+06\ ft^{-1}$
$Re_\infty = 1.57E+07\ m^{-1}$
$\alpha = 40$-deg
$M_\infty = 5.99$
$U_\infty = 895.0$ m/s
$\rho_\infty = 7.034E-02\ kg/m^3$
$T_\infty = 56.1$ K
$H_0 - H_w = 1.556E+05$ J/kg
$q_{FR,Ref} = 4.69E+04\ W/m^2$
$h_{FR,Rref} = 3.01E-01\ kg/m^2\text{-}s$

Figure 160. Run 044 Heating Data, COBRA-14297B (Model C-1), $Re_\infty = 4.79 \times 10^6$/ft

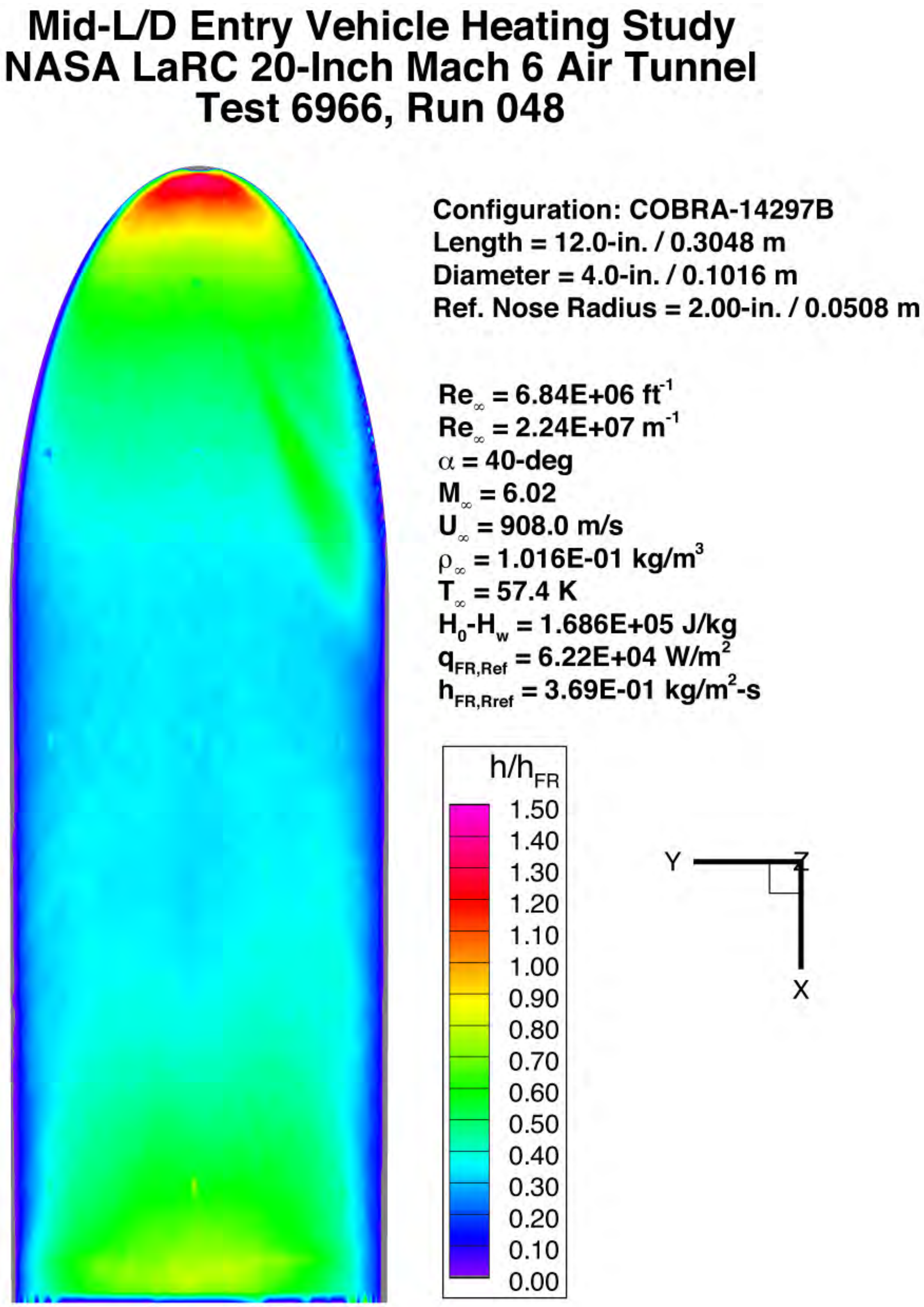

Figure 161. Run 048 Heating Data, COBRA-14297B (Model C-1), $Re_\infty = 6.84 \times 10^6$/ft

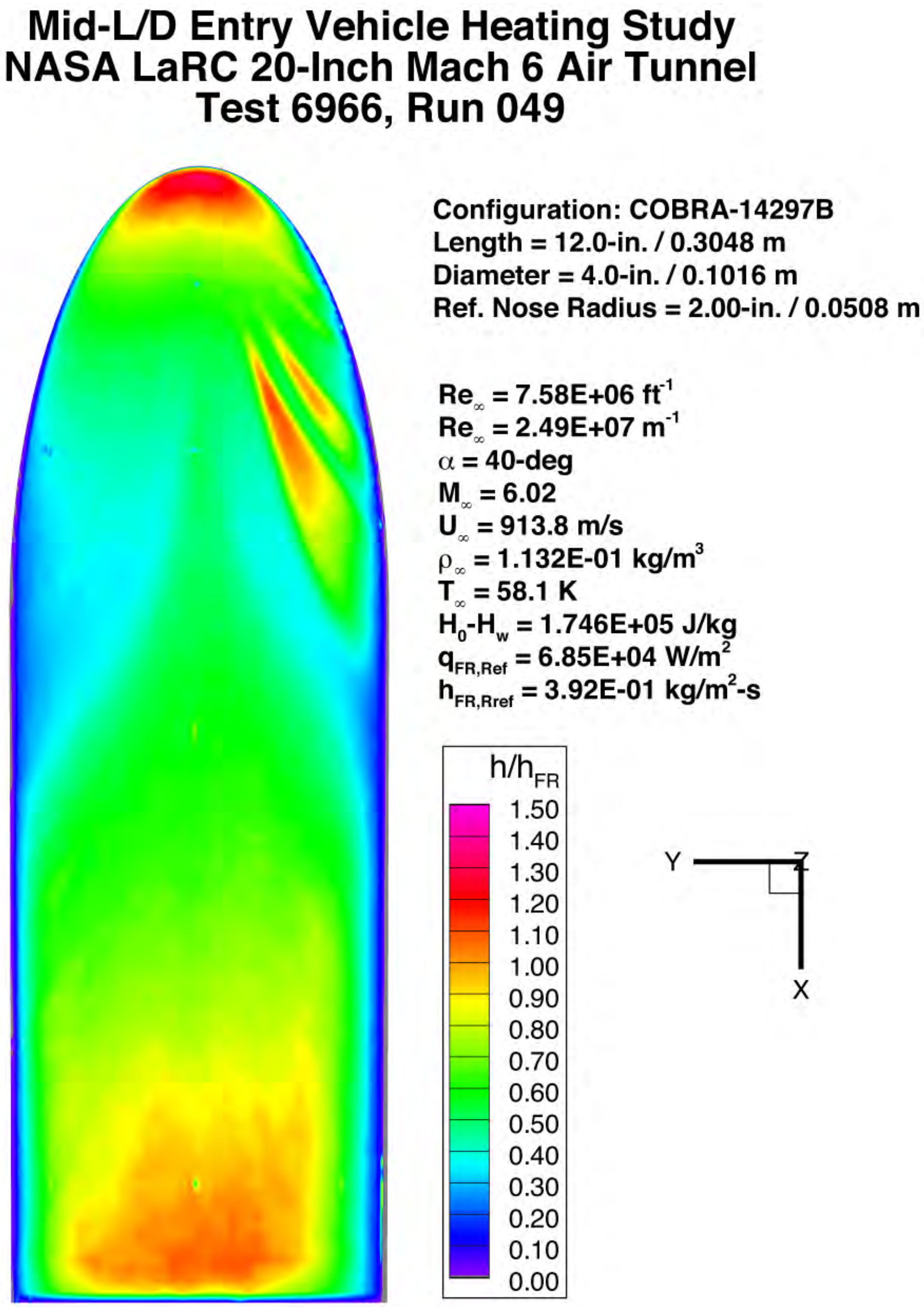

Figure 162. Run 049 Heating Data, COBRA-14297B (Model C-1), Re_∞=7.58×10^6/ft

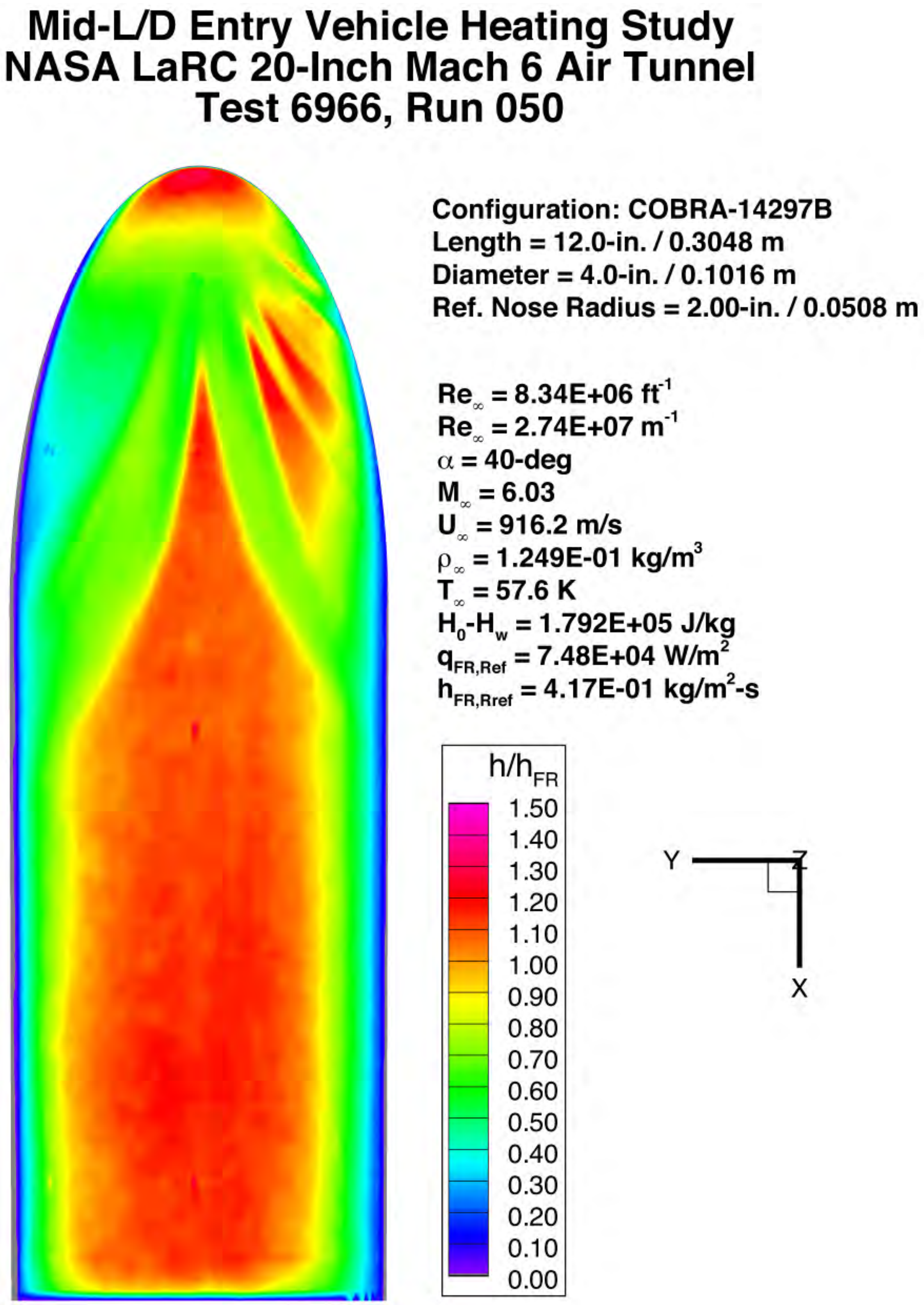

Figure 163. Run 050 Heating Data, COBRA-14297B (Model C-1), Re_∞=8.34×10^6/ft

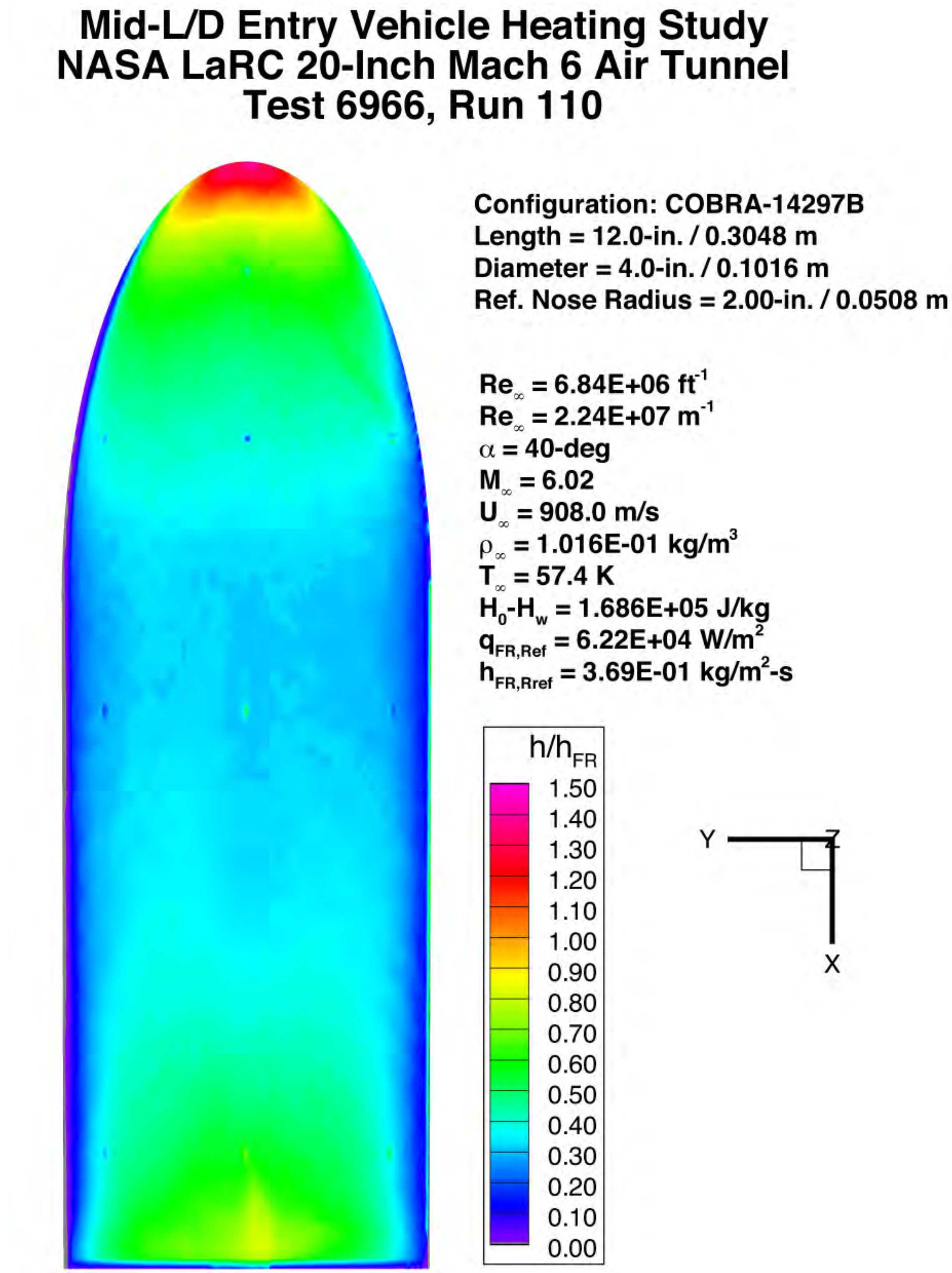

Figure 164. Run 110 Heating Data, COBRA-14297B (Model C-3), Re_∞=6.84×10^6/ft

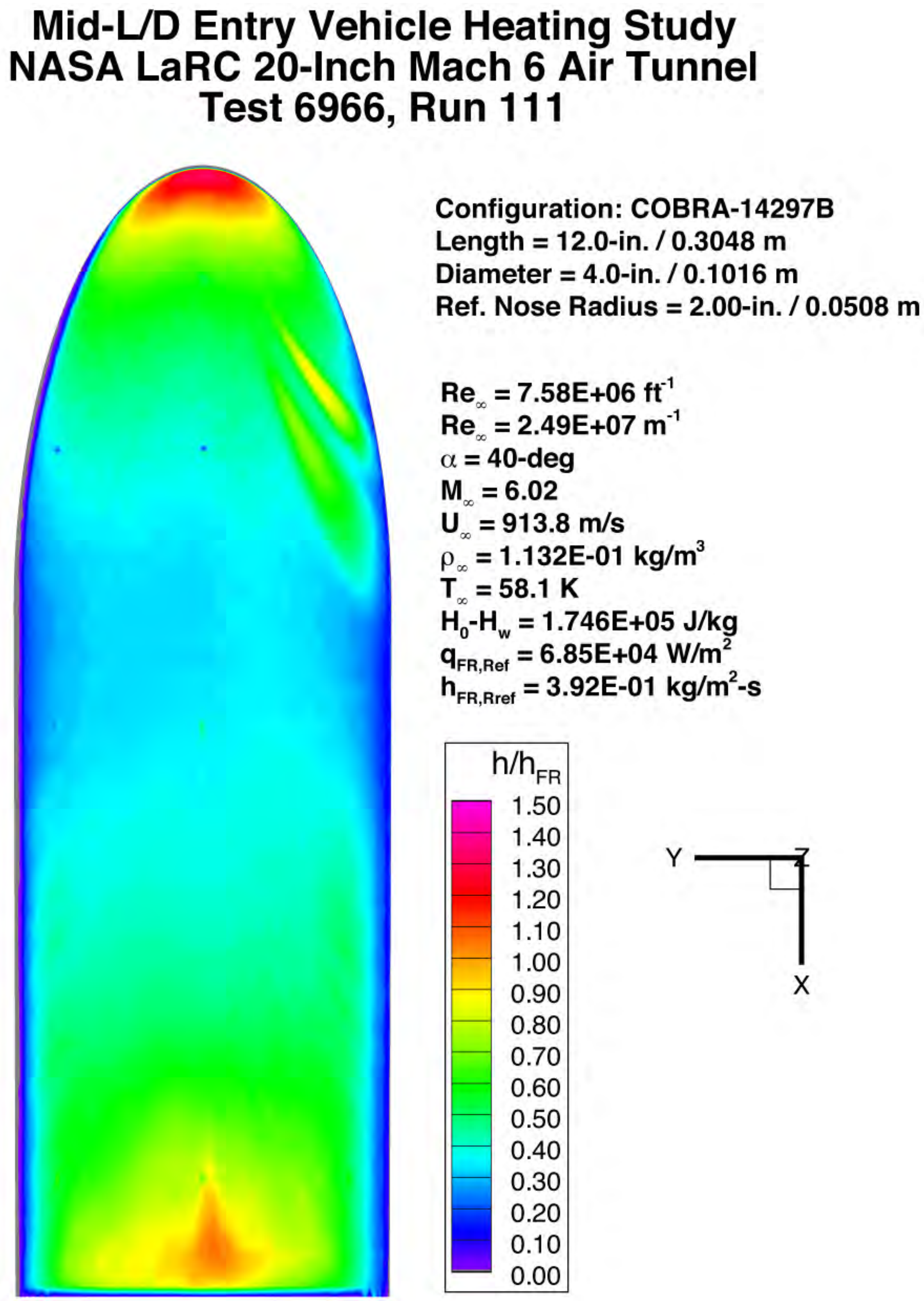

Figure 165. Run 111 Heating Data, COBRA-14297B (Model C-3), $Re_\infty=7.84\times10^6$/ft

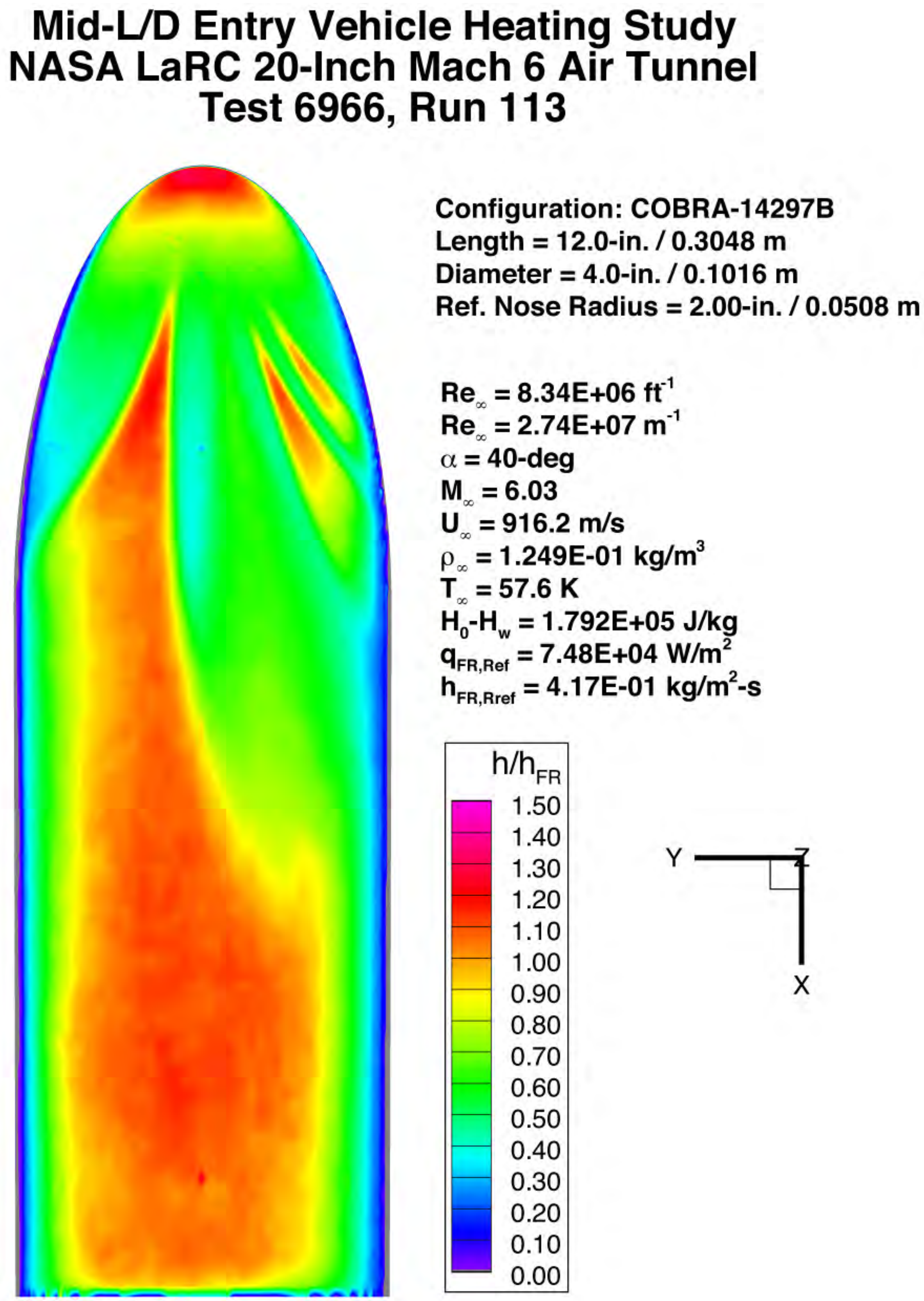

Figure 166. Run 113 Heating Data, COBRA-14297B (Model C-3), Re_∞=8.34×10^6/ft

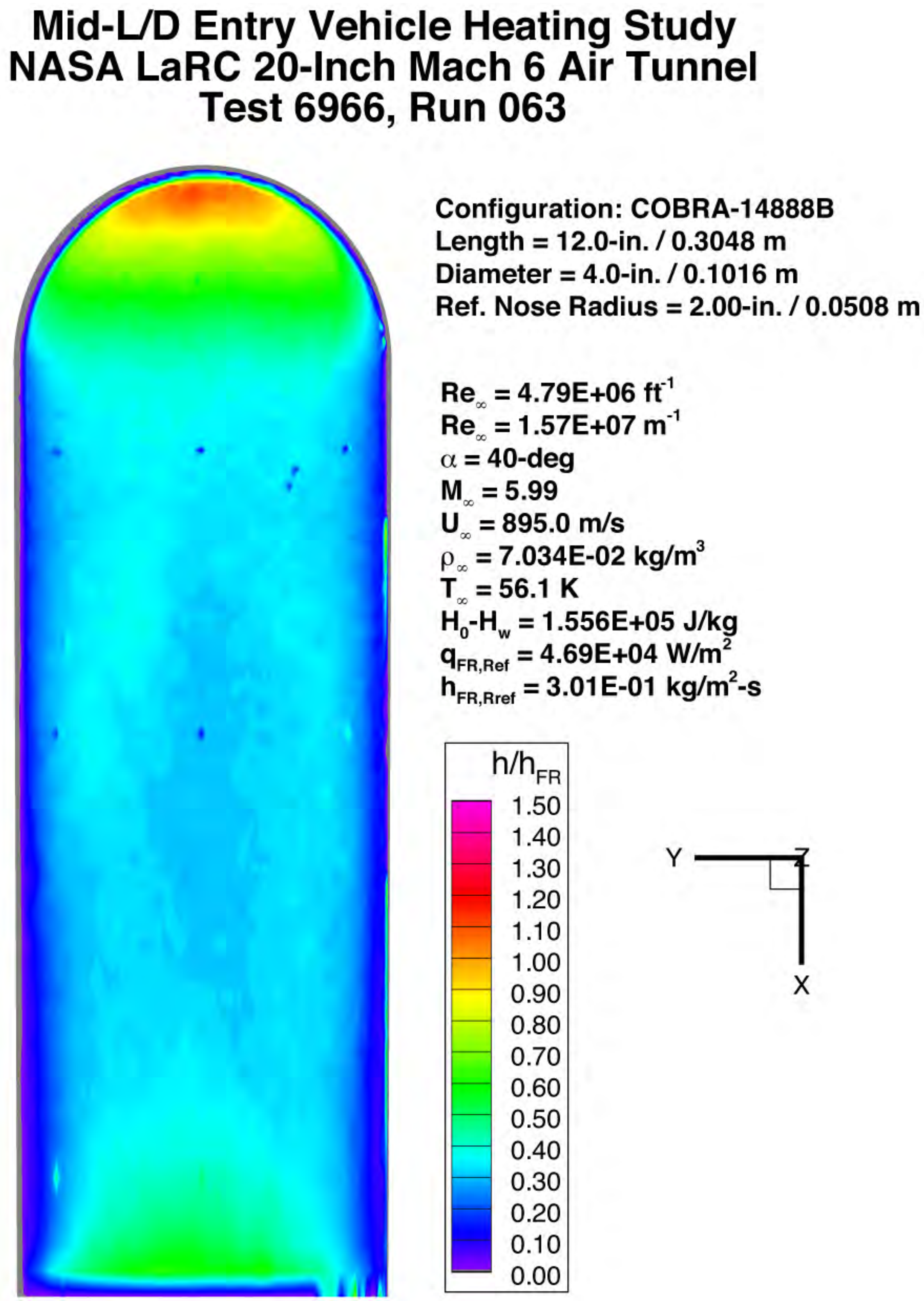

Figure 167. Run 063 Heating Data, COBRA-14888B (Model D-2), Re_∞=4.79×10^6/ft

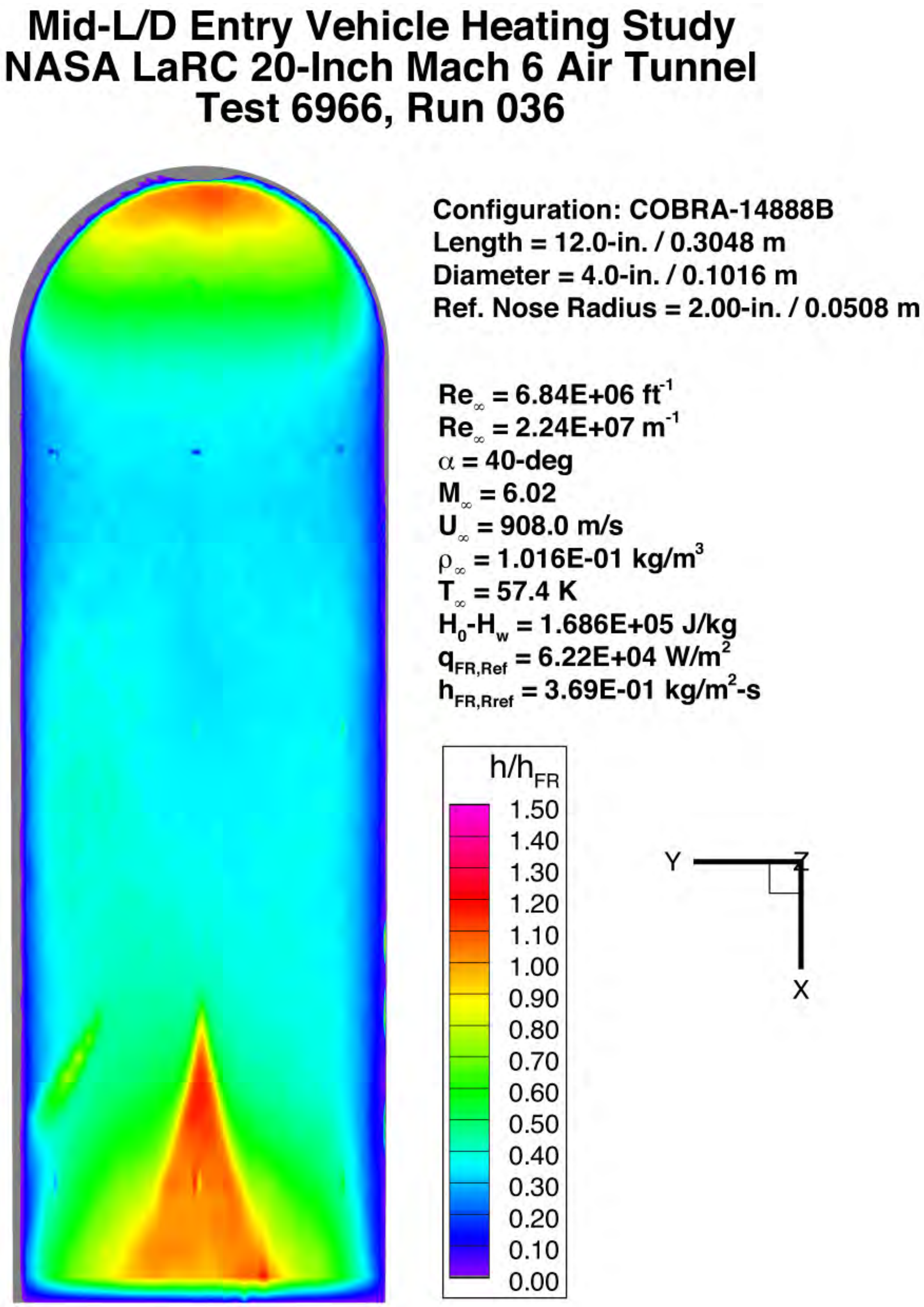

Figure 168. Run 036 Heating Data, COBRA-14888B (Model D-2), Re_∞=6.84×10^6/ft

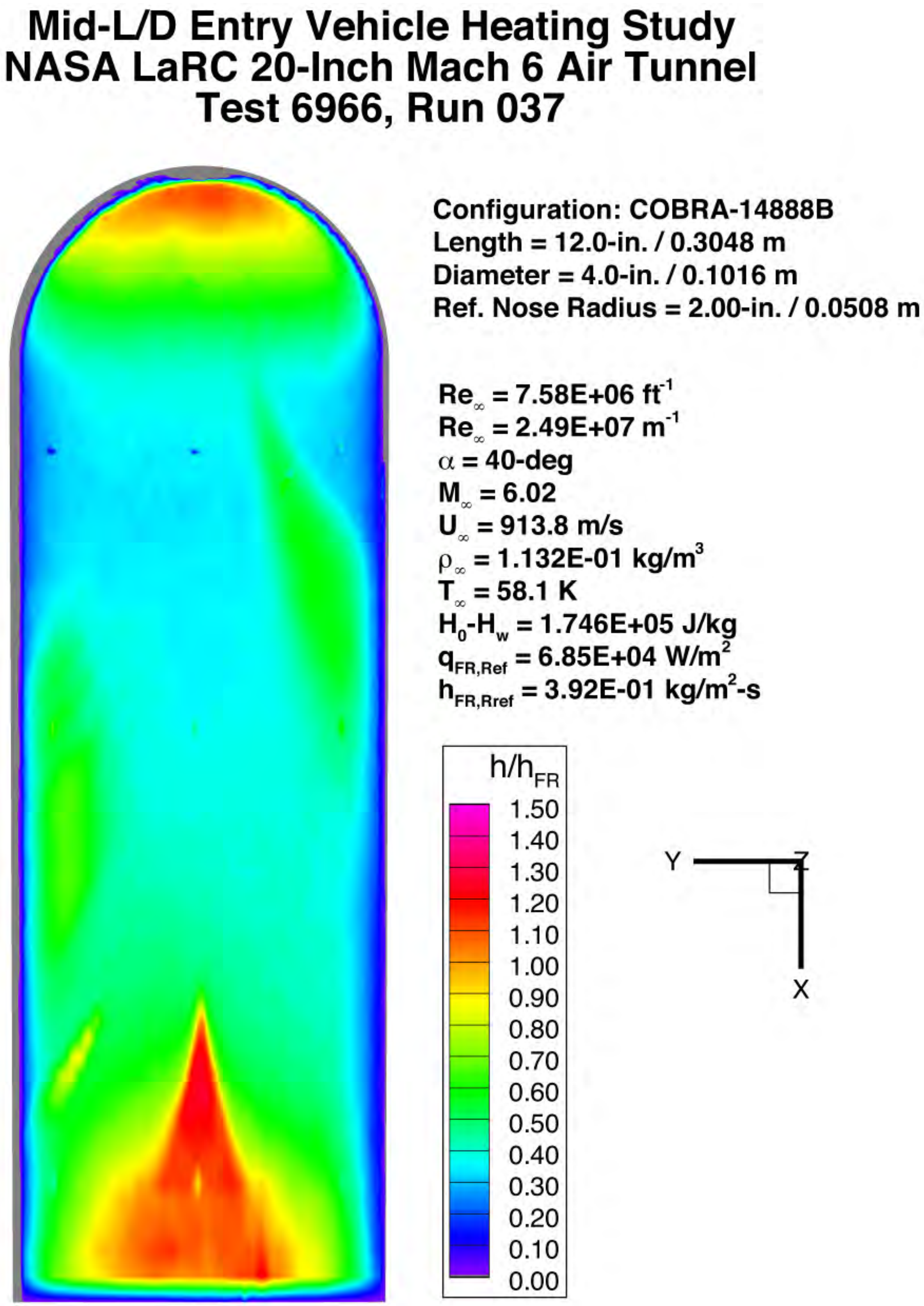

Figure 169. Run 037 Heating Data, COBRA-14888B (Model D-2), Re_∞=7.58×10^6/ft

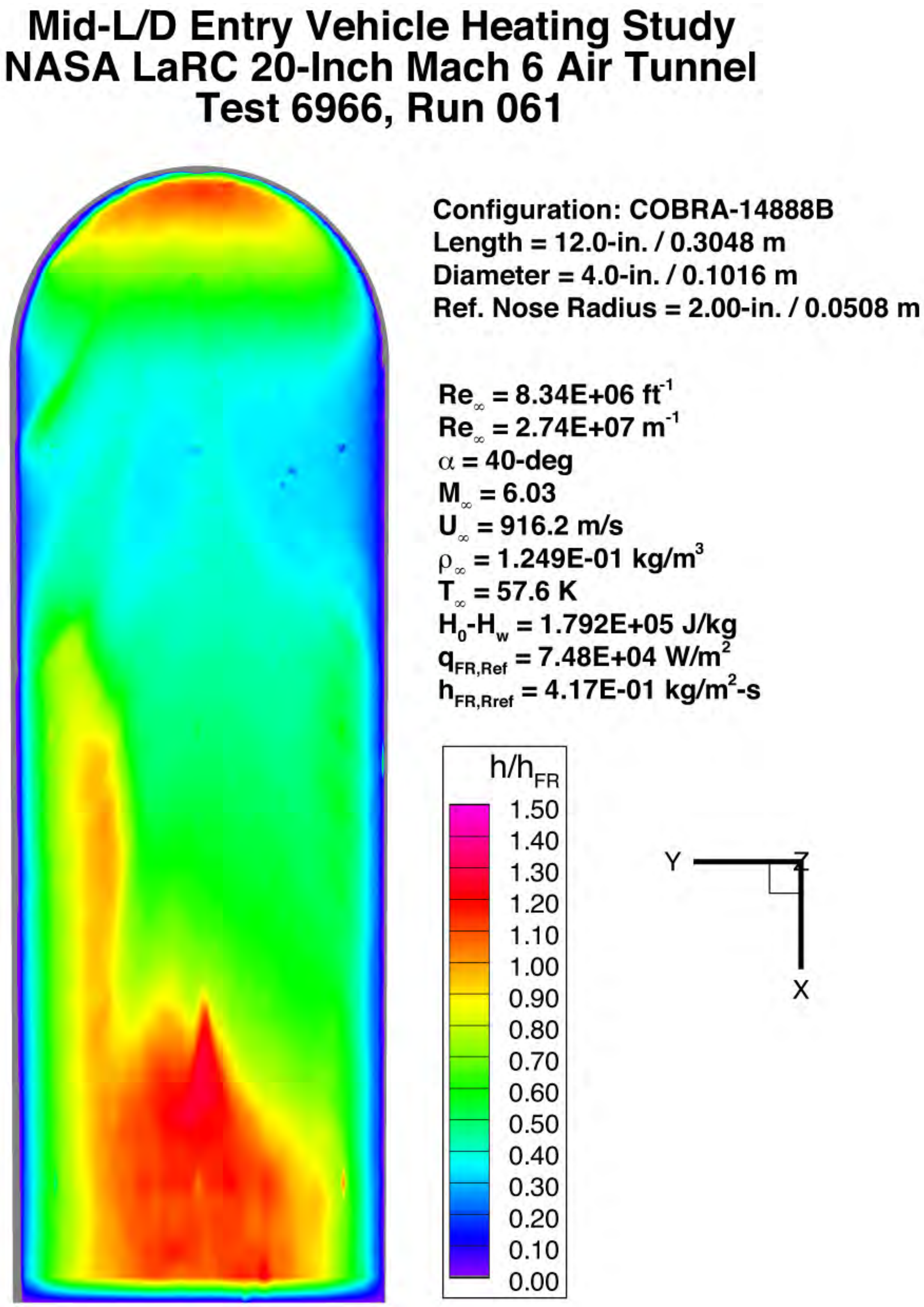

Figure 170. Run 061 Heating Data, COBRA-14888B (Model D-2), $Re_\infty=8.34\times10^6$/ft

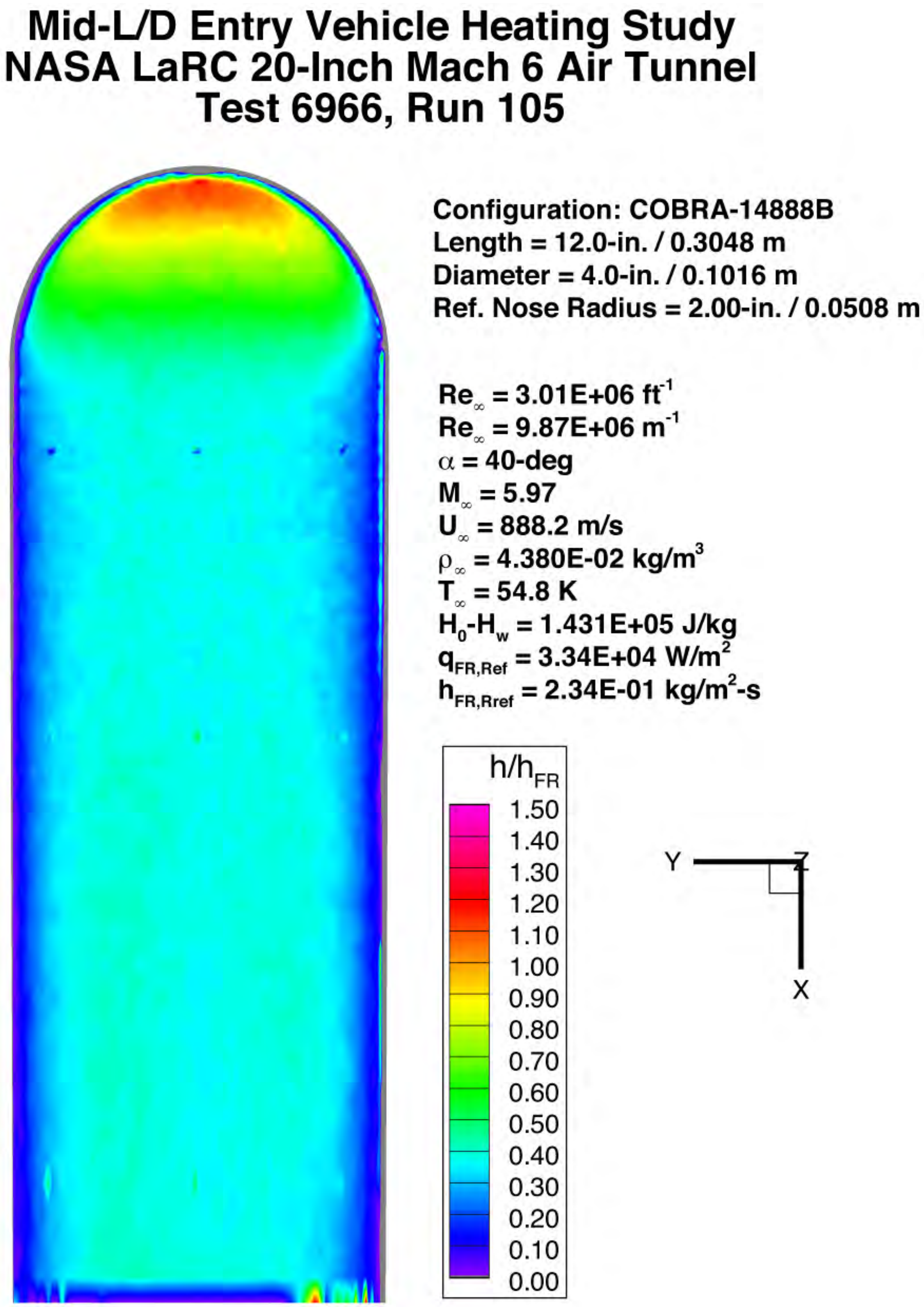

Figure 171. Run 105 Heating Data, COBRA-14888B (Model D-3), $Re_\infty = 3.01\times10^6$/ft

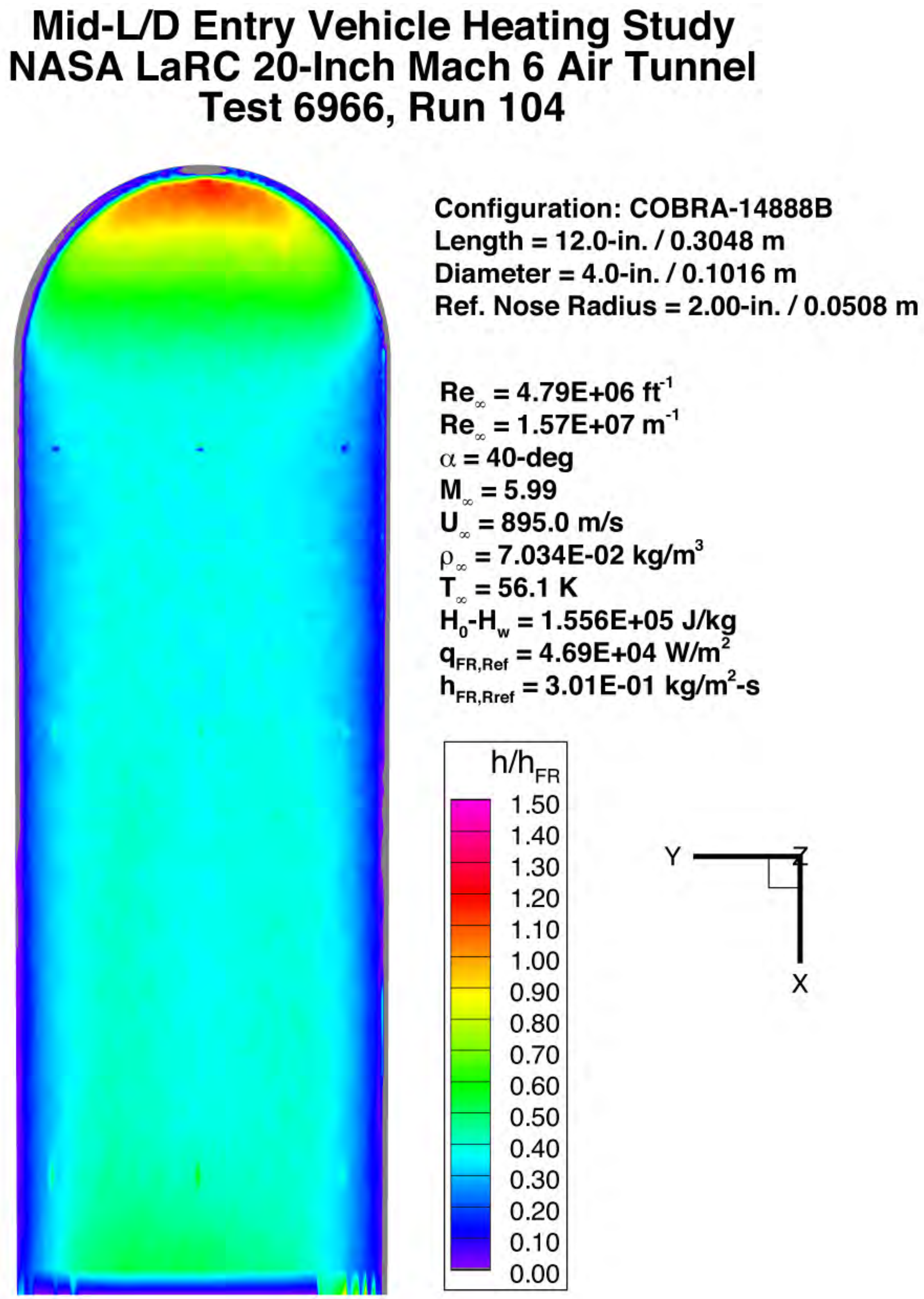

Figure 172. Run 104 Heating Data, COBRA-14888B (Model D-3), $Re_\infty=4.79\times10^6$/ft

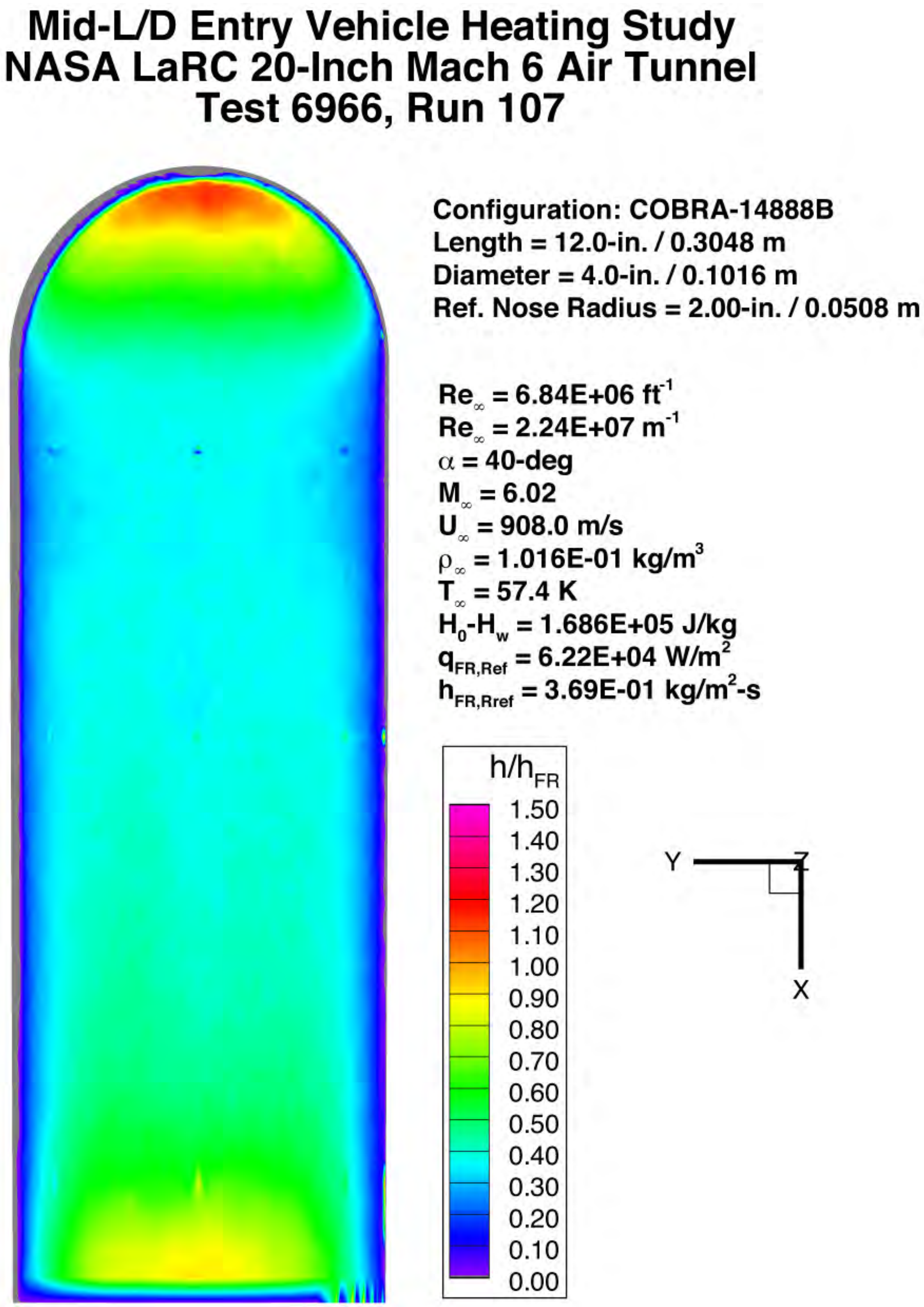

Figure 173. Run 107 Heating Data, COBRA-14888B (Model D-3), Re_∞=6.84×10^6/ft

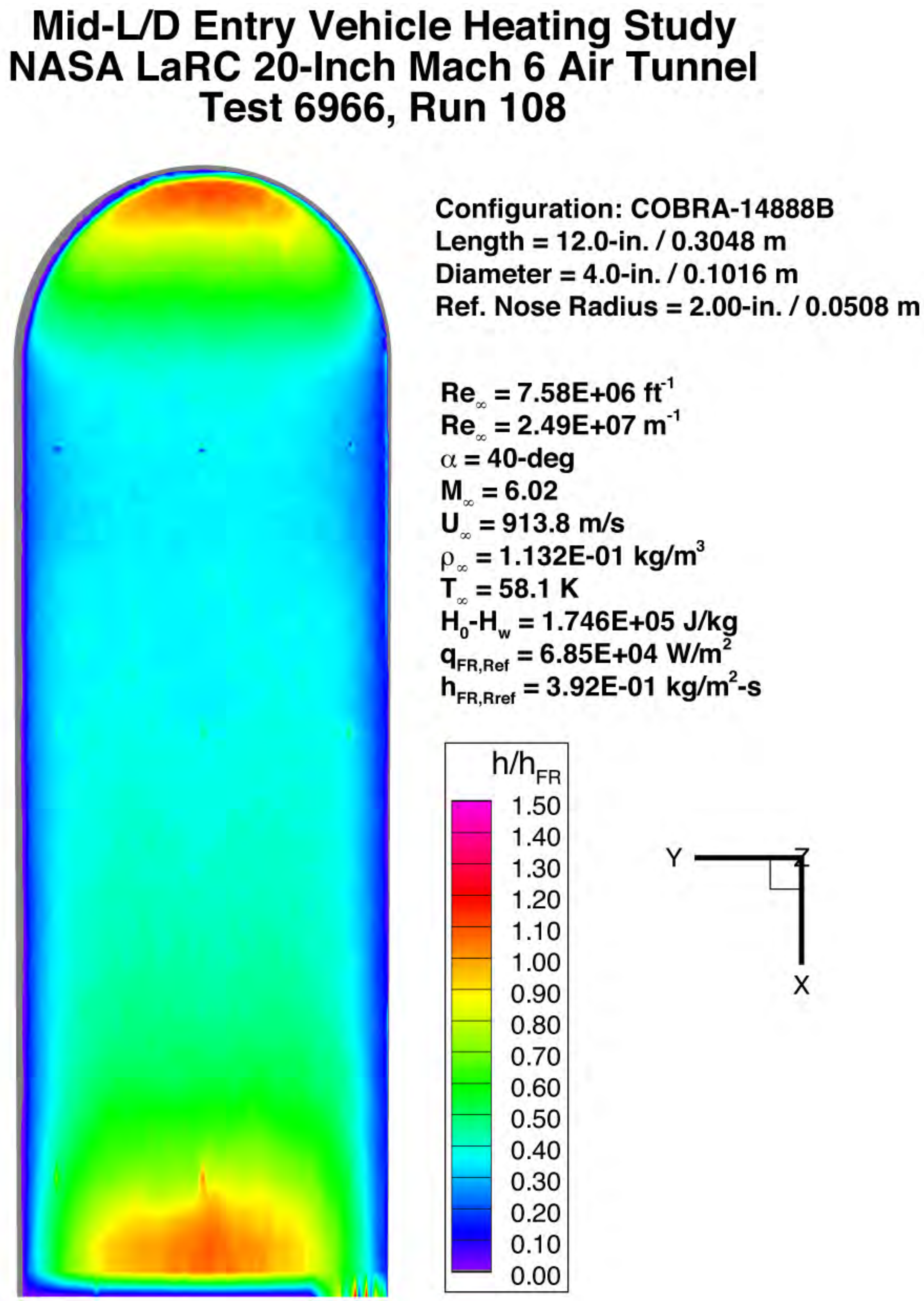

Figure 174. Run 108 Heating Data, COBRA-14888B (Model D-3), $Re_\infty=7.58\times10^6$/ft

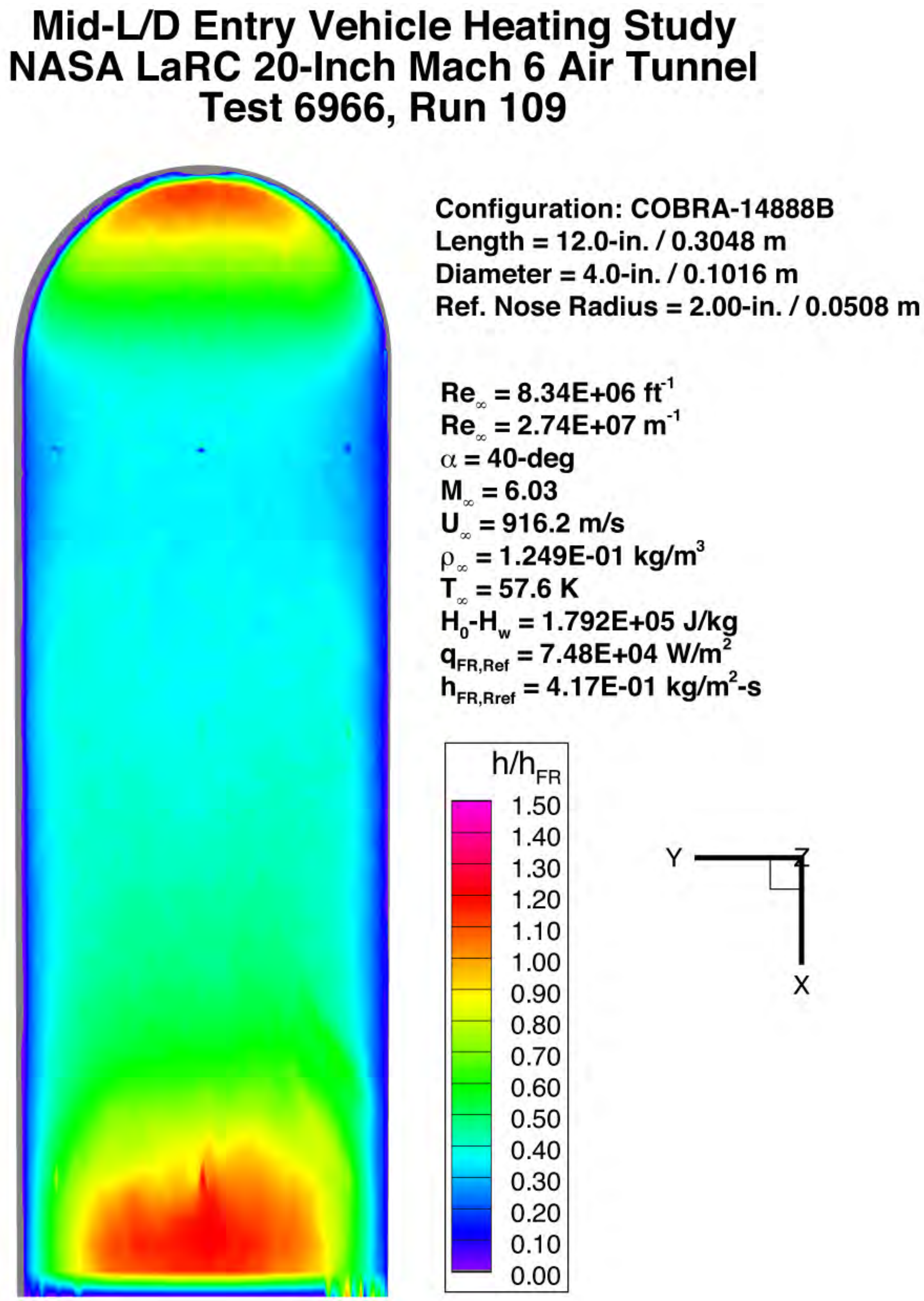

Figure 175. Run 109 Heating Data, COBRA-14888B (Model D-3), $Re_\infty=8.34\times10^6$/ft

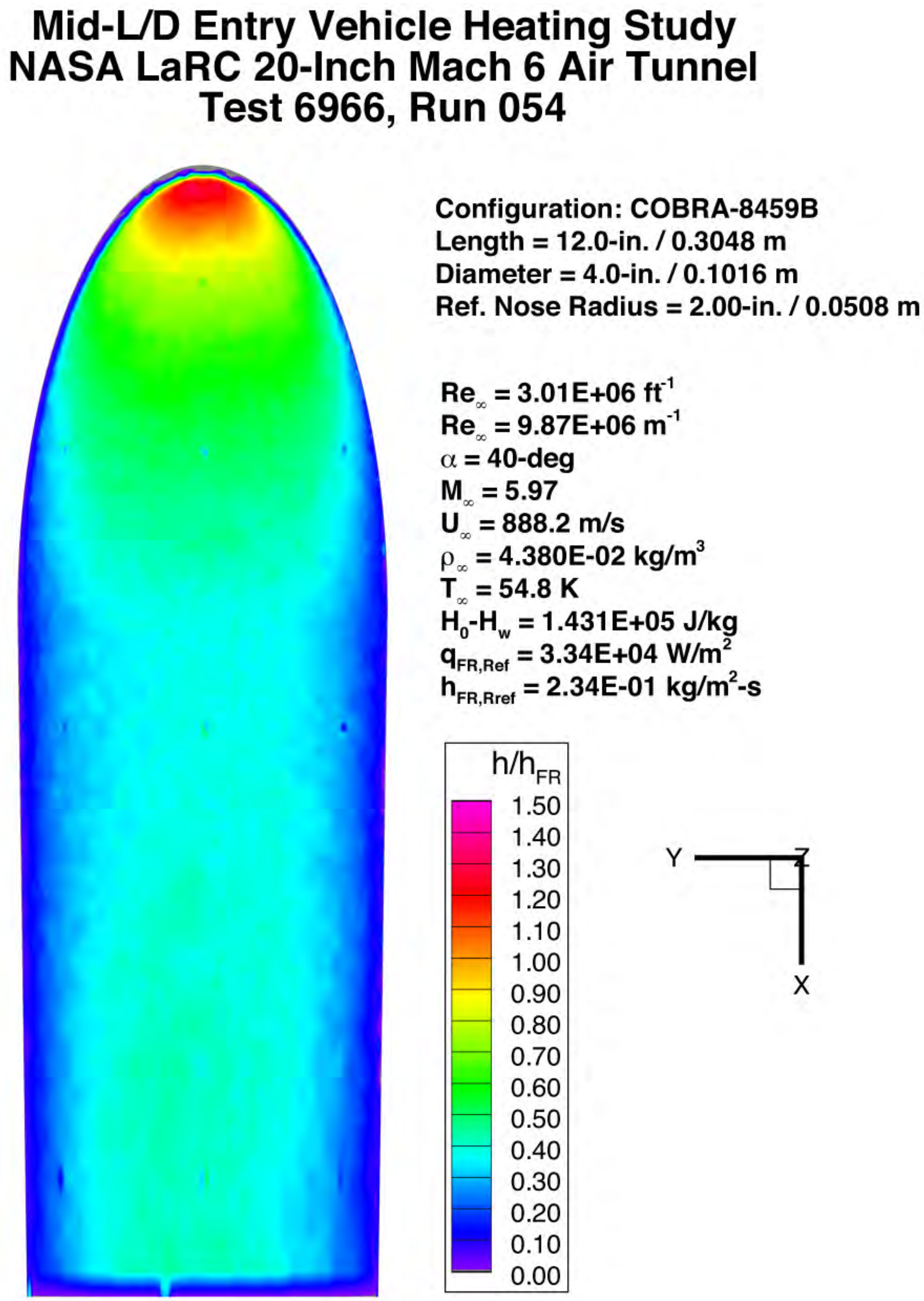

Figure 176. Run 054 Heating Data, COBRA-8459B (Model E-1), Re_∞=3.01×10^6/ft

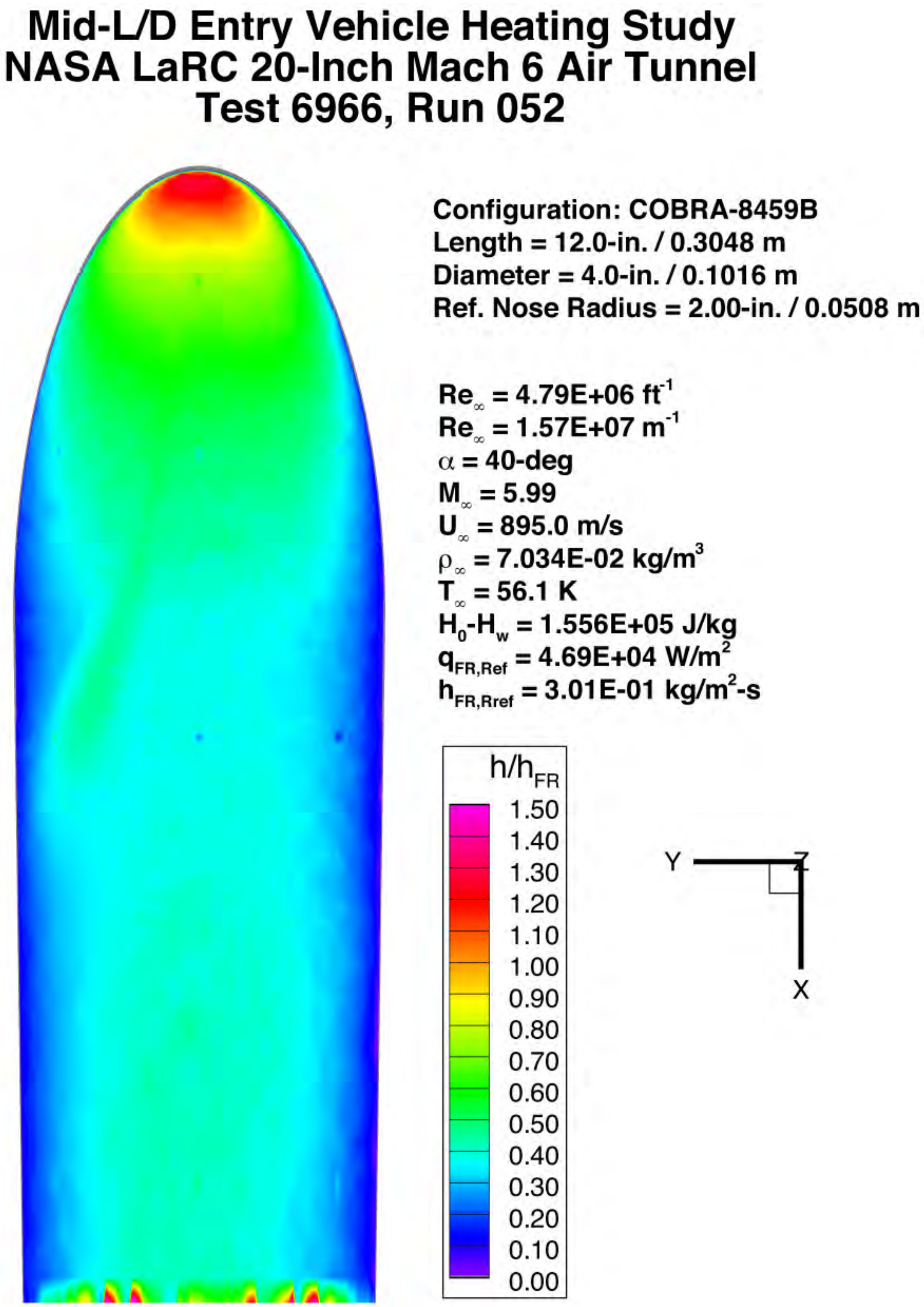

Figure 177. Run 052 Heating Data, COBRA-8459B (Model E-1), Re_∞=4.79×10^6/ft

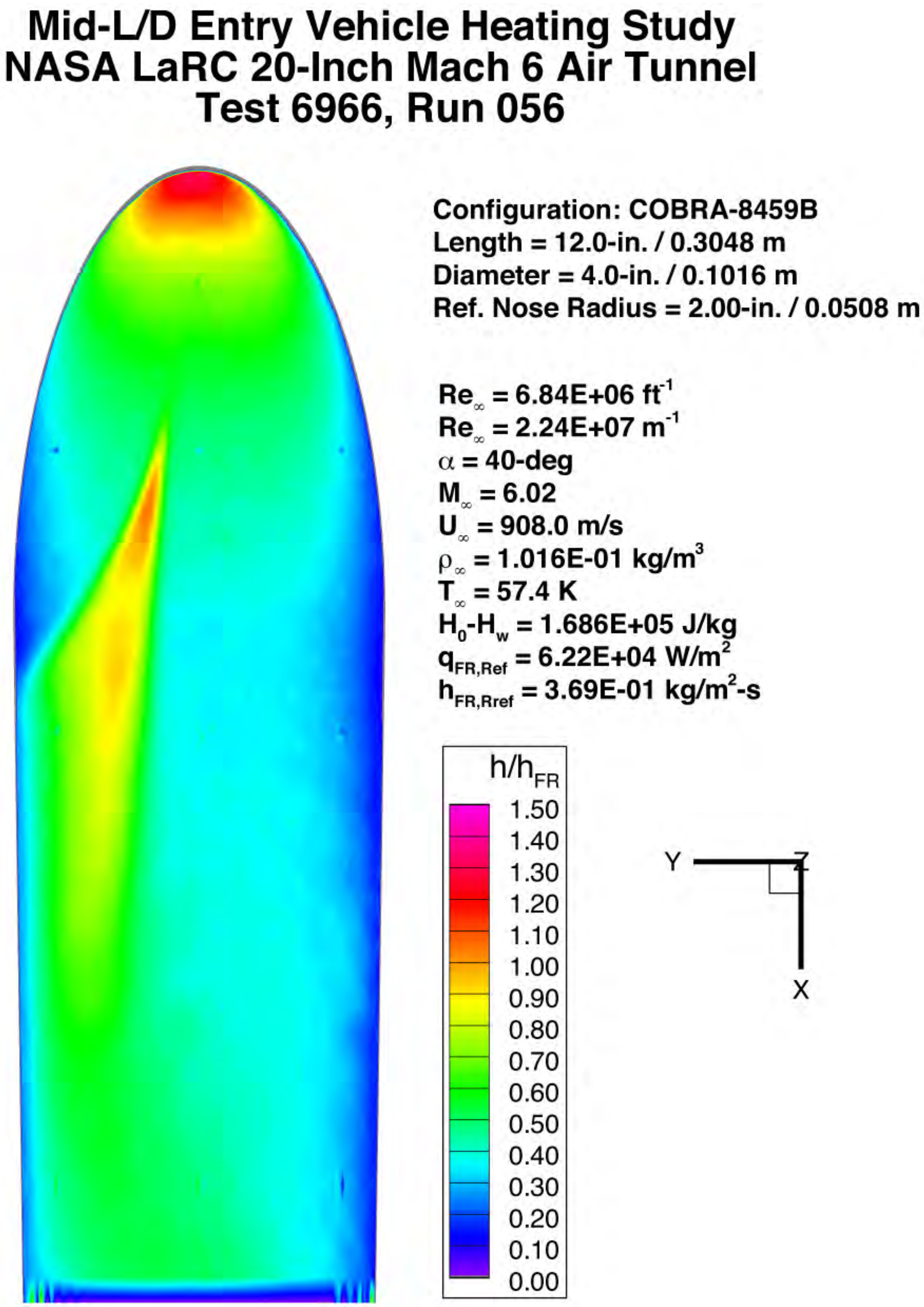

Figure 178. Run 056 Heating Data, COBRA-8459B (Model E-1), Re_{∞}=6.84×10^6/ft

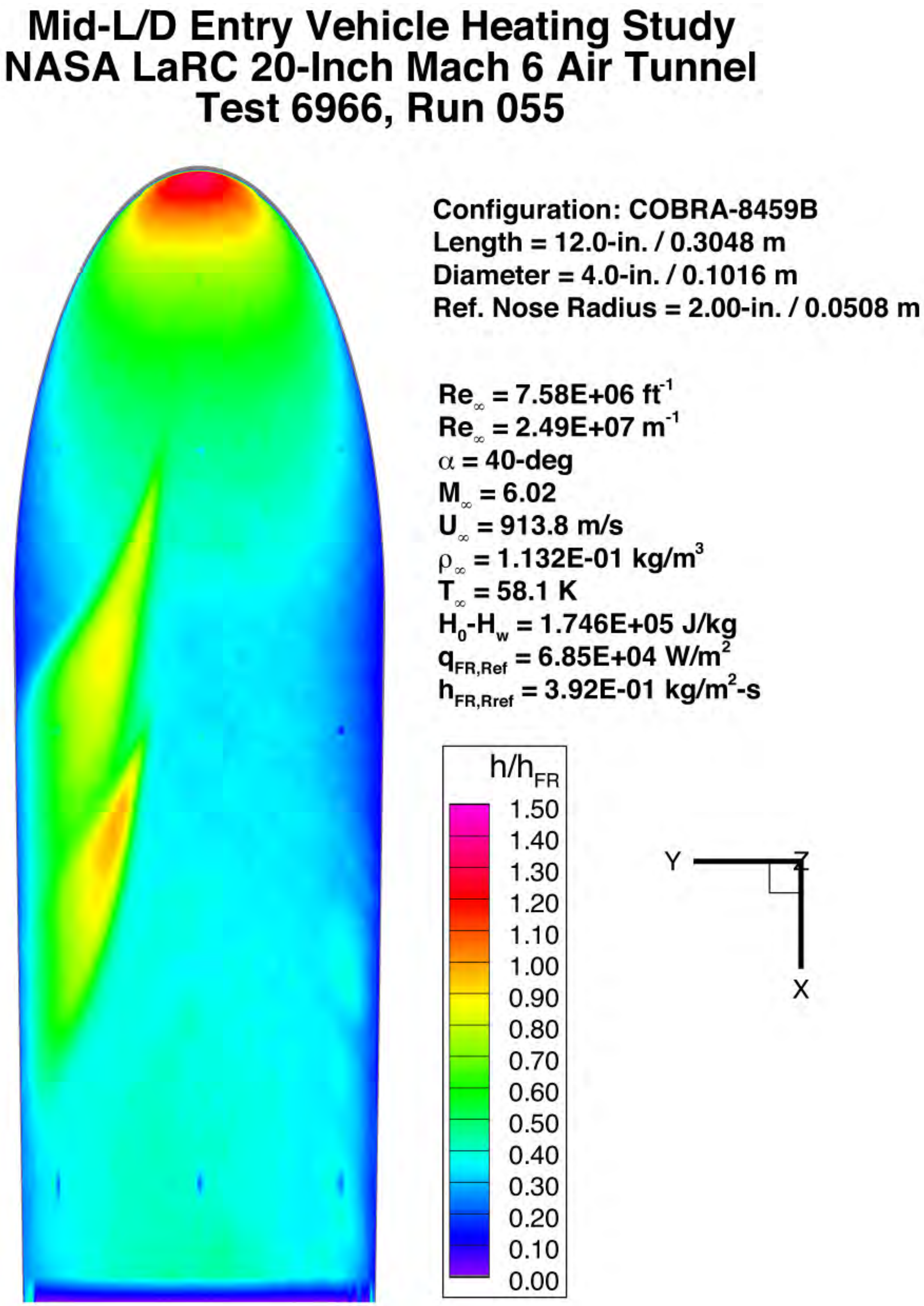

Figure 179. Run 055 Heating Data, COBRA-8459B (Model E-1), $Re_\infty=7.58\times10^6$/ft

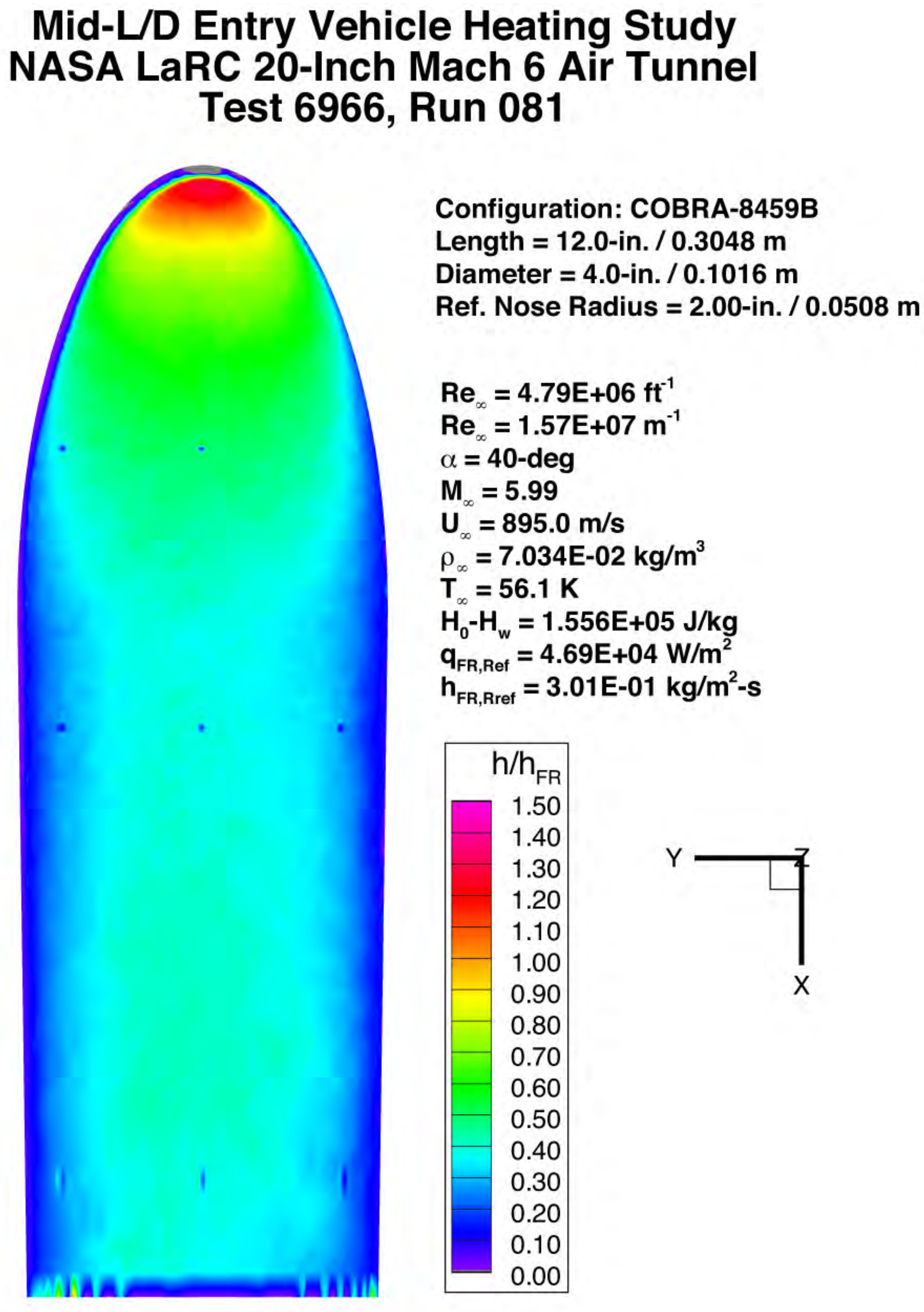

Figure 180. Run 081 Heating Data, COBRA-8459B (Model E-2), Re_∞=4.79×10^6/ft

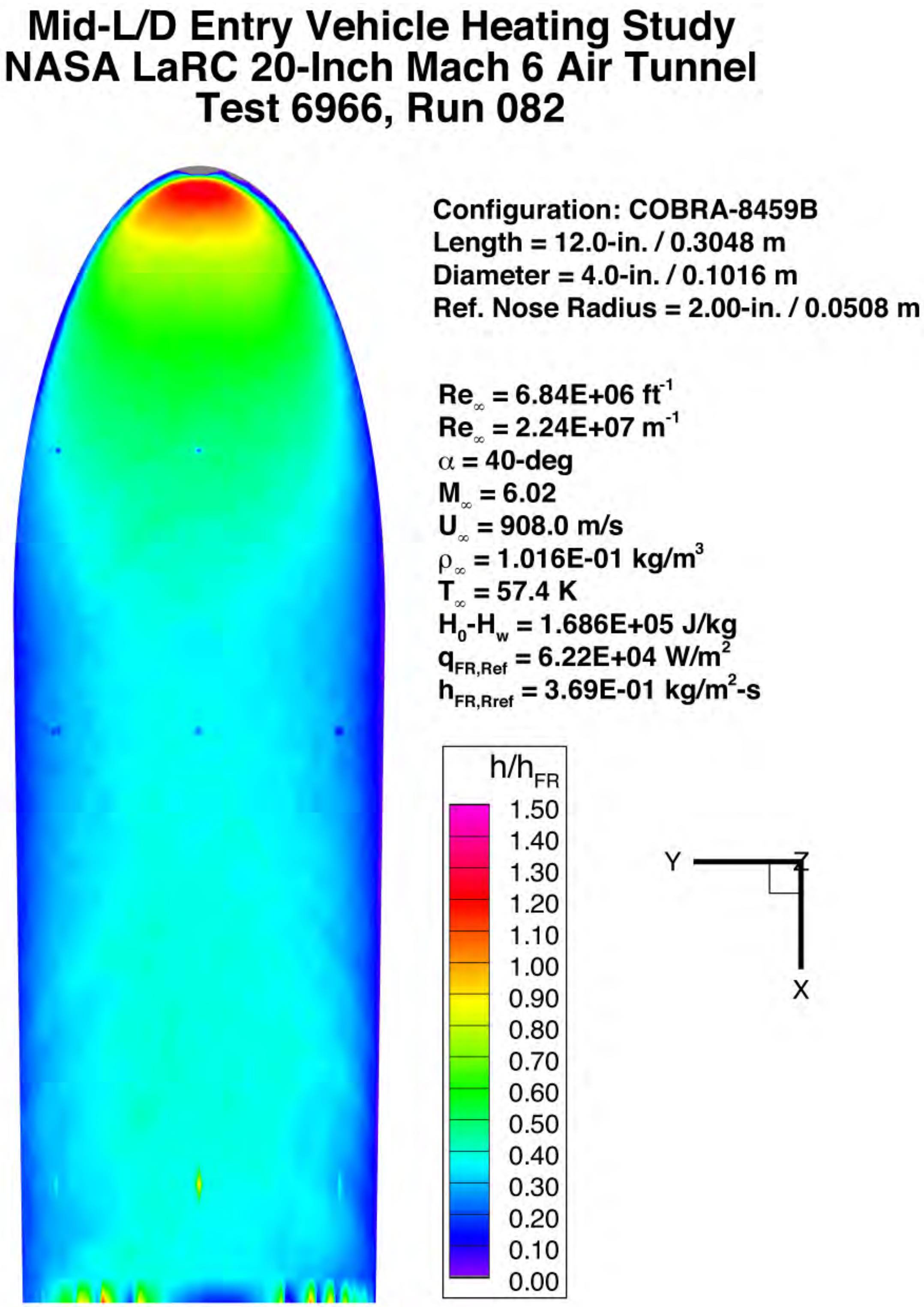

Figure 181. Run 082 Heating Data, COBRA-8459B (Model E-2), $Re_\infty = 6.84\times10^6$/ft

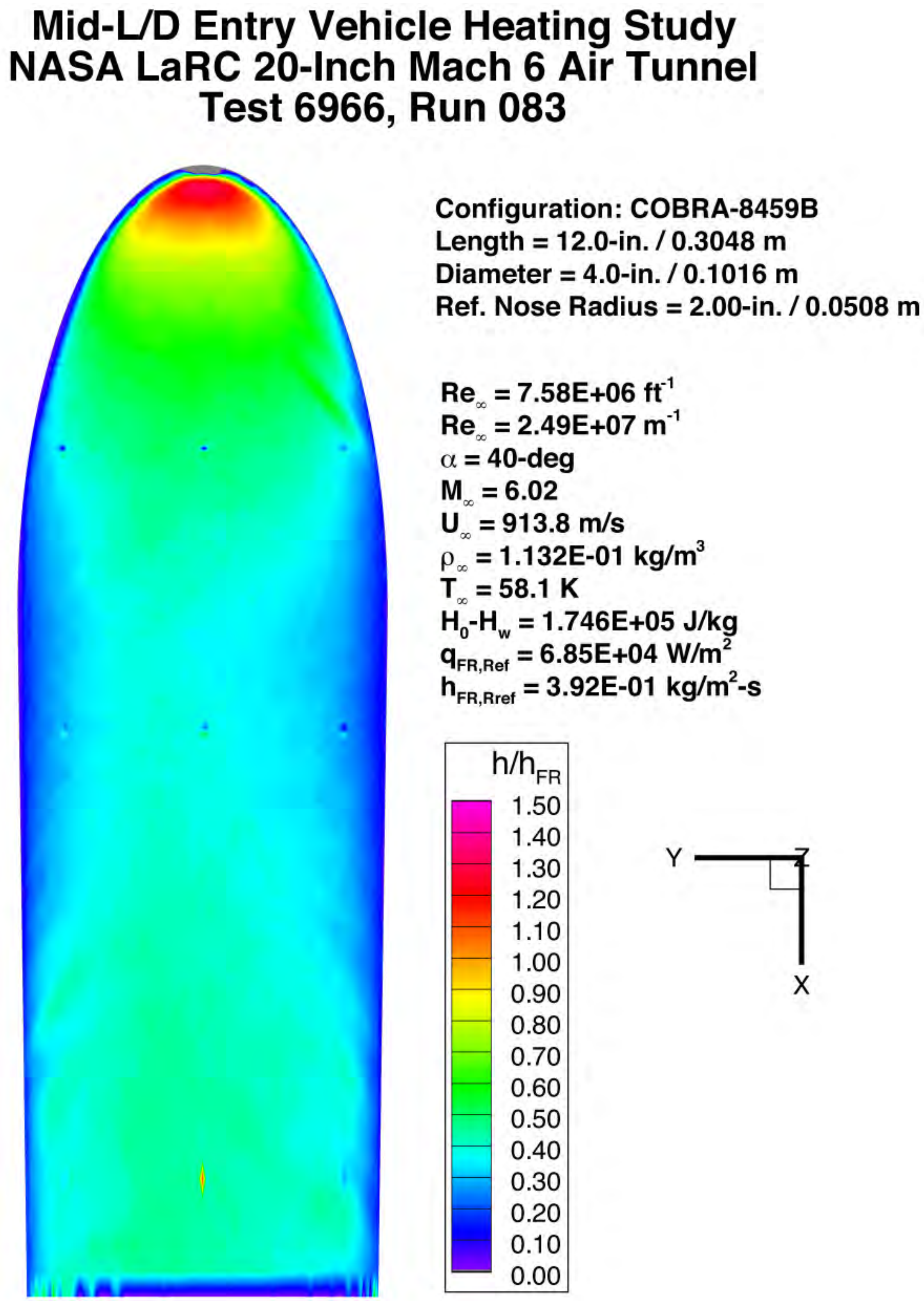

Figure 182. Run 083 Heating Data, COBRA-8459B (Model E-2), Re_∞=7.58×10^6/ft

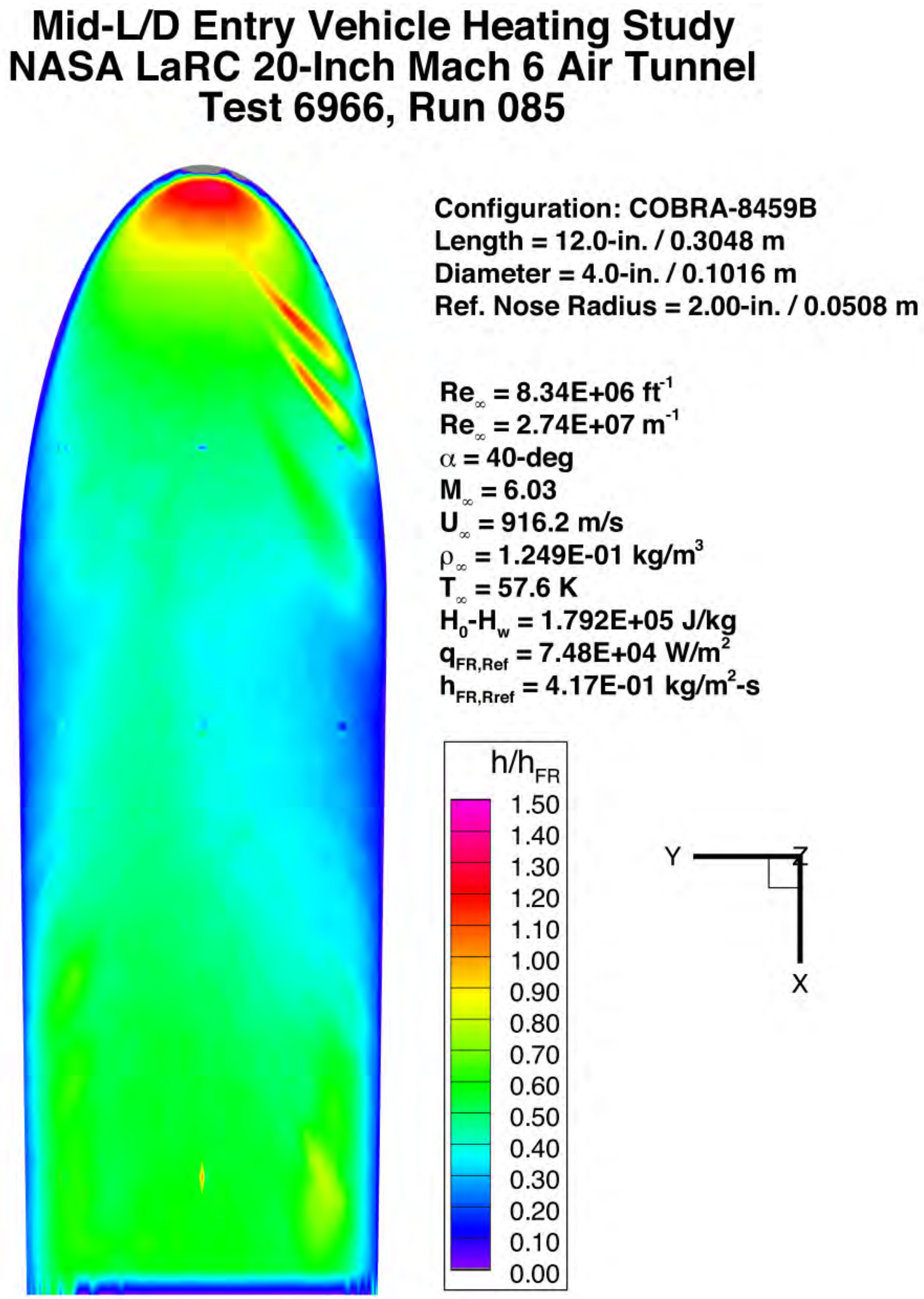

Figure 183. Run 085 Heating Data, COBRA-8459B (Model E-2), $Re_\infty=8.34\times10^6$/ft

Appendix C. Hammerhead-Biconic Global Image Heating Data

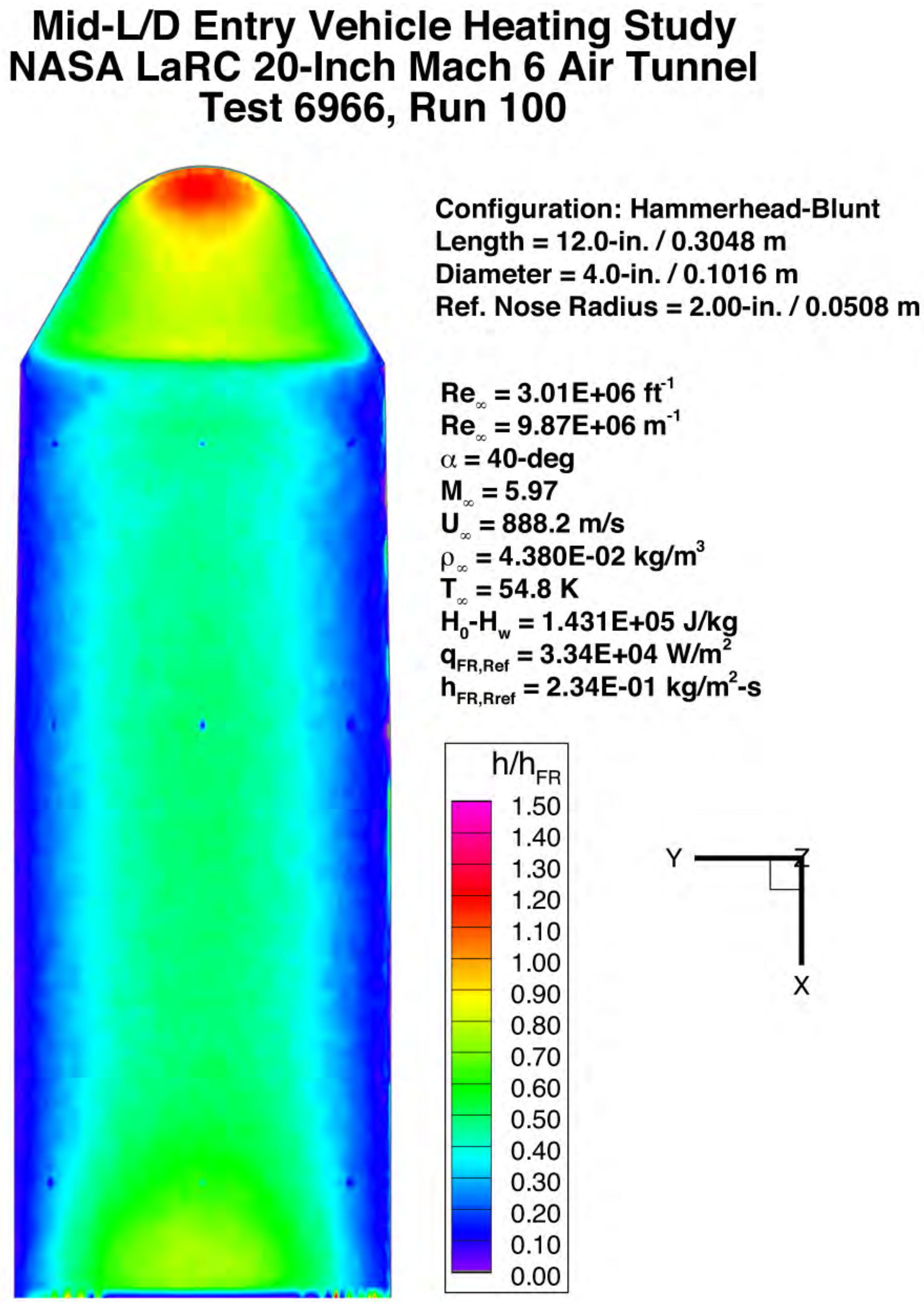

Figure 184. Run 100 Heating Data, Hammerhead-Blunt, $Re_\infty=3.01\times10^6$/ft

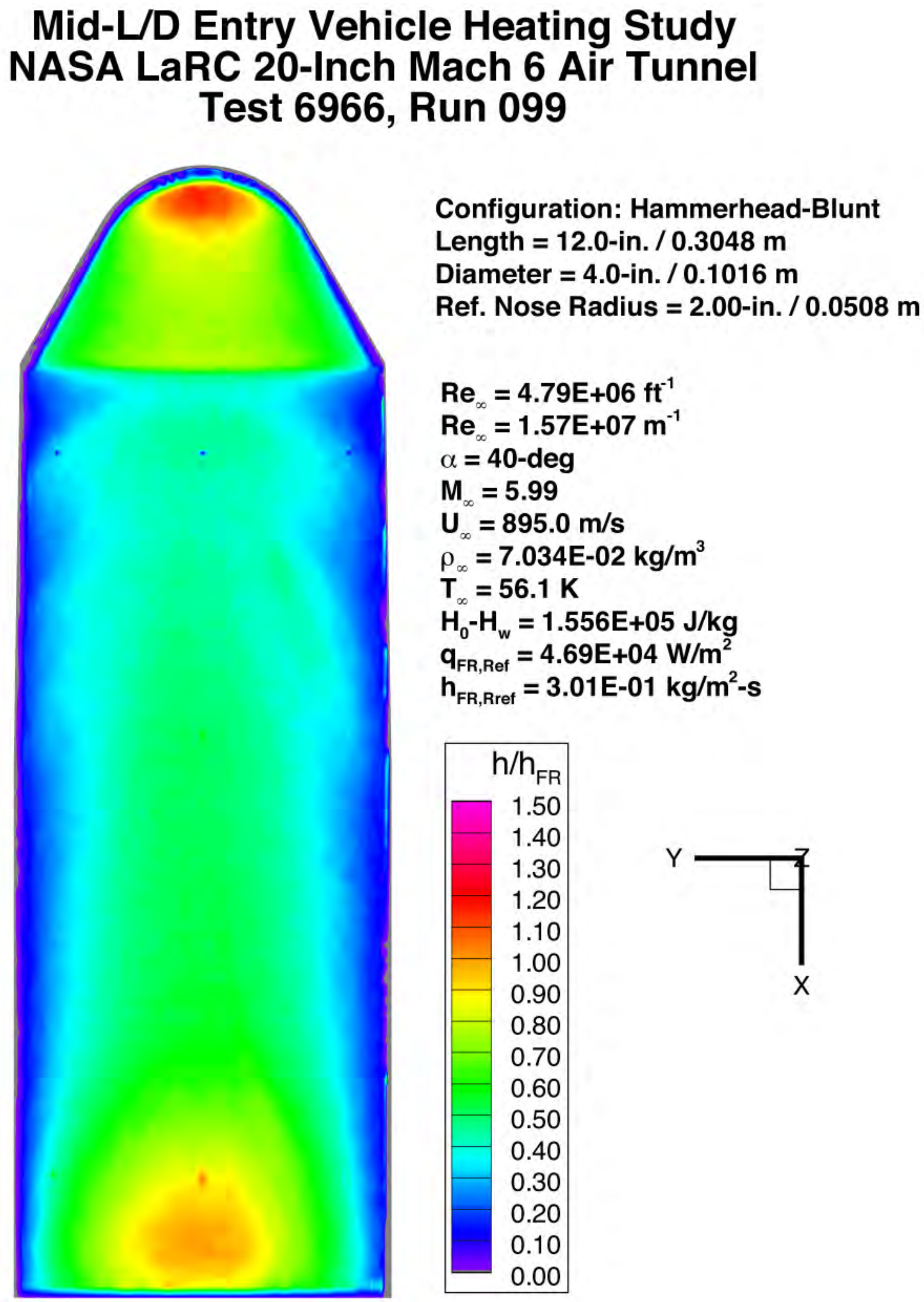

Figure 185. Run 099 Heating Data, Hammerhead-Blunt, $Re_\infty=4.79\times10^6$/ft

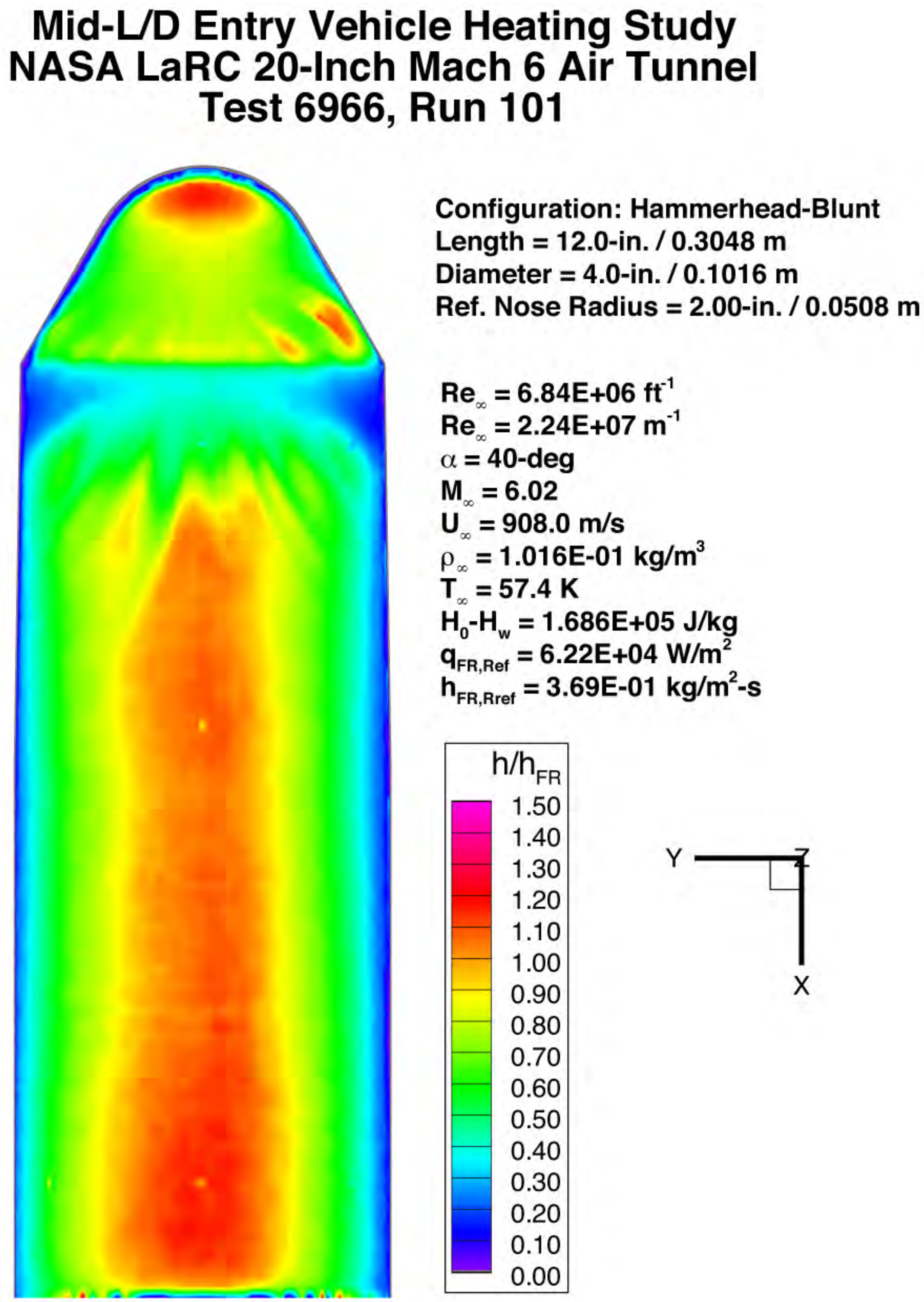

Figure 186. Run 101 Heating Data, Hammerhead-Blunt, $Re_\infty = 6.84\times10^6$/ft

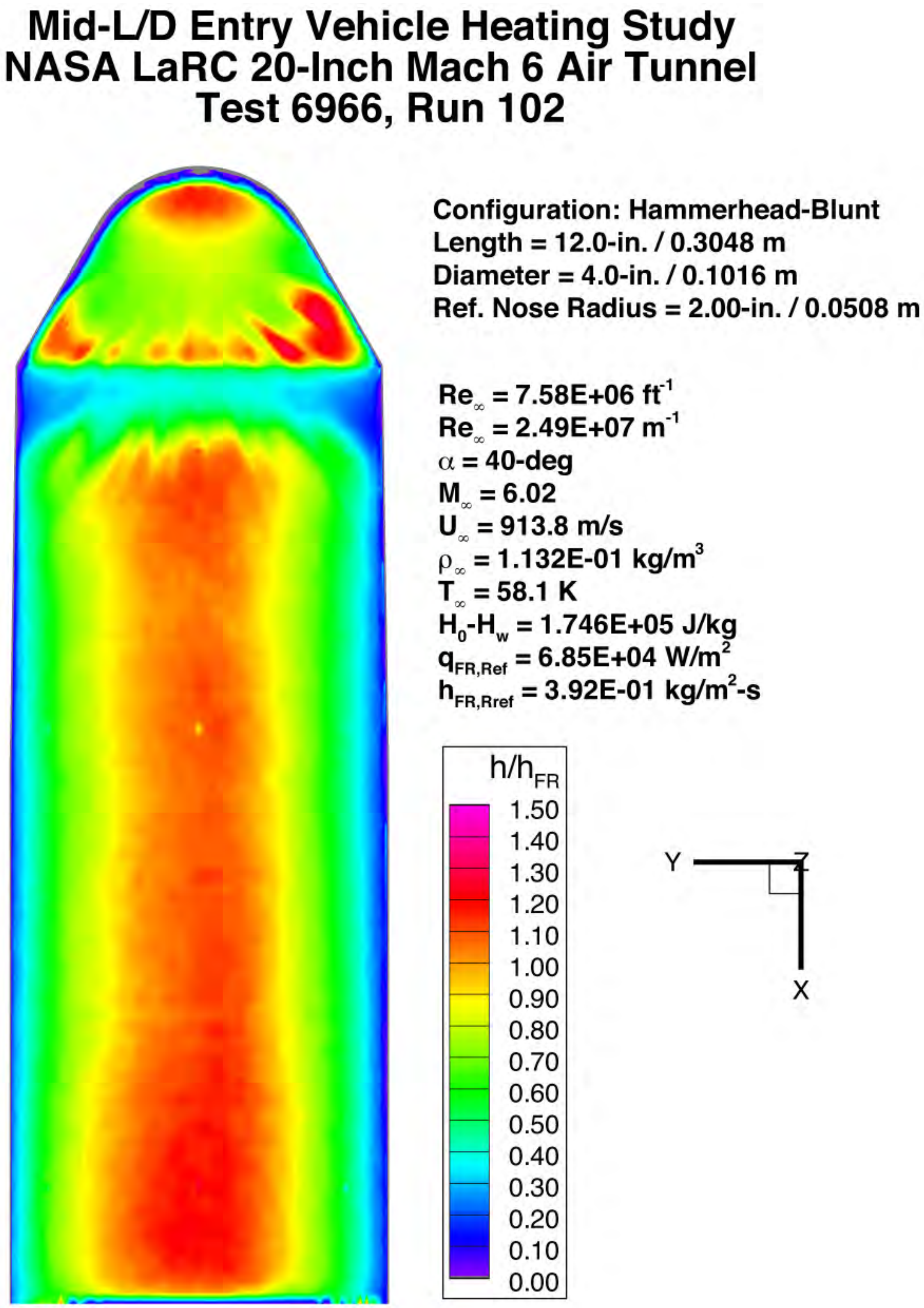

Figure 187. Run 102 Heating Data, Hammerhead-Blunt, Re_∞=7.58×10^6/ft

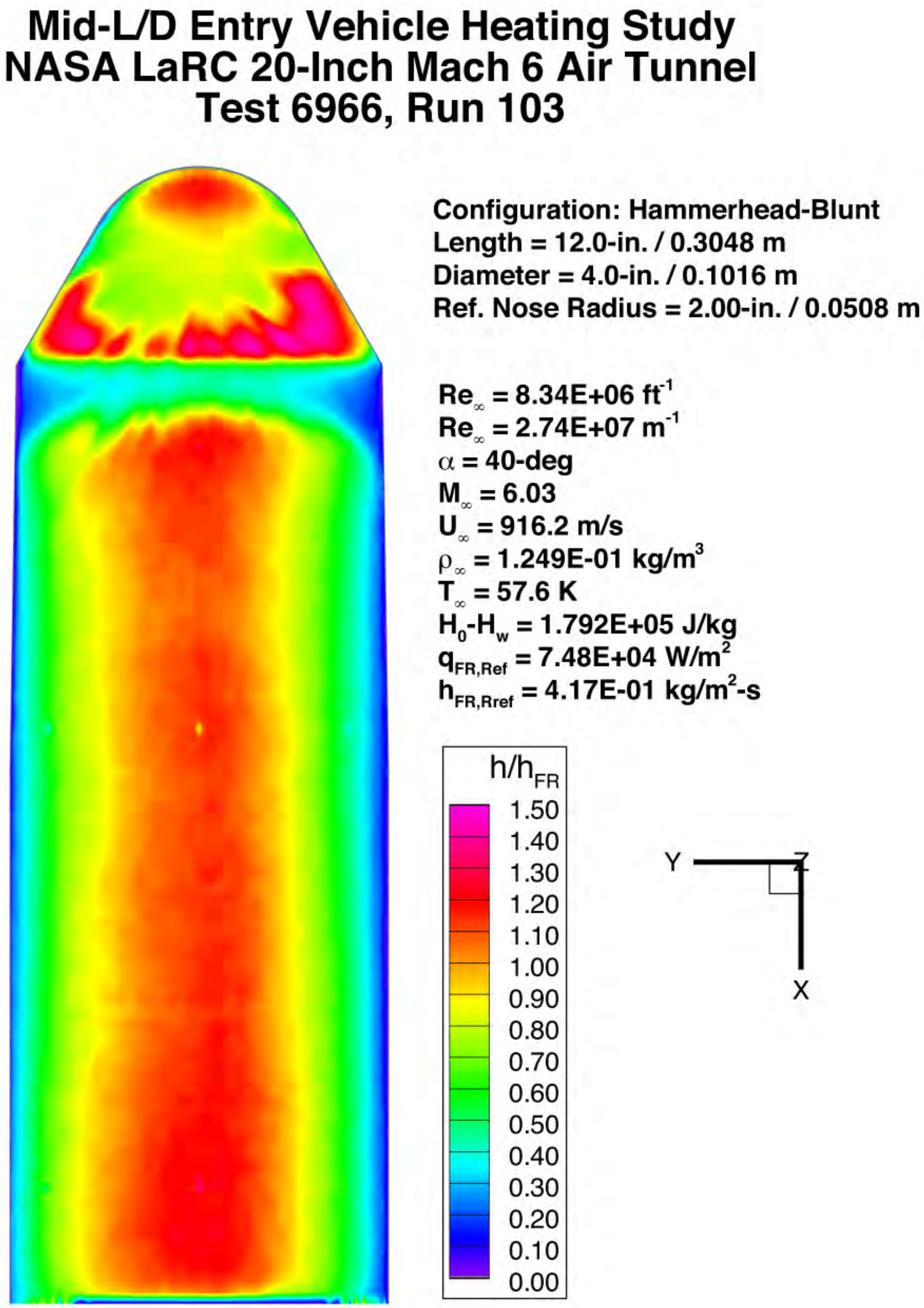

Figure 188. Run 103 Heating Data, Hammerhead-Blunt, Re_∞=8.34×10^6/ft

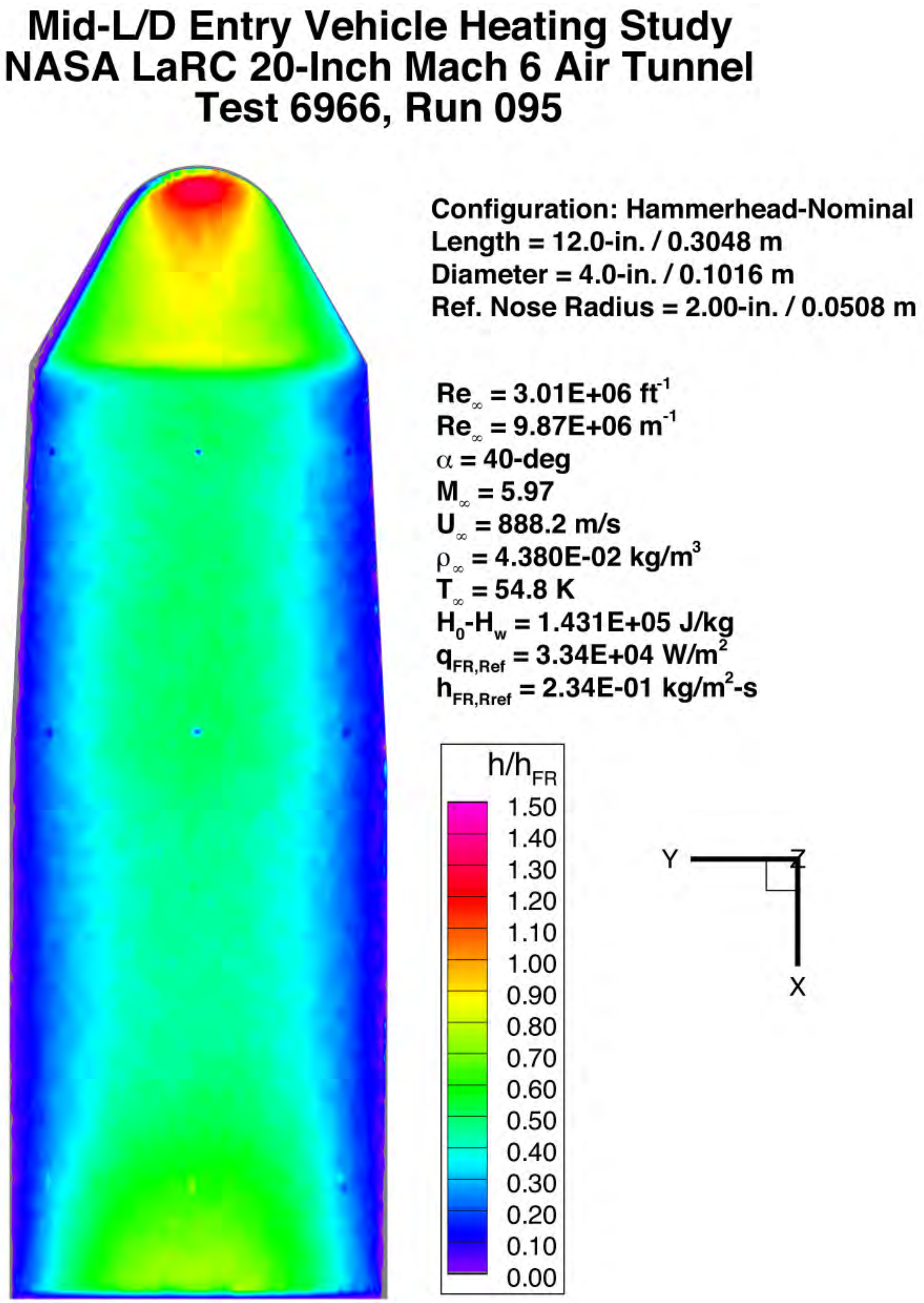

Figure 189. Run 095 Heating Data, Hammerhead-Nominal, $Re_\infty = 3.01 \times 10^6$/ft

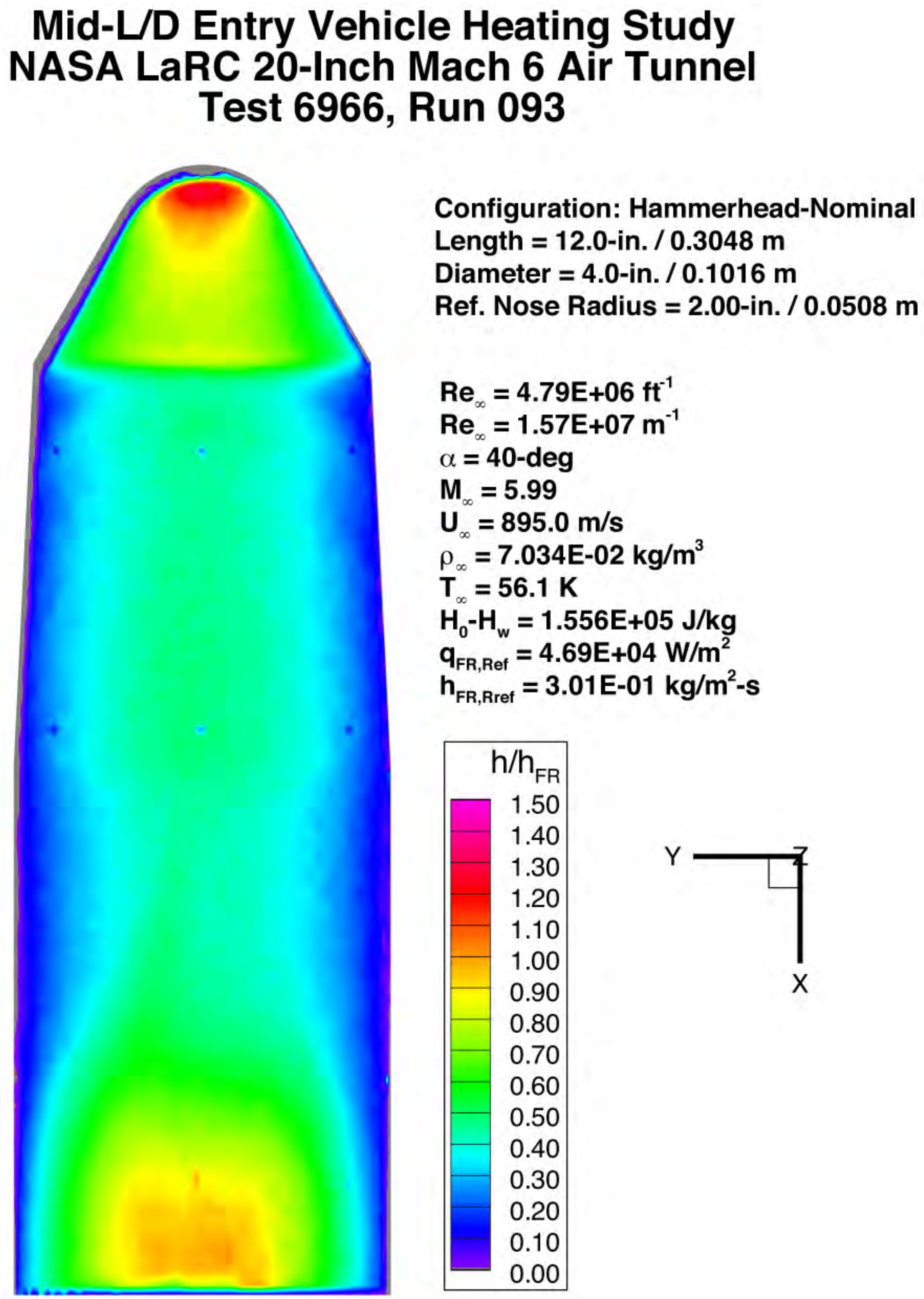

Figure 190. Run 093 Heating Data, Hammerhead-Nominal, $Re_\infty=4.79\times10^6$/ft

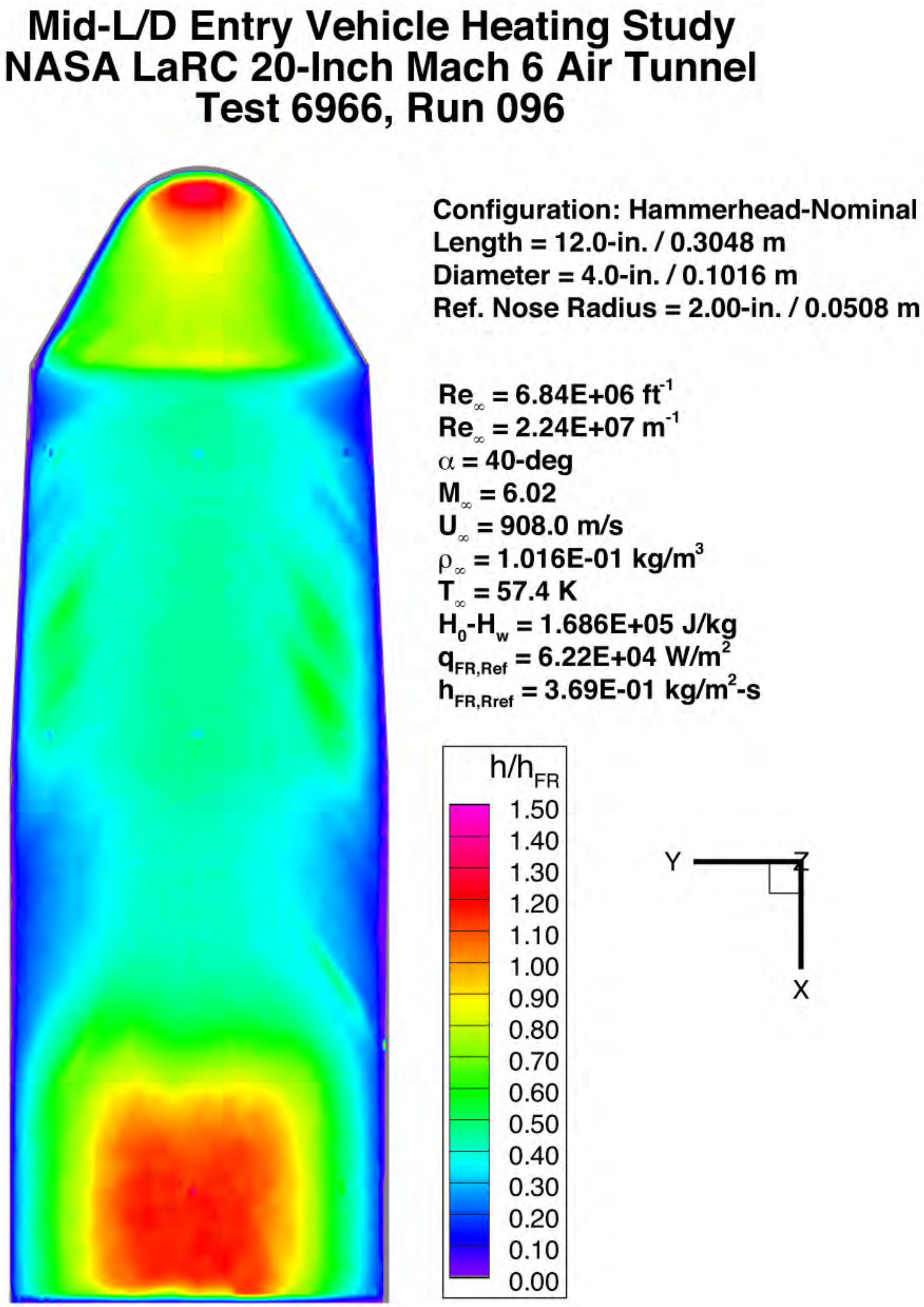

Figure 191. Run 096 Heating Data, Hammerhead-Nominal, Re_∞=6.84×10^6/ft

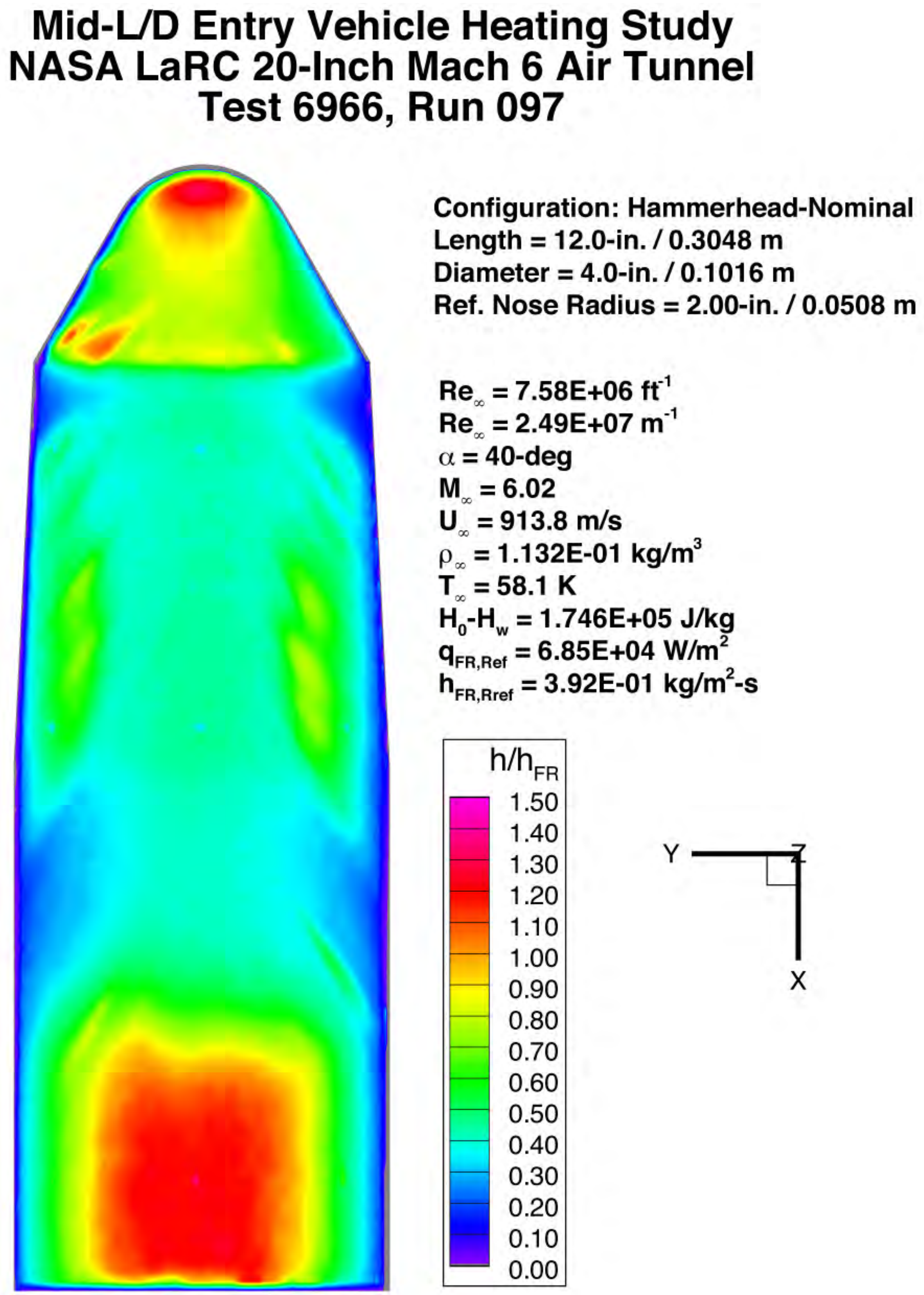

Figure 192. Run 097 Heating Data, Hammerhead-Nominal, Re_∞=7.58×10^6/ft

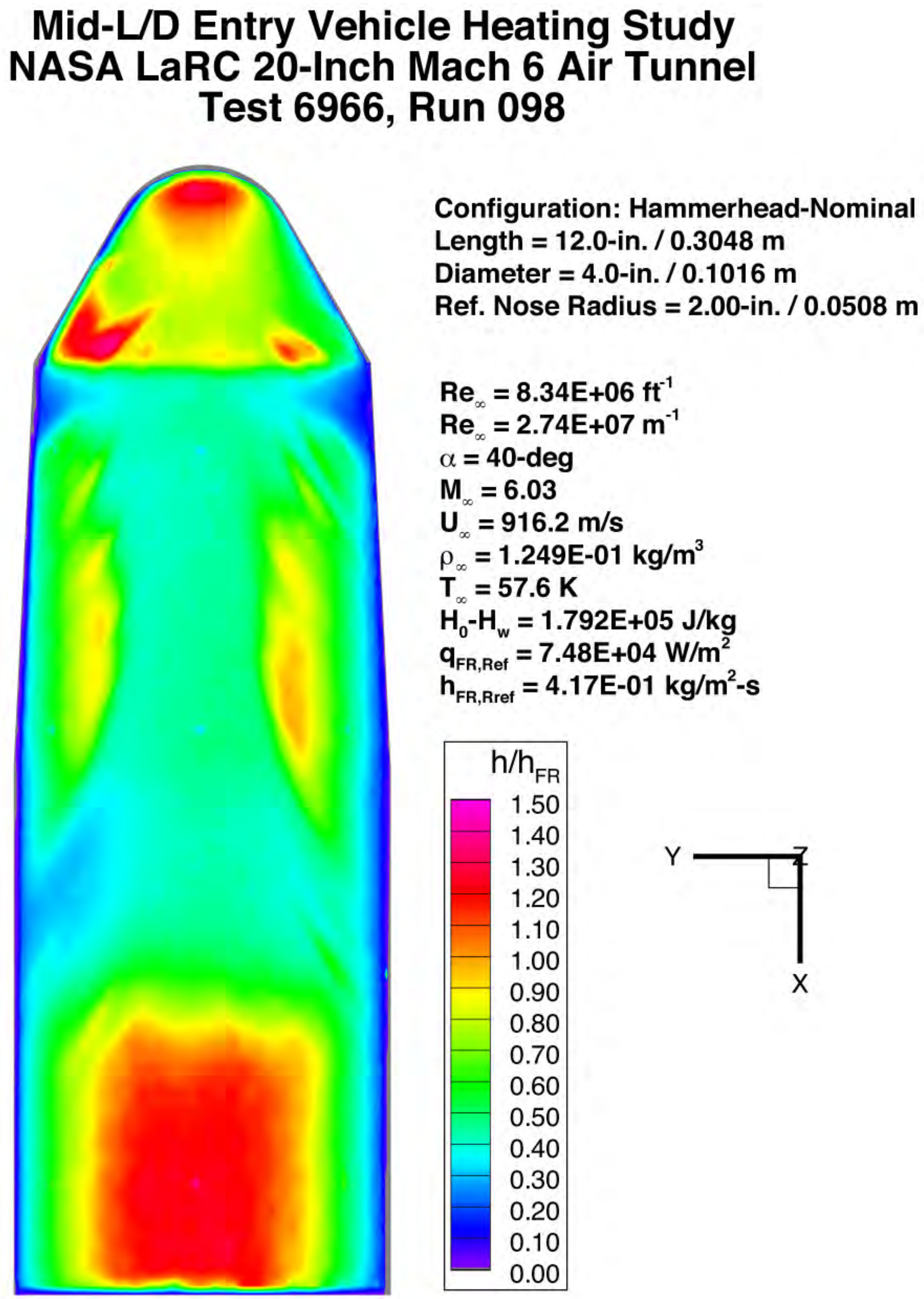

Figure 193. Run 098 Heating Data, Hammerhead-Nominal, $Re_\infty = 8.34 \times 10^6$/ft

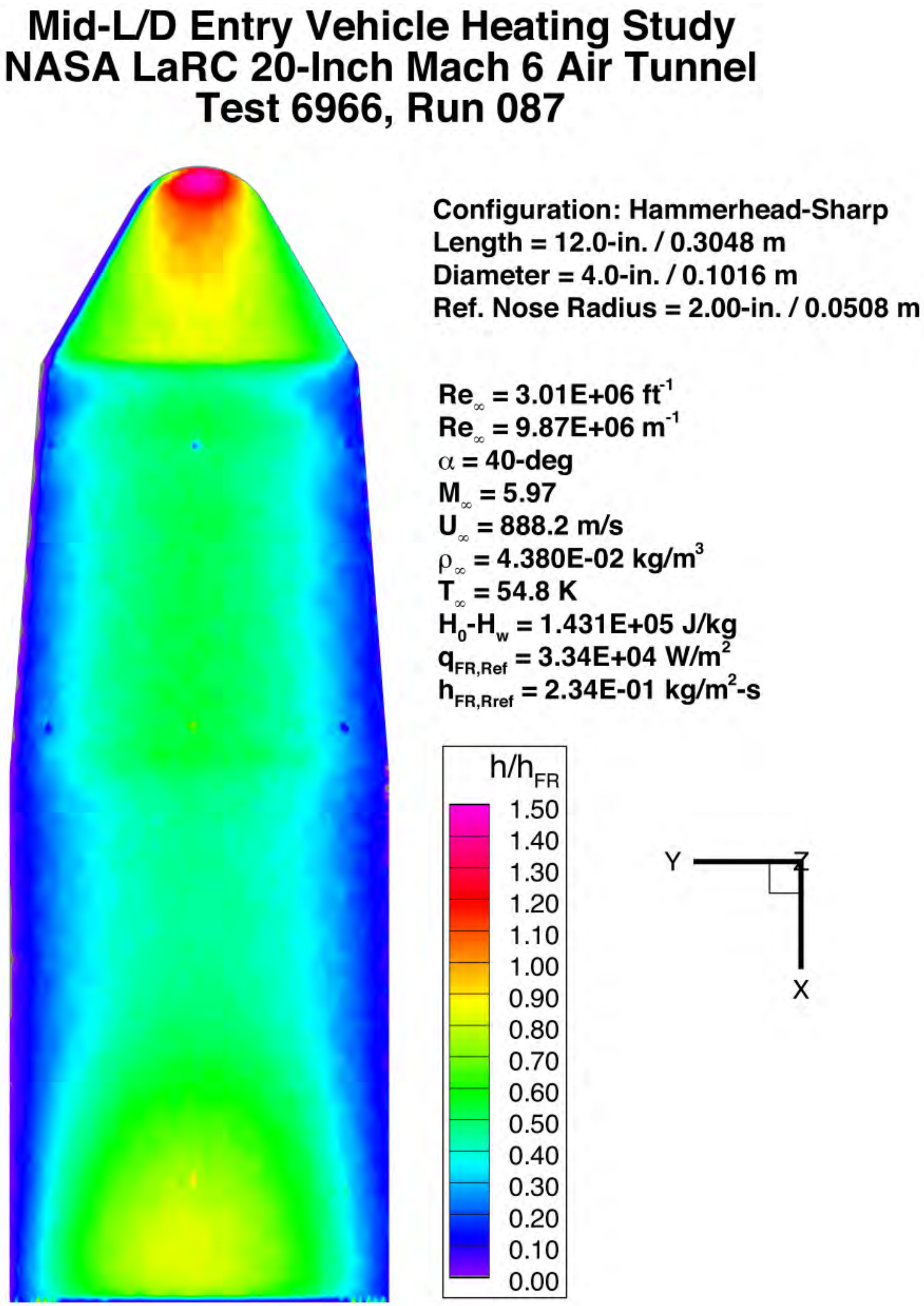

Figure 194. Run 087 Heating Data, Hammerhead-Sharp, Re_∞=3.01×10^6/ft

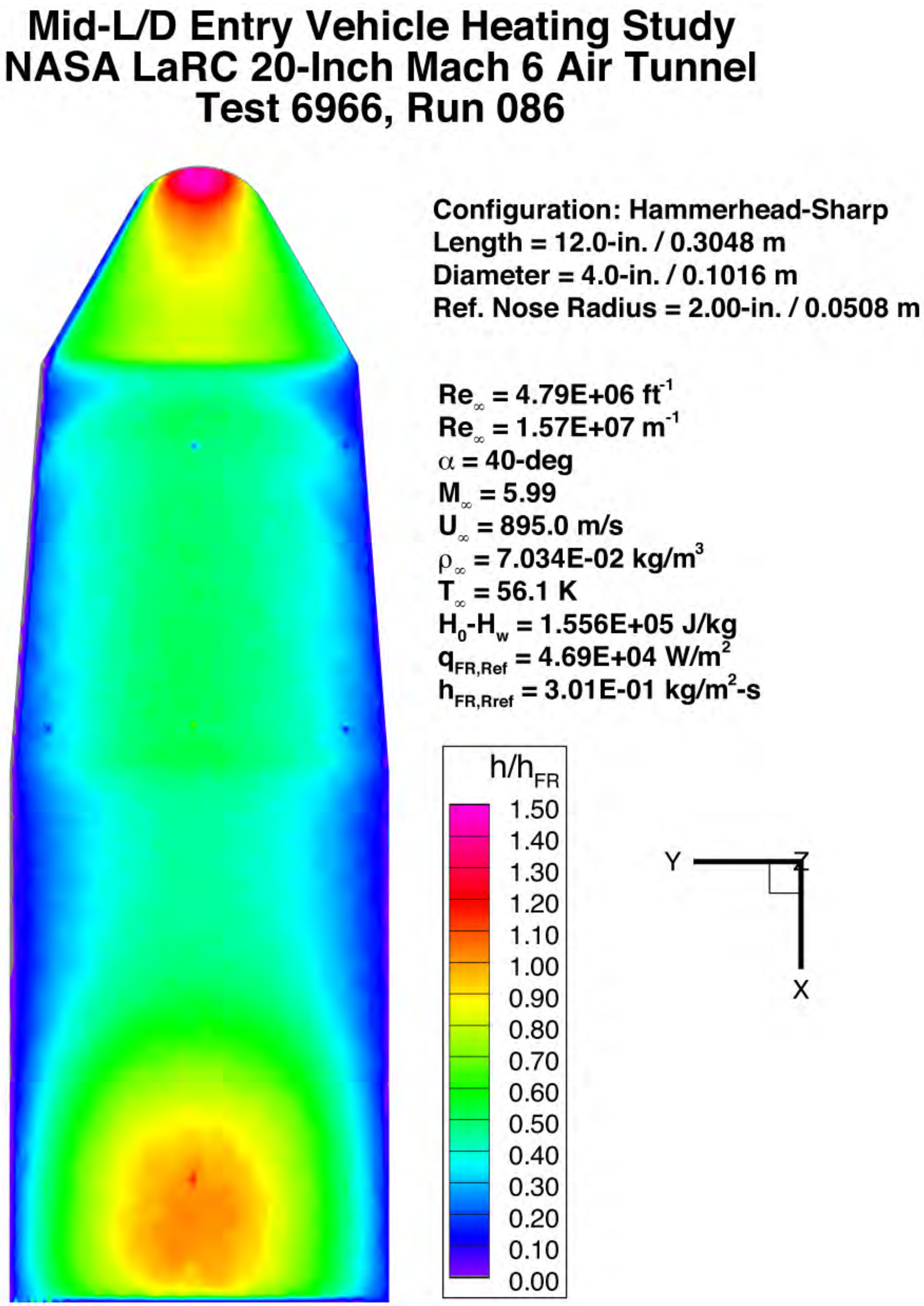

Figure 195. Run 086 Heating Data, Hammerhead-Sharp, Re_∞=4.79×10^6/ft

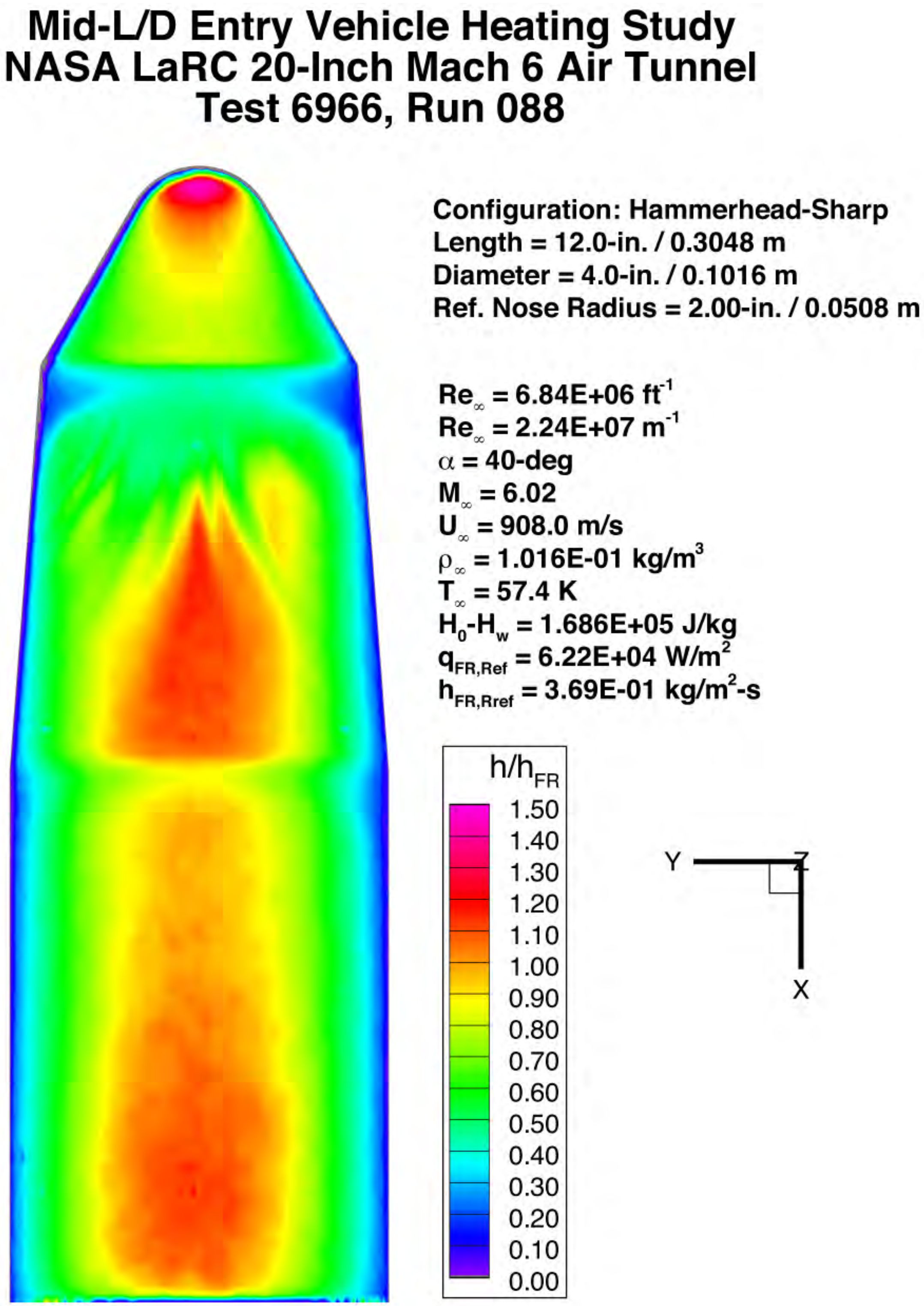

Figure 196. Run 088 Heating Data, Hammerhead-Sharp, Re_∞=6.84×10^6/ft

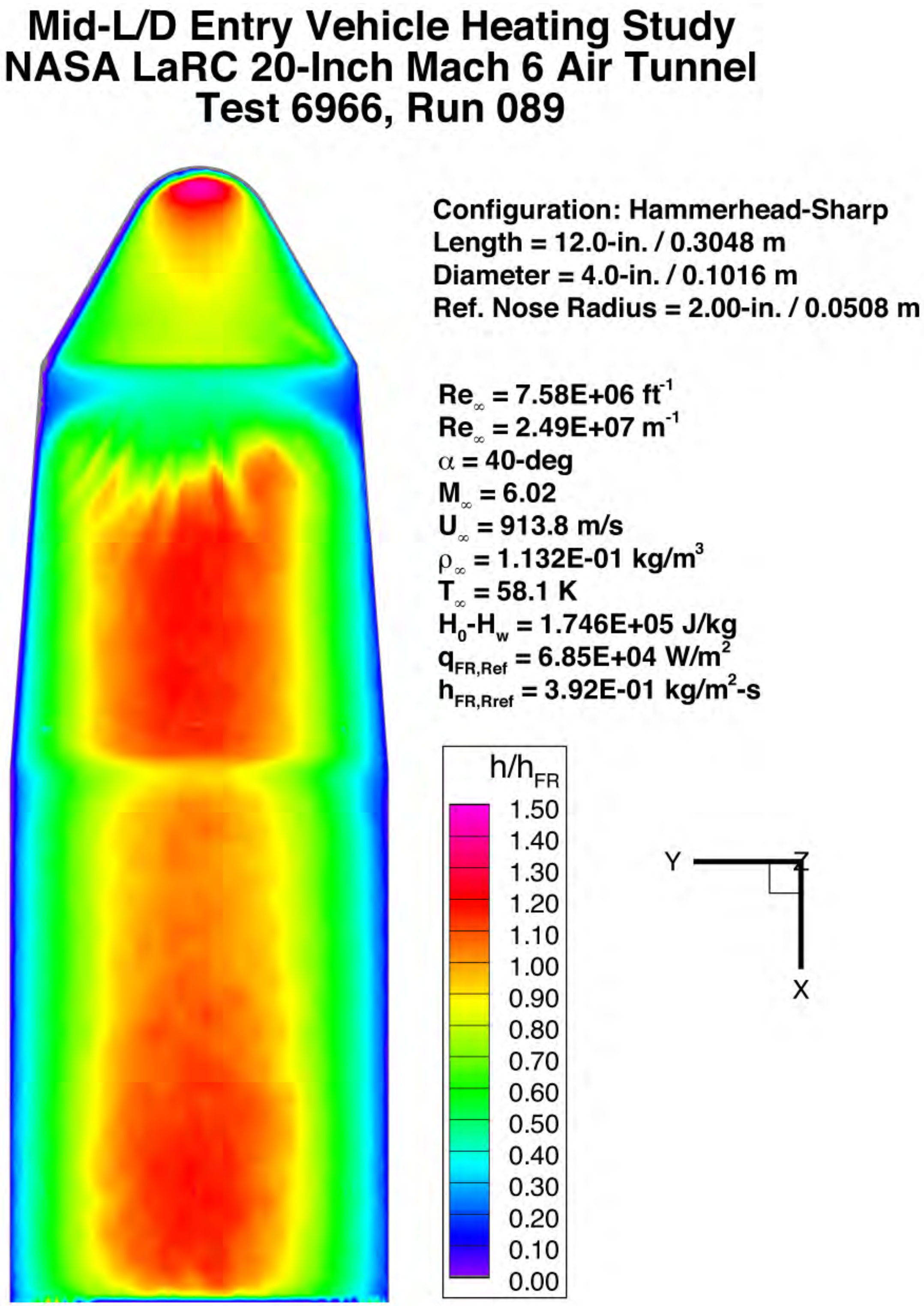

Mid-L/D Entry Vehicle Heating Study
NASA LaRC 20-Inch Mach 6 Air Tunnel
Test 6966, Run 089

Configuration: Hammerhead-Sharp
Length = 12.0-in. / 0.3048 m
Diameter = 4.0-in. / 0.1016 m
Ref. Nose Radius = 2.00-in. / 0.0508 m

$Re_\infty = 7.58E+06\ ft^{-1}$
$Re_\infty = 2.49E+07\ m^{-1}$
$\alpha = 40\text{-deg}$
$M_\infty = 6.02$
$U_\infty = 913.8\ m/s$
$\rho_\infty = 1.132E-01\ kg/m^3$
$T_\infty = 58.1\ K$
$H_0-H_w = 1.746E+05\ J/kg$
$q_{FR,Ref} = 6.85E+04\ W/m^2$
$h_{FR,Rref} = 3.92E-01\ kg/m^2\text{-}s$

Figure 197. Run 089 Heating Data, Hammerhead-Sharp, $Re_\infty=7.58\times10^6$/ft

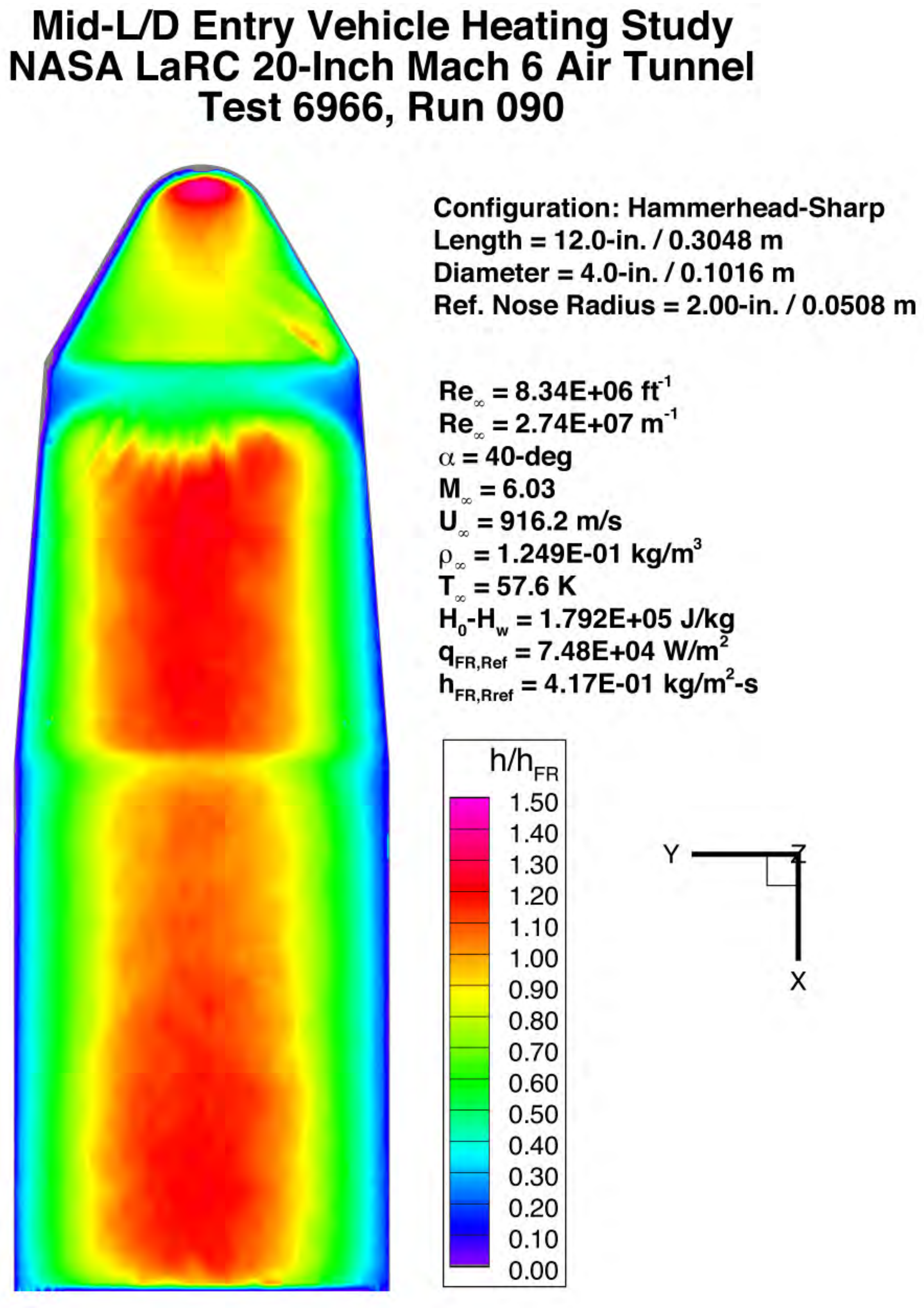

Figure 198. Run 090 Heating Data, Hammerhead-Sharp, Re_∞=8.34×10^6/ft

Appendix D. Tripped Models Global Image Heating Data

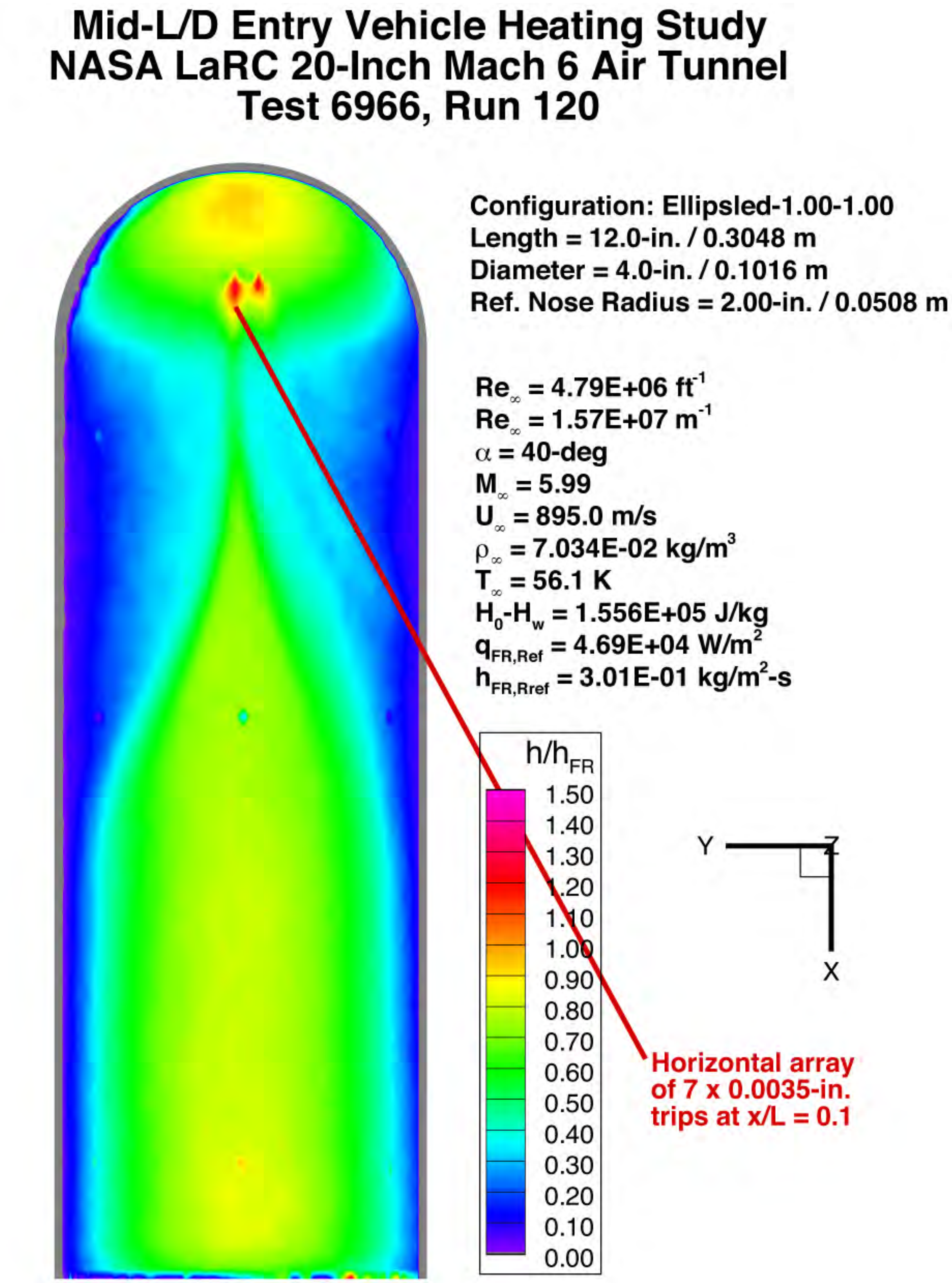

Figure 199. Run 120 Heating Data, Ellipsled-1.00-1.00, Re$_\infty$=4.79×10^6/ft, Trips at *x*/*L*=0.10

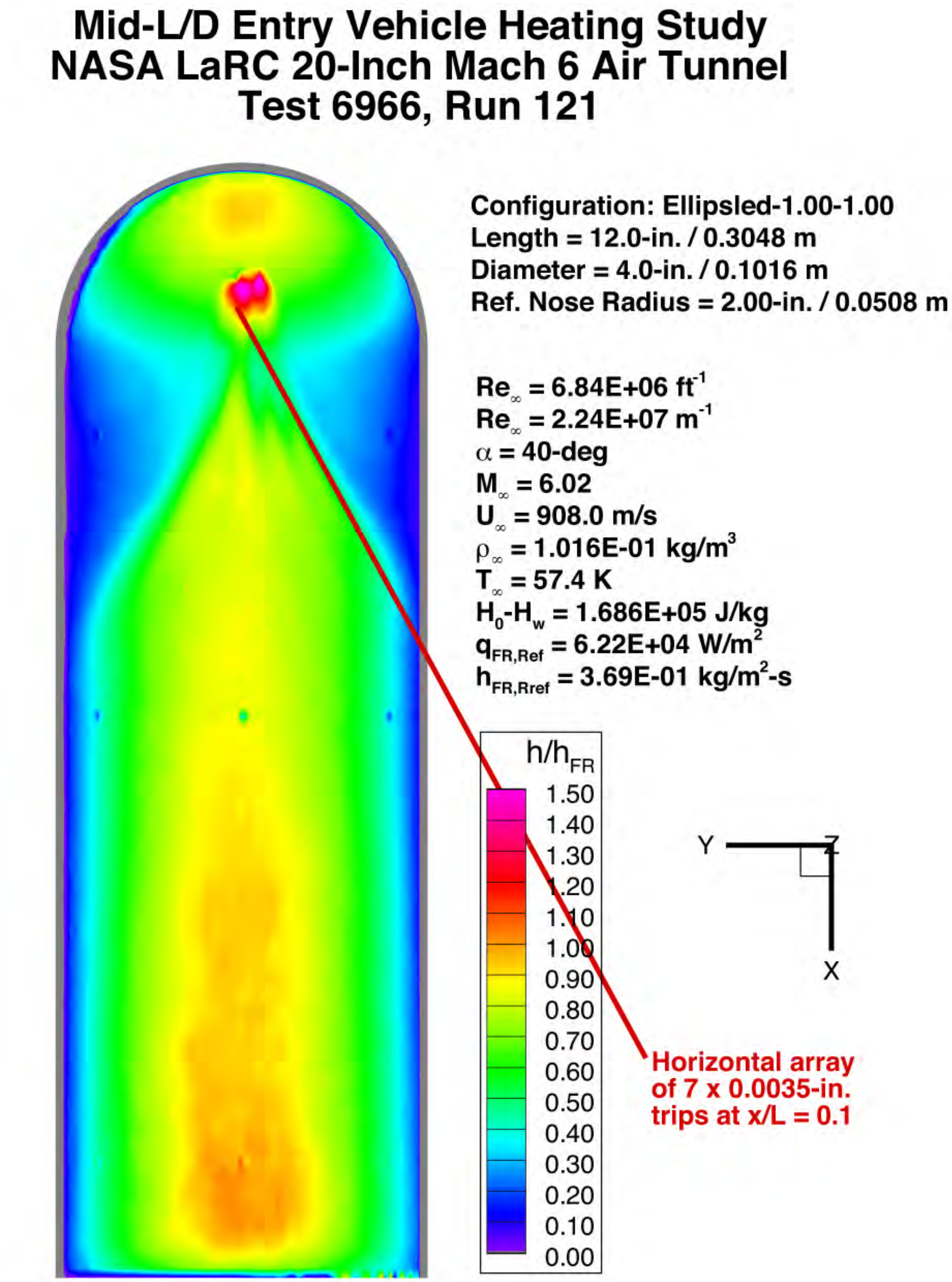

Figure 200. Run 121 Heating Data, Ellipsled-1.00-1.00, $Re_\infty=6.84\times10^6$/ft, Trips at x/L=0.10

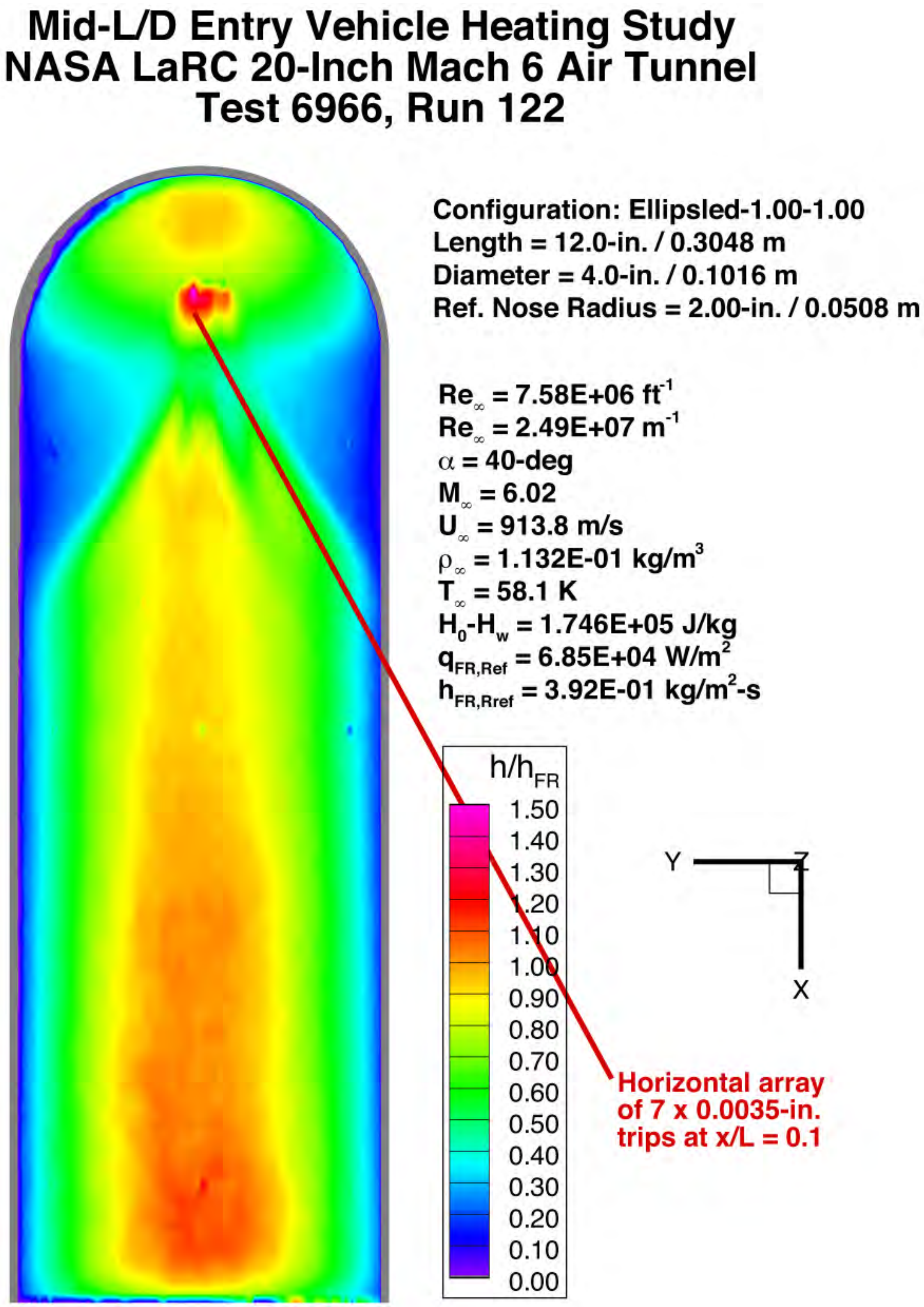

Figure 201. Run 122 Heating Data, Ellipsled-1.00-1.00, Re$_\infty$=7.58×10^6/ft, Trips at *x*/*L*=0.10

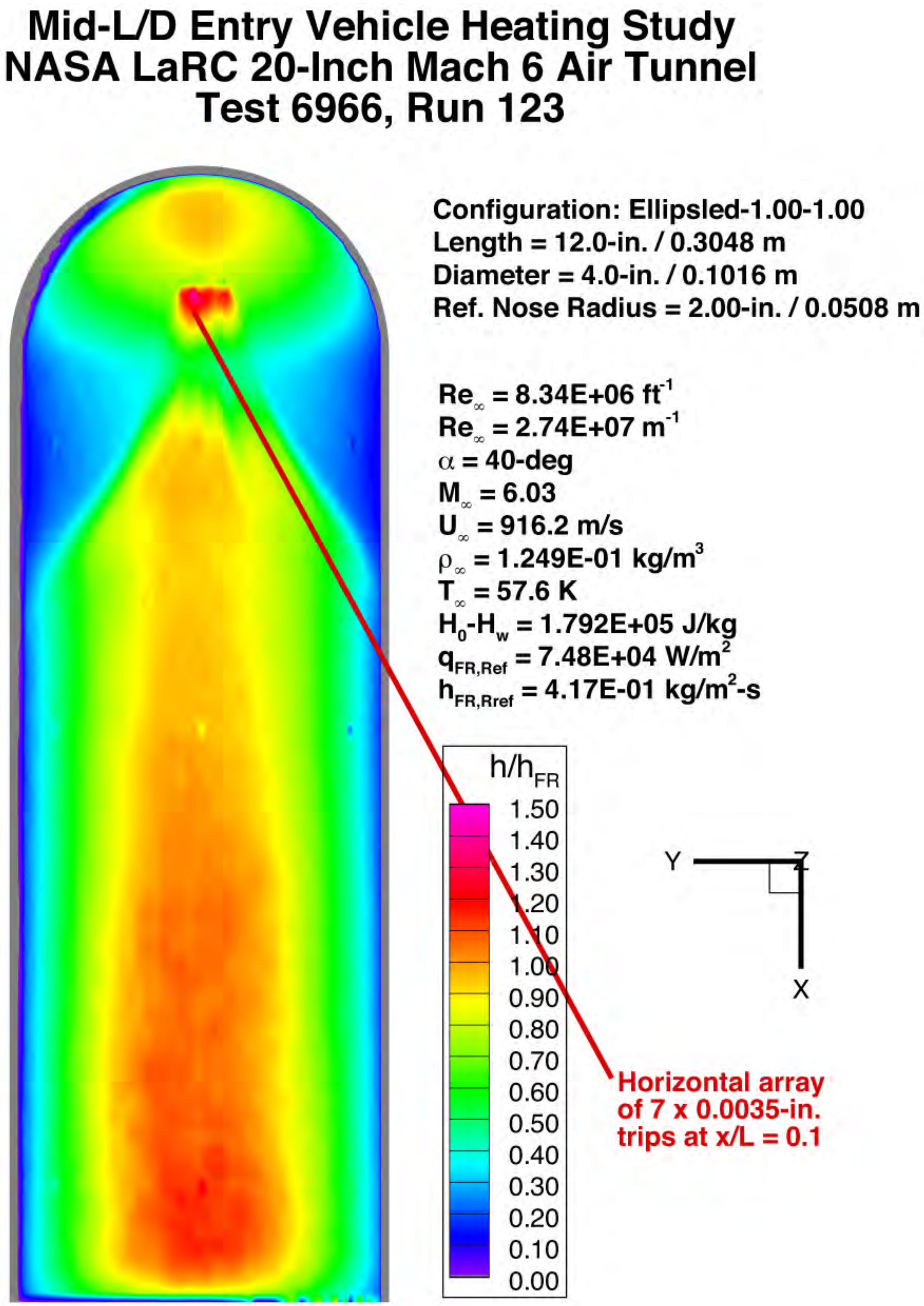

Figure 202. Run 123 Heating Data, Ellipsled-1.00-1.00, $Re_\infty=8.34\times10^6$/ft, Trips at x/L=0.10

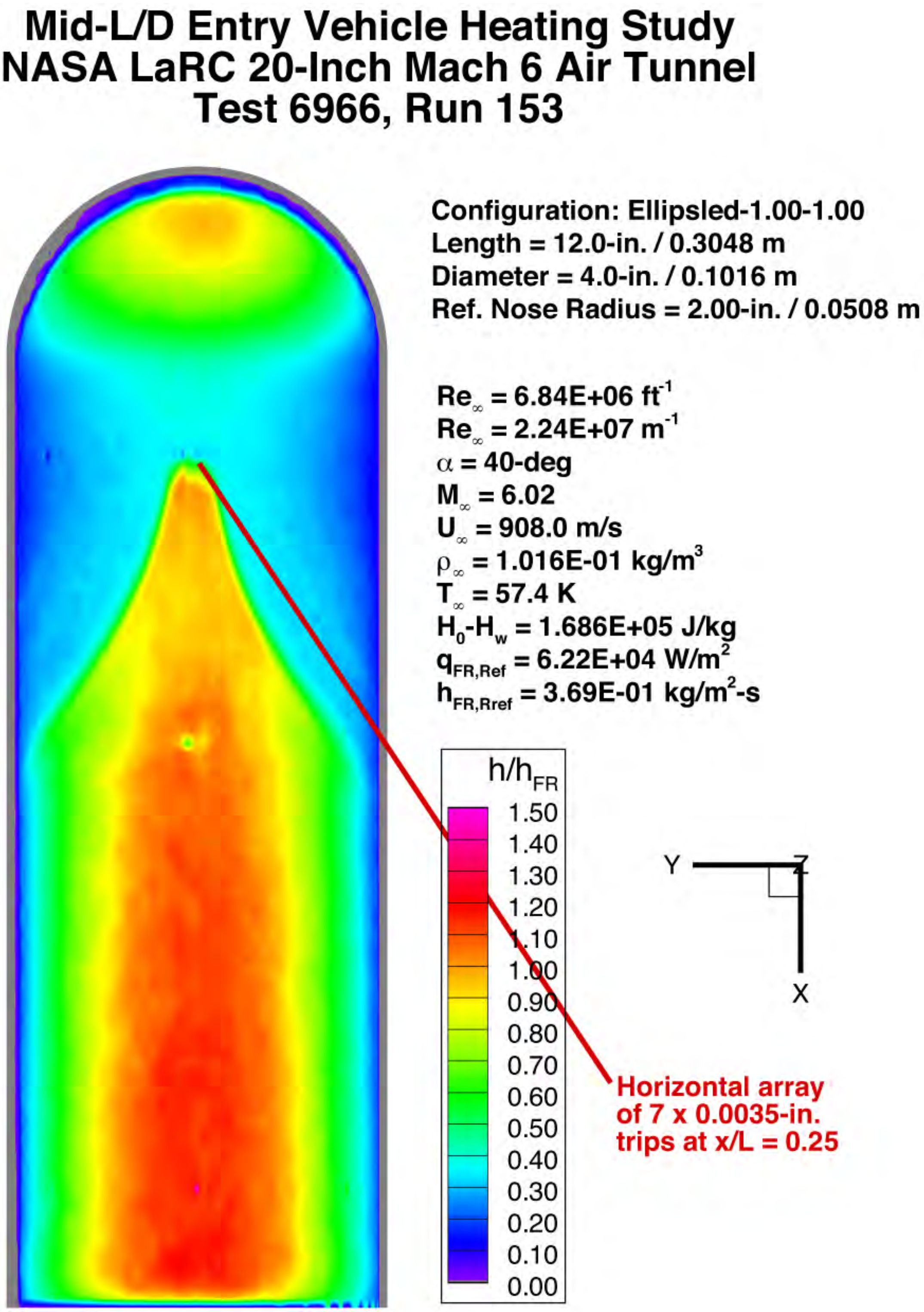

Horizontal array of 7 x 0.0035-in. trips at x/L = 0.25

Figure 203. Run 153 Heating Data, Ellipsled-1.00-1.00, Re_∞=6.84×10^6/ft, Trips at *x*/*L*=0.25

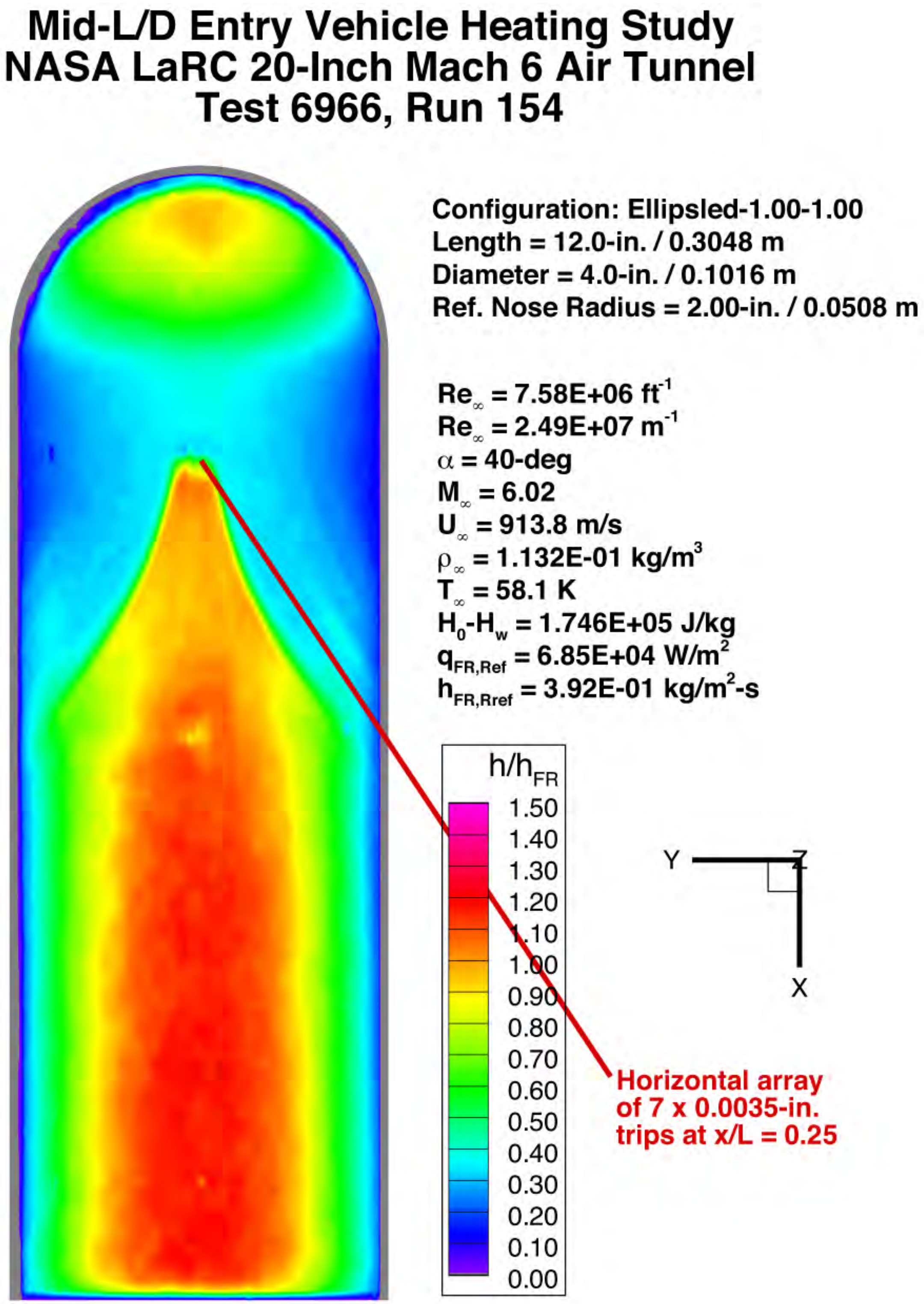

Figure 204. Run 154 Heating Data, Ellipsled-1.00-1.00, Re_∞=7.58×10^6/ft, Trips at x/L=0.25

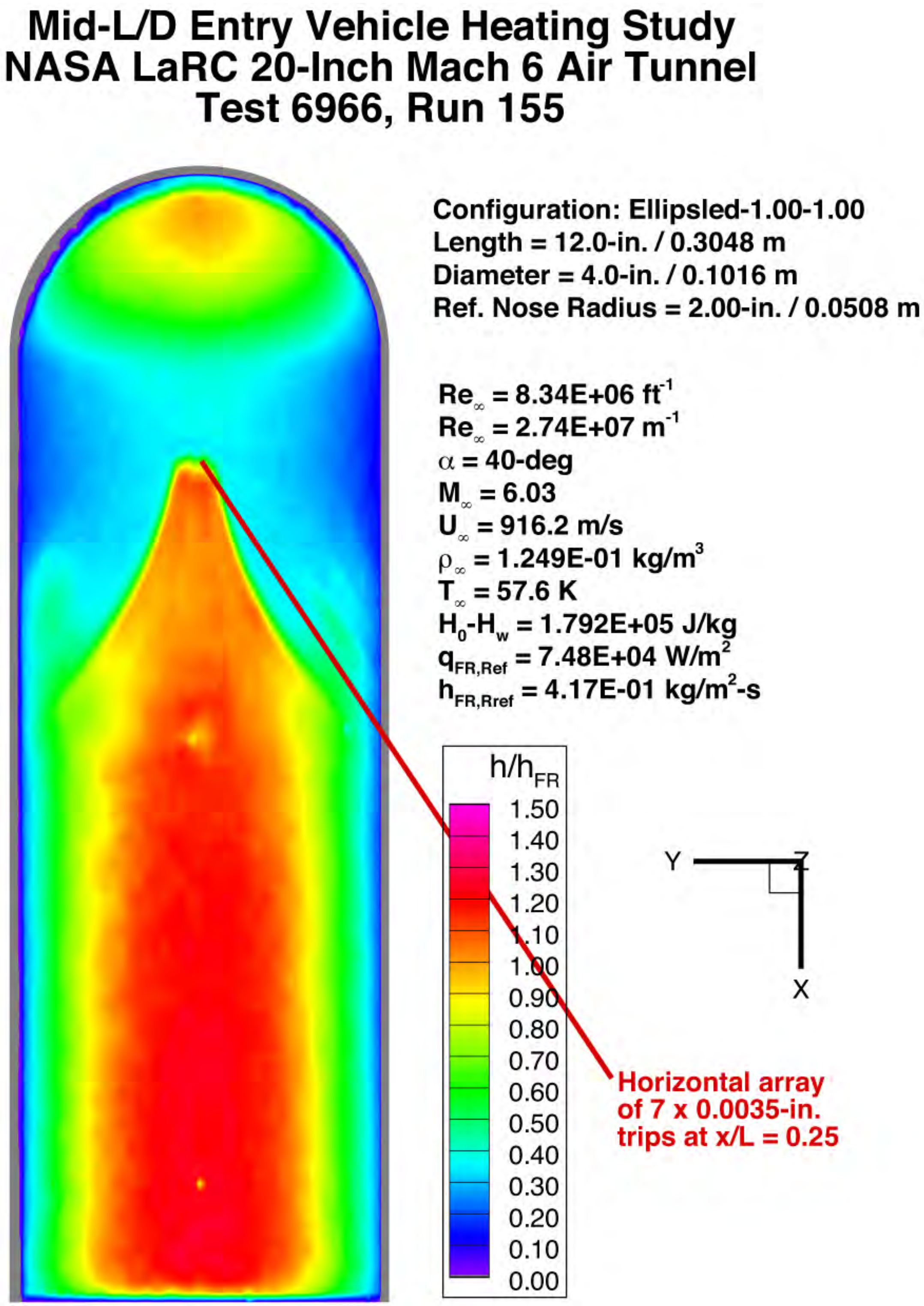

Figure 205. Run 155 Heating Data, Ellipsled-1.00-1.00, Re$_\infty$=8.34×10^6/ft, Trips at *x*/*L*=0.25

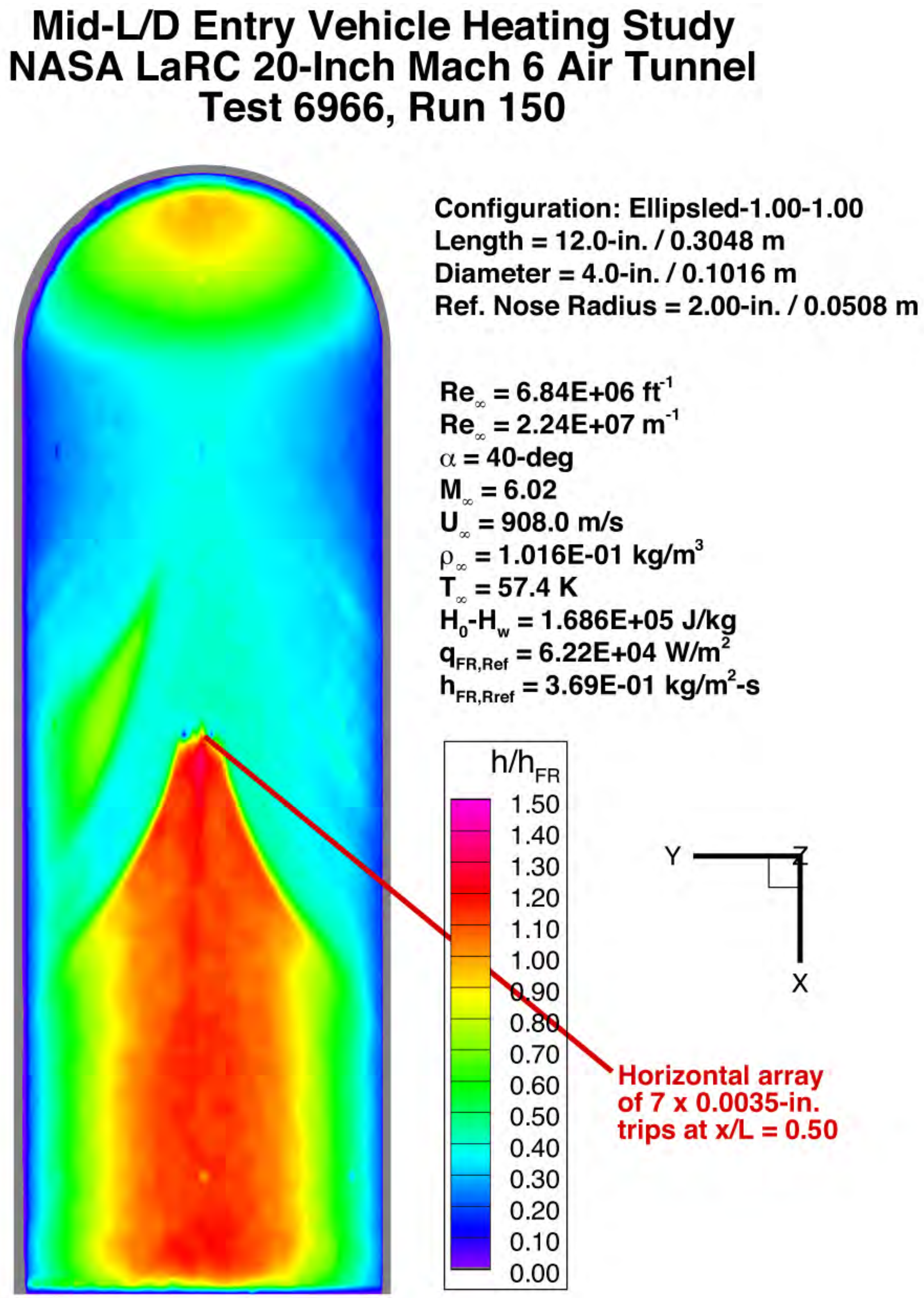

Figure 206. Run 150 Heating Data, Ellipsled-1.00-1.00, Re$_\infty$=6.84×10^6/ft, Trips at *x*/*L*=0.50

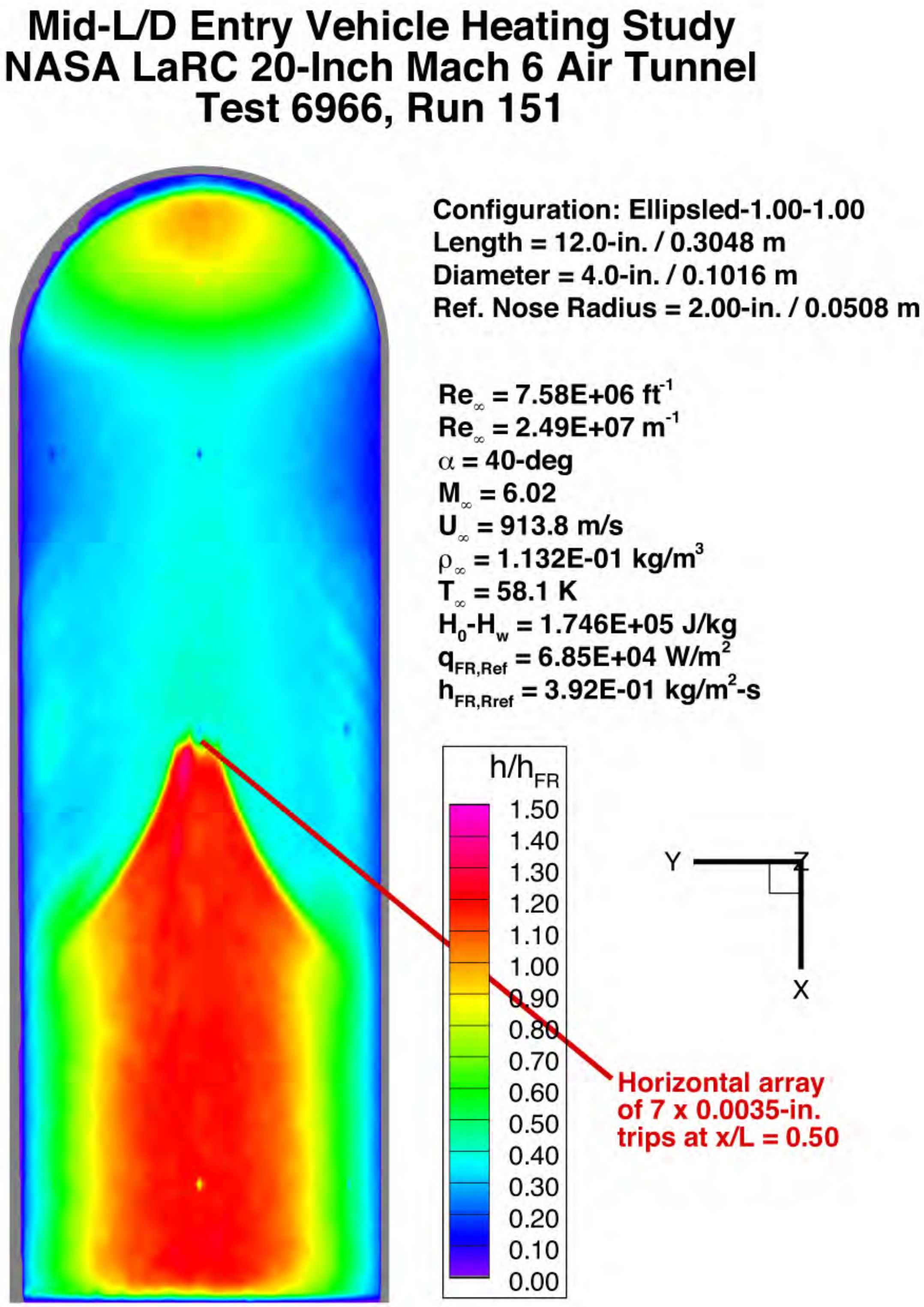

Figure 207. Run 151 Heating Data, Ellipsled-1.00-1.00, $Re_\infty=7.58\times10^6$/ft, Trips at $x/L=0.50$

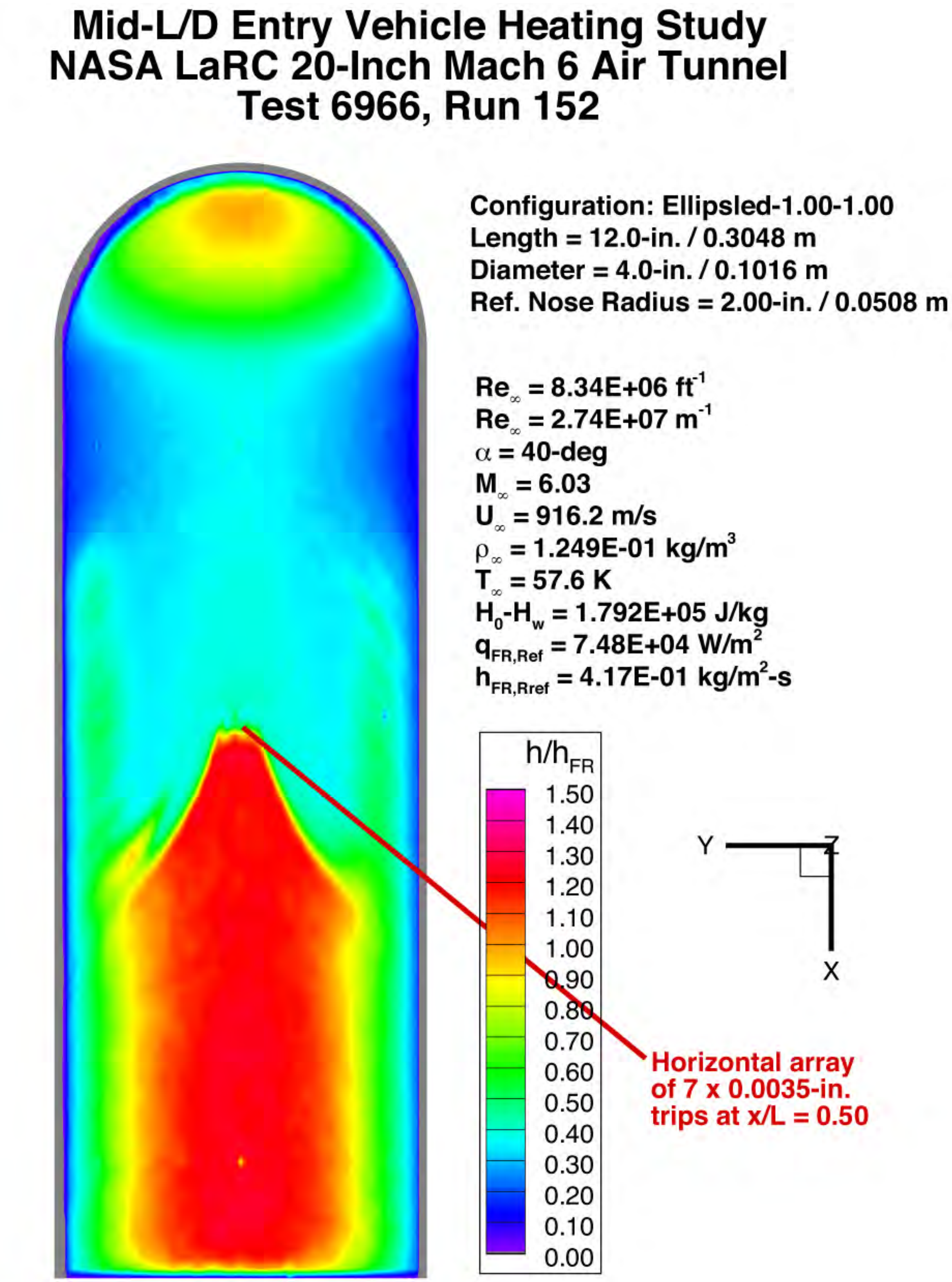

Figure 208. Run 152 Heating Data, Ellipsled-1.00-1.00, $Re_\infty=8.34\times10^6$/ft, Trips at x/L=0.50

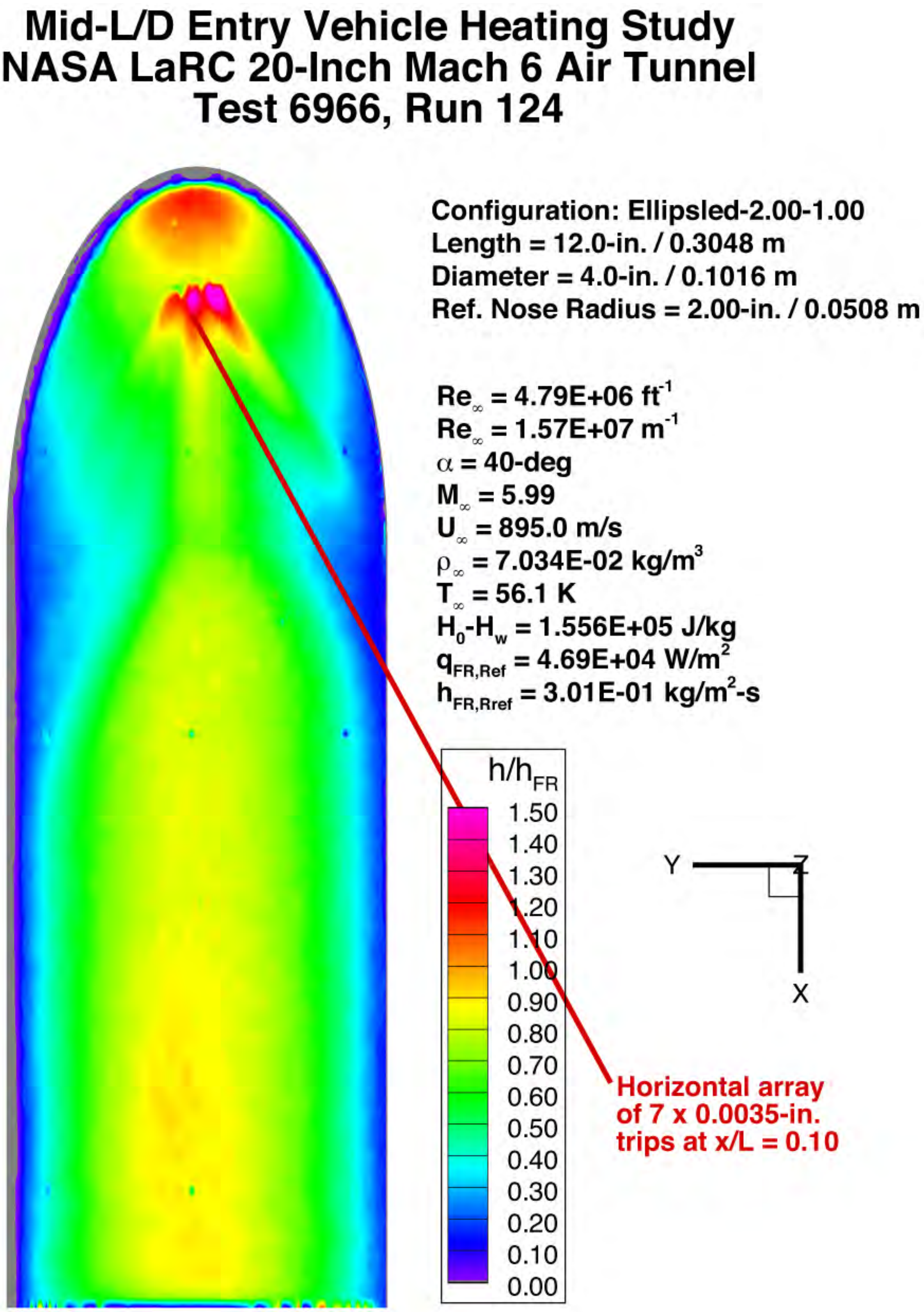

Figure 209. Run 124 Heating Data, Ellipsled-2.00-1.00, $Re_\infty=4.79\times10^6$/ft, Trips at *x*/*L*=0.10

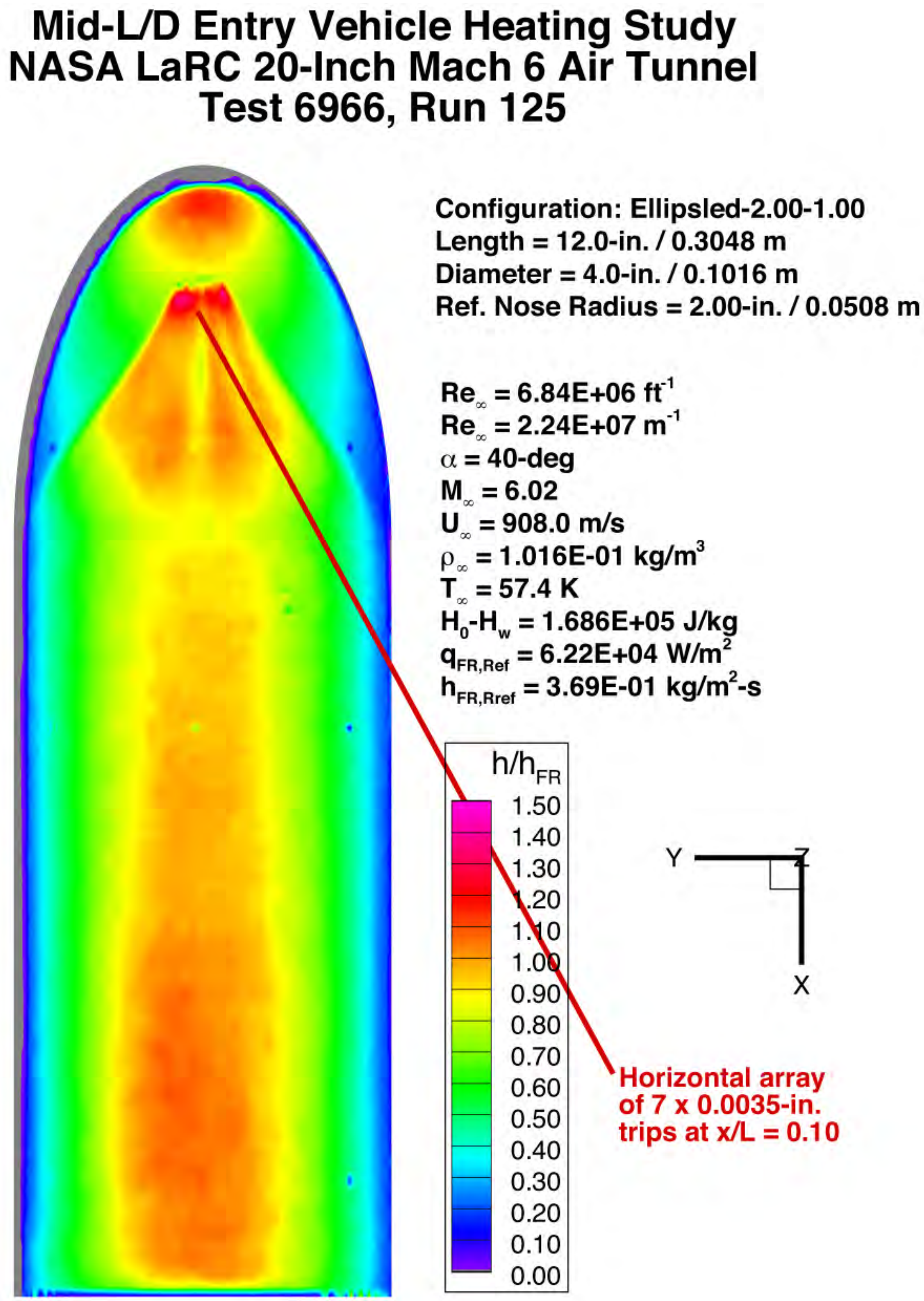

Figure 210. Run 125 Heating Data, Ellipsled-2.00-1.00, $Re_\infty=6.84\times10^6$/ft, Trips at *x*/*L*=0.10

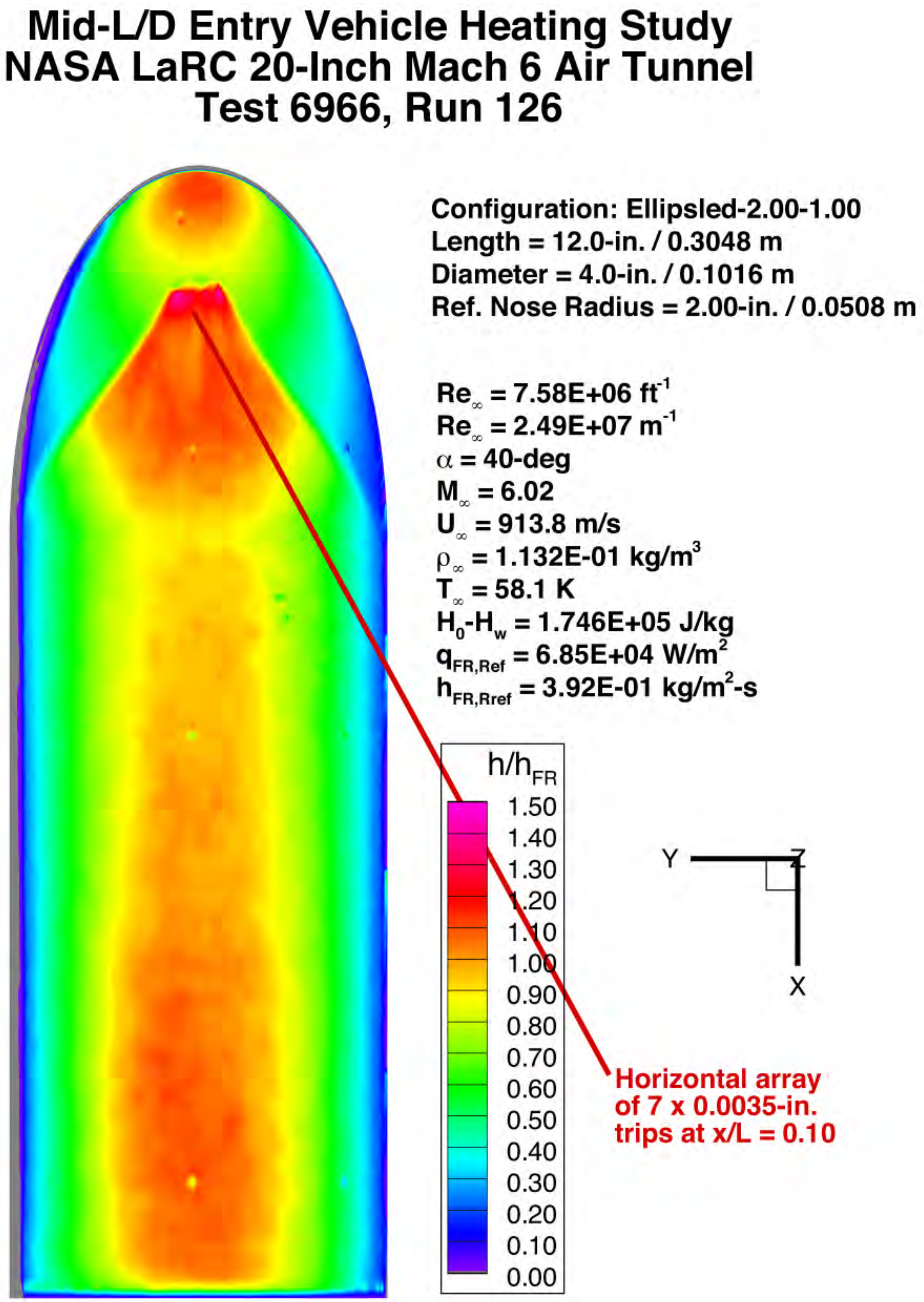

Figure 211. Run 126 Heating Data, Ellipsled-2.00-1.00, $Re_\infty=7.58\times10^6$/ft, Trips at $x/L=0.10$

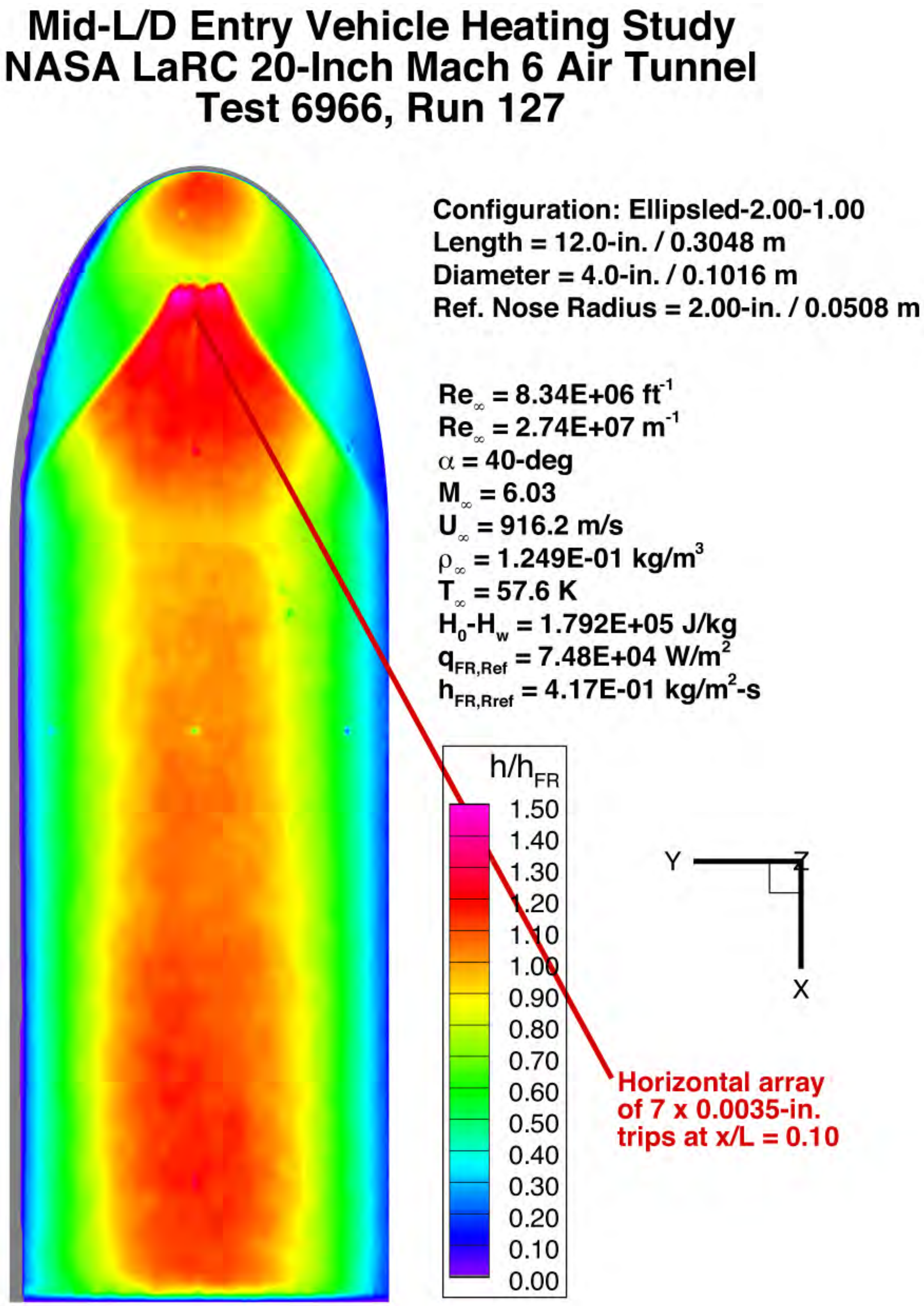

Figure 212. Run 127 Heating Data, Ellipsled-2.00-1.00, $Re_\infty=8.34\times10^6$/ft, Trips at *x*/*L*=0.10

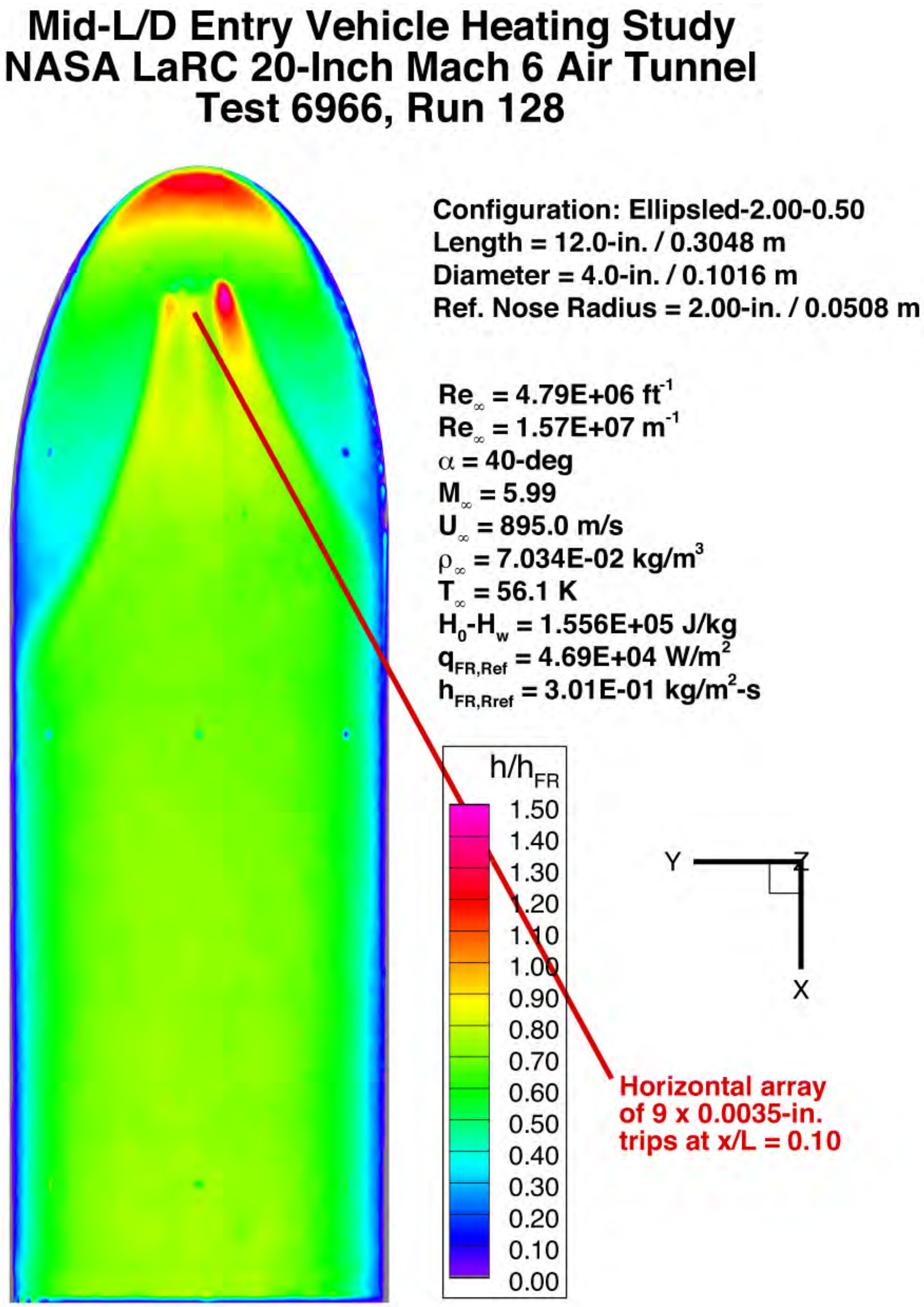

Figure 213. Run 128 Heating Data, Ellipsled-2.00-0.50, $Re_\infty=4.79\times10^6$/ft, Trips at *x*/*L*=0.10

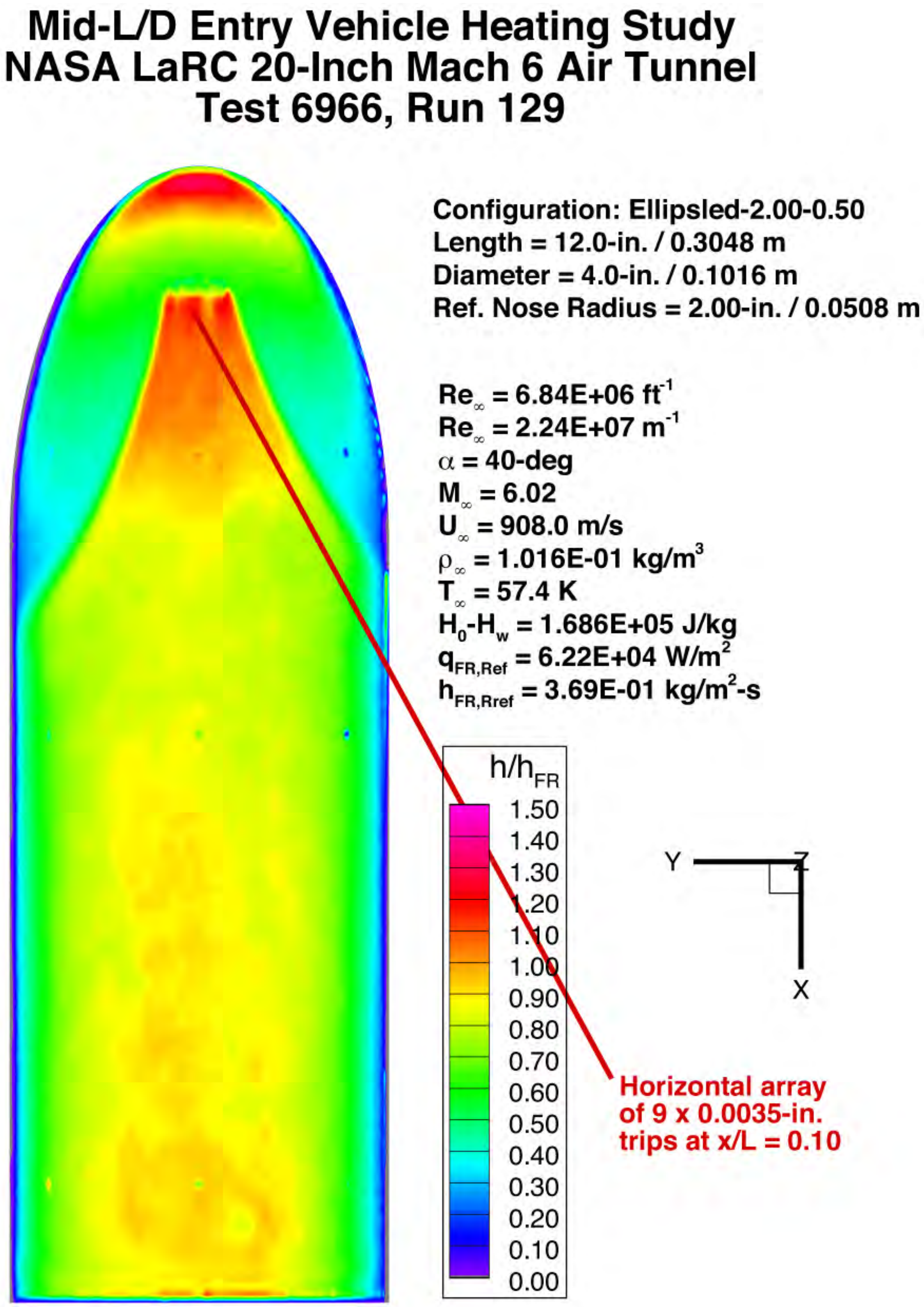

Figure 214. Run 129 Heating Data, Ellipsled-2.00-0.50, Re_∞=6.84×10^6/ft, Trips at *x*/*L*=01.0

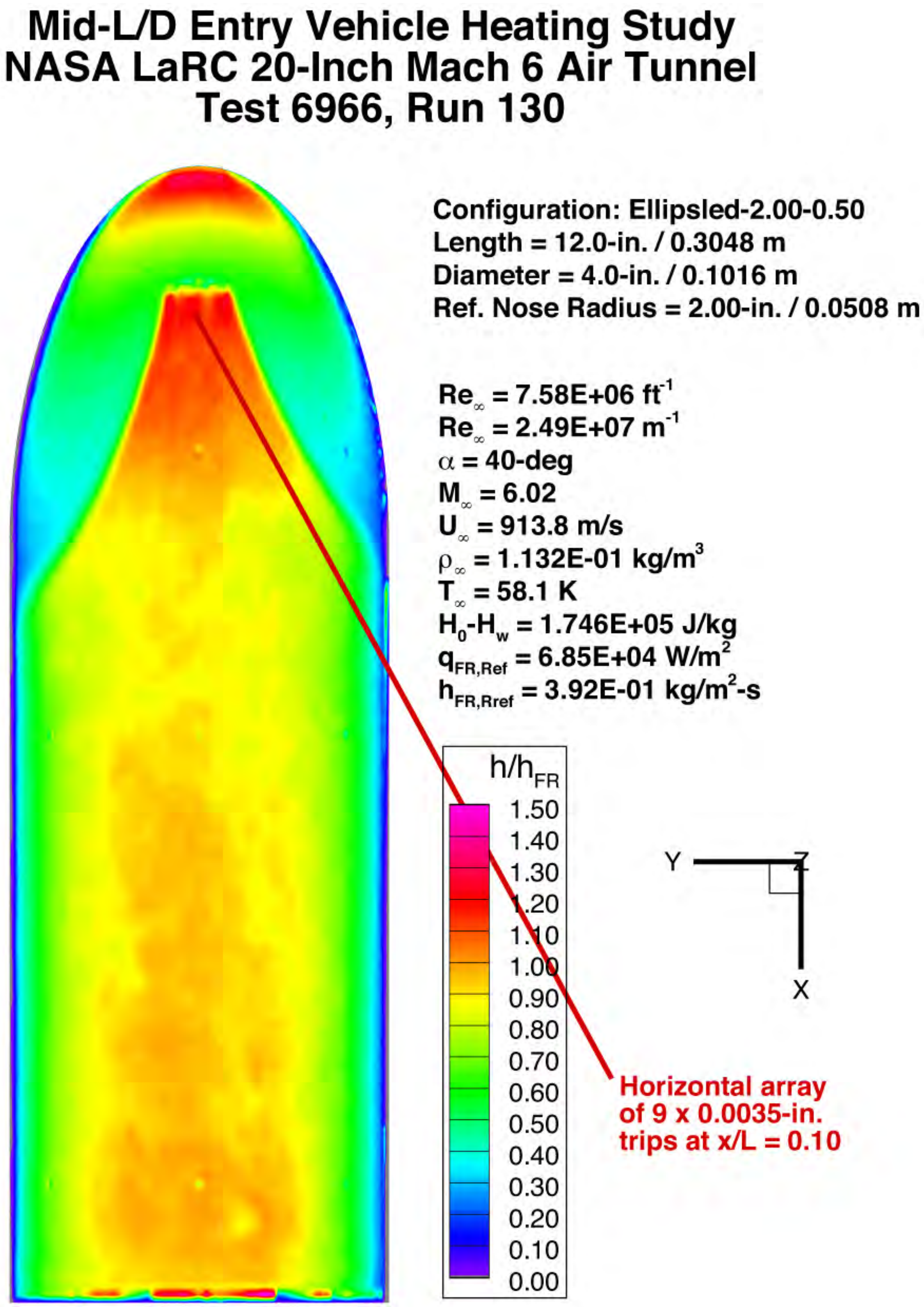

Figure 215. Run 130 Heating Data, Ellipsled-2.00-0.50, $Re_\infty=7.58\times10^6$/ft, Trips at *x*/L=0.10

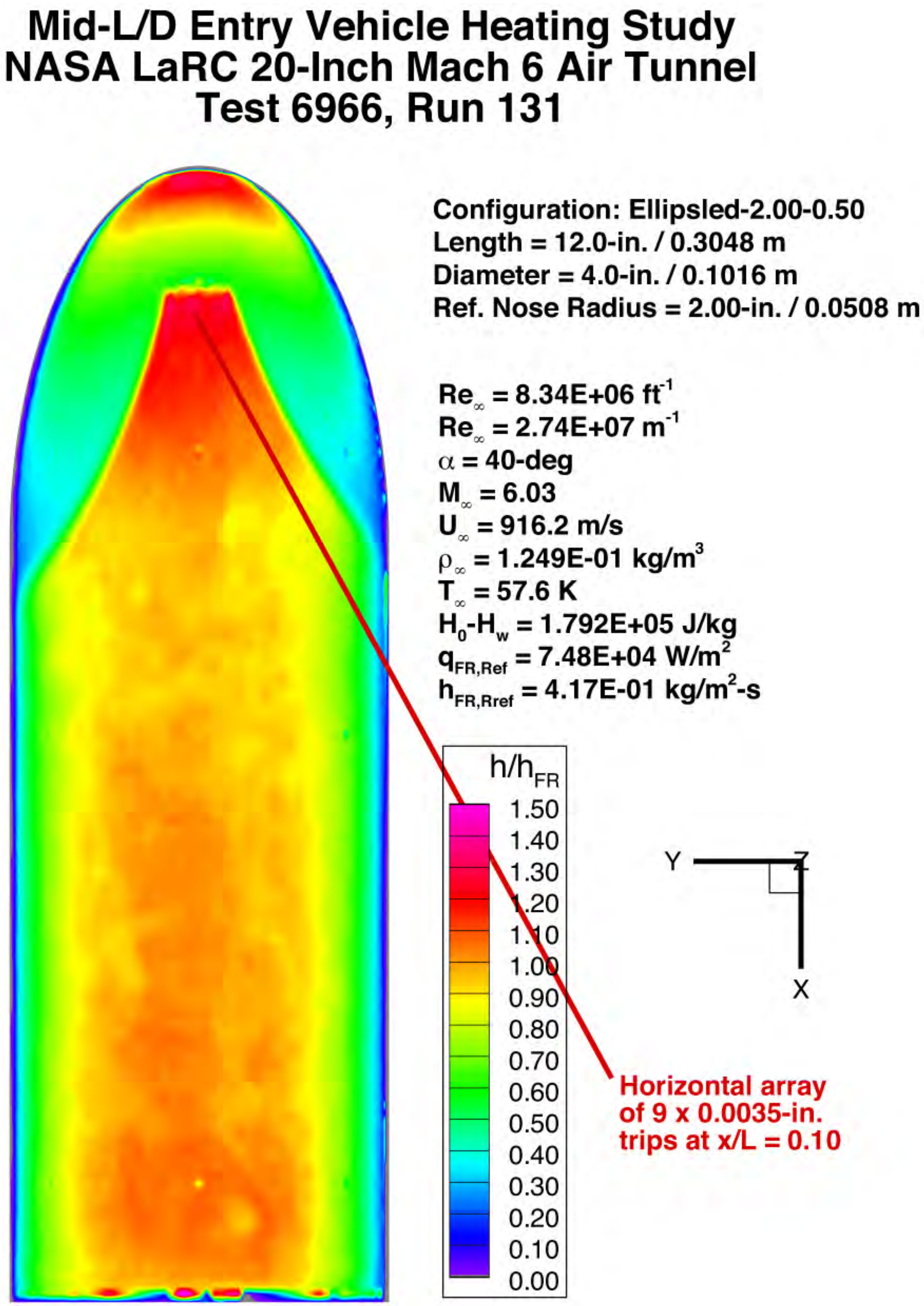

Figure 216. Run 131 Heating Data, Ellipsled-2.00-0.50, $Re_\infty=8.34\times10^6$/ft, Trips at x/L=0.10

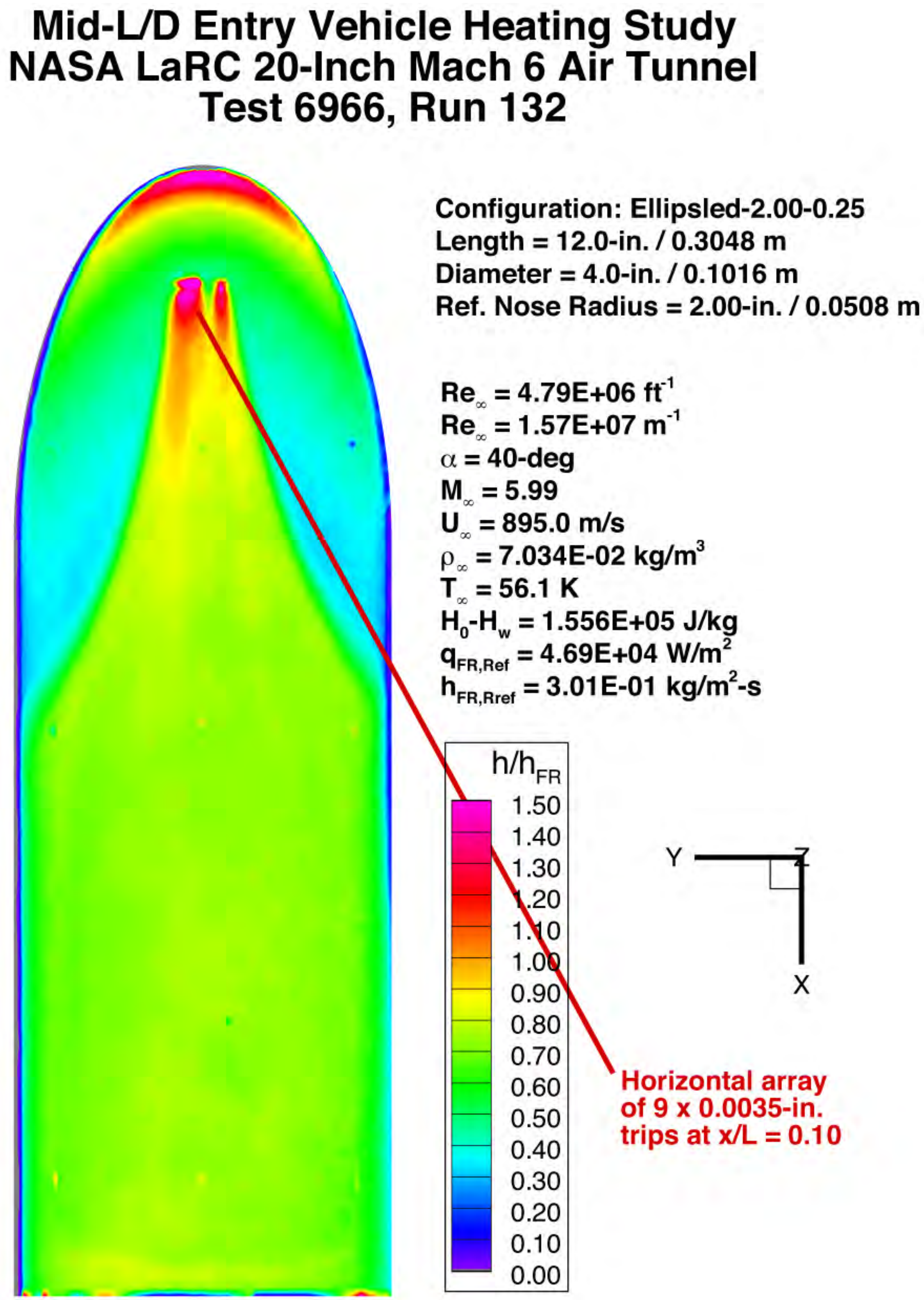

Figure 217. Run 132 Heating Data, Ellipsled-2.00-0.25, Re_∞=4.79×10^6/ft, Trips at *x*/*L*=0.10

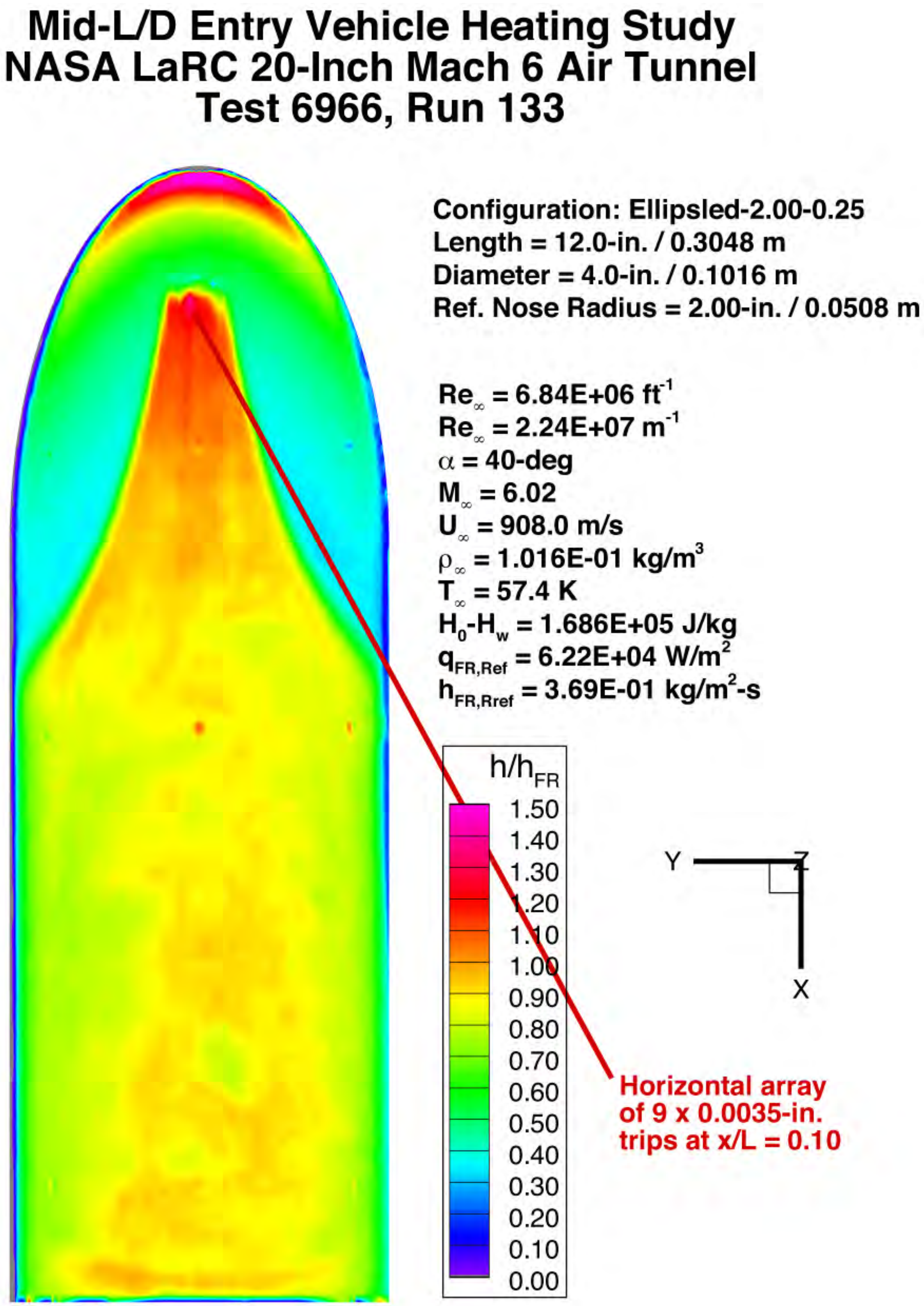

Figure 218. Run 133 Heating Data, Ellipsled-2.00-0.25, Re_∞=6.84×10^6/ft, Trips at *x*/*L*=0.10

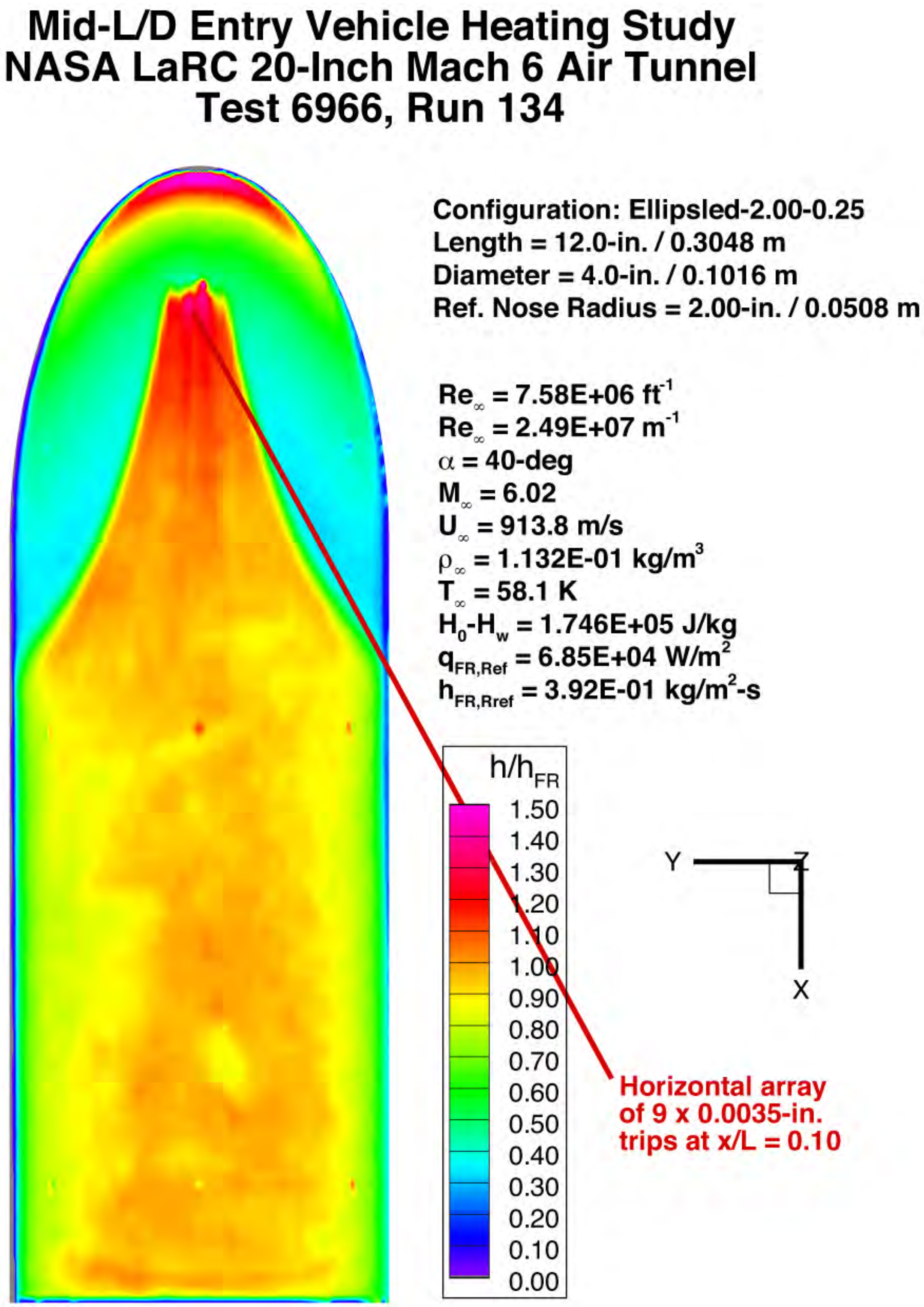

Figure 219. Run 134 Heating Data, Ellipsled-2.00-0.25, Re_∞=7.58×10^6/ft, Trips at *x*/*L*=0.10

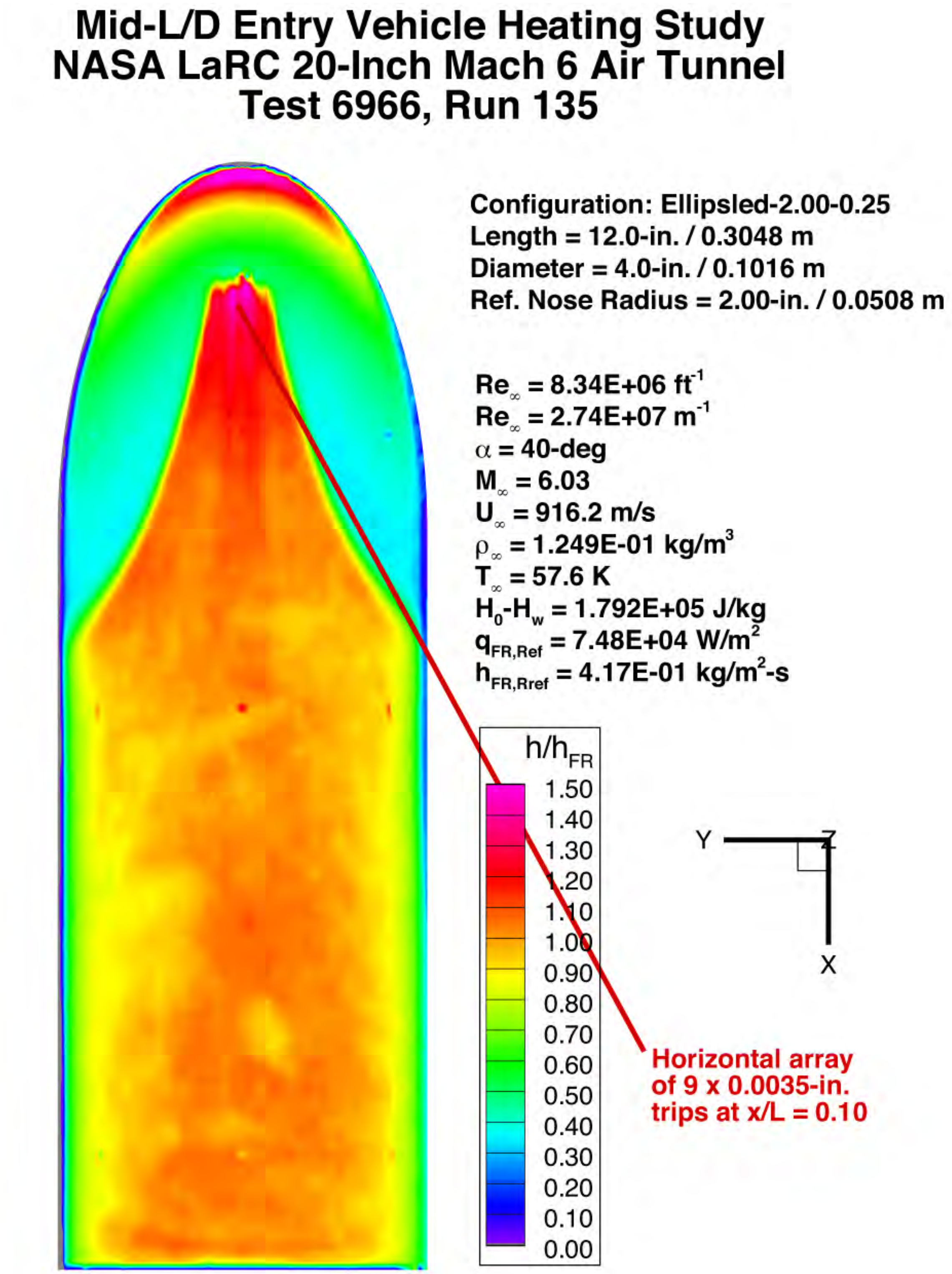

Figure 220. Run 135 Heating Data, Ellipsled-2.00-0.25, $Re_\infty=8.34\times10^6$/ft, Trips at *x*/*L*=0.10

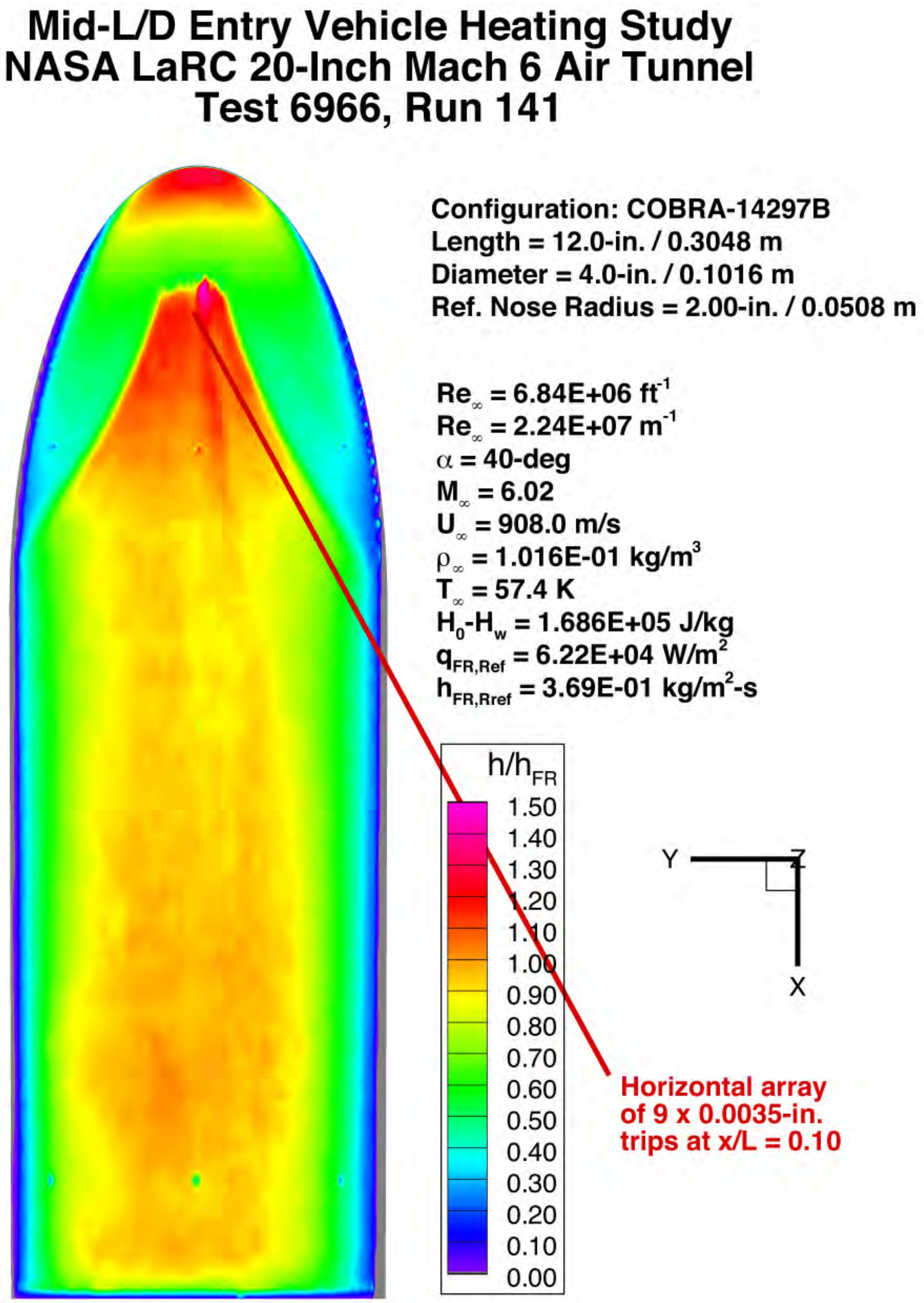

Figure 221. Run 141 Heating Data, COBRA-14297B (Model C-3), Re$_\infty$=6.84×10^6/ft, Trips at *x*/*L*=0.10

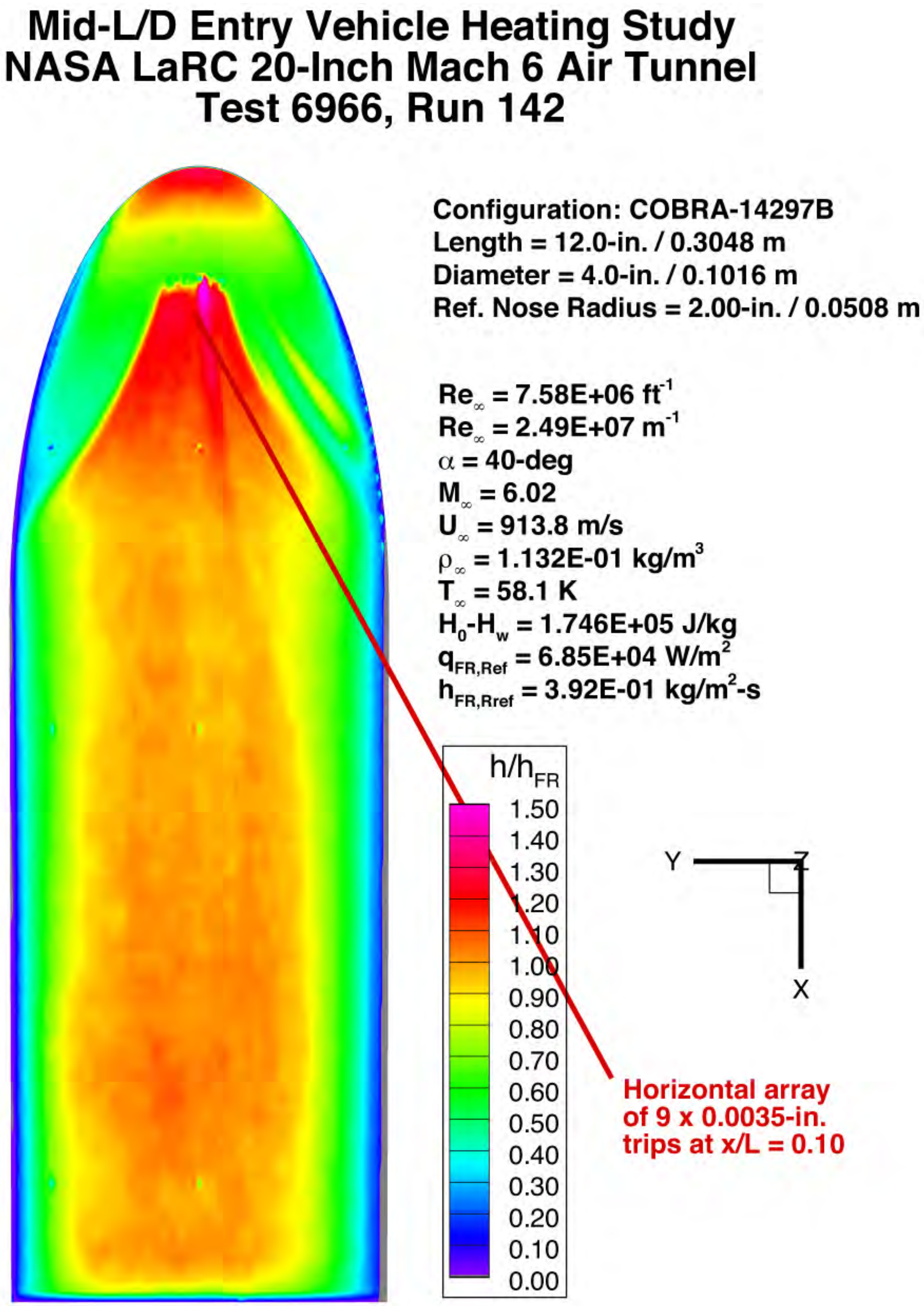

Figure 222. Run 142 Heating Data, COBRA-14297B (Model C-3), $Re_\infty=7.58\times10^6$/ft, Trips at x/L=0.10

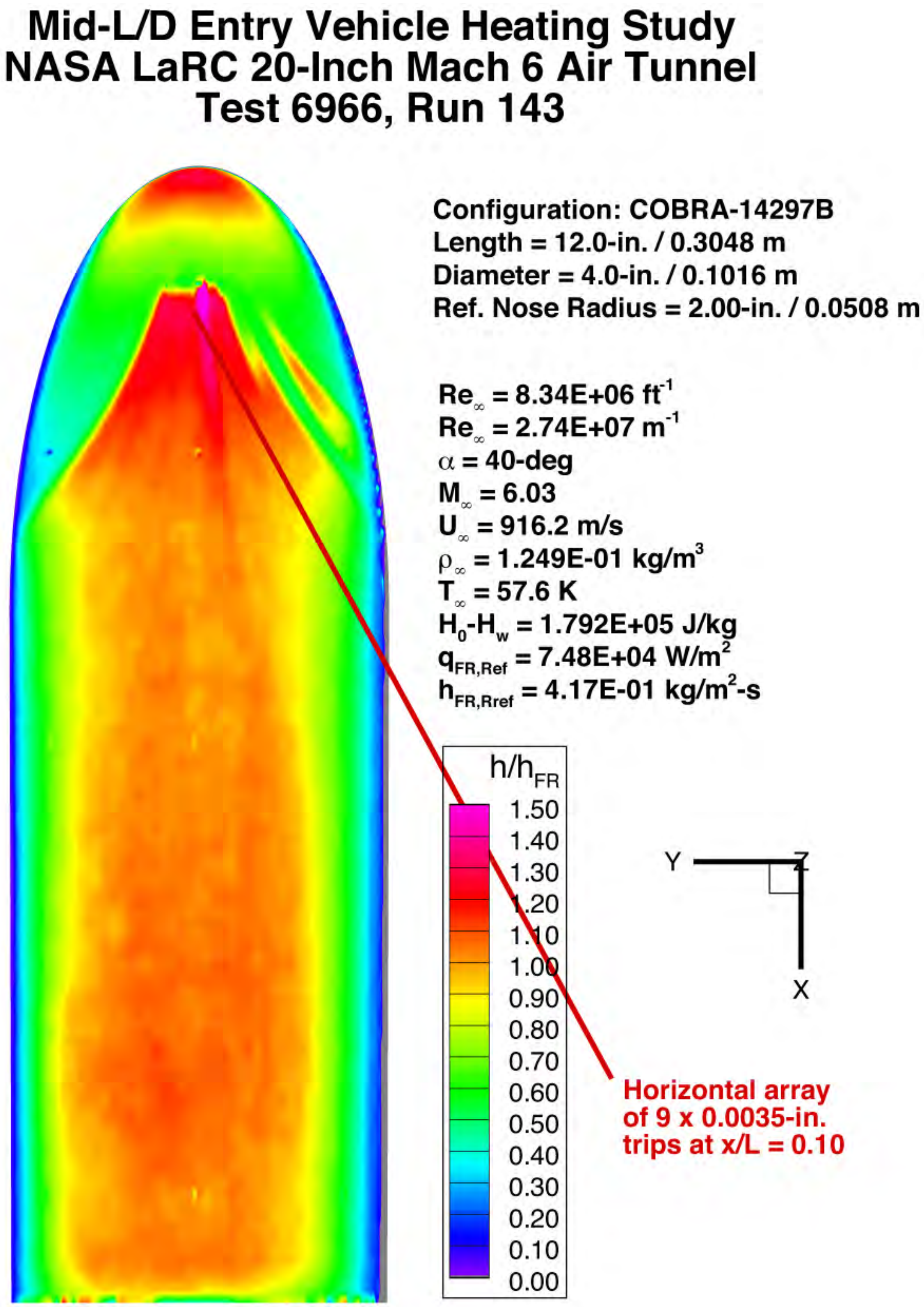

Figure 223. Run 143 Heating Data, COBRA-14297B (Model C-3), $Re_\infty = 8.34\times10^6$/ft, Trips at *x*/*L*=0.10

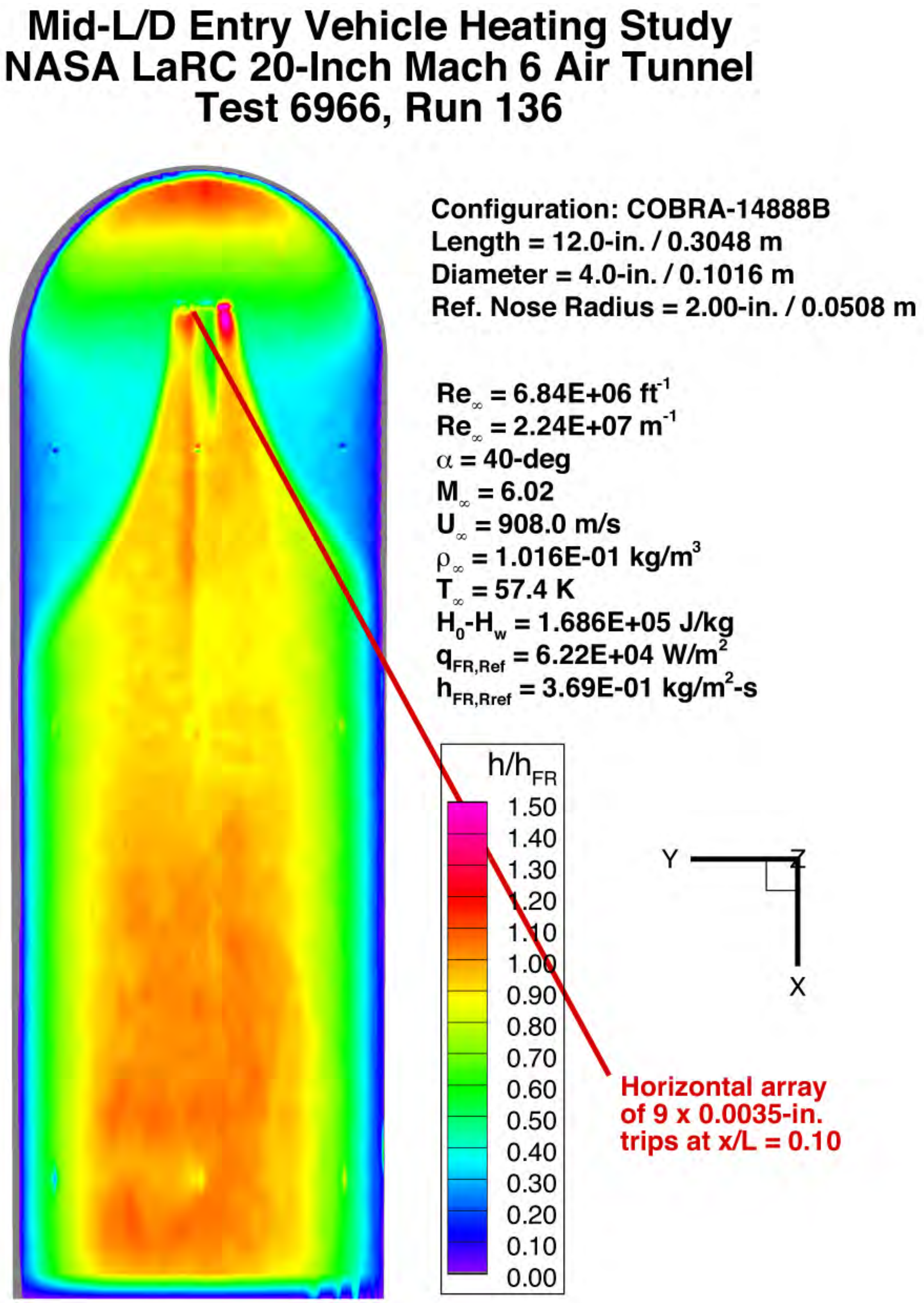

Figure 224. Run 136 Heating Data, COBRA-14888B (Model D-3), Re_∞=6.84×10^6/ft, Trips at *x*/*L* =0.10

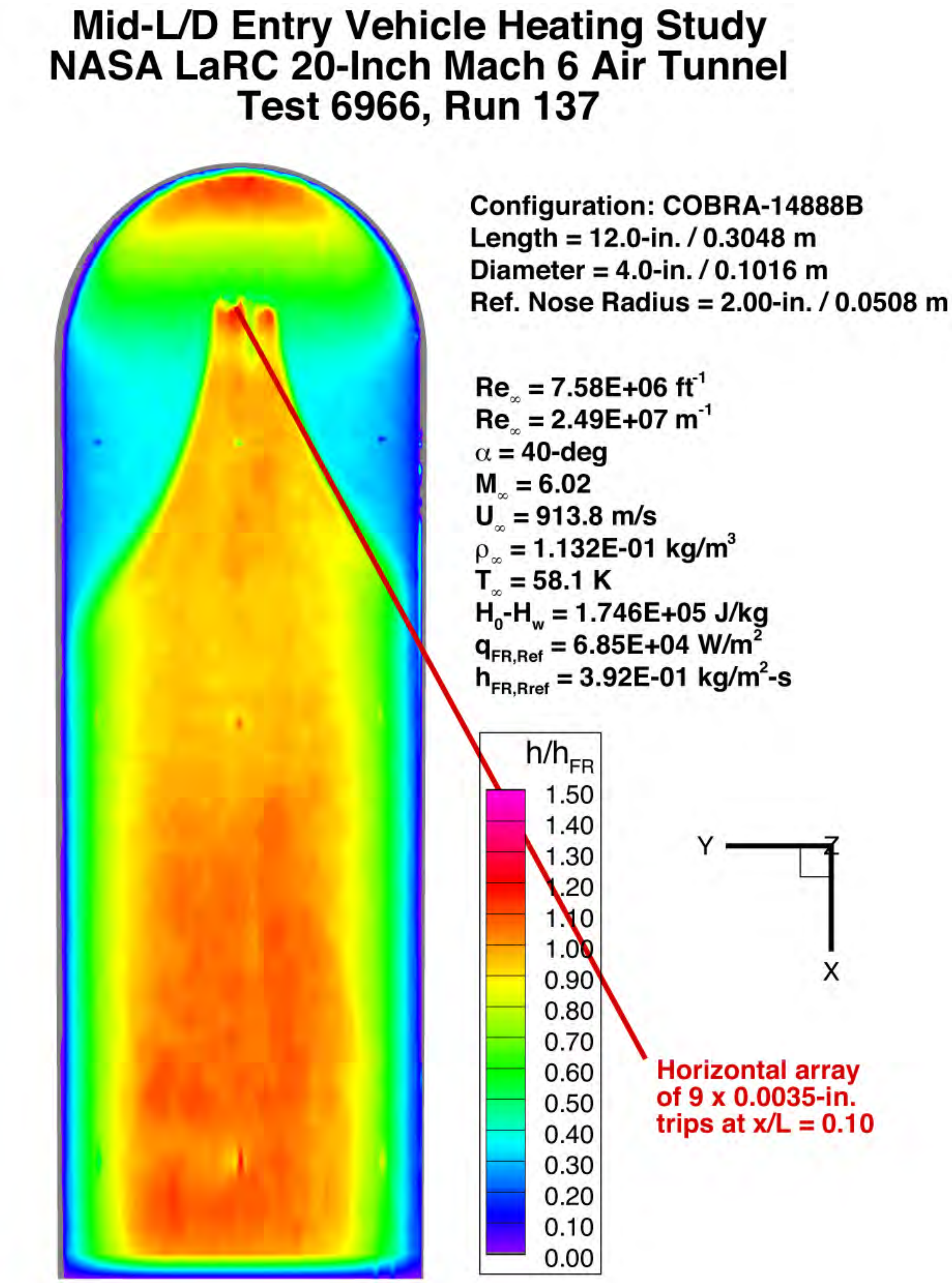

Figure 225. Run 137 Heating Data, COBRA-14888B (Model D-3), $Re_\infty=7.58\times10^6$/ft, Trips at *x*/*L*=0.10

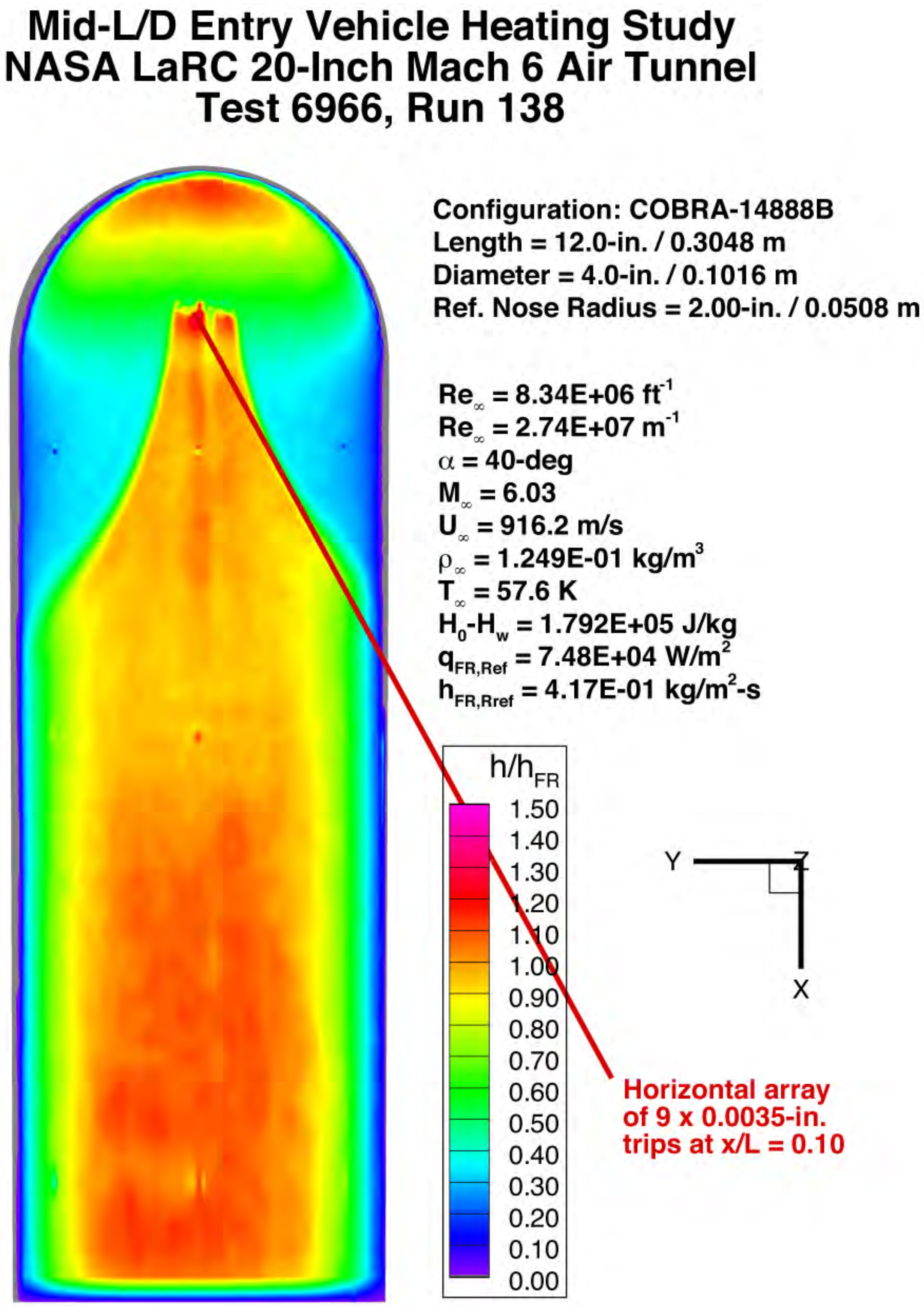

Figure 226. Run 138 Heating Data, COBRA-14888B (Model D-3), Re_∞=8.34×10^6/ft, Trips at *x*/*L*=0.10

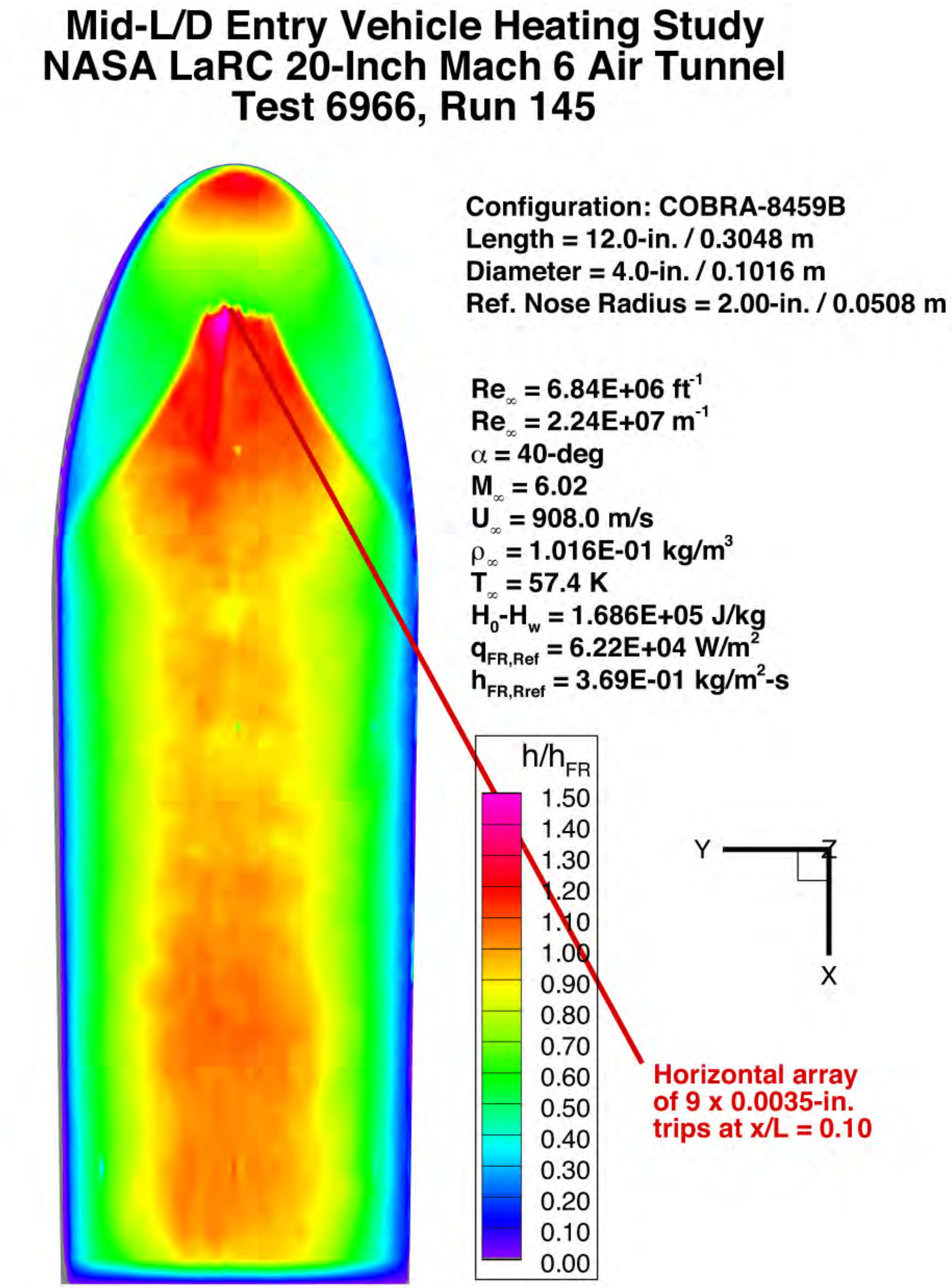

Figure 227. Run 145 Heating Data, COBRA-8459B (Model E-2), $Re_\infty=6.84\times10^6$/ft, Trips at *x*/*L*=0.10

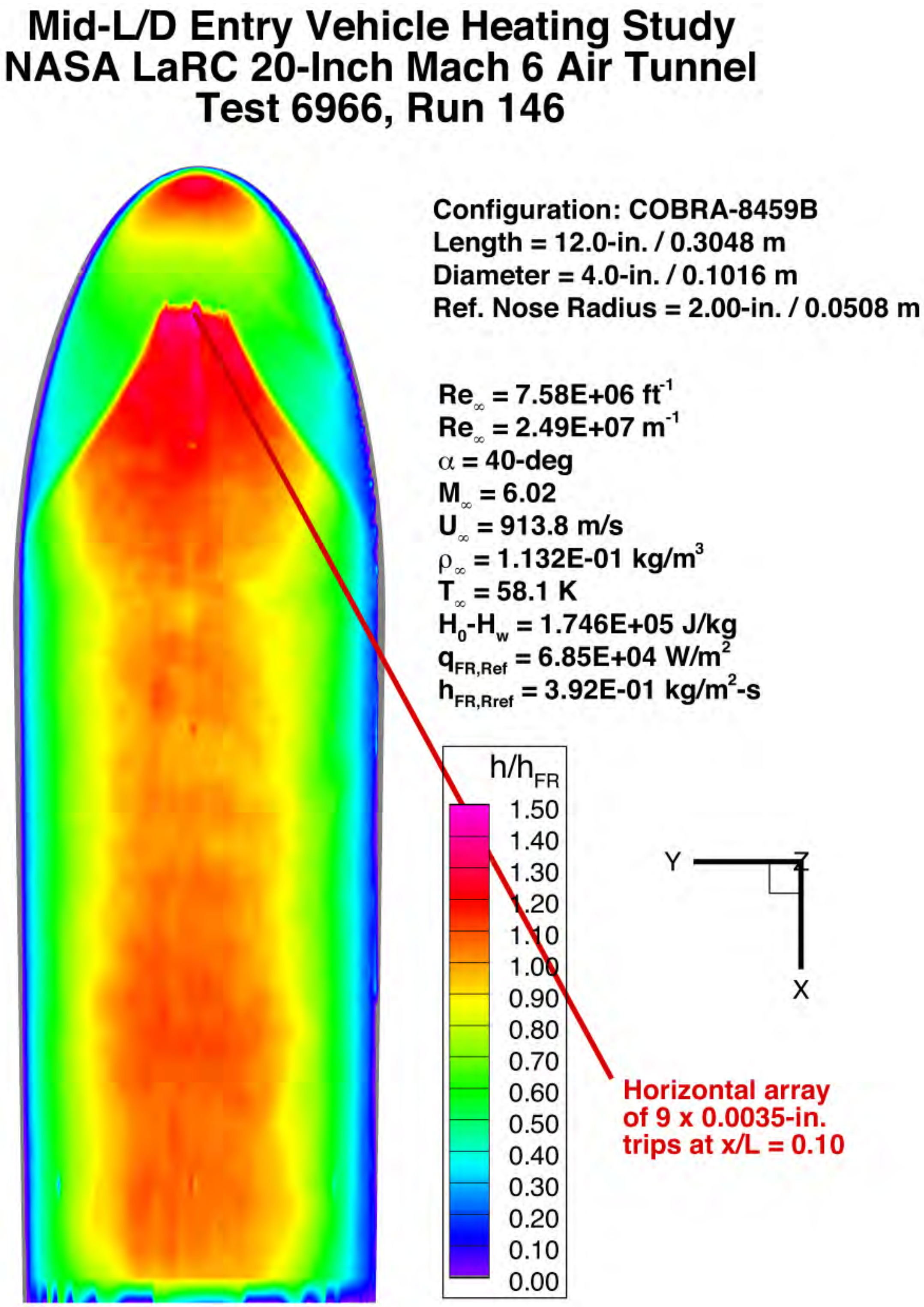

Figure 228. Run 146 Heating Data, COBRA-8459B (Model E-2), $Re_\infty=7.58\times10^6$/ft, Trips at *x*/*L*=0.10

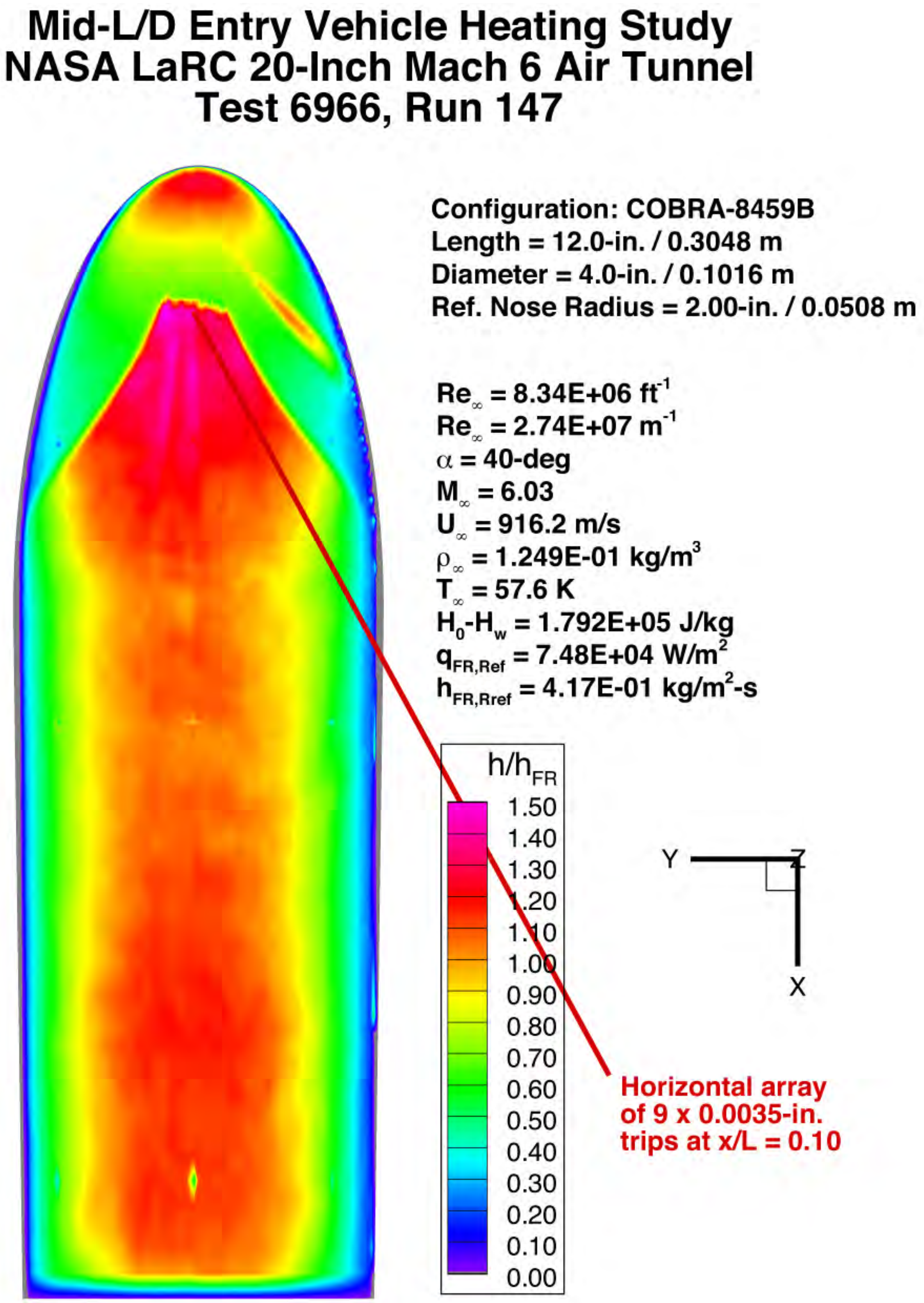

Figure 229. Run 147 Heating Data, COBRA-8459B (Model E-2), Re_∞=8.34×10^6/ft, Trips at *x*/*L*=0.10

REPORT DOCUMENTATION PAGE

Form Approved
OMB No. 0704-0188

1. REPORT DATE *(DD-MM-YYYY)*
01- 11 - 2014

2. REPORT TYPE
Technical Memorandum

3. DATES COVERED *(From - To)*

4. TITLE AND SUBTITLE
Experimental Aeroheating Study of Mid L/D Entry Vehicle Geometries:
NASA LaRC 20-Inch Mach 6 Air Tunnel Test 6966

5a. CONTRACT NUMBER

5b. GRANT NUMBER

5c. PROGRAM ELEMENT NUMBER

6. AUTHOR(S)
Hollis, Brian R.; Hollingsworth, Kevin E.

5d. PROJECT NUMBER

5e. TASK NUMBER

5f. WORK UNIT NUMBER
470883.04.07.01

7. PERFORMING ORGANIZATION NAME(S) AND ADDRESS(ES)
NASA Langley Research Center
Hampton, VA 23681-2199

8. PERFORMING ORGANIZATION REPORT NUMBER
L-20433

9. SPONSORING/MONITORING AGENCY NAME(S) AND ADDRESS(ES)
National Aeronautics and Space Administration
Washington, DC 20546-0001

10. SPONSOR/MONITOR'S ACRONYM(S)
NASA

11. SPONSOR/MONITOR'S REPORT NUMBER(S)
NASA/TM-2014-218549

12. DISTRIBUTION/AVAILABILITY STATEMENT
Unclassified - Unlimited
Subject Category 34
Availability: NASA CASI (443) 757-5802

13. SUPPLEMENTARY NOTES

14. ABSTRACT

Aeroheating data on mid lift-to-drag ratio entry vehicle configurations has been obtained through hypersonic wind tunnel testing. Vehicles of this class have been proposed for high-mass Mars missions, such as sample return and crewed exploration, for which the conventional sphere-cone entry vehicle geometries of previous Mars missions are insufficient. Several configurations were investigated, including elliptically-blunted cylinders with both circular and elliptical cross sections, biconic geometries based on launch vehicle dual-use shrouds, and parametrically-optimized analytic geometries. Testing was conducted at Mach 6 over a range of Reynolds numbers sufficient to generate laminar, transitional, and turbulent flow. Global aeroheating data were obtained using phosphor thermography. Both stream-wise and cross-flow transition occured on different configurations. Comparisons were made with laminar and turbulent computational predictions generated with an algebraic turbulence model. Predictions were generally in good agreement in regions of laminar or fully-turbulent flow; however for transitional cases, the lack of a transition onset prediction capability produced less accurate comparisons. The data obtained in this study are intended to be used for prelimary mission design studies and the development and validation of computational methods.

15. SUBJECT TERMS
Boundary-layer transition; Entry vehicle; Heat transfer; Wind tunnel testing

16. SECURITY CLASSIFICATION OF:			**17. LIMITATION OF ABSTRACT**	**18. NUMBER OF PAGES**	**19a. NAME OF RESPONSIBLE PERSON**
a. REPORT	**b. ABSTRACT**	**c. THIS PAGE**			STI Help Desk (email: help@sti.nasa.gov)
					19b. TELEPHONE NUMBER *(Include area code)*
U	U	U	UU	229	(443) 757-5802